# 1. Introduction to Nuclear and Electron Interactions

## 1.1 Dynamic Nuclear Polarization (DNP) and Hyperfine Coupling Constants

**1.1.1 DNP.** Spectroscopic techniques have been developed to provide insight into the subtleties of weak bonding mechanisms and dynamics of molecular interactions in solution. The collision or very weak transient complex between a nitroxyl radical and a closed shell diamagnetic molecule produces an NMR contact shift, which is dependent on the electron-nucleus hyperfine coupling. Morishima has shown that NMR contact shifts are sensitive probes to study the electron unpaired spin distribution on the diamagnetic solvent molecule perturbed by the interaction with the free radicals di-*tert*-butyl nitroxide (DTBN) and α,γ-bis-diphenylene-β-phenylallyl (BDPA).[1-3] The DTBN and BDPA radicals were used as paramagnetic shift reagents in proton NMR spectroscopy. The radicals induced $^{1}H$ and $^{13}C$ contact shifts which served as probes for studying the weak hydrogen-bonding and charge transfer interactions that occur between radicals and various organic or biologically important molecules. The radical used in the current study is 2,2,6,6,-tetramethyl-1-piperidinyloxy (TEMPO). While NMR spectroscopy yields radical induced upfield or downfield contact shift information about the radical-substrate interaction and indicates the preferential site of the interaction,[4] the attitude and distance of the interaction can not be determined. The current project computationally investigates the attitude and distance of TEMPO-substrate interactions by comparing to experimental DNP results performed by Juan Gu,[4] where the substrate is capable of hydrogen bonding or represents a biologically significant molecule.

A liquid-liquid molecular flow transfer ($L^2IT$) DNP technique developed by K.-H. Tsai[5, 6] and Dr. Harry Dorn[6] was used by Juan Gu[4] to determine experimental results presented in later sections. $L^2IT$ DNP provides high magnetic field chemical shift dispersion and insight into the radical receptor interaction at different nonequivalent nuclear positions in the transient complex.[5, 6] The combination of investigations of

nuclear-electron relaxation rates and DNP enhancement yields collision parameters such as correlation times, radical nucleus distances of closest approach and relative magnitude of scalar and dipolar interactions. The potential $^{15}$N DNP enhancements are very large, especially if a strong scalar interaction is present for a compound containing nitrogen.

DNP is a technique in which a NMR signal is observed during the simultaneous irradiation of the electron transition. The intensity of the NMR signal increases from the irradiation of the electron transition providing dynamic information of electron nuclear interactions and molecular motion. The DNP enhancement factor A is

$$A = \frac{\left\langle \hat{I} \right\rangle - I_0}{I_0} = \rho f s \frac{\gamma_S}{\gamma_I} \qquad [1]$$

where $\left\langle \hat{I} \right\rangle$ is the expectation value of the nuclear spin operator $\hat{I}$. The nuclear-electron coupling factor $\rho$ is defined as

$$\rho = \frac{W_2^D - W_0^D - W_0^{SC}}{W_0^D + W_0^{SC} + 2W_1^D + W_2^D} \qquad [2]$$

where $W_i$'s are transition probabilities. The leakage factor $f$ is defined as

$$f = \frac{W_0^D - W_0^{SC} + 2W_1^D + W_2^D}{W_0^D + W_0^{SC} + 2W_1^D + W_2^D + 2W_{10}} \qquad [3]$$

The saturation factor $s$ is defined as

$$s = \frac{S_0 - \left\langle \hat{S} \right\rangle}{S_0} \qquad [4]$$

where $\left\langle \hat{S} \right\rangle$ is the expectation value of the electron spin operator $\hat{S}$.

The nature of the DNP interaction is extremely sensitive to the radical-substituent coupling. The DNP enhancement factor A in the flow system have been calculated using the method developed by Dorn and Tsai.[6] The leakage factor f is determined from the low field spin-lattice relaxation time measurements in the presence and the absence of the free radical TEMPO (2,2,6,6,-tetramethyl-1-piperidinyloxy). The saturation factor s is calculated from an intercept of the plot of the inverse enhancement $A_{obs}^{-1}$ versus microwave power $p^{-1}$. In this way, the ultimate $^1$H and $^{13}$C DNP enhancements $A_\infty$ at 0.33T can be obtained. TEMPO tends to form a transient complex with a N-H group due

to the hydrogen bonding between the amino proton and the N-O group, causing a large scalar enhancement observed at the amino nitrogen.

The hyperfine coupling constant $A_{SI}$ is related to the Fermi contact shift by the relation[7, 8]

$$\Delta_0 = -\frac{\gamma_S}{\gamma_I}\frac{A_{SI}}{4kT} \qquad [5]$$

where $\gamma_s$ is the gyromagnetic ratio of electron and $\gamma_I$ is the gyromagnetic ratio of the nucleus. After obtaining the limiting contact shifts $\Delta_0$, the hyperfine coupling constants A/h are calculated based on equation 5.

Both dipolar and scalar interactions affect time-dependent phenomena such as relaxation processes. The relevant theory for these studies is summarized below.[5, 9-14] The observed nuclear relaxation rate is given by the sum of the radical induced dipolar and scalar contribution as well as the nuclear-nuclear interactions ($1/T_{10}$) as

$$\left(\frac{1}{T_1}\right)_{obs} = \left(\frac{1}{T_1}\right)_{rad} + \left(\frac{1}{T_{10}}\right) = W_0^D + 2W_2^D + W_0^D + W_0^{SC} + 2W_{10} \qquad [6]$$

Therefore, the radical induced relaxation time $(1/T_1)_{rad}$ may be obtained by subtracting the $1/T_{10}$ from the observed relaxation rate $(1/T_1)_{obs}$. In principle, dipolar interactions are always present between the electrons and the nuclei and can be modulated by either translational or rotational diffusion motion of the molecules. In the case of complex formation, the scalar interaction is also a possible relaxation mechanism. A sticking model or a diffusion model may account for the scalar coupling. The exact form of the transition probabilities $W_i$ will depend on the model chosen for modulation. When the receptor and radical molecules form a transient complex, the dipolar coupling can be modulated by rotational tumbling of the associated species and the scalar coupling can be modulated by the "on-off" mechanism of the complex formation. When the conditions $\omega_s\tau_r >> \omega_I\tau_r$ and $\omega_I\tau_r << 1$ are satisfied, and consider $J(\omega_s \pm \omega_I) \approx J(\omega_s)$ the radical induced relaxation rates are given as

$$\left(\frac{1}{T_1}\right)_{rad} = \frac{1}{10}\left(\frac{\mu_0}{4\pi}\right)^2 \frac{\gamma_I^2\gamma_S^2\pi^2\chi}{r^6}\left(\frac{3\tau_C}{1+\omega_I^2\tau_C{}^2} + \frac{7\tau_C}{1+\omega_I^2\tau_C{}^2}\right) + \frac{1}{2}\left(\frac{A}{h}\right)^2 \chi\left(\frac{\tau_{SC}}{1+\omega_I^2\tau_{SC}^2}\right) \qquad [7]$$

$$\left(\frac{1}{T_2}\right)_{rad} = \frac{1}{20}\left(\frac{\mu_0}{4\pi}\right)^2 \frac{\gamma_I^2\gamma_S^2\pi^2\chi}{r^6}\left(4\tau_C \frac{3\tau_C}{1+\omega_I^2{\tau_C}^2} + \frac{13\tau_C}{1+\omega_I^2{\tau_C}^2}\right) + \frac{1}{4}\left(\frac{A}{h}\right)^2 \chi\left(\tau_{SC} + \frac{\tau_{SC}}{1+\omega_S^2\tau_{SC}^2}\right)$$

[8]

where $\tau_r$ is the correlation time for rotation diffusion, $\tau_{SC}$ is the scalar correlation time, r is the average pair radius for the rotating adduct, $\mu_0$ is the permeability constant, $\chi$ is the fraction of time the nuclear spin is in the paramagnetic environment and can be considered as the fraction of associated radical-receptor complex in the fast exchange case, $\omega$ is the Larmor frequency, and $\tau_c$ is the rotational correlation time.

Overall, the relaxation rates of solvent molecules induced by free radicals contain all the important parameters of molecular collision in liquid, such as the radical-solvent closest distances, correlation times associated with radical-solvent molecules interaction, and intermolecular hyperfine constant. Depending on the specific contact between radicals and solvent molecules and on their motional behavior, the nuclear relaxation times show different types of frequency dependence, revealing details of the dynamic nature of the electron-nuclear interaction. Therefore, a set of parameters of solvent-solute interaction can be obtained by studying the radical induced relaxation times.
Almost all previous $^1H$ relaxation studies indicated dipolar interactions dominate between hydrogen and electron regardless of the free radical or the solvent employed. One exception is in a study by Bates[15] for the interactions $(CF_3)_3COH$:TEMPONE(4-oxo-2,2,6,6-tetramethylpiperidino-oxy) and $C_6F_5OH$:TEMPONE where a significant scalar interaction of the fluorine with the unpaired electron exists.

The results can be described in terms of a dipolar interaction modulated by either a translational diffusion or, in the case of complex formation, a rotational diffusion. By subtracting $(1/T_{10})$ from $(1/T_1)_{obs}$ at a given field strength, $(1/T_1)_{rad}$ can be obtained.

If it is assumed that the complex undergoes isotropic rotational diffusion and the nitroxyl radical is bound in a 1:1 complex to a solvent molecule $(1/T_1)_{rad}$ is given by

$$\left(\frac{1}{T_1}\right)_{rad} = \frac{1}{10}\left(\frac{\mu_0}{4\pi}\right)^2 \frac{\gamma_I^2\gamma_S^2\pi^2\chi}{r^6}\left(\frac{3\tau_C}{1+\omega_I^2{\tau_C}^2} + \frac{7\tau_C}{1+\omega_I^2{\tau_C}^2}\right) \qquad [9]$$

where $\chi$ is the fraction of the complex which is taken from the chemical contact shift measurement. The radical induced relaxation rates at different magnetic frequencies can be fitted to this equation using a nonlinear regression program, giving the rotational

correlation time $\tau_C$ and the hydrogen bond length r between the proton and the nitroxyl group.

Compared to a hydrogen, a carbon nucleus is more sensitive to scalar hyperfine interaction; therefore, the radical induced $^{13}C$ relaxation rate may be treated by a combination of the rotational model for the dipolar interaction and the sticking model for the scalar interaction based on equations 9 and 10. Under the condition of $\omega_I^2\tau^2 << 1$ and $\omega_S^2\tau >> 1$, and the difference between $(1/T_1)_{rad}$ and $(1/T_2)_{rad}$ is given as

$$\left(\frac{1}{T_2}\right)_{rad} - \left(\frac{1}{T_1}\right)_{rad} = \frac{1}{20}\left(\frac{\mu_0}{4\pi}\right)^2 \frac{\gamma_I^2\gamma_S^2\pi^2\tau_{C\chi}}{r^6} + \frac{1}{4}\left(\frac{A}{h}\right)^2 \chi\tau_{SC} \qquad [10]$$

Therefore, the scalar correlation time $\tau_{SC}$ may be determined based on equation 10 if all other parameters are known.

**1.1.2 Hyperfine Coupling Constant.** There are both dipolar and scalar couplings present for a nuclear-electron interaction.[5] This section will focus on the scalar coupling. The term "scalar" comes from the scalar product of $\hat{I}$ and $\hat{S}$ in equation 11.

$$\hat{H}_{SI}^{Sc}(t) = A_{SI} \cdot \hat{I} \cdot \hat{S} \qquad [11]$$

where

$$A_{SI} = -\left(\frac{8\pi}{3}\right)\gamma_S\gamma_I\left|\Psi(0)\right|^2 \qquad [12]$$

$A_{SI}$ is the hyperfine coupling constant, $\hat{I}$ is the nuclear spin operator, $\hat{S}$ is the electron spin operator, and $\left|\Psi(0)\right|^2$ is the square of the electronic wave function evaluated at the nucleus. The hyperfine coupling constant evaluated for a neutral atom ($A_0$) is a good indication of the tendency for a nucleus to exhibit a scalar coupling in a molecular system.[5, 16] Table 1 shows the hyperfine coupling constants ($A_0$) for some common nuclei. In the table, $^{19}F$ and $^{31}P$ exhibit a large $A_0$, and therefore have a tendency for scalar interactions. However, the $^{1}H$ nucleus has a small $A_0$ and exhibits a lower tendency for scalar interactions.

**Table 1.** Hyperfine coupling constants for common nuclei.[16]

| Nucleus | $A_0$ (MHz) |
|---|---|
| $^{1}H$ | 1420 |
| $^{13}C$ | 3110 |
| $^{15}N$ | -2160 |
| $^{19}F$ | 47910 |
| $^{31}P$ | 10178 |

This interaction occurs if unpaired electron spin density on the free radical is transferred to the solvent nuclei during the collision. Therefore, this mechanism is also called contact coupling. The term "contact" comes from the contact of the electron and nucleus. Contact interaction was first introduced by Fermi.[17] The interaction is isotropic because there is no directional aspect to the contact of the nuclear and electron spin. The hyperfine coupling constant is dependent on the sample system and the nucleus monitored.

Two mechanisms for scalar coupling are possible: exchange polarization and complex formation. First, exchange polarization: Intermolecular coupling involves the unpaired electron and the magnetic nucleus on different molecules. During a collision, the unpaired electron may slightly unpair the electrons at the magnetic nucleus of the solvent on which some spin density is transferred. The degree of the polarization depends on the time of the contact and the relative angle of orientation of the two colliding species. Complex formation occurs when the electrons of both molecules become delocalized during contact. Hence, the unpaired electron perturbs the substrate molecule, causing the electron density to change, and consequently the hyperfine constant.

In an earlier study, the intermolecular hydrogen bond between a proton donor solvent and nitroxyl radical was studied using *ab initio* Hartree-Fock MO (molecular orbital) calculations.[18] Methanol was the solvent under investigation, and two nitroxyls were used: DTBN (di-tert-butyl nitroxide, $[(CH_3)_3C]_2NO$) radical and DMNO (di-methyl nitroxide, $(CH_3)_2NO$) radical. The unrestricted Hartree-Fock method was used with the STO-3G and 6-31G(d,p) basis sets. Four types of geometrical arrangements were used

for the proton donor-nitroxide radical bimolecular systems $CH_3OH$ and DMNO, and also $CH_3OH$ and DTBN. Figure 1 illustrates the four arrangements for the $CH_3OH$ and DTBN system (the $CH_3OH$ and DMNO system is similarly arranged). Figure 1(a) represents hydrogen interaction to the π-orbital of oxygen, Figure 1(b) represents hydrogen interaction to the π-orbital of nitrogen, Figure 1(c) represents hydrogen interaction at various angles ($0<\theta<90°$) to the σ-orbital of oxygen, and Figure 1(d) represents hydrogen interaction at various angles ($0<\theta<90°$) to the π-orbital of oxygen.

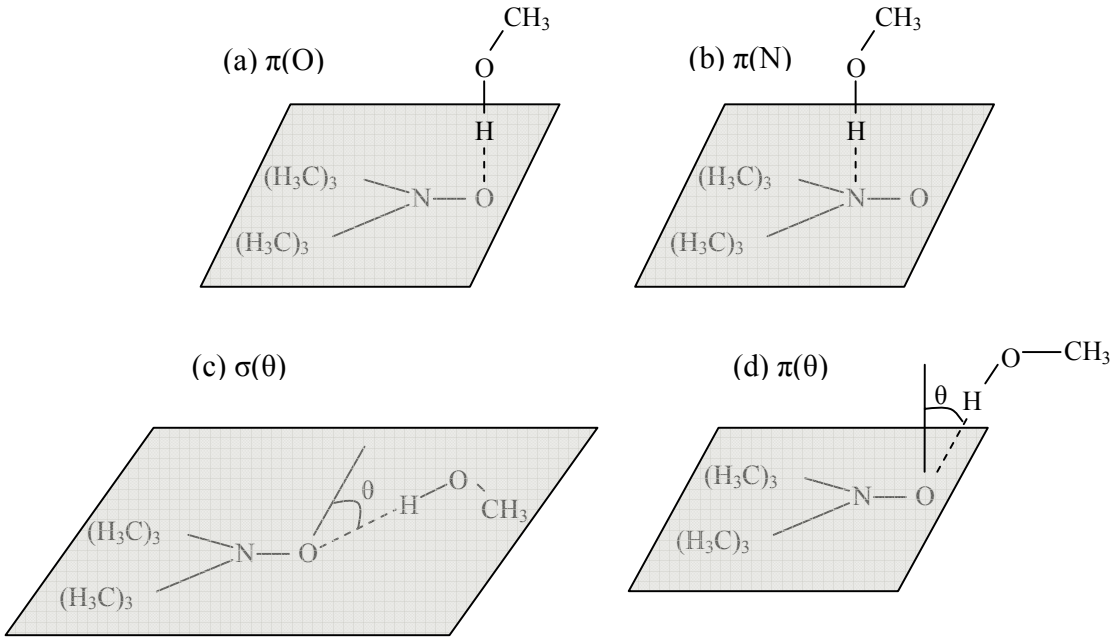


**Figure 1.** Four geometrical arrangements of the $CH_3OH$ and DTBN system.

The π(O) geometry (Figure 1 (a)) was found as the most reasonable arrangement due to the stabilization energy and spin density calculation results.

## 1.2 Chemistry of Nitroxyl Radicals

Nitroxyl radicals are unusually persistent radicals capable of being handled under ordinary conditions in the laboratory.[19-27] Many long-lived nitroxide radicals have been

prepared and isolated, usually stabilized by conjugation with π-electrons of aromatic systems or by protection with bulky substituents (see TEMPO, Figure 2 below).

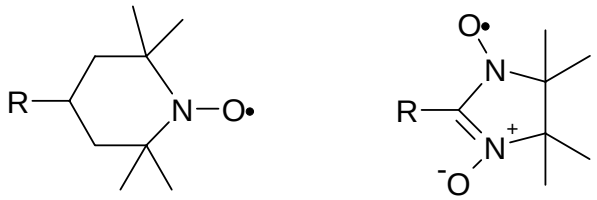


(a) TEMPO radicals (b) Nitronyl nitroxide radicals

**Figure 2.** Nitroxyl radicals.

One class of nitroxyl radicals are TEMPO radicals (Figure 2(a)). A second class is nitronyl nitroxide (2-substituted 4,4,5,5-tetramethylimidazoline-1-oxyl-3-oxide; NN) radicals (Figure 2(b)). From a theoretical point of view, the unpaired electron of TEMPO is localized mainly on the N-O moiety, and delocalized between the nitrogen and the oxygen atoms.

Nitroxyl radicals have been developed and used widely as spin-labeling or spin-trapping reagents for biological studies.[28-36] They have been especially central to the development of molecular-based magnetic materials; among them TEMPO radicals and nitronyl nitroxyl radicals are two representative classes of compounds widely used and studied for this purpose.[37-39] Intermolecular H-bonding has also been studied using nitroxyl radicals and proton donating solvents.[18]

The TEMPO radicals have been used as preparative reagents, and have been recognized as mild oxidants in recent years.[40-43] Also, nitroxyl mediated living radical polymerizations for polymer synthesis have been developed with TEMPO based derivatives.[44]

Electron Paramagnetic Resonance (EPR) and DNP have been used to study nitroxyl radicals in biological fluids.[45, 46] EPR is also used to study spin exchange of nitroxyl free radicals in liquids[47] as well as their use as a spin relaxer.[48] The nitrogen hyperfine splitting constant of the nitroxyl functional group in the Electron Spin Resonance (ESR) spectrum has been shown to be a parameter for solvent polarity

description.[49] Laser Flash Photolysis (LFP) has been used to study the solvent effects on the kinetics of the nitroxyl radical trapping of different carbon radicals.[50]

## 1.3 Magnetic Resonance Imaging (MRI) Relaxivity

MRI is a technique capable of producing remarkable three-dimensional images of internal organs or tissues. When an MRI scan is performed, the patient is positioned in a powerful magnetic field which aligns the nuclear spins of $^{1}H$ nuclei within the body. A perturbing magnetic field (administered through a radio frequency (RF) coil) tips the nuclear spins from the magnetic field. A certain amount of time is required before the protons "relax" back to their aligned state. (For water, this occurs in approximately three seconds.) In $T_1$-weighted imaging, multiple scans are made and compiled with a computer into a black and white image. If the sample possesses higher relaxivity, the image produced is brighter. Also, more scans produce a brighter image; however, that requires an increase in the total scanning time.

A contrast agent lowers the time required for protons to relax. Therefore, more scans can be performed per unit time, yielding amplified signal intensity or an overall decrease in scan time. Also, contrast agents that are absorbed more readily in certain tissue types (*e.g.* cancer cells) would be able to enhance the appearance of those tissues. To design a contrast agent with a higher relaxivity value than the current commercial contrast agents (Magnevist™ and Omniscan™) that enhances MR images could lead to earlier cancer detection and present surgeons with a more intricately detailed image of the tissues they will be working on.

There are two types of relaxation processes: spin-lattice relaxation and spin-spin relaxation.[51-53] Spin-lattice relaxation is the experimentally measured $T_1$ relaxivity. During the magnetization process, energy flows from the nuclei to the surroundings. The surroundings absorbing the transferred energy are referred to as the "lattice." Therefore, "spin-lattice" is the named relaxation time for this energy flow. Spin-spin relaxation is the experimentally measured $T_2$ relaxivity. Each hydrogen has spin and produces a magnetic field around its neighboring hydrogens. Energy is transferred between the spins

in the sample. For a given set of hydrogens, there must be a distribution of local fields at various sites. Therefore, the spins precess about the constant magnetic field with a distribution of frequencies. Following a 90° pulse, all spins are precessing in phase; however, they quickly move out of phase. The net transverse magnetization goes to zero. $T_2$ can be determined by plotting the decay of the magnetization, also known as the free induction decay (FID).

**1.3.1 $T_1$ Relaxivity Measurements.** The relaxation time, $T_1$ is defined as the spin-lattice relaxation time. The relaxivity term $r_1$, is defined as

$$r_1 = \frac{1}{T_1} \qquad [13]$$

with units of $s^{-1}$.

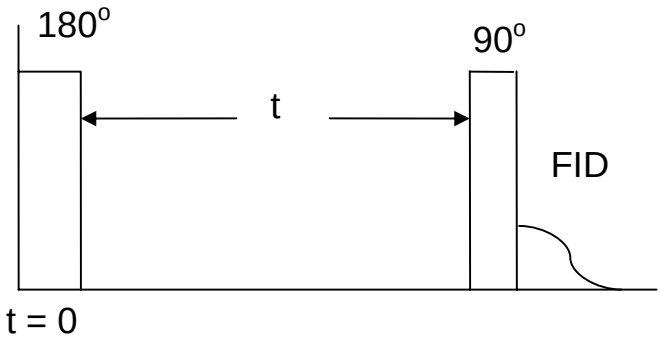


**Figure 3.** Pulse sequence illustration for a $T_1$ measurement experiment.

A 180° – t – 90° – T pulse sequence was used to measure the $T_1$'s (Figure 3), where t is the delay time and T is the repetition time.[54, 55] The t value was varied and measured in milliseconds. The t values are tabulated for each measurement. For each t value, the change in magnetic field measurements (Delta) was recorded and tabulated in Volts. The $T_1$ measurements were then calculated based on the following equations. The general equation is

$$M(t) = Ae^{\left(\frac{-t}{T_1}\right)} + B \qquad [14]$$

where M(t) is the magnetic field, A and B are constants, and t is the time (ms) after the 180° pulse and before the 90° pulse. At t = ∞,

$$M(\infty) = B = M_0 \quad [15]$$

$M_0$ is the maximum signal. It occurs when only a 90° pulse is applied to the sample. At t = 0,

$$M(0) = A + M_0 = -2M_0 \quad [16]$$

Therefore, M(t) is

$$M(t) = -2M_0 e^{\left(\frac{-t}{T_1}\right)} + M_0 \quad [17]$$

Rearranging the equation yields

$$M(t) - M_0 = -2M_0 e^{\left(\frac{-t}{T_1}\right)} \quad [18]$$

or

$$M_0 - M(t) = 2M_0 e^{\left(\frac{-t}{T_1}\right)} \quad [19]$$

Substituting Δ for $[M_o - M(t)]$ and taking the natural log of the equation yields

$$\ln(\Delta) = 2\ln(M_0) - \frac{t}{T_1} \quad [20]$$

Equation 20 is the equation used to calculate $T_1$. The slope of this equation is $-1/T_1$. A plot was made of ln(Δ) vs t. $T_1$ was determined from the slope as discussed earlier. Delta, or ln(Δ), is measured from the instrument.

**1.3.2 $T_2$ Relaxivity Measurements.** $T_2$ is the spin-spin relaxation time and represents relaxation along the transverse axis. A 90° – t – 180° – t – echo sequence is used (Figure 4), where the number of the 180° pulses is varied. Following the 90° pulse, the spins de-phase (free induction decay, FID) because they are precessing at different frequencies. The spin echo occurs due to the spins re-phasing following the 180° pulse

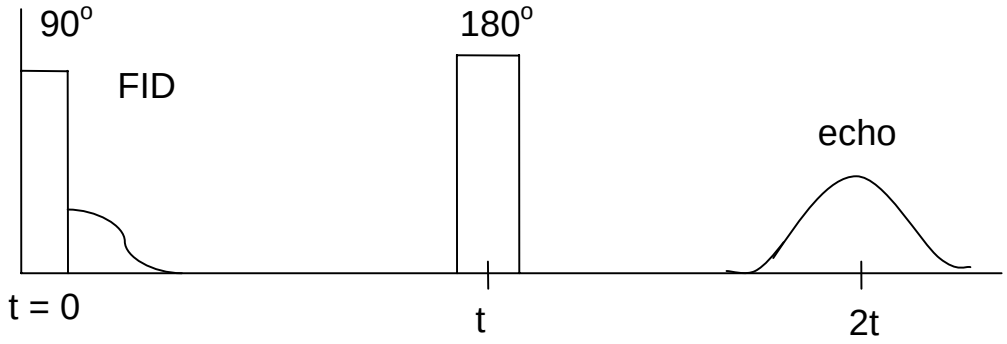


**Figure 4.** Pulse sequence illustration for a $T_2$ measurement experiment.

along the transverse plane.[52] The equations determining $T_2$ also begin with equation 14.

At t = ∞,

$$M(\infty) = B = 0 \qquad [21]$$

At t = 0,

$$M(0) = A + B = -M_0 \qquad [22]$$

Therefore, M(t) is

$$M(t) = M_0 e^{\left(\frac{-t}{T_2}\right)} \qquad [23]$$

Taking the natural log of each side and rearranging equation 23 yields

$$\ln(M(t)) = \ln(M_0) - \frac{t}{T_2} \qquad [24]$$

M(t) is measured for each 180° pulse. Then t is plotted versus M(t) and the slope is $1/T_2$.

Relaxivity, $r_2$, is defined as

$$r_2 = \frac{1}{T_2} \qquad [25]$$

where $r_2$ is in $s^{-1}$.

The $r_1$ and $r_2$ relaxivities previously discussed were in units of $s^{-1}$, which are not concentration dependent. For medical applications, the concentration of each species is critical to determine the effectiveness of a MRI contrast agent. Therefore, the relaxivities measured in this work, $r_1$ ($s^{-1}$) and $r_2$ ($s^{-1}$), are plotted with respect to concentration (mM). Consequently, the concentration dependent relaxivities tabulated and presented in latter sections, are $r_1$ and $r_2$ with units of $mM^{-1}s^{-1}$.

## 1.4 MRI Contrast Agents and Endohedral Metallofullerenes

**1.4.1 MRI Contrast Agents.** The dependence of $^1$H NMR signal intensity on tissue and water relaxation times is the basis of image enhancement using paramagnetic MRI contrast agents. Pulsed NMR techniques are used to measure the spin-lattice and spin-spin relaxation times.[56] The net magnetization of hydrogen spins is aligned parallel with the applied field along the z-axis and is perturbed by the application of one or more radio frequency pulses. The magnetization component along the z-axis relaxes back to its equilibrium value with an exponential time constant, $T_1$, longitudinal (spin-lattice) relaxation time. The magnetization perpendicular to the z-axis is characterized by the time constant, $T_2$, transverse (or spin-spin) relaxation time, which measures the time for the decay of the transverse magnetization to return to its equilibrium value.

The development of Nuclear Magnetic Resonance (NMR) imaging techniques, Magnetic Resonance Imaging (MRI), prompted the need for a new class of MRI contrast agents. The new contrast agents must enhance the image contrast between normal and diseased tissue and/or indicate the status of organ function or blood flow. The $^1$H NMR image intensity, dependent on nuclear relaxation times, is largely composed of the NMR signal of water hydrogens. Complexes of paramagnetic ions decrease the relaxation times of nearby water hydrogens. In tissue, MRI contrast agents are not visualized directly on the NMR image, but are detected indirectly by changes in proton relaxation behavior. The development of new contrast agents creates exciting challenges for scientists, including the design and synthesis of stable, nontoxic, and tissue-specific metal complexes, as well as the quantitative understanding of their effect on relaxation behavior and biological tissue.

The first use of a contrast agent was suggested by Lauterbur[57] in 1978 at a conference at Virginia Tech. He presented the relaxivity effects of the manganese ion. A human NMR imaging study involving a paramagnetic agent was conducted in 1981 by Young et al.; ferric nitrate was administered orally to enhance the gastrointestinal tract.[58] Carr et al. first demonstrated the diagnostic potential of a paramagnetic contrast agent in 1984; Gd(III) diethylenetriaminepentaacetate [[Gd(DTPA)($H_2O$)]$^{2-}$] was intravenously

administered to patients with cerebral tumors, providing enhancement of the lesion in the region of cerebral capillary breakdown.[59]

There are two common commercial MRI contrast agents that are used to compare with the new potential agents: Magnevist™ Gd-DTPA and Omniscan™ Gd(DTPA-BMA) (see Figure 5). Both commercial agents contain one complexed Gadolinium ion. The $r_1$ and $r_2$ relaxivities are ~4 $mM^{-1}s^{-1}$ at 2.4 T[60] for Omniscan™ and ~4 $mM^{-1}s^{-1}$ at 0.47 T[61] for Magnevist™.

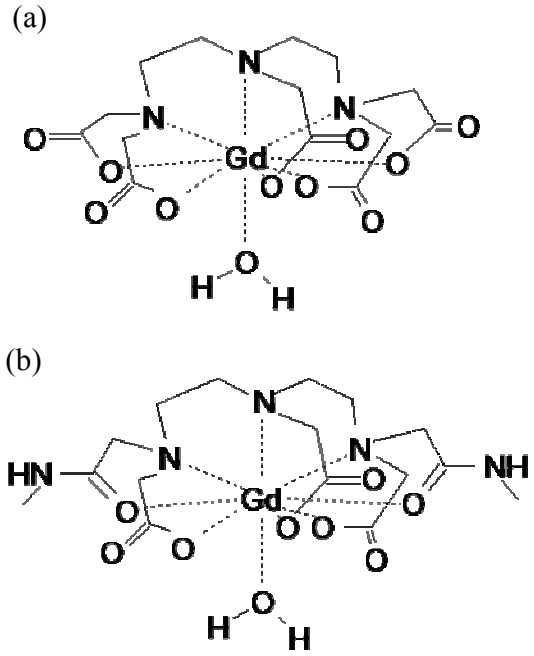


**Figure 5.** Structures of commercial MRI agents (a) Magnevist™ and (b) Omniscan™.

**1.4.2 Fullerenes and Endohedral Metallofullerenes.** Fullerenes were discovered in 1985 by Kroto, et al.[62] Fullerenes are empty carbon cages. Figure 6(a) illustrates the most common fullerene, containing 60 carbon atoms. Endohedral fullerenes are fullerene cages that encapsulate atoms, clusters, or small molecules.[63-68] When one or more metals are encapsulated inside the carbon cage, it is called an endohedral metallofullerene.[69] There can be one or more metals inside. Figure 6(b) illustrates an 80 carbon cage endohedral metallofullerene with a cluster of three gadolinium atoms and one nitrogen atom encapsulated inside, and is denoted $Gd_3N@C_{80}$.

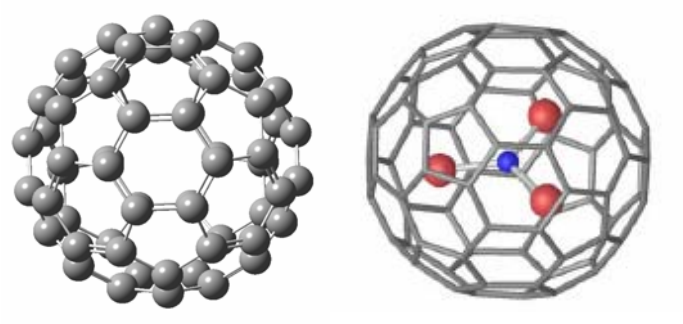

(a) $C_{60}$ (b) $Gd_3N@C_{80}$

**Figure 6.** Example of a fullerene and TNT endohedral metallofullerene.

$Gd_3N@C_{80}$ is an example of a TNT (trimetallic nitride template) endohedral metallofullerene. The endohedral metallofullerene can be covalently chemically functionalized for nonspecific or target delivery in the body.[61, 70-74] The property of an endohedral metallofullerene is dependent on the metal encapsulated inside. Various monometals have been encapsulated, for example La,[63] Tm,[75, 76] Ce,[77] Pr,[78] Gd,[61, 70, 72, 73, 79, 80], Sc,[81] and Eu[82] in a $C_{82}$ cage. Also, numerous metals have been encapsulated as part of a TNT cluster, $M_3N@C_{80}$ (e.g. Gd,[60, 83] Sc,[84, 85] Lu,[60, 86, 87] and Ho[83, 88] in $C_{80}$). The functionalized $Gd_3N@C_{80}$ is under investigation as a potential MRI contrast agent. Most of the key results presented in later sections for this project involve the Gd containing TNT-fMF due to their high water relaxation properties. The Lu and Ho containing TNT-fMFs are being investigated as therapeutic agents using radiolabeled $^{177}Lu$ and $^{166}Ho$.

**1.4.3 Endohedral Metallofullerenes as MRI Contrast Agents.** Many fullerene derivatives have been recognized to be important in the field of medicine.[61, 70-74, 89-92] The encapsulation of metals and metal clusters inside the fullerene cage represents a new area in medical research. The carbon cage has inherent advantages due to the high stability of the carbon cage, as well as resistance to any metabolic cage-opening process, which prevents toxic metal ion release into the surrounding tissue or any other possible surrounding tissue.[93] Various medical applications have been examined for the

endohedral metallofullerenes, such as MRI agents,[61, 70, 72, 73, 94] x-ray contrast agents,[95] and nuclear medicine.[74, 92]

Endohedral metallofullerenes are being studied as potential MRI contrast agents. However, the hydrophobic nature of the endohedral metallofullerenes has hindered the ability to thoroughly study the biological application. Water soluble derivatives are gathering substantial attention because of their potential as MRI contrast agents or therapeutic agents. The metallofullerenes are functionalized in order to be water soluble, and can be denoted TNT-fMF (trimetallic nitride template-functionalized metallofullerene.)

In order for an endohedral metallofullerene to be a prime candidate for a MRI contrast agent, some requirements must be met: (1) high relaxivity, (2) specific distribution, and (3) stability, excretability, and low toxicity. These are explained as follows: (1) The new contrast agent must enhance the proton relaxation rate of water enough to significantly increase the relaxation rate of the target tissue, as much as a 10-20% increase in $r_1$ can be detected by NMR imaging. In order to enhance the proton relaxation of water, the endohedral metallofullerene must be water soluble. (2) The contrast agent should localize for a period of time in the target tissue and preference to nontarget tissues. (3) The toxicity of the agent is related to its stability. The dissociation of the complex agent cannot occur to any significant degree. Toxicity becomes a factor if the complex dissociates or is unstable. If the complex dissociates, the metals are released, subjecting the patient to metal poisoning. Also, the contrast agent should be excreted within hours of administration.

Figure 7 illustrates two new TNT-fMFs that are being studied as potential MRI contrast agents, and each has unique characteristics. Each gadolinium atom has 7 unpaired electrons and so is paramagnetic,[96, 97] whereas lutetium has none, and is diamagnetic.[87, 98] The gadolinium species has significantly enhanced $^1$H water relaxivity compared to Omniscan$^{TM}$,[60] and the lutetium species has a low $^1$H water relaxivity due to the diamagnetic property of the lutetium atoms.[87, 98]

The $r_1$ relaxivities of endohedral metallofullerenes are studied because this relaxivity is a quantitative way to compare the efficiency of the new metallofullerenes to that of other paramagnetic ions and their complexes. The Gd containing TNT-fMFs have

inherent advantages with a maximum of three Gd atoms encapsulated inside the carbon cage, ex. $Gd_3N@C_{80}$ as reported in 2004 and 2005,[96, 97] or with different metals, providing a multi-modal platform, for example a combination of MRI, X-ray, or radiochemical contrast agents (Lu, Ho, and/or Gd).

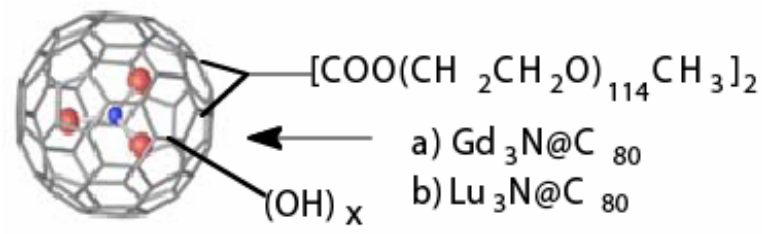


**Figure 7.** Gadolinium and lutetium functionalized endohedral metallofullerenes.

# 2. Calculating TEMPO/Substrate Intermolecular Interactions

## 2.1 Computational Methods and Geometries

Density Functional Theory (DFT) calculations were performed using Gaussian 98 and Gaussian 03.[99, 100] The UB3LYP[101, 102] level of theory with the Chipman DZP + Diffuse (with the first d-type polarization function removed for C, N, and O) basis set were used.[103] First, the geometry of TEMPO was obtained by performing an optimization calculation on the monoclinic crystal structure of TEMPO. The geometry of TEMPO acquired from the optimization calculation was used for the TEMPO/substrate system evaluated. The substrate molecule was drawn in GaussView,[104] followed by a geometry optimization calculation using the same level of theory and basis set as TEMPO. The optimized substrate and TEMPO molecule were then joined together. Hyperfine coupling constants for the TEMPO/substrate molecule systems were calculated at various distances, angles, and sites for each interacting pair to complete a thorough study. Additional computational details are located in the appendix. Figure 8 illustrates the problem that this research is addressing. R could be a hydrogen, carbon, or nitrogen

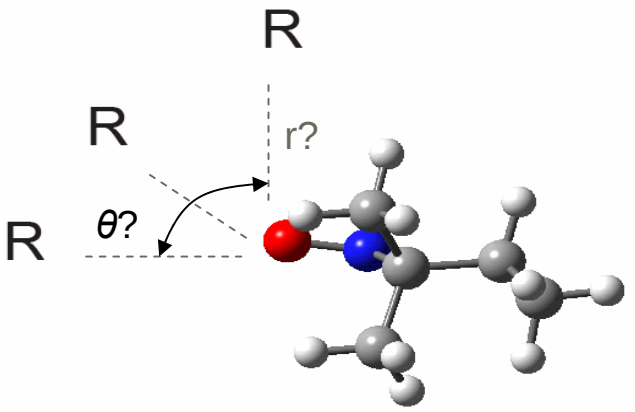


**Figure 8.** Illustration of attitude and distance.

atom from the molecule of interest. Figure 8 models the unknown attitude and distance of interactions in solution.

## 2.2 TEMPO as a Model

The TEMPO molecule was used as a model system to test the reliability of the hyperfine coupling constant calculations and to be confident the experimental coupling constants can be reproduced. Multiple TEMPO structures were calculated to establish the structure that correctly reproduced experimental values reported by Hatch and Kreilick in 1972 from NMR experiments[105] and by Briere et al. by EPR experiments.[106, 107] The following TEMPO structures were calculated: monoclinic crystal structure (single point calculation), orthorhombic crystal structure (single point calculation), optimized monoclinic crystal structure (geometry optimization of the monoclinic crystal structure using Gaussian98 program), optimized orthorhombic crystal structure (geometry optimization of the orthorhombic crystal structure using Gaussian98 program), and optimized GaussView structure (geometry optimization of the TEMPO structure built in GaussView). The Cartesian coordinates for the conformations are located in the appendix. The TEMPO conformation that best reproduced the experimental coupling constants was the optimized monoclinic crystal structure. Table 2 summarizes the computed coupling constants for the various TEMPO structures. As shown in Table 1, the optimized monoclinic crystal structure best reproduces the experimental data. Figure 9 compares the computed hyperfine coupling constants to the experimental coupling constants for the optimized monoclinic crystal structure. The values measured and calculated in Figure 9 represent intramolecular interactions among the individual atoms in TEMPO. As Figure 9 shows, most of the electron density is shared between the oxygen and nitrogen atoms. The values decrease and alternate in sign moving farther away from nitrogen and going around the ring.

**Table 2.** Computed hyperfine coupling constants A (MHz) of the various TEMPO structures.

| (MHz) | Experimental [105-107] | Monoclinic Crystal Structure | Orthorhombic Crystal Structure | Optimized Monoclinic Crystal Struct. | Optimized Orthorhombic Crystal Struct. | Optimized GaussView Structure |
|---|---|---|---|---|---|---|
| α | -10.1 | -9.9 | -11.0 | -9.3 | -11.5 | -9.0 |
| β1 | 13.7 | 10.4 | 12.5 | 12.2 | 12.6 | 12.1 |
| β2 | 2.3 | 1.1 | 3.5 | 1.7 | 3.6 | 1.5 |
| γ | -0.90 | -0.53 | -0.50 | -0.63 | -0.54 | -0.60 |
| N | 45.7 | 29.8 | 28.4 | 33.6 | 29.6 | 32.7 |
| H(β1) | -0.64 | -1.1 | -0.36 | -0.61 | -0.45 | -0.53 |
| H(β2) | -1.1 | -0.72 | -0.81 | -1.0 | -0.87 | -0.97 |
| H(γ) | 0.50 | 0.43 | 0.50 | 0.43 | 0.49 | 0.44 |
| Relative error | | 2.8 | 2.2 | 1.3 | 2.1 | 1.6 |

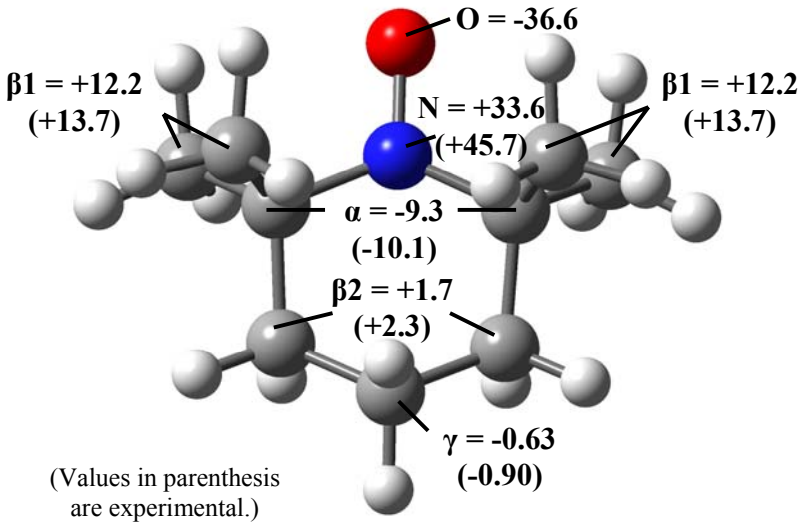


**Figure 9.** Experimental and calculated hyperfine coupling constants (MHz) for TEMPO.

## 2.3 Calculated TEMPO/Substrate Intermolecular Interactions

**2.3.1 Acetonitrile/TEMPO System.** Acetonitrile is a polar molecule, therefore is studied because of its excellent hydrogen bonding properties. Previous calculations have been performed on acetonitrile when complexed to water,[108] methanol,[109] or hydrogen chloride.[110] Rissi et al. performed calculations on the acetonitrile/water system

using four different sets of level of theory and basis set, shown in Figure 10. The hydrogen bonding distance (x) ranges from 2.036-2.106 Å, and the angle (θ) ranges from 162.9-169.7° for the acetonitrile water complex. Coussan et al. studied the acetonitrile hydrogen bond formation with methanol through the nitrogen lone pair using B3LYP/6-311++G(2d,2p) level of theory. Figure 11 summarizes the distance

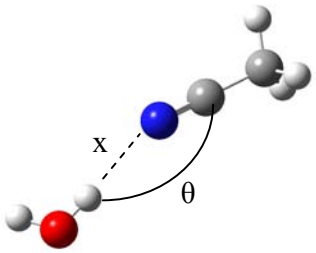


| | MP2/ 6-311++G(d,p) | MP2/ aug-cc-pVDZ | B3LYP/ 6-311++G(d,p) | B3P86/ 6-311++G(d,p) |
|---|---|---|---|---|
| x (Å) | 2.106 | 2.060 | 2.079 | 2.036 |
| θ (°) | 162.9 | 169.7 | 167.3 | 167.4 |

**Figure 10.** Previous data for the acetonitrile/water system.

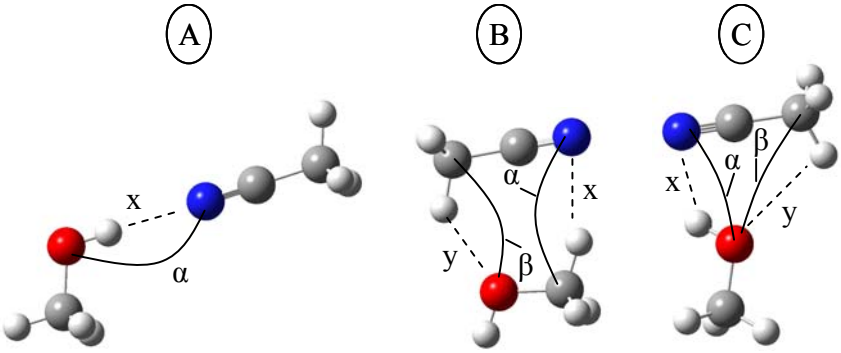


| | A | B | C |
|---|---|---|---|
| x (Å) | 2.0687 | 3.1555 | 2.4241 |
| y (Å) | - | 2.3413 | 2.8100 |
| α (°) | 178.7 | 153.2 | 141.2 |
| β (°) | - | 154.9 | 118.4 |

**Figure 11.** Previous data for the acetonitrile/methanol system.

and angle dependence of the acetonitrile/methanol system. The N-H and O-H bond distances are in the 2-3 Å range and the angles of interaction are from about 115-180° for the acetonitrile/methanol system. George et al. examined the acetonitrile/HCl system using the B3LYP/6-311++G(2d,2p) level of theory. The results are summarized in Figure 12. The N-H bond distance is about 2 Å and the angle of the hydrogen bond formation is 180°. Overall, the distances of the hydrogen bond formation with acetonitrile are approximately 2-3 Å and the angle varies from about 155-180°.

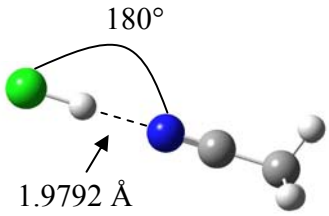


**Figure 12.** Previous data for the acetonitrile/HCl system.

In this work, **s**even orientations were examined to understand the acetonitrile/TEMPO system. (Figure 13) Orientations (a)-(c) are the typical orthogonal,

45 degrees, and straight-on models for acetonitrile in which the hydrogen is interacting with the oxygen of TEMPO, and were calculated at hydrogen-oxygen distances of 0.9Å, 1.1Å, 1.3Å, 1.6Å, 2.1Å, 2.6Å, 3.1Å, 3.6Å, 4.1Å, and 4.6Å. Orientations (e)-(g) are also orthogonal, 45 degrees, and straight-on models; however, the nitrogen of acetonitrile is now interacting with the oxygen of TEMPO, and were calculated at nitrogen-oxygen distances of 0.9Å, 1.1Å, 1.3Å, 1.6Å, 2.1Å, 2.6Å, 3.1Å, 3.6Å, 3.9Å, 4.2 Å, 4.5Å, and 4.8Å. Orientation d models the hydrogen interacting with the nitrogen of TEMPO, and was calculated at hydrogen-nitrogen distances of 2.1 – 4.1 Å with 0.5 Å increments.

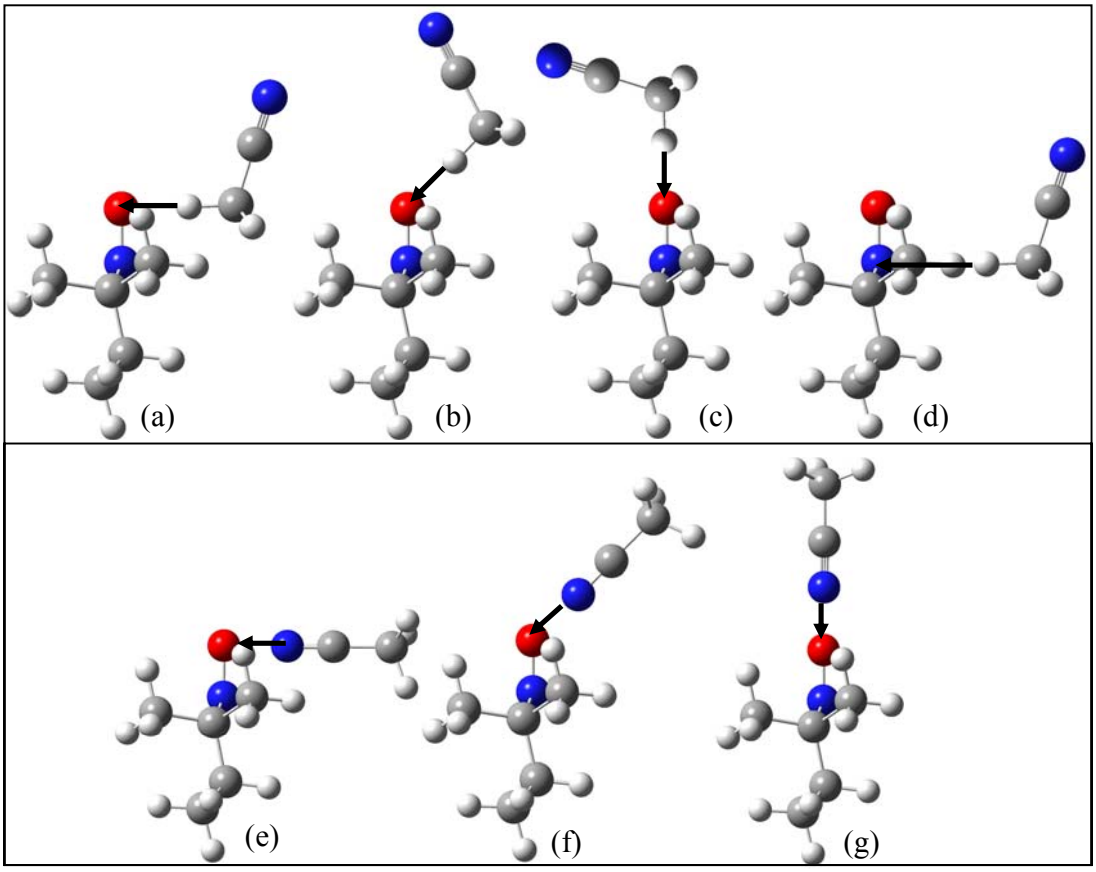


**Figure 13.** Acetonitrile/TEMPO orientations.

The experimental data for the acetonitrile/TEMPO system was obtained by Juan Gu in 1992.[4] Juan Gu measured the paramagnetic induced chemical shifts for $^{15}N$, $^{13}CH_3$, and $^{13}CN$ by varying the concentration of acetonitrile from 0.4-2.0 M in TEMPO using a Varian Unity 400 FT-NMR. The methyl carbon had greater paramagnetic shifts (7.90 to

3.94 ppm) than the cyano carbon (-1.01 to -0.42 ppm) or nitrogen (2.19 to 1.38 ppm). The greater contact shifts of the methyl carbon indicate there is a stronger interaction between the methyl group and the free radical of TEMPO. Therefore, the calculation results are expected to show the interaction site at the methyl carbon end of acetonitrile. Juan Gu also determined the hyperfine coupling constants for $^{13}CH_3$, $^{15}N$, and $^{13}CN$. The methyl carbon has a positive hyperfine coupling constant (0.66 ± 0.04 MHz), whereas the nitrogen exhibits a small negative hyperfine coupling constant (-0.08 ± 0.02 MHz), and the cyanocarbon has a hyperfine coupling constant of 0. Figure 14 presents the computed coupling constant data for orientations (a)-(c), and Figure 15 presents the single point energy curves for those orientations. The minimum energy for each orientation is indicated by an arrow. The energy minimum for orientation (a) is at 2.6Å, and for (b) and (c) is at 2.1Å (Figure 15). The experimental data is represented as a range of about 1 Å in each graph of data, depending on the location of the energy minimum. Only the data of the model interaction is presented here, and subsequent graphs are in the appendix. Due to previous work, the interaction distance was suggested to be approximately 2-3Å.[4, 108-110] Therefore, for orientations that have an energy curve with no local miniumum, the experimental value is estimated to be between 2-3Å.

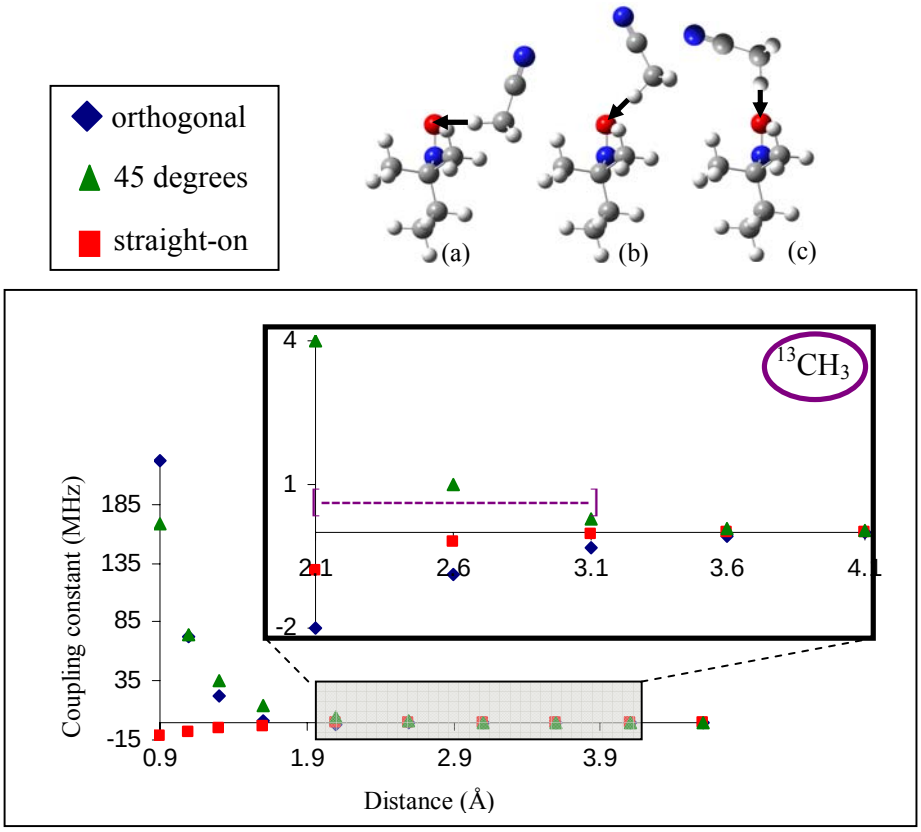


**Figure 14.** Acetonitrile/TEMPO ($^{13}CH_3$) hyperfine coupling constant data for interactions (a), (b), and (c).

Comparing the experimental value to the calculated values only the methyl carbon data is reproduced by the calculations at the 45 degree orientation. (Figure 14) The orientations to the methyl hydrogen are not expected to reproduce coupling constant values on the nitrogen of acetonitrile which is two atoms removed from the methyl carbon. Spin density does not appear to be transferred three bonds away in this case. Nevertheless, the 45 degree orientation reproduces the experimental value of 0.66 between 2.6Å and 3.1Å, which is in the range previously noted for the interaction.

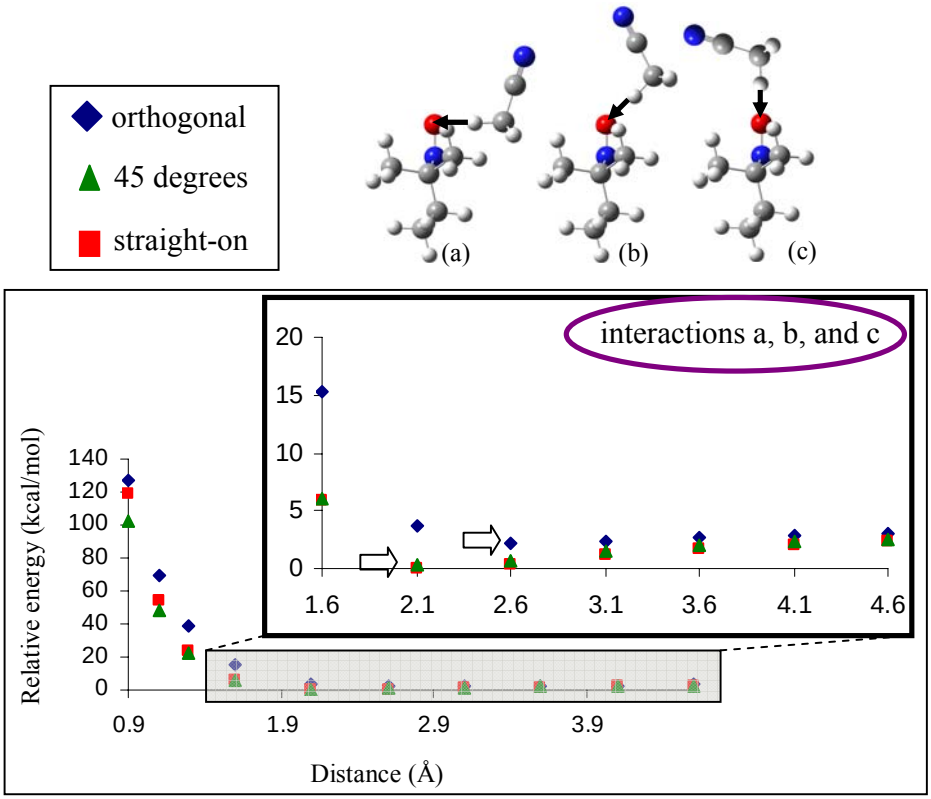


**Figure 15.** Relative energy curves for interactions (a)-(c) (acetonitrile/TEMPO).

Only one orientation calculated reproduced the nitrogen experimental value of -0.08 (interaction g: data in the appendix); however, that value is very small and close to zero. Three orientations reproduced the methyl carbon value of 0.66 ((b),(d), and (f): data for (d) and (f) in the appendix). The 45 degree orientations ((b) and (f)) and the methyl hydrogen to N on TEMPO (d) were the most favored interactions when compared to experiment. However, examining the energy curves, only interaction (b) exhibits a minimum energy. Orientations (d) and (f) both do not have a minimum energy; for interaction (d) that could be due to steric effects when the methyl group of acetonitrile is in proximity to the methyl groups on TEMPO. The hydrogens would repel each other. Similarly with interaction (f), the oxygen and nitrogen atoms would demonstrate a repulsive force between them. Therefore, interaction (b) (Figure 16) best describes the acetonitrile/TEMPO collision, using both minimum energy and reproduction of the $^{13}CH_3$ experimental value. The predicted interaction at the methyl end of acetonitrile by the

experimental contact shift measurements was confirmed by the calculations, and the interaction distance was determined to be 2.1 Å, which is in the range of previous work discussed earlier. The reproducibility of the $^{13}CH_3$ experimental data at the 45° orientation (at the methyl end) may be due to a combination of less steric hindrances

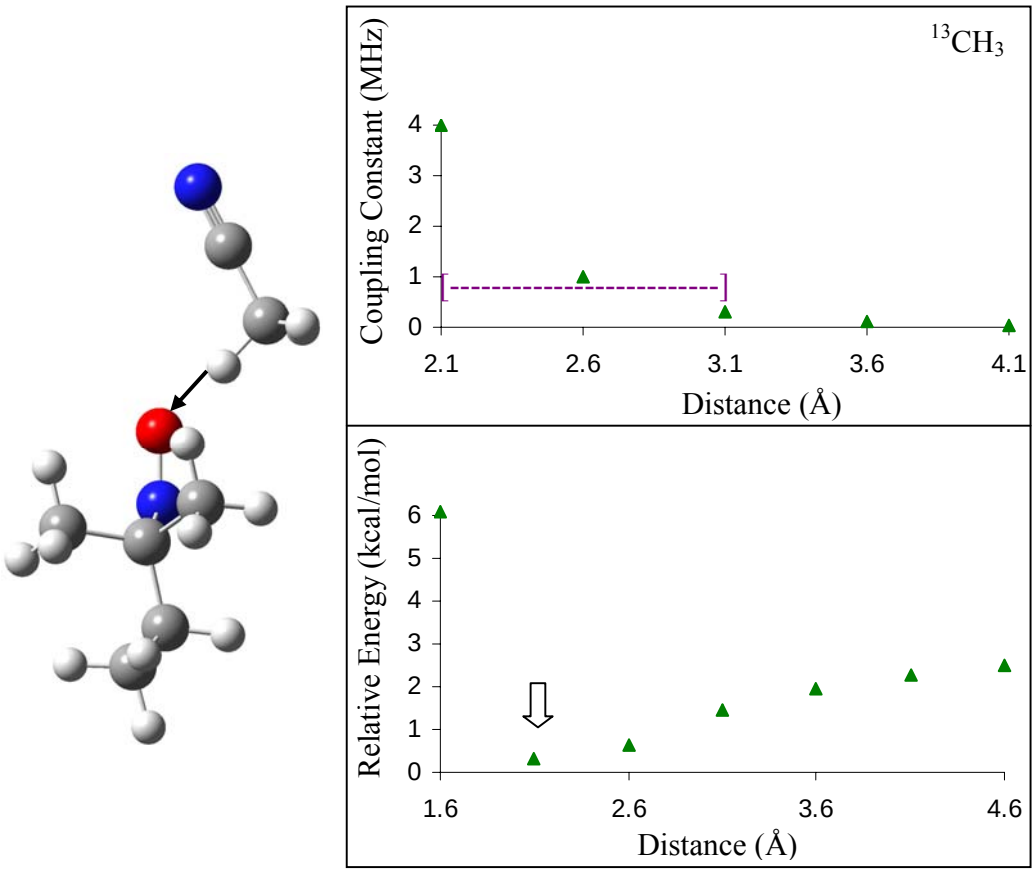


**Figure 16.** Acetonitrile/TEMPO favored orientation summary.

(lower energy) and transference of spin density through a π-orbital. With this premise, the best spin density transfer would occur at the orthogonal orientation (a), where the methyl hydrogen is interacting directly with the π-orbital of the TEMPO oxygen; however, there are more steric interactions between the methyl hydrogens of acetonitrile and the methyl hydrogens of TEMPO. The steric interactions cause the energy to increase for the orthogonal orientation. Therefore, the 45° orientation (Figure 16) has the most balanced combination of less steric interactions and interaction at a π-orbital.

**2.3.2 Acetamide/TEMPO System.** Many biologically important molecules have an amide group (i.e. proteins). Acetamide is studied because it is a smaller representative of biological molecules,[111, 112] and so the N-H bond interactions can be studied more thoroughly using less computational time and resources. Thirteen orientations were calculated for the acetamide/TEMPO system. (Figure 17) Orientations (a)-(c) are orthogonal, 45 degrees, and straight-on, respectively, for a methyl hydrogen interacting with the oxygen on TEMPO. The orientations were calculated at the following hydrogen-oxygen distances: 0.9Å, 1.1Å, 1.3Å, 1.6Å, 2.1Å, 2.6Å, 3.1Å, 3.6Å, 4.1Å, and 4.6Å. Orientations (d)-(f) are orthogonal, 45 degrees, and straight-on, respectively, for the oxygen of acetamide interacting with the oxygen of TEMPO calculated at the following oxygen-oxygen distances: 0.9Å, 1.1Å,1.3Å, 1.6Å, 2.1Å, 2.6Å, 3.1Å, and 3.6Å. Orientations (g)-(i) are orthogonal, 45 degrees, and straight-on, respectively, for an amide hydrogen of acetamide interacting with the oxygen on TEMPO calculated at the same distances noted for orientations (a)-(c). Orientations (j) and (k) model an amide hydrogen of acetamide interacting with the nitrogen in TEMPO calculated at 2.1-4.6 Å, in 0.5 Å increments. The arrows for orientations (j) and (k) are just above the interaction since they would be hidden by the atoms in the structures. Orientation (l) models an interaction between the π-orbital of the acetamide nitrogen with the π-orbital of the TEMPO oxygen, and orientation m models an interaction between the π-orbital of the acetamide nitrogen and the σ-orbital of the TEMPO oxygen. Orientations (l) and (m) were calculated at the following oxygen-nitrogen distances: 1.1Å-4.6Å at 0.5Å intervals. The $-NH_2$ group of acetamide is planar, as is seen in Figure 17. The crystal structure of acetamide determined by Senti et al.[113] confirms the planar structure calculated. The Cartesian coordinates of the calculated acetamide molecule are in the appendix.

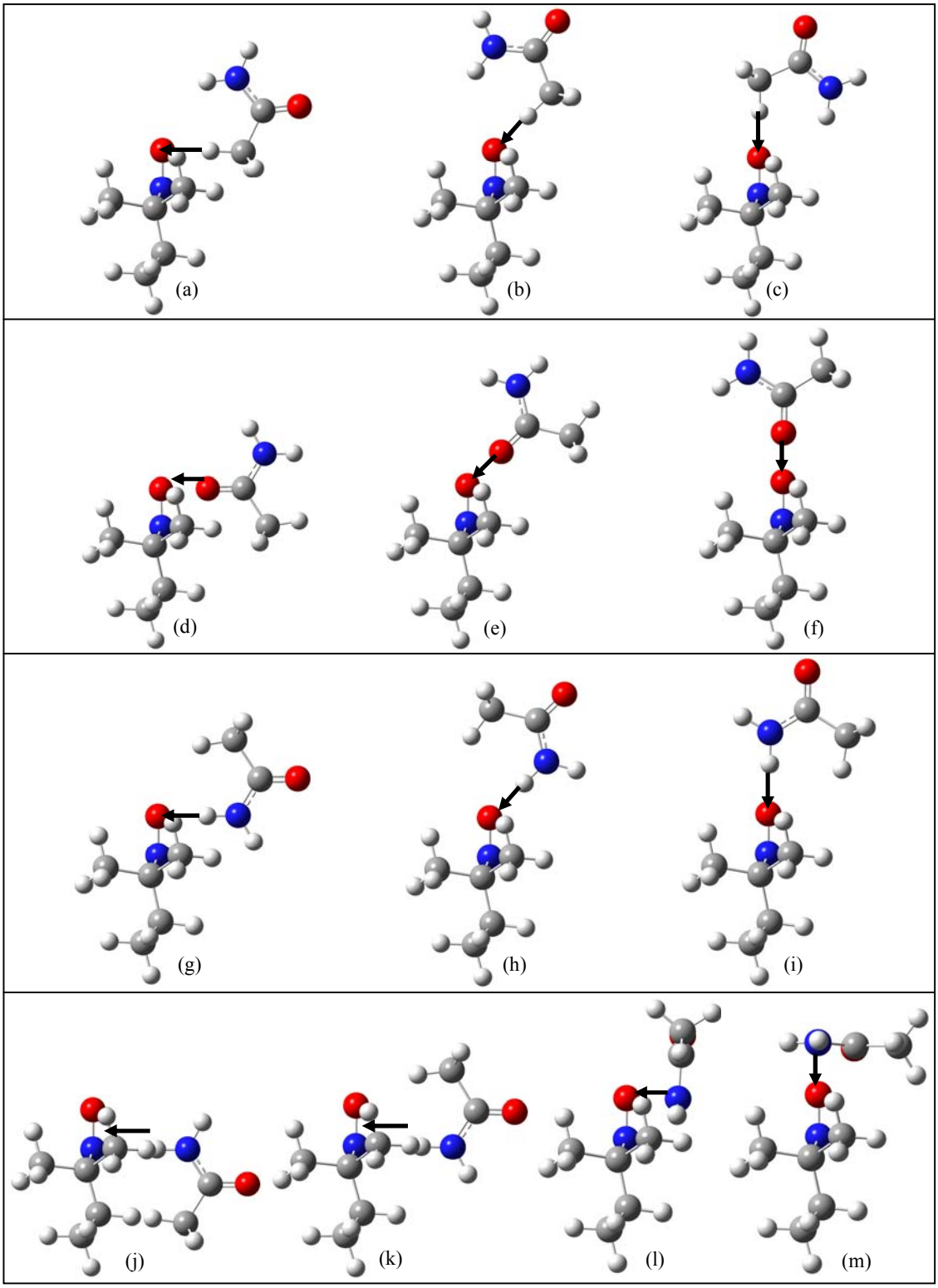


**Figure 17.** Acetamide/TEMPO orientations.

The experimental DNP enhancements for the acetamide/TEMPO system were also measured by Juan Gu in 1992.[4] She measured the paramagnetic induced chemical shifts for $^{13}CH_3$, $^{13}CO$, and $^{15}NH_2$ by varying the concentration of acetamide from 0.05-0.5 M in TEMPO using a Varian Unity 400 FT-NMR. The greater contact shifts of the nitrogen indicate there is a stronger interaction between the amine group and the free radical of TEMPO. The nitrogen had greater paramagnetic shifts (5.99 to 5.10 ppm) than the methyl carbon (0.60 to 0.51 ppm) or the carbonyl carbon (-0.34 to -0.26 ppm). Therefore, the calculation results are expected to show the interaction site at the amide end of acetamide. Juan Gu also determined hyperfine coupling constants for $^{13}CH_3$, $^{13}CO$, and $^{15}NH_2$. The methyl carbon has a positive hyperfine coupling constant (0.16 ± 0.01 MHz), the carbonyl carbon has a hyperfine coupling constant of basically zero (-0.01 ± 0.02 MHz), while the nitrogen has a negative hyperfine coupling constant (-0.5 ± 0.04). The sign of the nitrogen enhancement was confirmed by NMR using $^{15}N$ labeled acetamide.

Figures 18, 19, and 20 illustrate the computed coupling constant data for the acetamide/TEMPO orientations that best model the experimental data, and Figures 21, 22, and 23 show the energy curves for these orientations. Figure 18 illustrates the calculated coupling constant data for interactions (a)-(c). According to the energy plots in Figure 21, the minimum energy occurs at 2.6 Å for orthogonal, 45 degrees, and straight-on. When a methyl carbon is interacting with the TEMPO oxygen at a 45 degree angle, the calculated coupling constant reproduces the experimental value in the correct distance range (2.1-3.1 Å). The 45 degree orientation also reproduces the correct sign on the nitrogen, but not the correct magnitude.

Figure 19 illustrates the calculated hyperfine coupling constants for interactions (g)-(i) (to an amide hydrogen). According to the energy plots in Figure 22, the minimum energy is at 2.1 Å for all three orientations. The data shows that the orthogonal and straight-on orientations reproduce both the methyl carbon and nitrogen experimental data (both sign and magnitude). Figure 20 illustrates coupling constant data for interaction m (to N on acetamide, a nitrogen-oxygen $\sigma$-$\pi$ interaction). According to the energy curve in Figure 23, the energy minimum occurs at 3.6 Å. Calculations of this orientation yield

coupling constants that reproduce the experimental value of the methyl carbon and the nitrogen.

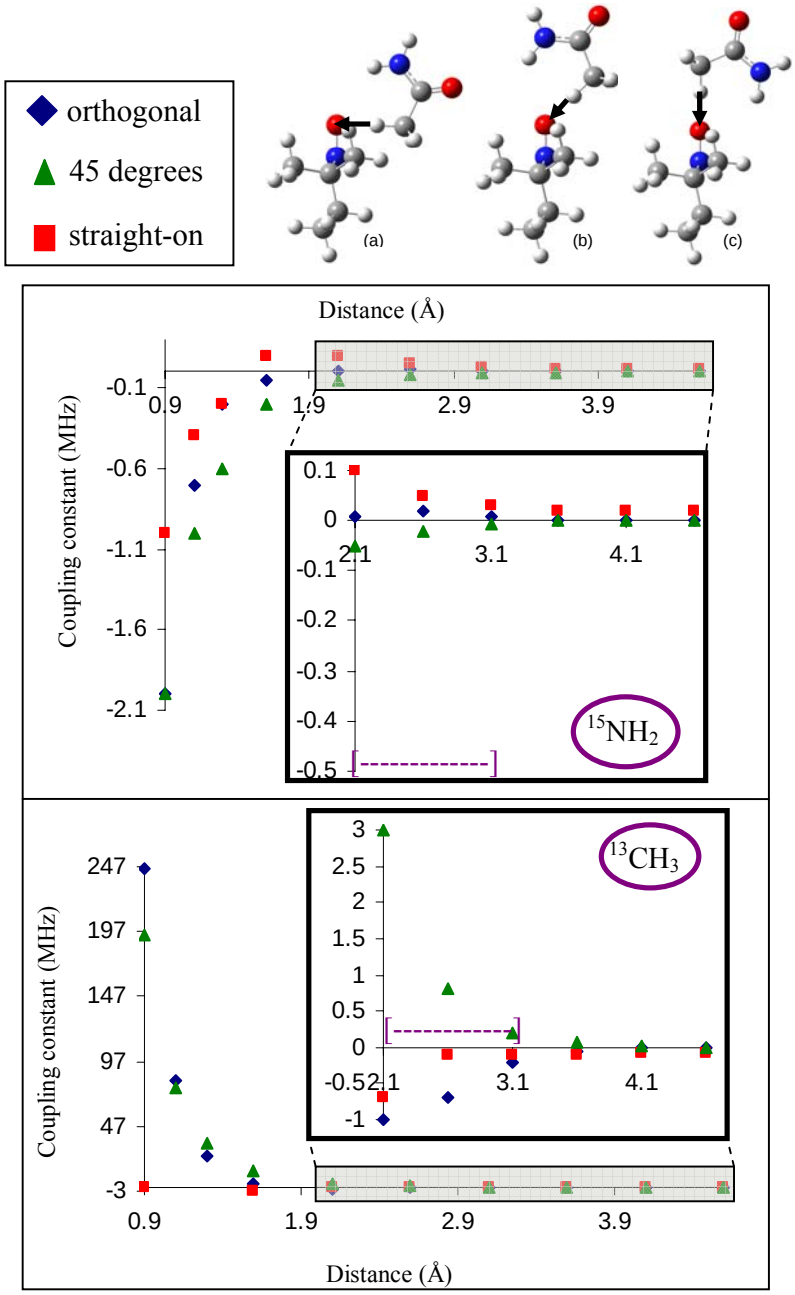


**Figure 18.** Acetamide/TEMPO ($^{15}NH_2$ and $^{13}CH_3$) hyperfine coupling constant data for interactions (a)-(c) (to $^{1}H_3C$).

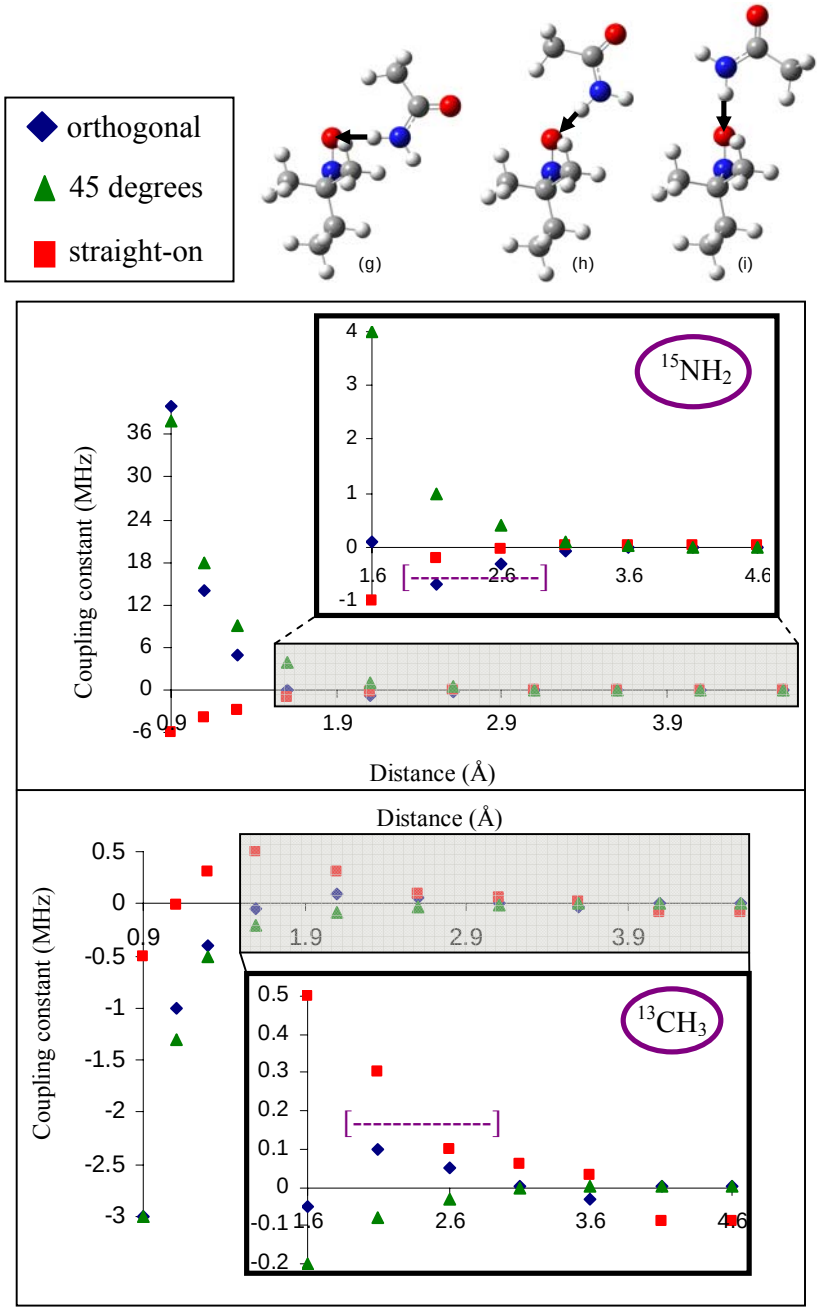


**Figure 19.** Acetamide/TEMPO ($^{15}NH_2$ and $^{13}CH_3$) hyperfine coupling constant data for interactions (g)-(i) (to $^{1}H_2N$).

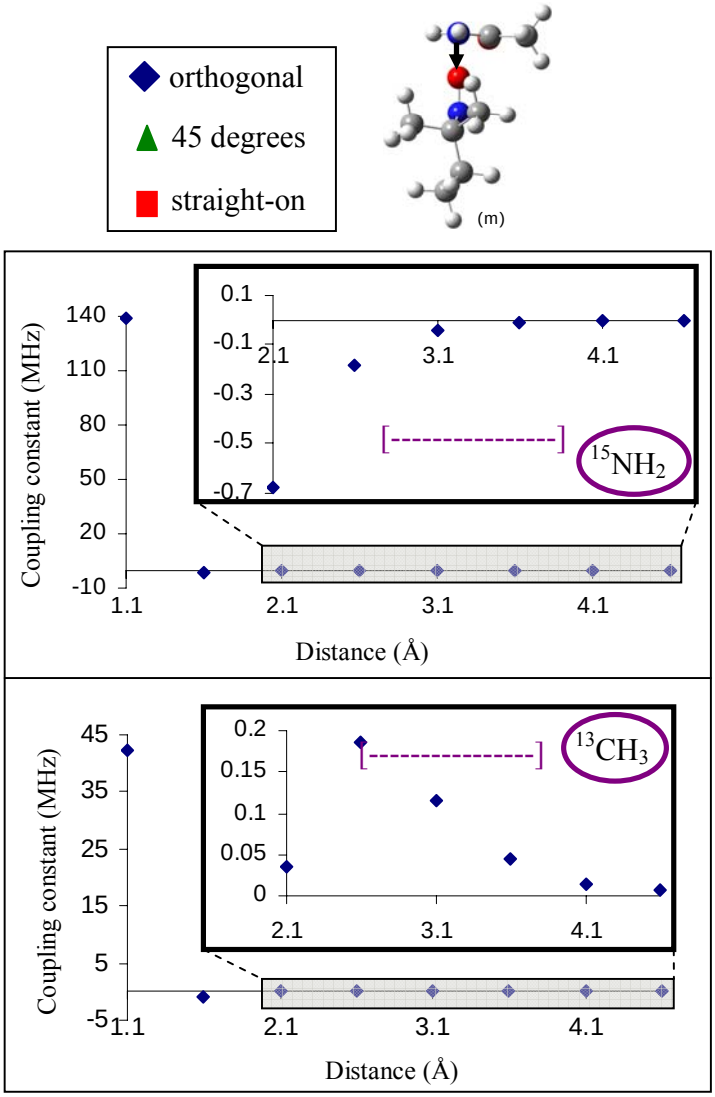


**Figure 20.** Acetamide/TEMPO coupling constant data for interaction (m) (to N on acetamide).

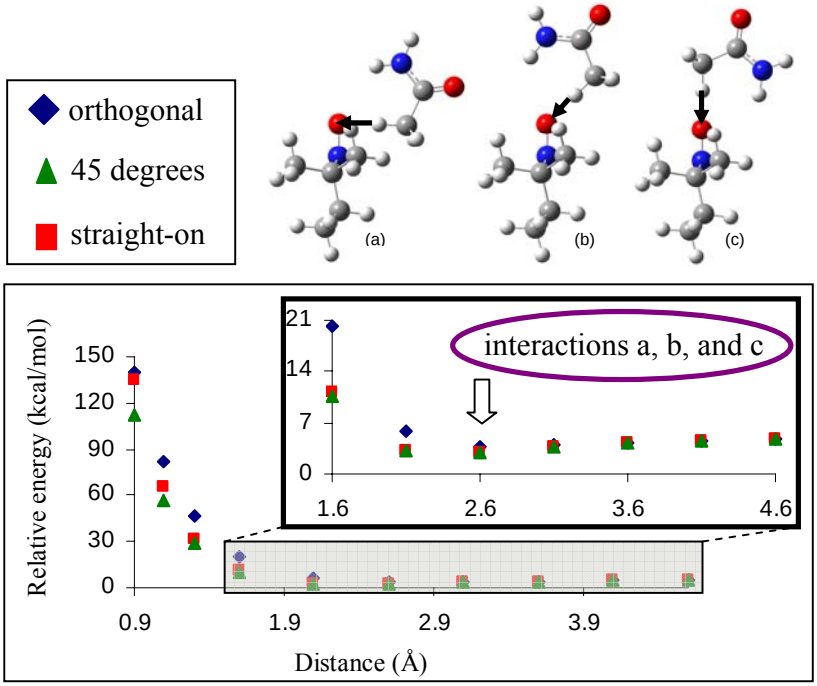


**Figure 21.** Relative energy curves for interactions (a)-(c).

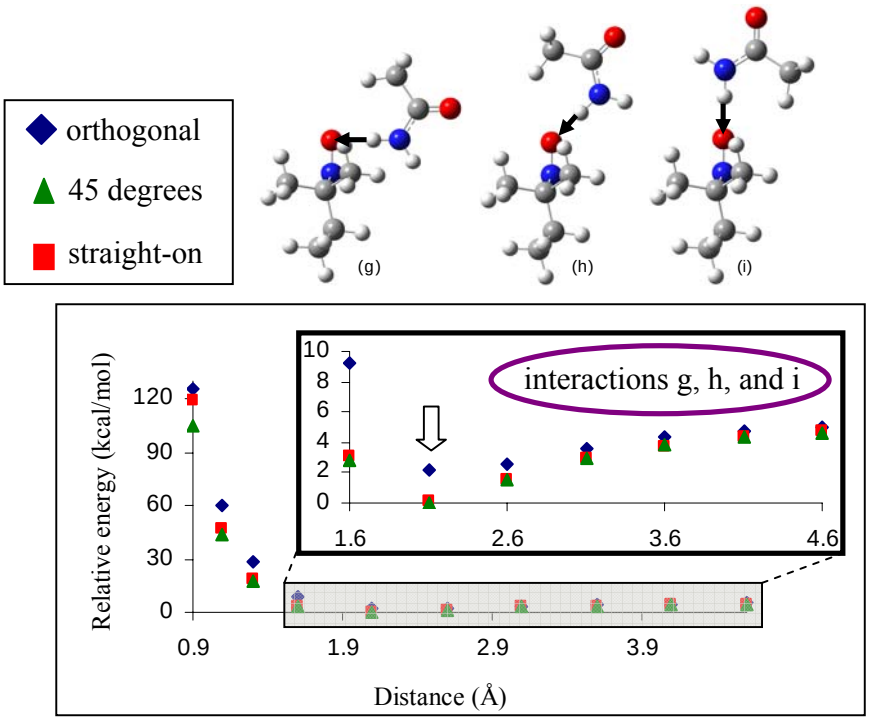


**Figure 22.** Relative energy curves for interactions (g)-(i).

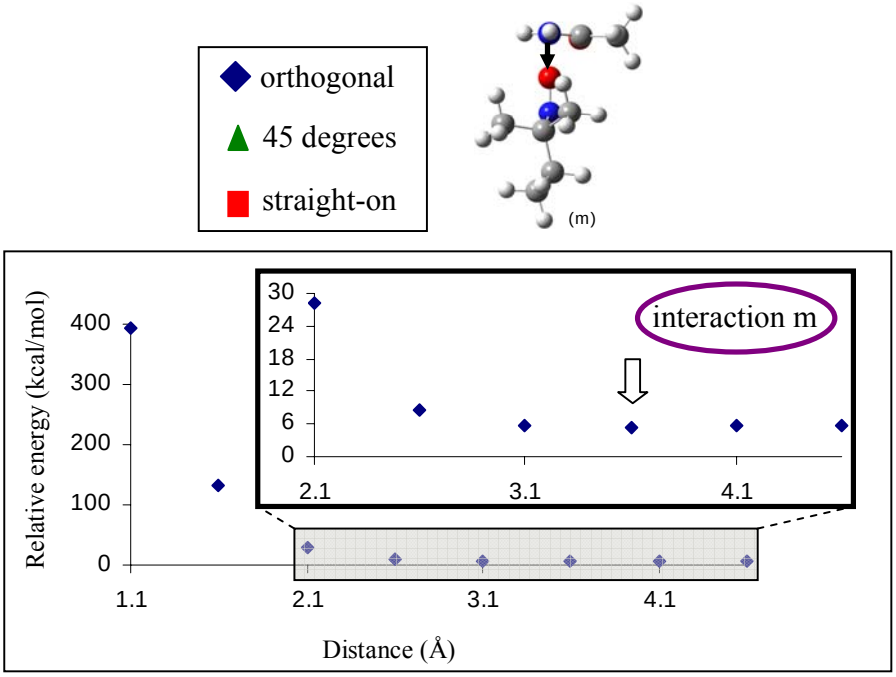


**Figure 23.** Relative energy curve for interaction (m).

Of the thirteen orientations considered, only four reproduced both the methyl carbon and nitrogen experimental data. (Figure 24) Interactions (d), (f), (j), and (k) from Figure 17 reproduced the methyl carbon value of 0.16, but not the nitrogen value of -0.5. Interaction (l) reproduced the nitrogen value, but not the methyl carbon value. (Data for (d), (f), (j), (k), and (l) in the appendix) Each of the interactions in Figure 24 exhibited a local energy minimum ((b)-2.6Å, (g) and (i)-2.1Å, and (m)-3.6Å). Upon examination of the orientations in Figure 24, it appears that the methyl carbon prefers to interact at an angle of approximately 45 degrees (45°-63° in the structures) to the TEMPO oxygen (same as acetonitrile $^{13}CH_3$ favored orientation). Each orientation represented in Figure 24 confirms this premise. The nitrogen, however, is not as specific to its positioning. Each orientation in Figure 24 also reproduces the nitrogen experimental data, either in sign or in sign and magnitude. The nitrogen either prefers to interact via a σ-π ((g) and (m)) or a σ-σ interaction ((b) and (i)). The σ-π interactions are between the σ-orbital of TEMPO oxygen and the π-orbital of the acetamide nitrogen (m), or the σ-orbital of the amide hydrogen and the π-orbital of the TEMPO oxygen (g). The σ-σ interactions are between the σ-orbital on the TEMPO oxygen and the σ-orbital on the amide hydrogen.

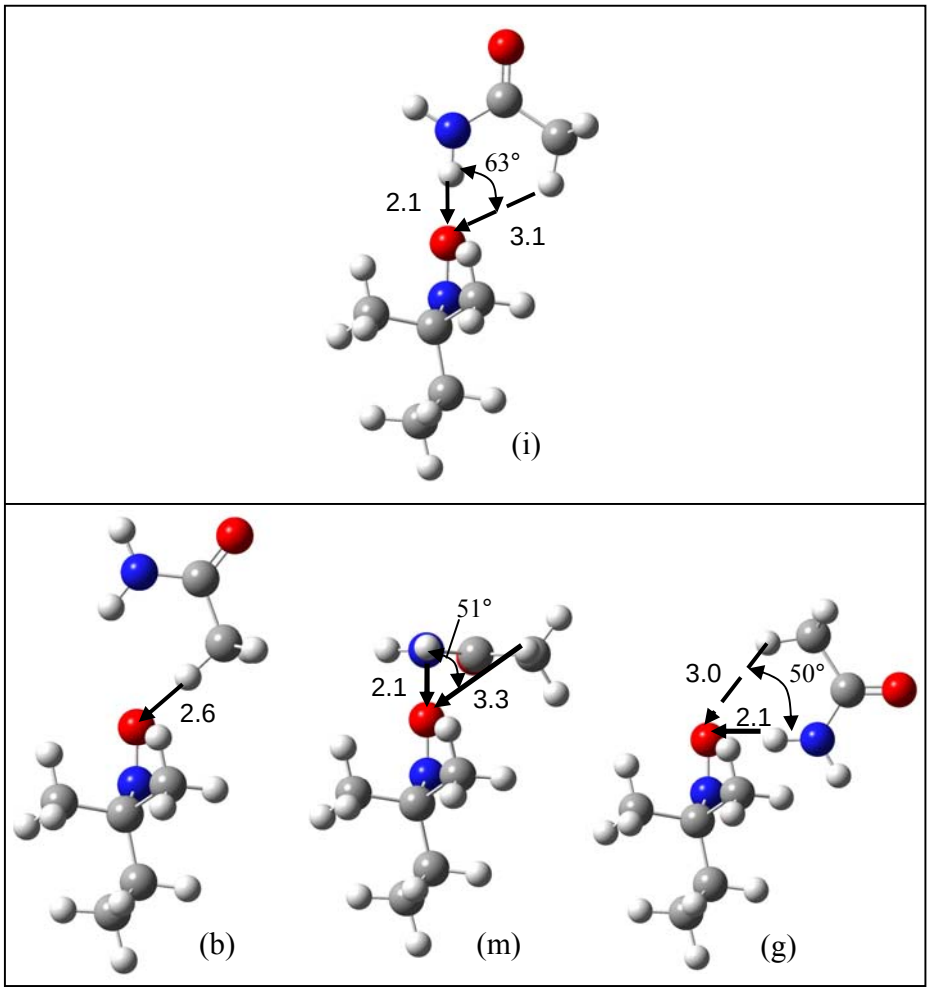


**Figure 24.** Acetamide/TEMPO favored orientations.

Of the four orientations in Figure 24, (i) has the lowest relative energy and also reproduces the experimental data more accurately for both the $^{15}NH_2$ and $^{13}CH_3$ nuclei at the calculated relative energy minimum (2.1 Å). Based on the data, orientations (b), (m), and (g) do contribute to the acetamide/TEMPO collision model; however, orientation (i) is the primary interacting orientation of this system. Figure 25 illustrates orientation (i) and summarizes the calculated data. Both the $^{15}N$ and $^{13}CH_3$ nuclei experimental values are reproduced in the distance range suggested by the minimum energy curve. The orientation that best reproduces the experimental data, (i), is not surprising because the experimental contact shift data measured by Juan Gu suggested acetamide interacted with TEMPO at the amine end, and the straight-on orientation has less steric interactions than

other orientations. Also, orientation (i) places the methyl hydrogen at a 63° angle to the TEMPO oxygen (Figure 24). The 63° compares with the 45° orientation found for acetonitrile. Based on acetamide experimental data and the acetonitrile/TEMPO calculated results, it makes sense that orientation (i) is the key collision geometry.

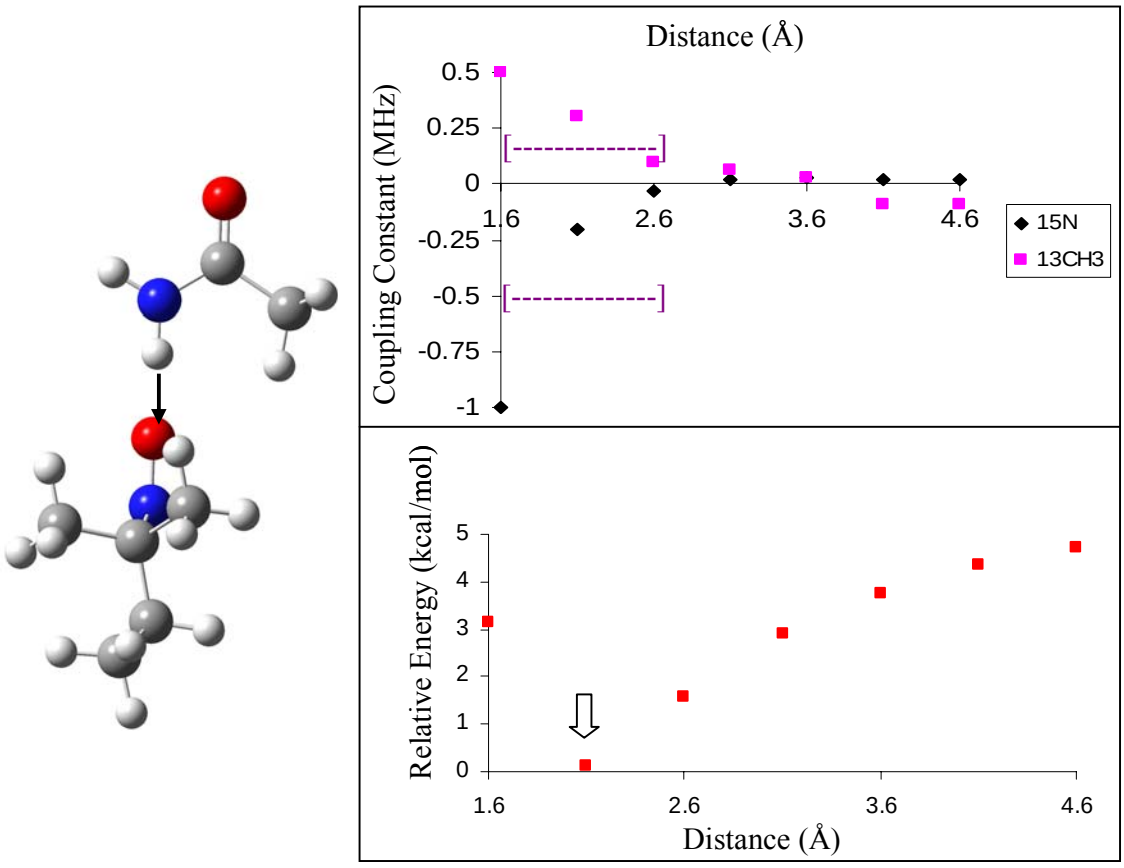


**Figure 25.** Acetamide/TEMPO key orientation data summary.

**2.3.3 Substituted Benzene/TEMPO Systems.** Substituted benzenes were studied to observe the relationship between the $^{13}C$ enhancements of the aromatic ring carbons as different substituents are added to the benzene ring (Figure 26), and to study the mechanism of intermolecular electron spin density transfer between TEMPO and the aromatic carbon nuclei. As summarized in Figure 26, if an electron-withdrawing group is on a benzene ring the TEMPO/substrate interaction will be scalar dominated, and if an electron donating group is the substituent the TEMPO/substrate interaction will be

dipolar dominated. The experimental $^{13}C$ DNP enhancements were determined by Li Song and are shown in Table 3. Since the hyperfine coupling constants were not

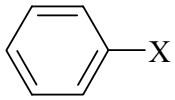


X = electron-withdrawing group ⟶ scalar interaction
($-NO_2$ and -F)

X = electron-donating group ⟶ dipolar interaction
($-CH_3$ and -C≡C-H)

**Figure 26.** Effect of benzene substituents.

determined, the experimental data cannot be directly compared to the calculated hyperfine coupling constants as was done with acetamide and acetonitrile. However, the trends in magnitude of the experimental numbers can be compared to the calculated results. The data for each system is presented in the order shown in Table 3, increasing enhancement values. The one orientation that best follows the magnitude trend is presented for each system. All other data are located in the appendix.

**Table 3.** Experimental $^{13}C$ DNP Enhancements for substituted benzene/TEMPO systems.[114]

| | Ipso | Ortho | Meta | Para |
|---|---|---|---|---|
| Benzene/TEMPO | -199 | -199 | -199 | -199 |
| Toluene/TEMPO | -562 | -179 | -153 | -207 |
| Phenylacetylene/TEMPO | -280 | -36 | -32 | - |
| Fluorobenzene/TEMPO | -572 | 63 | 71 | -51 |
| Nitrobenzene/TEMPO | -572 | 582 | 198 | 366 |

**2.3.3.1 Benzene/TEMPO System.** Two orientations were studied for the benzene/TEMPO system. (Figure 27) Interaction (a) is the σ-orbital of the TEMPO oxygen interacting with the π-orbital of the benzene carbon, and orientation (b) is the π-orbital of TEMPO oxygen interacting with the π-orbital of the benzene carbon. The

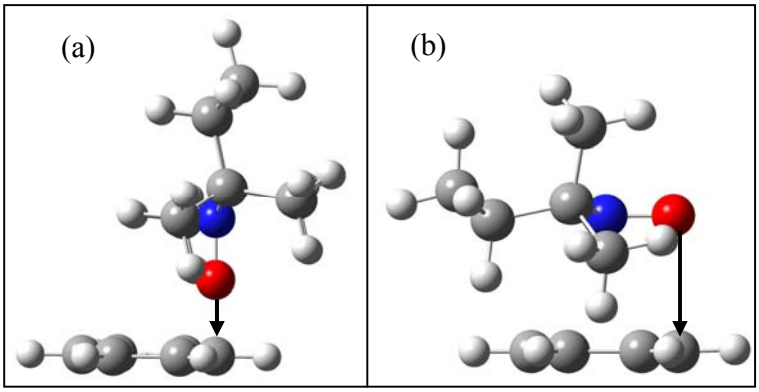


**Figure 27.** Benzene/TEMPO orientations.

calculated data indicates orientation (a) best agrees with the magnitude expected for the benzene/TEMPO system (Figure 28). The relative energy curve for orientation (a) does not exhibit a local minimum. (Figure 29). The lack of an energy minimum closer than 4.6Å could be due to a repulsion between the TEMPO oxygen and the π-orbital on the benzene carbon. Also, steric effects between the hydrogens of TEMPO and benzene could cause the energy to not show a minimum.

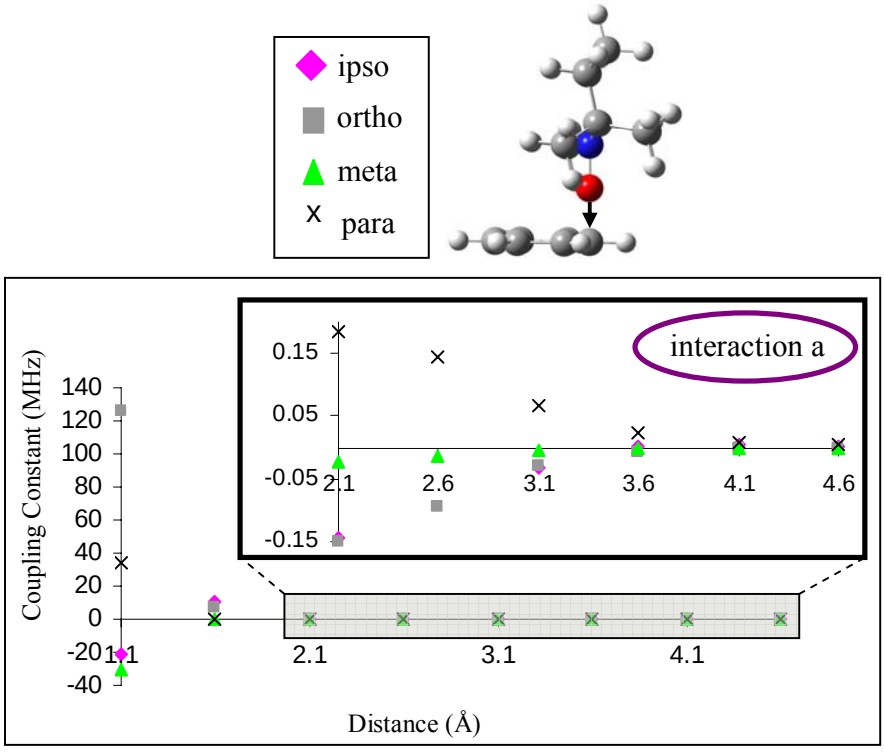


**Figure 28.** Benzene/TEMPO coupling constant data for interaction (a).

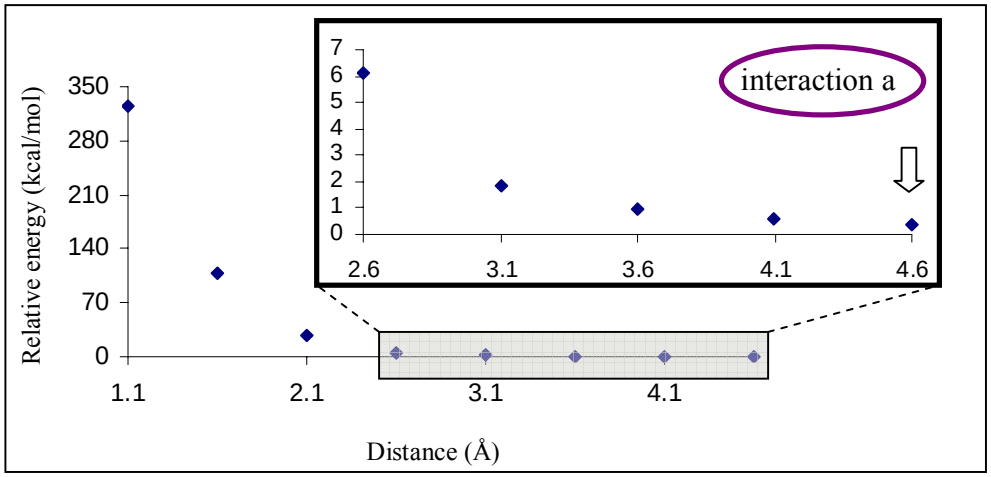


**Figure 29.** Benzene/TEMPO energy curves for interaction (a).

**2.3.3.2 Toluene/TEMPO System.** Next in the trend of increasing magnitudes is toluene/TEMPO. Thirteen orientations were studied for the toluene/TEMPO system. Orientations (a)-(i) are the interactions between the TEMPO oxygen and the hydrogen of the named carbon of toluene (illustrated in Figure 30). The ortho, meta, and para carbons are illustrated in Figure 31. Orientations (g)-(i) are pictured in Figure 32, and orientations (a)-(f) are modeled in a similar manner.

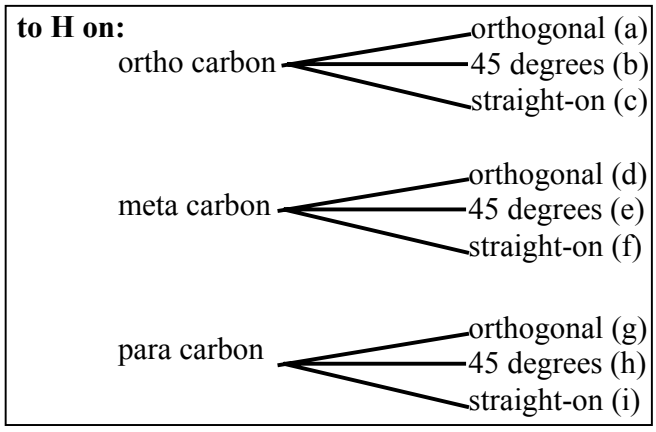


**Figure 30.** Schematic of H-C bond interactions for toluene.

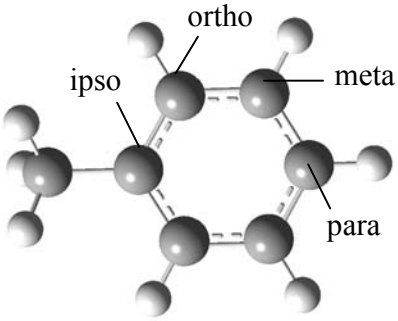


**Figure 31.** Toluene.

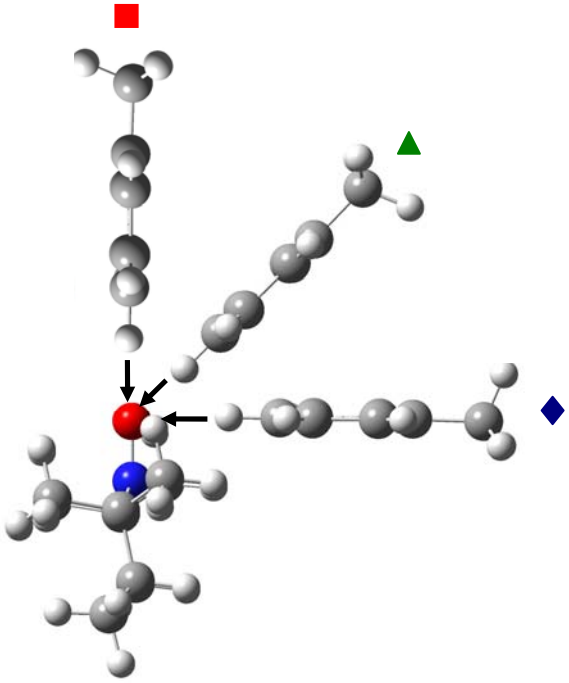

**Figure 32.** Illustration of para carbon-hydrogen bond interaction for toluene: ( ♦ ) orthogonal, ( ▲ ) 45 degrees, and ( ■ ) straight-on.

The remaining four orientations studied are illustrated in Figure 33. Orientations (j)-(m) model a σ-π interaction between the σ-orbital of the TEMPO oxygen and the π-orbital of the respective toluene carbon.

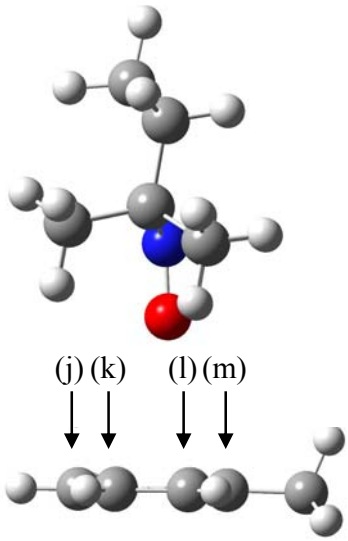


(j) to $\pi$ orbital on para carbon
(k) to $\pi$ orbital on meta carbon
(l) to $\pi$ orbital on ortho carbon
(m) to $\pi$ orbital on ipso carbon

**Figure 33.** Additional toluene orientations.

Analysis of all toluene/TEMPO data shows that interaction (k) follows the magnitude trend according to Table 3 most accurately (Figure 34). Only data for the interaction (k) is presented here. The remaining data is located in the appendix. The shaded purple boxes in the figures are the distance range of the minima energies for the two interactions. Interaction (k) does not have a local energy minimum (Figure 35).

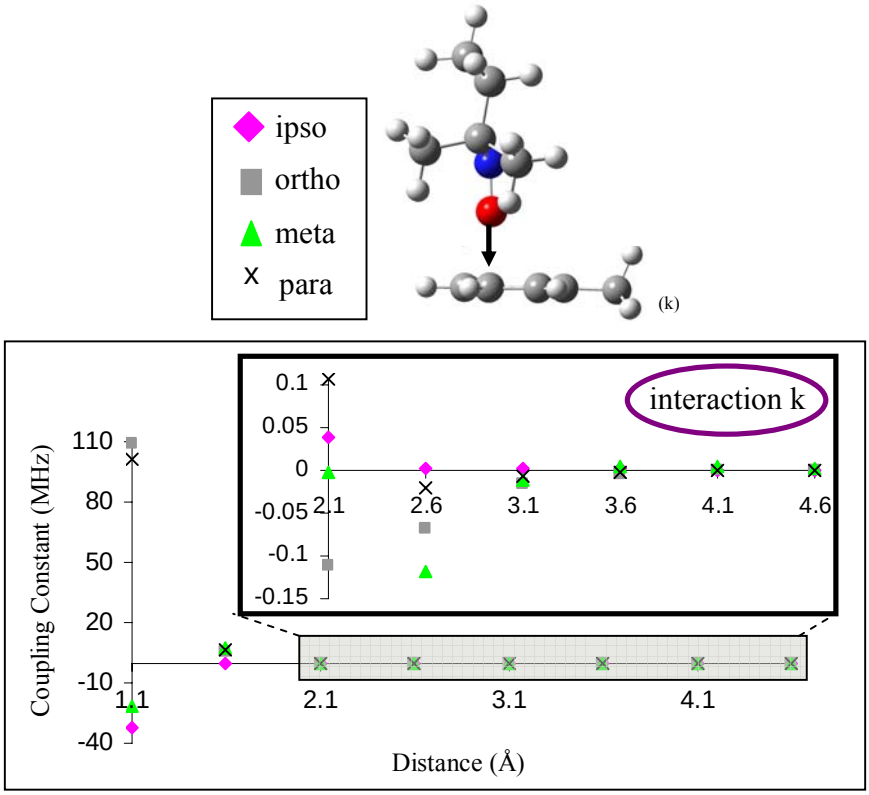


**Figure 34.** Toluene/TEMPO coupling constant data for interaction (k).

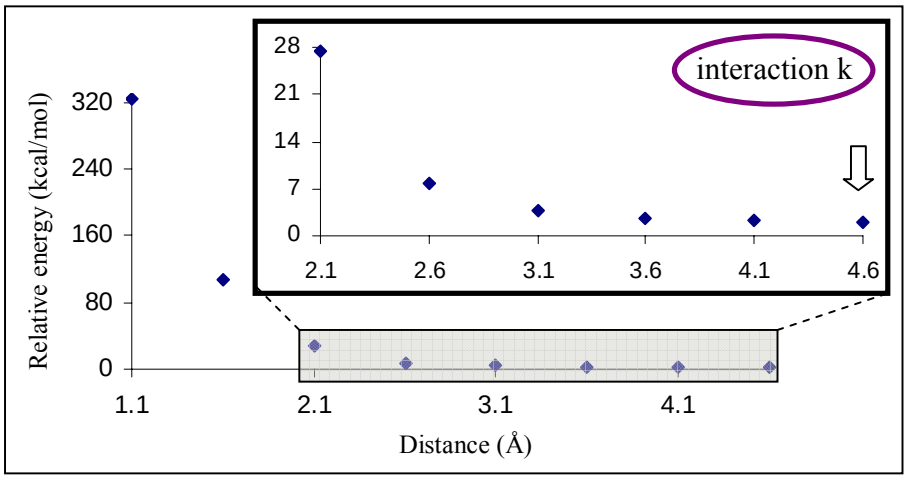


**Figure 35.** Toluene/TEMPO energy curve for interaction (k).

**2.3.3.3 Phenylacetylene/TEMPO System.** Phenylacetylene follows toluene in magnitude. Nine orientations were studied for the phenylacetylene/TEMPO system, and are illustrated in Figure 36.

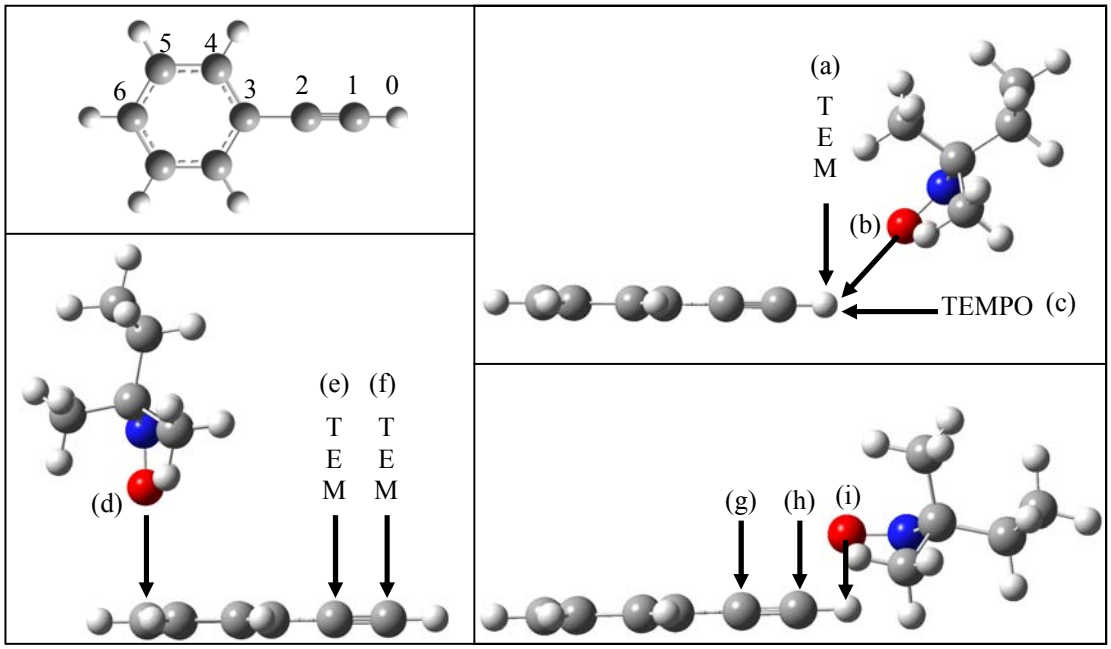


(a) orthogonal interaction at atom #0
(b) 45 degree interaction at atom #0
(c) straight-on interaction at atom #0
(d) σ-π interaction between O and C at atom #6
(e) σ-π interaction between O and C at atom #2
(f) σ-π interaction between O and C at atom #1
(g) π-π interaction between O and C at atom #2
(h) π-π interaction between O and C at atom #1
(i) π- σ interaction between O and H at atom #0

**Figure 36.** Phenylacetylene orientations.

Orientations (a)-(c) model a σ-σ interaction between σ-orbital of TEMPO oxygen and the σ-orbital on the hydrogen (atom #0). Orientations (d)-(f) model a σ-π interaction between the σ-orbital of TEMPO oxygen and the π-orbital of the respective carbon atom. Orientations (g) and (h) model a π-π interaction between the π-orbitals of TEMPO oxygen and the respective carbon atom. Orientation (i) models a π-σ interaction between the π-orbital of TEMPO oxygen and the σ-orbital of hydrogen (atom #0).

The data for orientation (c) follows the trend in magnitude from Table 3 most accurately. Figure 37 illustrates the calculated hyperfine coupling constants for interaction (c), and Figure 38 contains the relative energy curve. The minimum energy is at 2.1 Å.

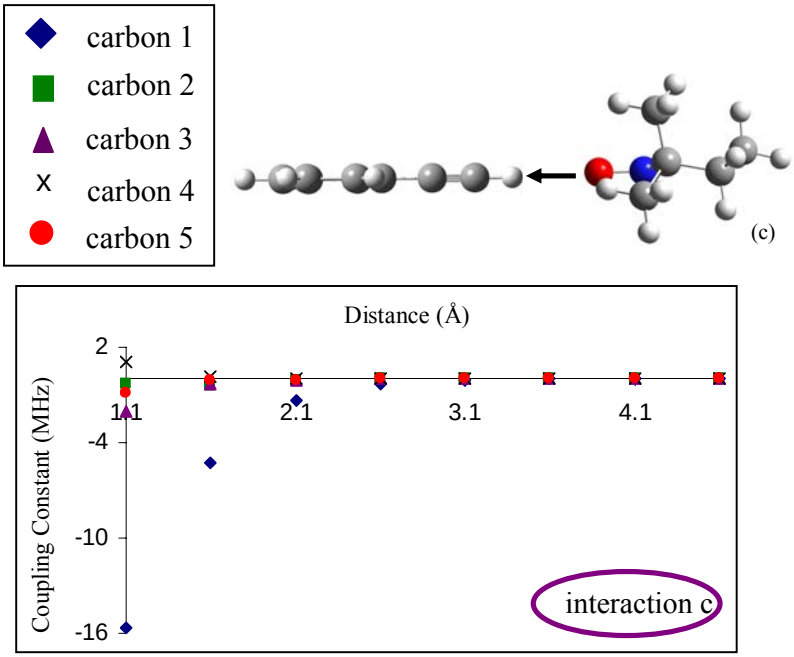


**Figure 37.** Phenylacetylene calculated hyperfine coupling constants for interaction (c).

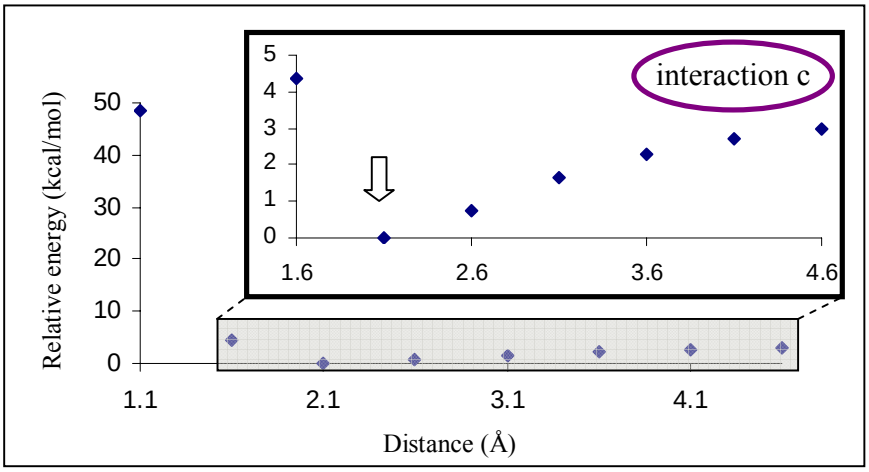


**Figure 38.** Phenylacetylene/TEMPO relative energy curve for interaction (c).

**2.3.3.4 Fluorobenzene/TEMPO System.** The fluorobenzene/TEMPO system follows phenylacetylene/TEMPO with increasing enhancement values. The fluorobenzene/TEMPO system was studied at the five different orientations illustrated in Figure 39. Figure 40 shows the fluorobenzene carbon notation. Orientations (a)-(d) model a σ-π interaction between the σ-orbital of TEMPO oxygen and the π-orbital of the

respective carbon atom, and orientation (e) models a σ-σ interaction between the σ-orbital of TEMPO oxygen and the σ-orbital of fluorine.

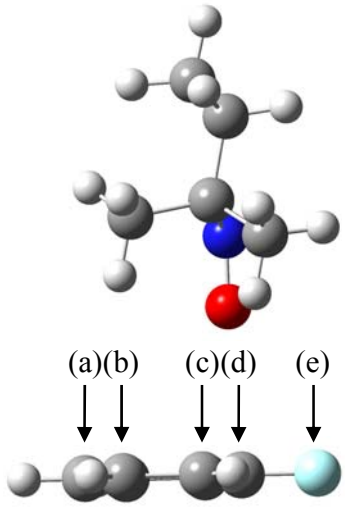


(a) to $\pi$ orbital on para carbon
(b) to $\pi$ orbital on meta carbon
(c) to $\pi$ orbital on ortho carbon
(d) to $\pi$ orbital on ipso carbon
(e) to fluorine atom

**Figure 39.** Fluorobenzene orientations.

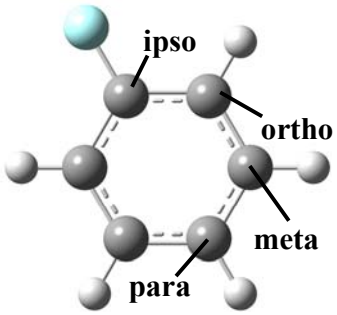


**Figure 40.** Fluorobenzene.

The calculated hyperfine coupling constant data for interaction (c) follows the trend in increasing magnitude most accurately after phenylacetylene in Table 3. Figure 41 contains the coupling constant data and Figure 42 contains the relative energy curves for interaction (c). The relative energy curve from Figure 42 does not exhibit a local

minimum. More calculations need performed for the fluorobenzene/TEMPO system to better understand the intermolecular interactions in the system.

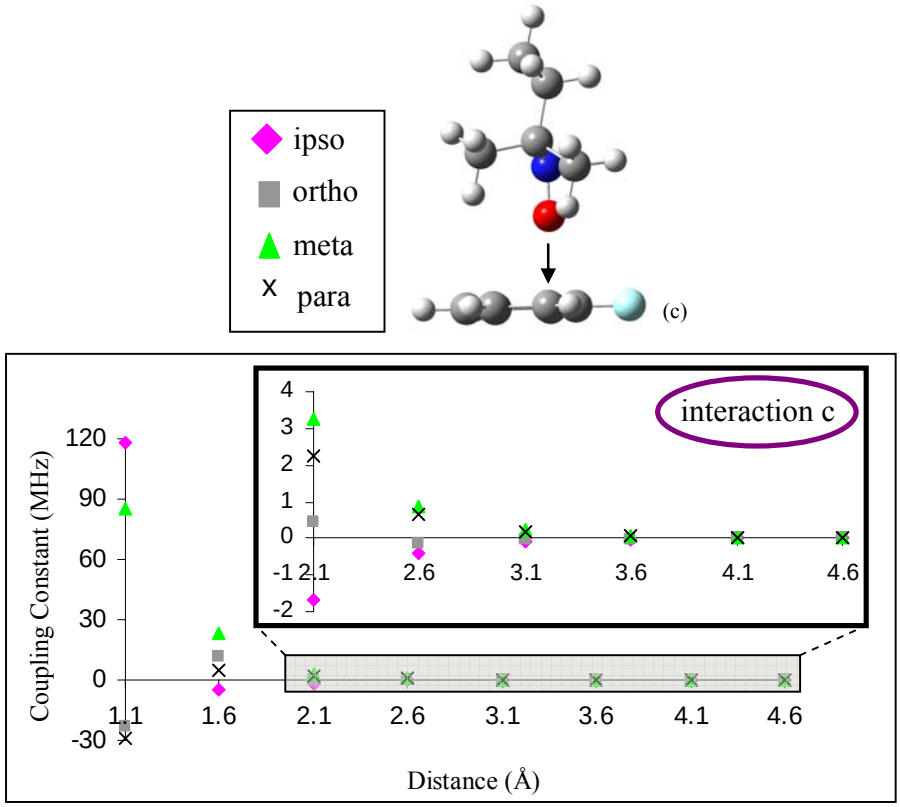


**Figure 41.** Fluorobenzene/TEMPO coupling constant data for interaction (c).

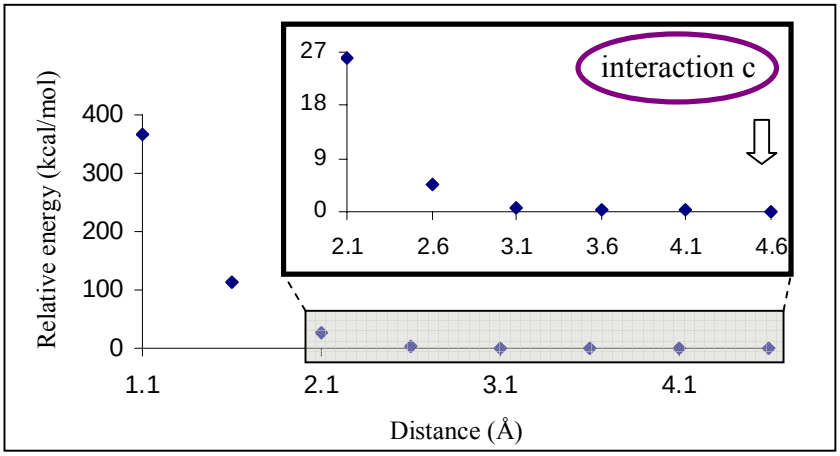


**Figure 42.** Fluorobenzene/TEMPO energy curves for interaction (c).

**2.3.3.5 Nitrobenzene/TEMPO System.** The nitrobenzene/TEMPO system has the largest enhancements according to the experimental data in Table 3. Fifteen orientations were studied for the nitrobenzene/TEMPO system. Orientations (a)-(i) are interactions between the TEMPO oxygen and the hydrogen of the named carbon of nitrobenzene (ortho, meta, or para from Figure 43) comparable to orientations (a)-(i) of toluene/TEMPO (illustrated in Figure 30 in the toluene/TEMPO section). For example, orientations (g)-(i) are interactions between the hydrogen on the para carbon on nitrobenzene and the TEMPO oxygen, as shown in Figure 44. Orientations (a)-(f) are set up the same way as described for orientations (g)-(i).

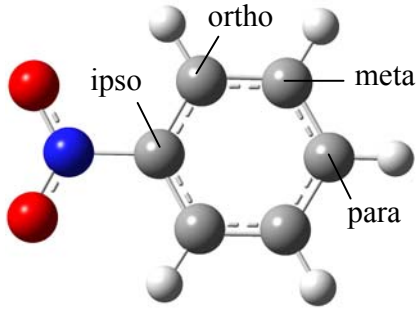


**Figure 43.** Nitrobenzene.

The remaining six orientations studied are illustrated in Figure 45. Orientations (j), (k), (m), and (n) model a σ-π interaction between the σ-orbital of the TEMPO oxygen and the π-orbital of the respective carbon. Orientation (l) is the interaction of the TEMPO oxygen at the center of the nitrobenzene ring. Finally, orientation (o) is the interaction between the σ-orbital of TEMPO oxygen and the π-orbital on nitrogen.

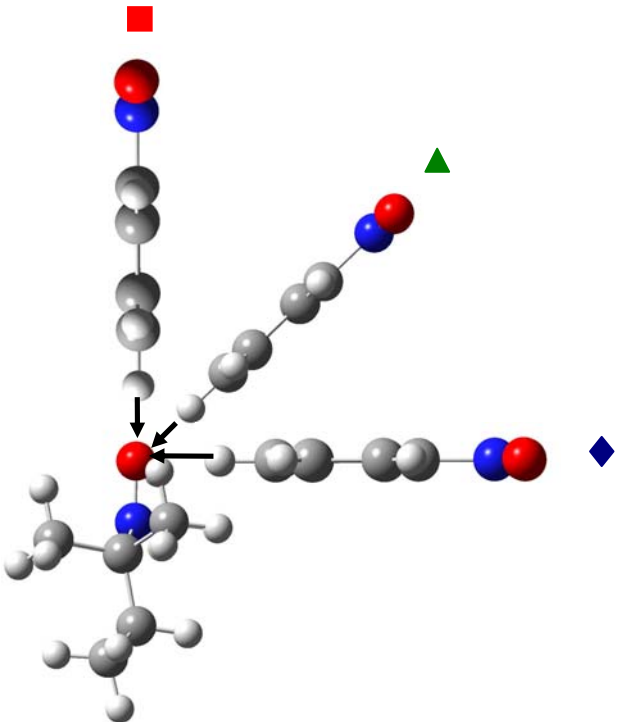

**Figure 44.** Illustration of para carbon-hydrogen bond interaction for nitrobenzene: (♦ ) orthogonal, (▲ ) 45 degrees, and (■ ) straight-on.

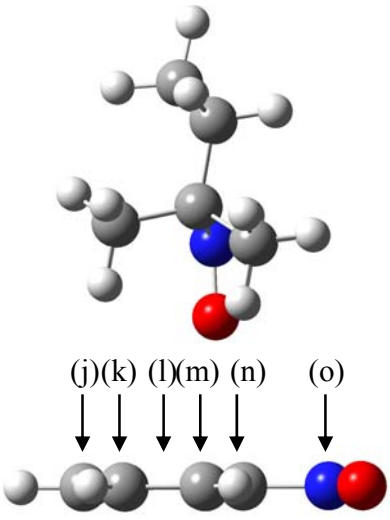


(j) to $\pi$ orbital on para carbon
(k) to $\pi$ orbital on meta carbon
(l) to center of ring
(m) to $\pi$ orbital on ortho carbon
(n) to $\pi$ orbital on ipso carbon
(o) to $\pi$ orbital on nitrogen

**Figure 45.** Additional nitrobenzene orientations.

After analyzing all calculated data for nitrobenzene/TEMPO orientations, orientation (e) most accurately follows the magnitude trend set in Table 3. Figure 46 shows the calculated hyperfine coupling constant data for orientation (e). The minimum energy distance is 2.1 Å. (Figure 47)

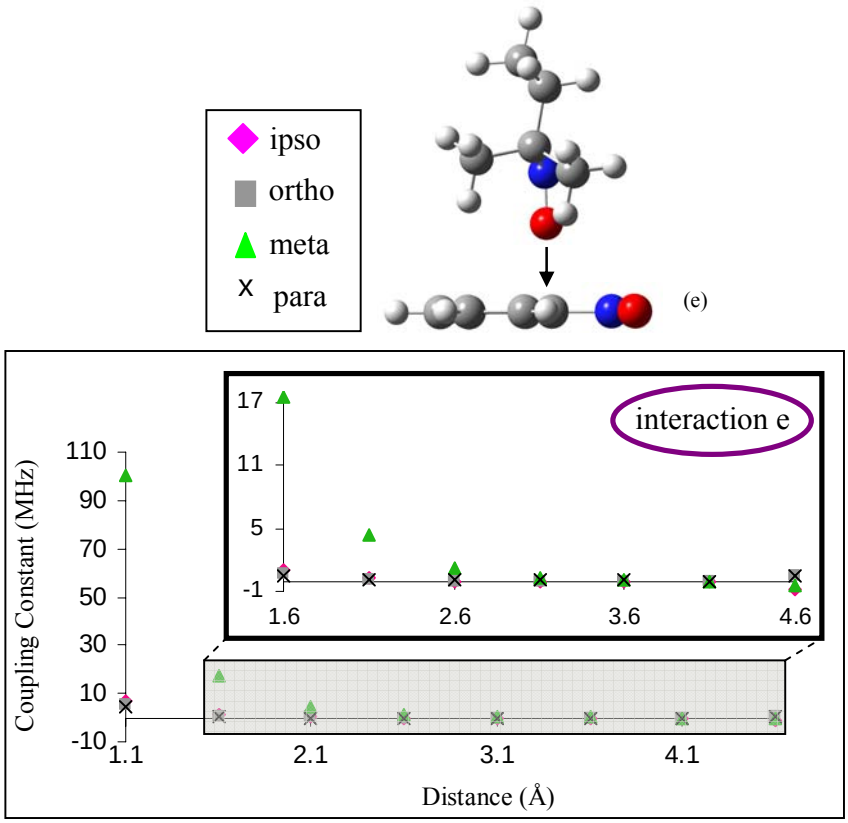


**Figure 46.** Nitrobenzene/TEMPO coupling constant data for interaction (e).

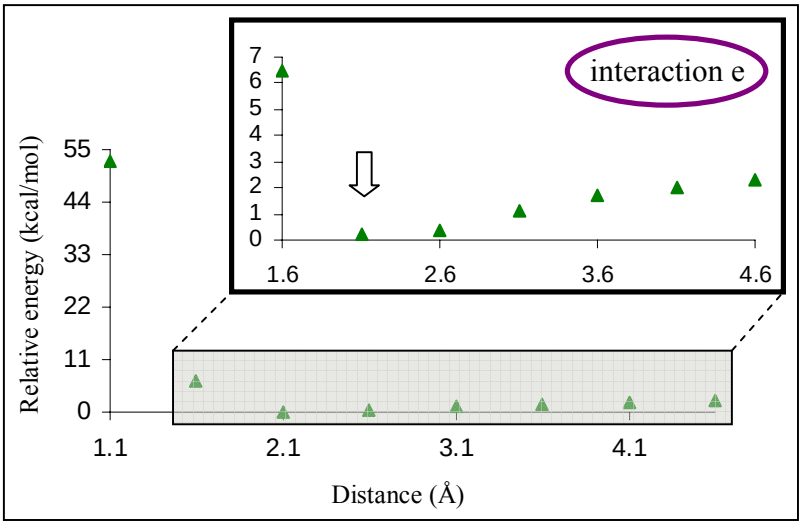


**Figure 47.** Nitrobenzene/TEMPO energy curve for interaction (e).

### 2.3.4 Nitromethane/TEMPO and ethane/TEMPO Systems.

Nitromethane and ethane were investigated to study the substituent effect on a methyl group, studying an electron donating group (i.e. ethane) versus an electron withdrawing group (i.e. nitromethane). Nine nitromethane/TEMPO orientations were investigated. (Figure 48) Orientations (a)-(c) are orthogonal, 45 degrees, and straight-on. Orientations (d)-(f) are also orthogonal, 45 degrees, and straight-on; however, the oxygen atoms of the nitro group have a different orientation in (d)-(f) compared to (a)-(c). These were calculated to find out if the rotation of the nitro group had any effect on the Fermi contact coupling constant computed values. Orientation (g) is to the N on TEMPO, and was calculated for the same explanation given for ethane. Orientations (h) and (i) are referred to as "to the N of nitromethane." Orientation h models a σ-π interaction between the σ-orbital of oxygen and the π-orbital of nitrogen. Orientation (i) models a π-π interaction between the π-orbital of oxygen and the π-orbital of nitrogen. Each orientation was calculated at eight distances: 1.1 – 4.6 Å at 0.5 Å intervals.

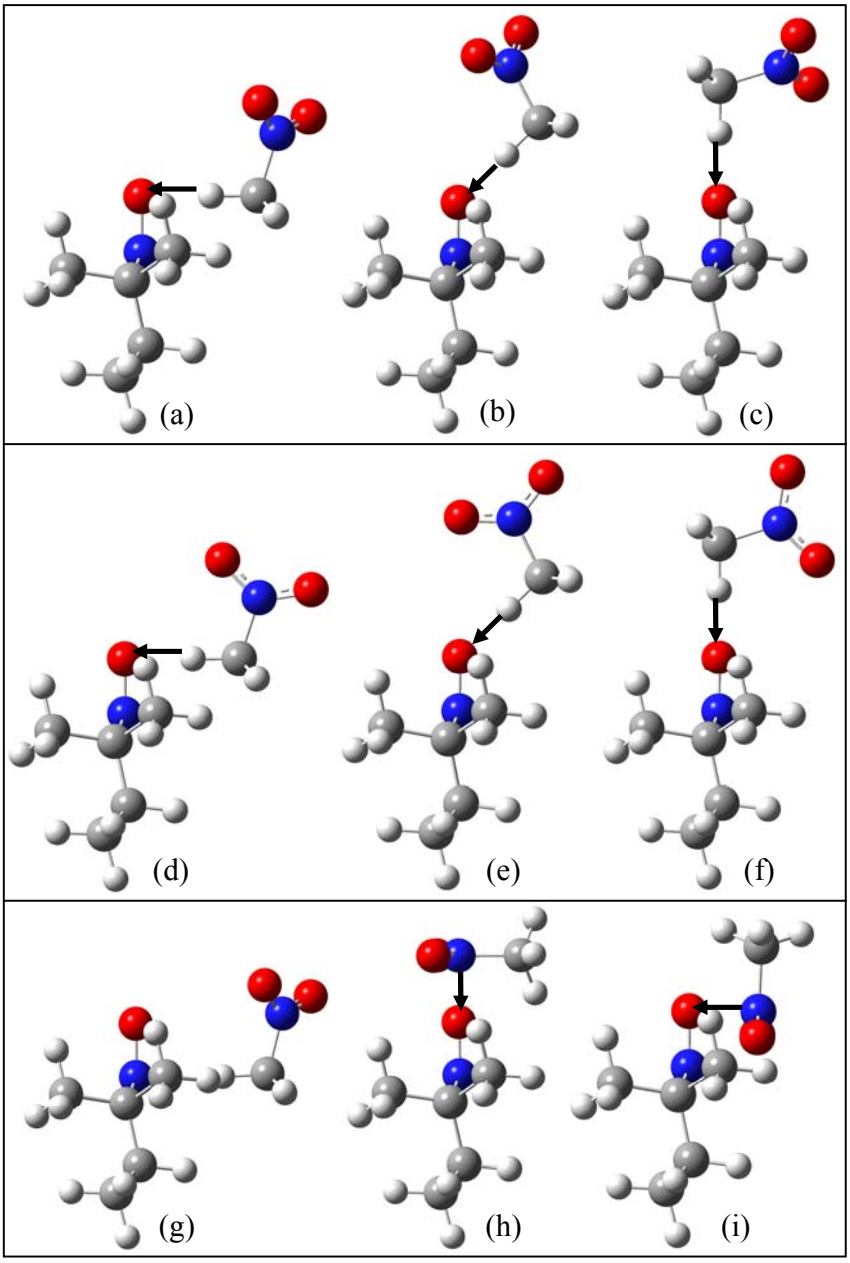


**Figure 48.** Nitromethane/TEMPO orientations.

The relevant calculation results are summarized in graphs in Figures 49 and 50 (other data in appendix). Each figure contains coupling constant data for the carbon atom of nitromethane. Figures 51 and 52 illustrate the minimum energy curves for each interaction. Based on previous data measured by Ziqi Sun,[115] the carbon of nitromethane should exhibit a large positive coupling constant indicating a large scalar interaction is

occurring. As with the substituted benzene data, the calculations cannot be directly with the experimental data. Summarizing the relative energy plots for all orientations indicates orientations (a)-(f) have the lowest relative energy. Only the relevant data is shown in the text, the remainder nitromethane data is in the appendix. Figure 49 illustrates data for orientations (a)-(c), and based on the energy plots of Figure 51, the minimum energy of the orthogonal interaction is at 2.6 Å and the minimum energy for the straight-on and 45 degree orientations are at 2.1 Å. Inspecting the graph of the carbon data, in Figure 49, the 45 degree orientation indicates a positive coupling constant value at 2.1Å.

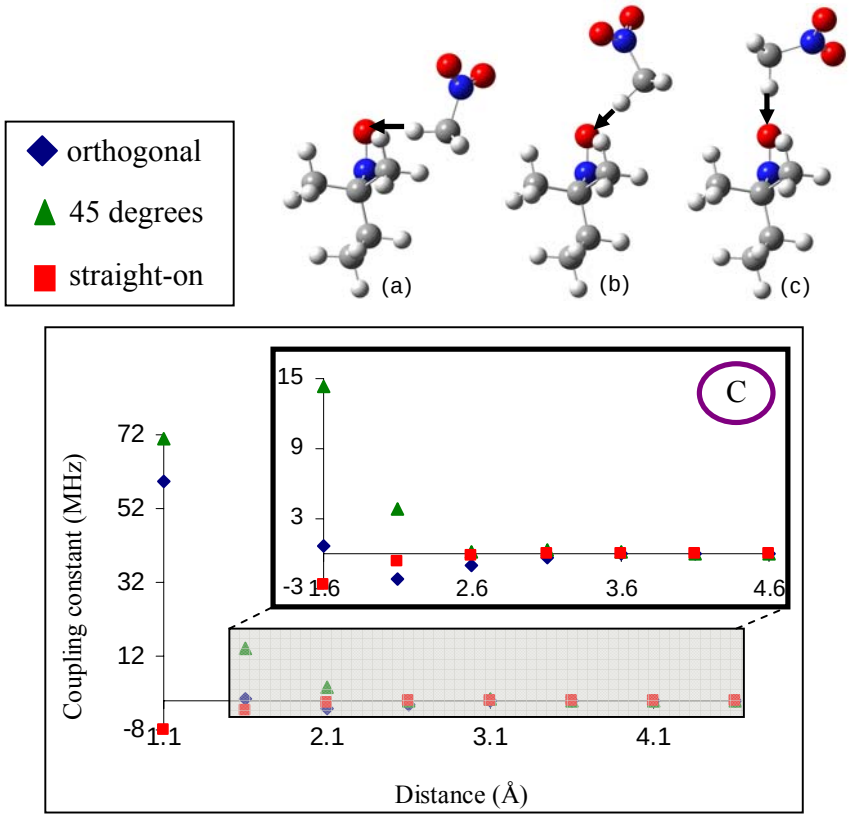


**Figure 49.** Nitromethane/TEMPO ($^{13}C$) coupling constant data for interactions (a)-(c).

Figure 50 illustrates data for orientations (d)-(f), and based on the energy plots of Figure 52, the minimum energy of the orthogonal interaction is at 2.6 Å and the minimum energy for the straight-on and 45 degree orientations are at 2.1 Å. Inspecting

the graph of the carbon data, in Figure 50, the 45 degree orientation indicates a positive coupling constant value at 2.1 Å. Noting only slight geometrical differences in the nitro group rotation in orientations (a)-(c) and (d)-(f), it would be expected that they have similar results.

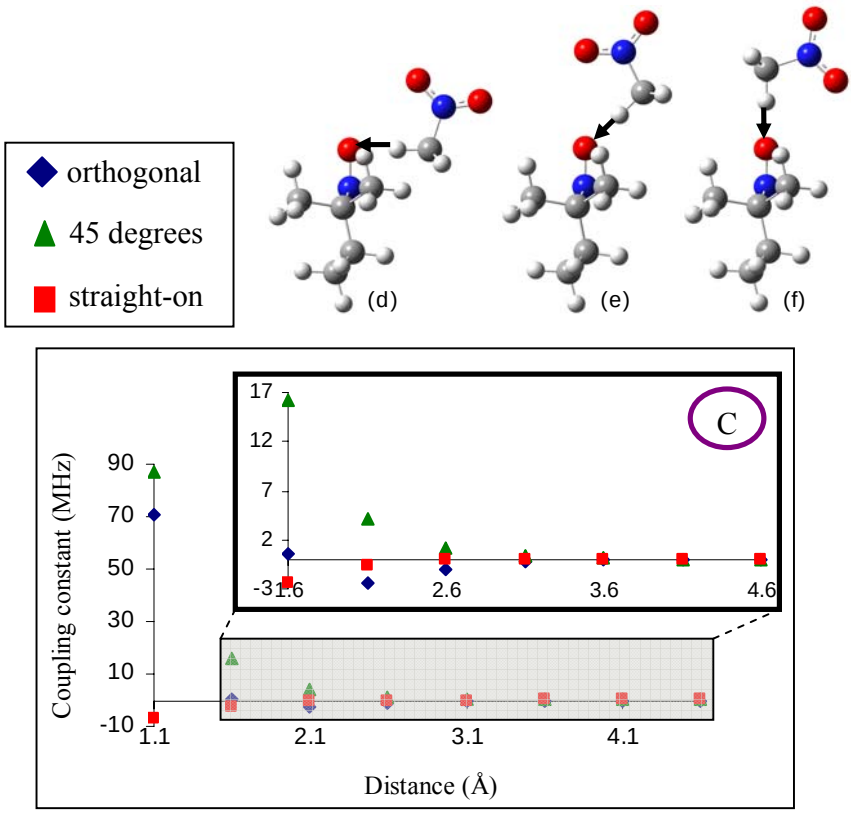


**Figure 50.** Nitromethane/TEMPO ($^{13}$C) coupling constant data for interactions (d)-(f).

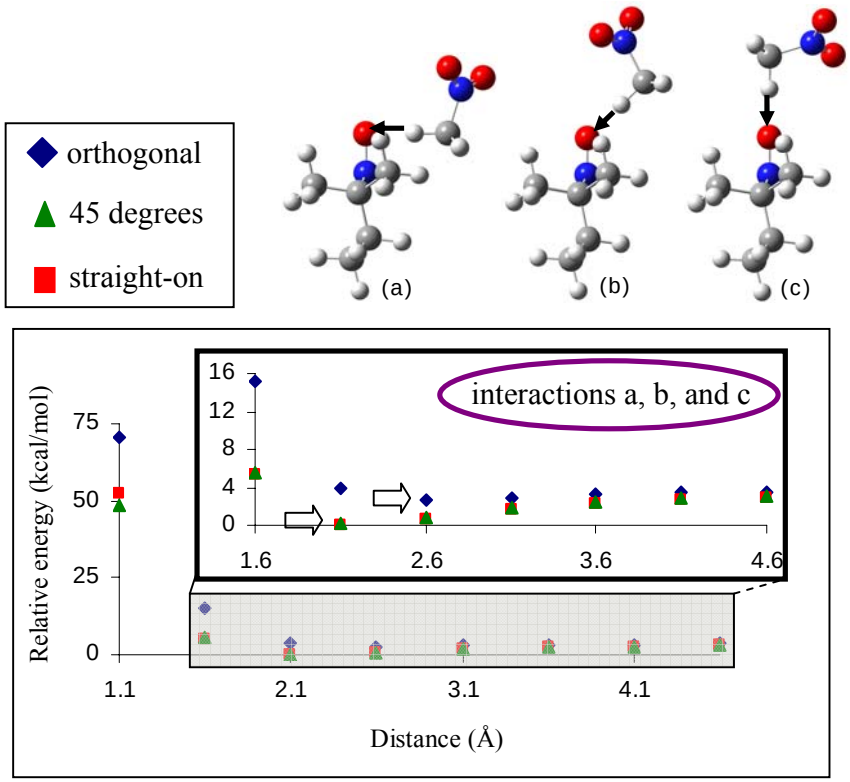


**Figure 51.** Nitromethane/TEMPO energy curves for interactions (a)-(c).

Based on the calculations performed, nitromethane/TEMPO system is not fully understood. The experimental data predicted the carbon of nitromethane to have a large positive enhancement, and the orientations that follow that trend are illustrated in Figure 53. Orientations (b) and (e) model the 45° orientation also favored by the acetonitrile/TEMPO system, which is the best combination of less steric interactions and interaction to the π-orbital of TEMPO oxygen.

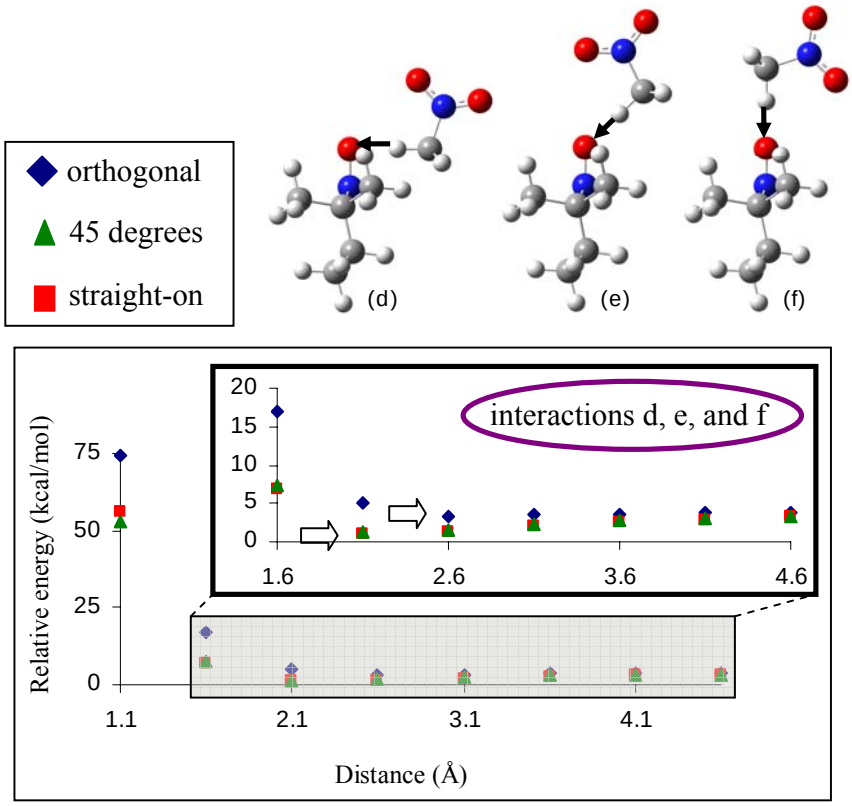


**Figure 52.** Nitromethane/TEMPO energy curves for interactions (d)-(f).

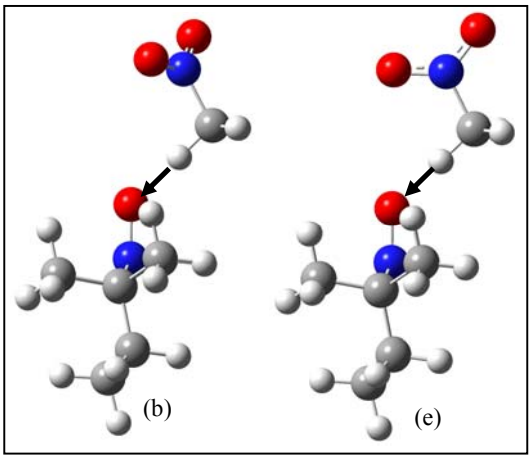


**Figure 53.** Nitromethane/TEMPO favorable orientations.

Hyperfine coupling constants were calculated for each ethane/TEMPO orientation in Figure 54. Orientation (a) is referred to as "orthogonal," (b) is referred to as "45 degrees," (c) is "straight-on," and (d) is "to N on TEMPO." Eight distances were calculated for each orientation to ensure a thorough study was performed: 1.1 - 4.6 Å, with 0.5 Å increments. The orthogonal interaction models hydrogen interacting with the π-orbital on the oxygen of TEMPO. This interaction would be expected to yield high calculated Fermi contact coupling constants due to the significant amount of spin density that would be transferred through the π-orbital. The straight-on interaction models a σ-σ interaction where the σ-orbital of the hydrogen is interacting with the σ-orbital of the oxygen, and the 45 degree orientation is half way in between them. Since the spin density is shared between the oxygen and nitrogen on TEMPO, calculations were performed such that the hydrogen is interacting with the π-orbital of the nitrogen.

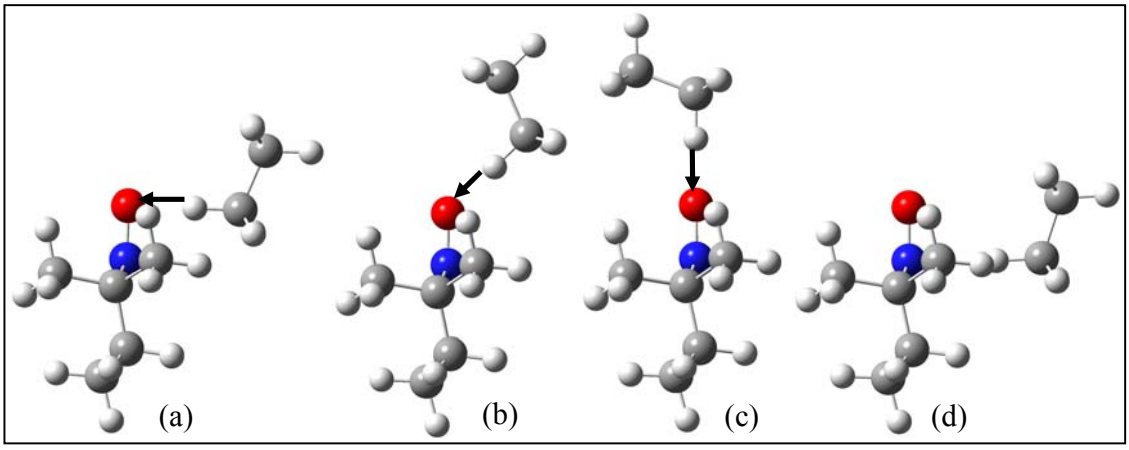


**Figure 54.** Ethane/TEMPO orientations.

The calculation results are summarized in graphs that follow, where C1 is the carbon adjacent to the interacting hydrogen. The relative energy curves were examined for all orientations studied. Orientations (a)-(c) yielded the lowest relative energy, and so data for orientation (d) is located in the appendix. The graphs in Figure 55 contain the calculated coupling constant data for the orthogonal, 45 degrees, and straight-on orientations (a)-(c). There is no experimental data for ethane; however, based on previous data for nitromethane, C1 would be expected to give a negative enhancement

experimentally, opposite of the nitromethane value since $–CH_3$ is an electron-donating group and $–NO_2$ is an electron withdrawing group. The orthogonal (a) and straight-on (c) orientations exhibit the negative value expected. Based on previous data, the distance of interactions is expected to be in the range of 2-3 Å. It is in that range that orthogonal and straight-on have negative values on the graph. It is not surprising that the orthogonal orientation yields the correct values due to the π-orbital of the oxygen since spin density would be likely to transfer through a π-orbital, and the straight-on orientation has low steric interactions. The single point energies of the interactions were also graphed to see where a minimum in energy occurred. For the ethane/TEMPO system this occurred at 3.1 Å for orthogonal, 2.6 Å for straight-on and 45°, and at 3.6 Å for to N on TEMPO as indicated in Figure 56. These computed energy minima set the range location for the experimental values. For example, because the energy minimum is at 3.1 Å for the orthogonal orientation, the calculated data is examined from 3.1 Å ± 0.5 Å. The same analysis is performed for all orientations.

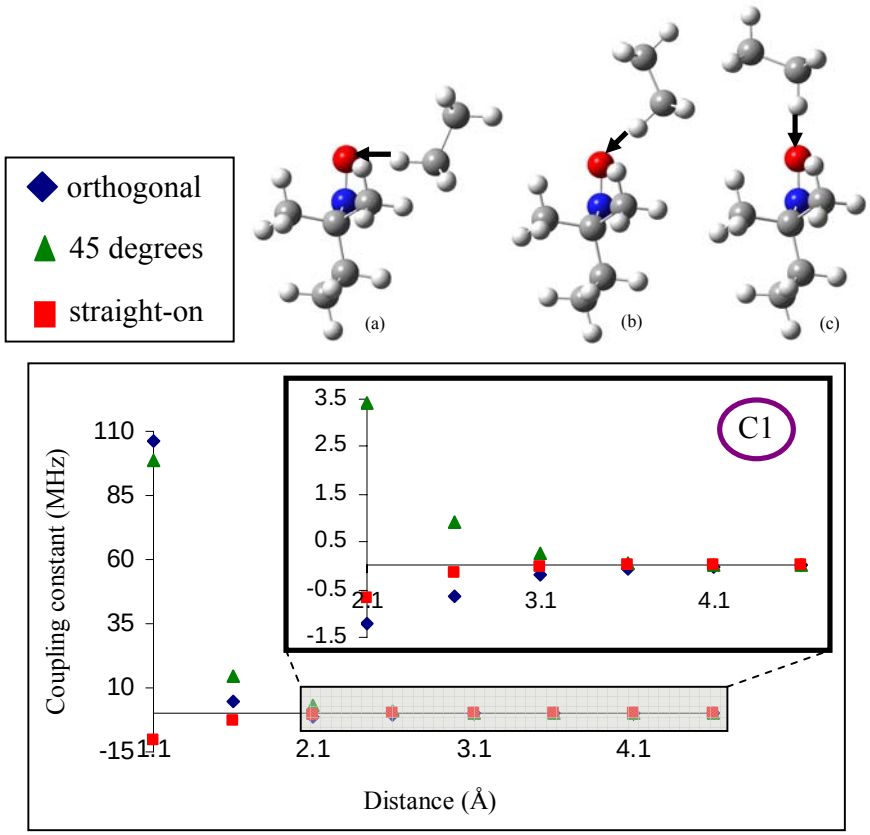


**Figure 55.** Ethane/TEMPO (C1) coupling constant data for interactions (a)-(c).

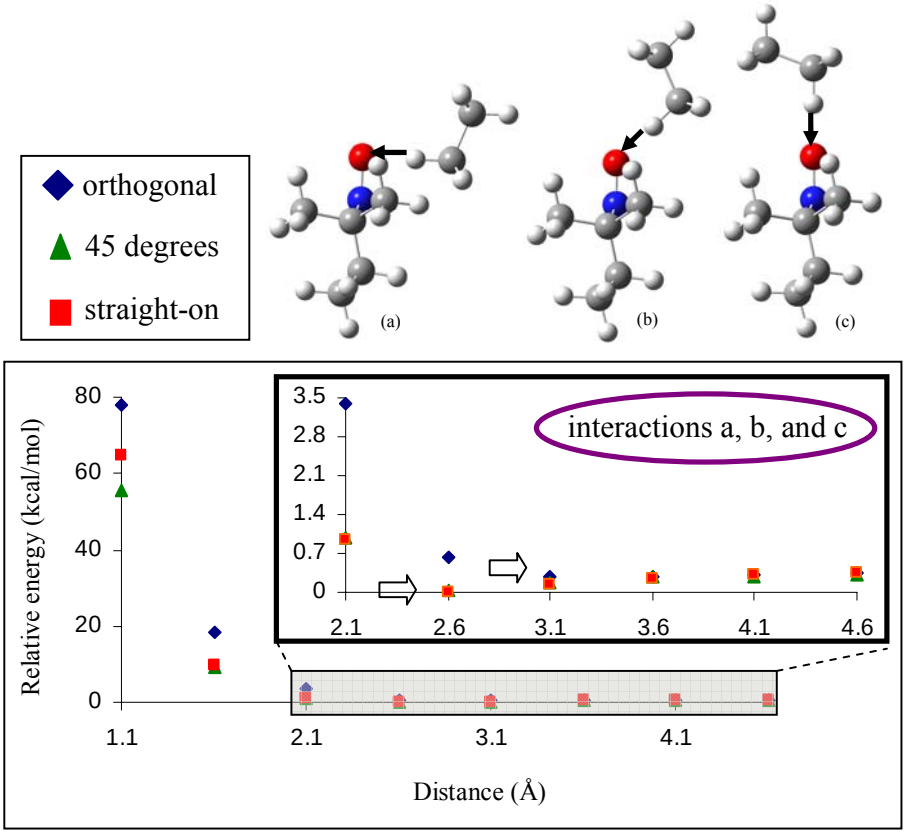


**Figure 56.** Ethane/TEMPO energy curves for interactions (a)-(c).

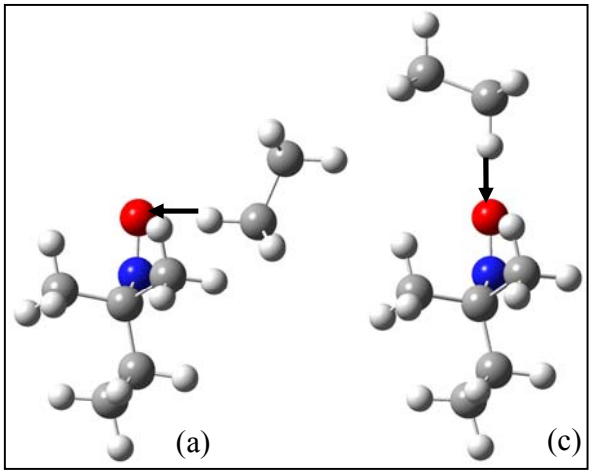


**Figure 57.** Ethane/TEMPO favorable orientations.

The ethane/TEMPO system is also not fully understood. Also, there is no experimental data to directly compare with the calculations. However, the C1 in ethane

should have the opposite enhancement sign as the carbon of nitromethane, which has a negative enhancement, the orientations that follow that trend (and have the lowest relative energy) are orthogonal and straight-on. (Figure 57)

## 2.4 Conclusions for TEMPO/Substrate Interactions

Nine TEMPO/substrate systems have been studied. The systems are experimentally interacting in solution, but the calculations are in the gas-phase. However, they are single point calculations of the TEMPO-substrate complexes at various distances and orientations to determine the most favored collision parameters. For any given system, there are multiple collisions occurring at once. The calculation results show which attitude and distance is most favored compared to experimental DNP results for the TEMPO-substrate system under investigation. The criteria for the favored interaction parameters were minimum energy and reproducibility of the experimental data. The attitude and distance of collisions in solution are dependent on the system studied. Generally, the distance of a favorable collision is within 2 – 3 Å. The attitude depends on the substrate of interest.

The key collision for the acetonitrile/TEMPO system was at the methyl end of acetonitrile at a 45° angle with respect to TEMPO oxygen, and at a distance of 2.1 Å. The distance of 2.1 Å falls into the range previously suggested for a hydrogen-bonding intermolecular interaction. The 45° angle can be explained by a combination of steric interactions and spin density transfer through a π-orbital. The 45° angle orientation has low steric hindrances, and so exhibits a very low relative energy compared to the other orientations. Spin density transfer would be greater through a π-orbital than a σ-orbital. Although, the orthogonal orientation models a π-orbital interaction, the steric interations are larger there, and it is more difficult for the acetonitrile molecule to interact at that site. Therefore, the 45° orientation maximizes the desire for a low energy interaction and a π-orbital interaction.

The key collision for the acetamide/TEMPO system was at the amide ($NH_2$) end of acetamide at the straight-on orientation with respect to the TEMPO oxygen, also at a distance of 2.1 Å. The 2.1 Å distance again falls into the range previously suggested for a hydrogen-bonding intermolecular interaction. The straight-on orientation is the least steric hindering orientation for the amine end, yielding very low relative energy compared to the other acetamide/TEMPO orientations. The unique feature about the straight-on orientation for the amine end is that it beautifully positions the methyl end at 63°, which is approximately the same angle as the acetonitrile methyl group's key collision. The straight-on orientation of the amine end of acetamide is a low energy interaction and remarkably reiterates the ~45° orientation of the methyl end with respect to the TEMPO oxygen.

The dynamics of the acetonitrile/TEMPO and acetamide/TEMPO systems were studied by Juan Gu[4] using NMR and DNP and were not addressed computationally in this research project. Studying the dynamics using calculations is future work for this project.

The substituted benzenes, nitromethane, and ethane systems are not fully understood. There is not a direct comparison between the calculated and the experimental results, as was the case with the acetonitrile and acetamide systems. Further experimental and computational studies need performed on the substituted benzene/TEMPO series, as well as the ethane and nitromethane/TEMPO systems to fully understand the calculated results and the collisions in solution.

# 3. The Relaxivity of Paramagnetic and Diamagnetic TNT Metallofullerenes

## 3.1 High and Low Field NMR

The $T_1$ and $T_2$ relaxivity measurements were conducted at 9.4 T on a Varian Inova 400 by Tom Glass, at 2.4 T on a Bruker/Biospecby Dr. Panos Fatouros and Frank Corwin at VCU, and at 0.35 T on a TEACHSPIN PS1-B pulsed NMR instrument. All of the data measured at 0.35 T were part of this research project and were measured by the author. The 0.35 T NMR instrument is shown in Figure 58. The sample is placed at the sweet spot of the magnet (where the maximum signal occurs), and the data acquired was manually read from the oscilloscope. The data was then entered into a Microsoft Excel spreadsheet on a separate computer and graphed.

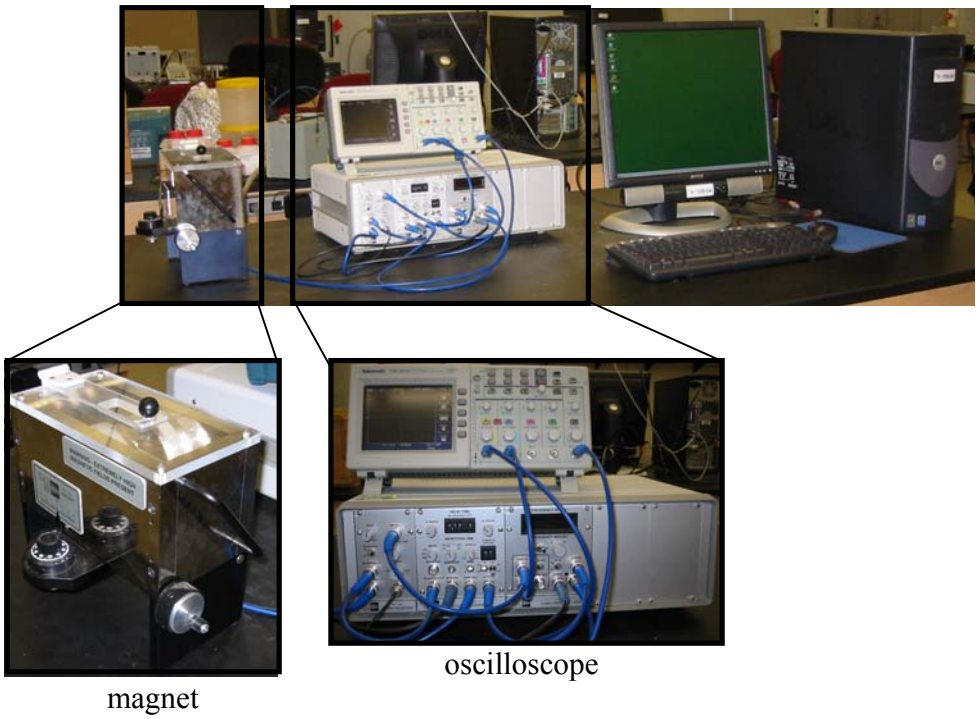


**Figure 58.** Illustration of 0.35 T pulsed NMR instrument.

A simplified schematic of the 0.35T low field pulsed NMR instrument is presented in Figure 59.[116] The pulse programmer generates the pulse stream that guides

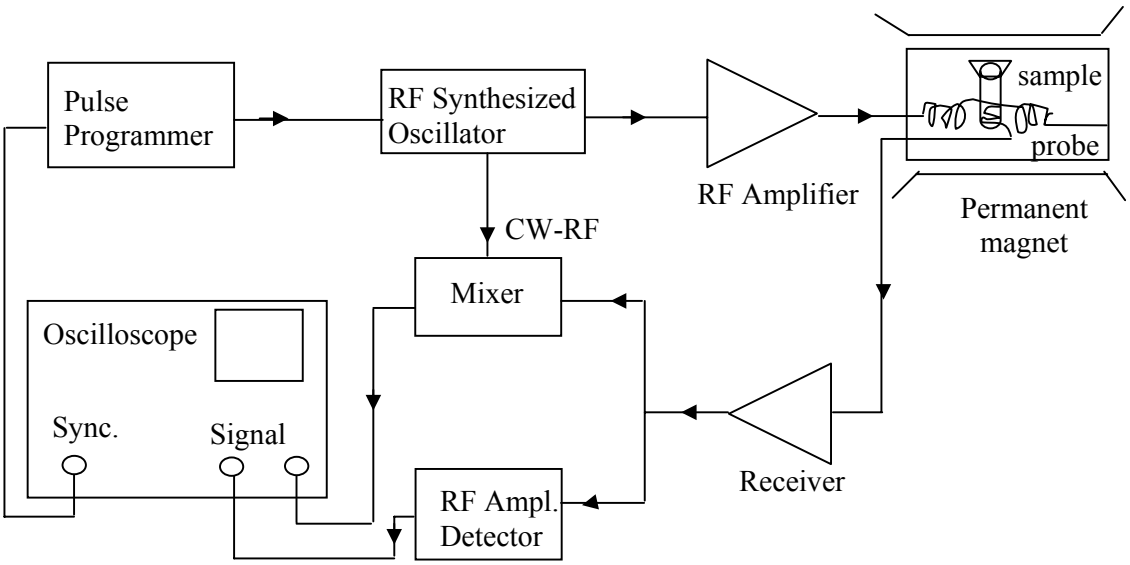


**Figure 59.** Schematic of a pulsed NMR instrument.

the RF synthesized oscillator to produce radio frequency (RF) pulse bursts, as well as directs the oscilloscope to trigger on the appropriate pulse. The RF amplifier amplifies the pulse bursts from the synthesized oscillator and sends the pulses to the transmitter coils in the sample probe. The RF pulse bursts produce a homogeneous 12 gauss rotating magnetic field in the coils around the sample. This rotating magnetic field is the time-dependent B1 field that produces the precession of the magnetization (also known as the 90° or 180° pulses). An electromagnetic field (EMF) is induced in the receiver coils resulting from the nuclear magnetization precessing in the direction transverse to the applied magnetic field. The RF signal is then amplified by the receiver, and detected by the mixer and the RF amplitude detector. The mixer combines the precession signal from the sample with the signal from the oscillator, and the output frequency (the proper frequency of the oscillator) is proportional to the difference between the two frequencies. The RF amplitude detector rectifies the received signal and produces an output that is

proportional to the peak amplitude of the RF precessional signal. This output is used by the oscilloscope to display the free induction decay and the spin echo signals.

## 3.2 MRI Relaxivity Results at 0.35 T

**3.2.1 Sample Preparation.** Each concentration in the series of measurements was prepared from a stock solution of the sample. The stock concentration was determined using ICP (refer to appendix) and the dilutions were made from the stock solution. Each sample was inspected for precipitate and monitored for possible evaporation over time. The relaxivity data is not corrected for diamagnetic water and the sample could contain impurities, such as iron and oxygen.

The errors for the $r_1$ and $r_2$ values for each sample were determined in Microsoft Excel using the standard error (*S.E.*) equation

$$S.E. = \sqrt{\frac{\sum_{s=1}^{m}\sum_{i=1}^{n} y_{is}^2}{(n_y - 1)(n_y)}} \qquad [26]$$

where $s$ is the series number, $i$ is the point number in the series, $m$ is the number of series for point $y$ in the graph, $n$ is the number of points in each series, $y_{is}$ is the data value of series $s$ and the $i^{th}$ point, and $n_y$ is the total number of data values in all series.

The metallofullerene sample preparations were performed by Dr. Zhongxin Ge and Xuelei Wang. The concentrations were determined by inductively coupled plasma optical emission spectroscopy (ICP-OES) measurements performed by Dr. Zhongxin Ge and Xuelei Wang with the help of Dr. Gary Long, Wes Gordon, and David Roach. All sample preparation and ICP measurement discussion is located in the appendix (sections 6.2 and 6.3).

**3.2.2 Pure Water.** As a comparison, water was measured at 0.35 T. The $r_1$ and $r_2$ of water were determined to be 0.42 ± 0.03 and 0.99 ± 0.02 $mM^{-1}s^{-1}$ at 0.35 T. At higher field strengths (i.e. 9.4 T), the $r_1$ and $r_2$ of water are 0.33 s. The values listed in Table 4 were measured at 0.35 T and are not 3 s for $r_1$ and $r_2$. The relaxivity of water

would be expected to change slightly at a lower field strength, but not to the extent shown in Table 4. This could be due to impurities in the water, such as iron and oxygen. These impurities would affect $r_2$ much more than $r_1$, especially at low solute concentrations. This is shown in the data. The $r_1$ is measured as 0.4 s and $r_2$ is measured as 1 s, compared to the 0.33 s expected. The $r_2$ value is noticeably different, even taking the lower field strength into consideration. From the water data, it can be noted how appreciably the $^1H$ relaxivity of water is affected by the new contrast agents.

**Table 4.** Water relaxivity data at 0.35T.

| | $r_1$ ($s^{-1}$) | $r_2$ ($s^{-1}$) | $T_1$ (s) | $T_2$ (s) |
|---|---|---|---|---|
| water | 0.4 | 1.0 | 2.4 | 1.0 |

**3.2.3 $Lu_3N@C_{80}$[DiPEG5000$(OH)_x$].** $Lu_3N@C_{80}$ was functionalized with poly(ethylene glycol) units and the carbon cage was hydroxylated by Dr. Zhongxin Ge to provide improved water solubility and biodistribution.[60] This TNT-fMF was designed as a diamagnetic control to determine whether the cluster inside ($Gd_3N$ or $Lu_3N$) or the significant electron spin density on the carbon cage was responsible for the enhanced $^1H$ water relaxivity that was observed for the $Gd_3N@C_{80}$[DiPEG5000$(OH)_x$] sample. The Lu species is expected to yield low relaxivity, and this is shown by the data in Figure 60. The concentration dependent $r_1$ and $r_2$ values for $Lu_3N@C_{80}$[DiPEG5000$(OH)_x$] are 0.60 ± 0.09 $mM^{-1}s^{-1}$ and 1.5 ± 0.4 $mM^{-1}s^{-1}$, respectively at a concentration range of 0.1-0.8 mM. These relaxivity values are very small compared to the Gd TNT-fMF data presented in later sections. Therefore, the Lu species proves to be a suitable control.

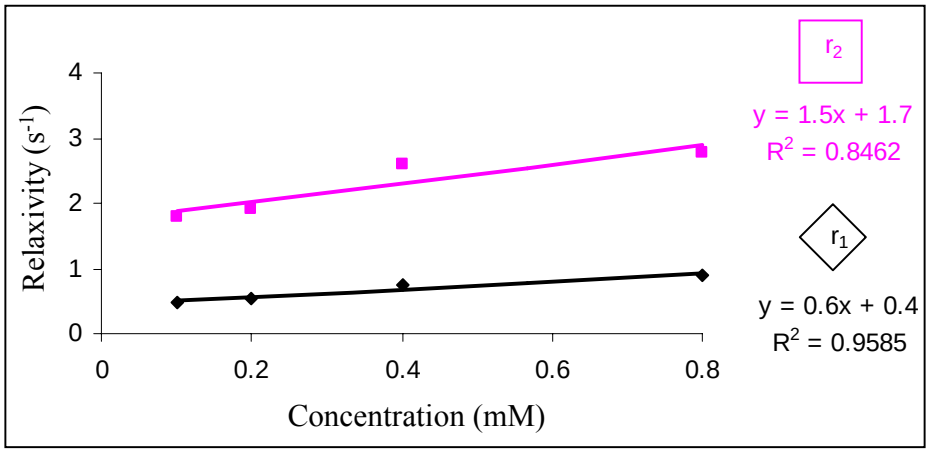


**Figure 60.** $Lu_3N@C_{80}$[DiPEG5000$(OH)_x$] 0.35T relaxivity data. The standard deviation (σ) for each $r_1$ point is ± 0.0003 to 0.0106, and σ for each $r_2$ point is ± 0.0047 to 0.0283. See Table 14 in the appendix for individual σ values.

**3.2.4 $Gd_3N@C_{80}$[DiPEG5000$(OH)_x$].** $Gd_3N@C_{80}$ was functionalized with poly(ethylene glycol) units and the carbon cage was hydroxylated by Dr. Zhongxin Ge to provide improved water solubility and biodistribution.[60] Figure 61 shows the relaxivity values of all concentrations; however, the data appears to show a break in the middle between the highest four concentrations and the lowest four concentrations. (Figure 62)

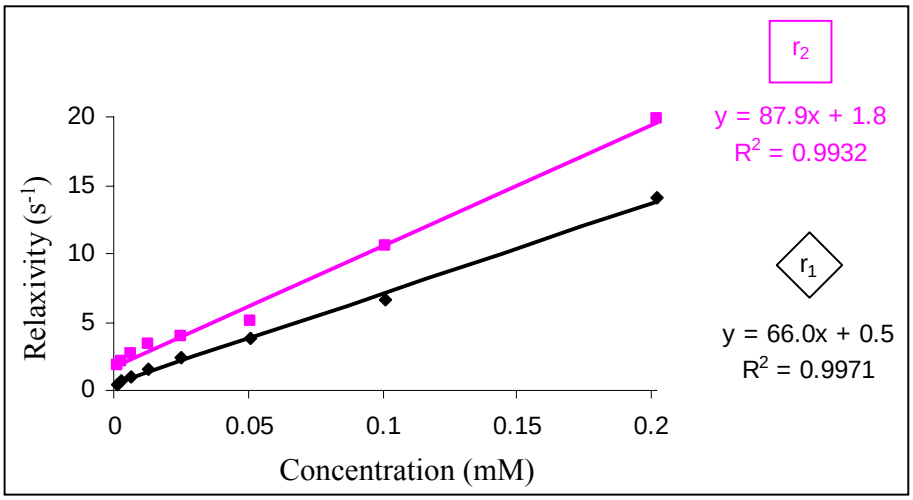


**Figure 61.** $Gd_3N@C_{80}$[DiPEG5000$(OH)_x$] 0.35T relaxivity data at all concentrations. The standard deviation (σ) for each $r_1$ point is ± 0.0028 to 0.1429, and σ for each $r_2$ point is ± 0.0015 to 0.8519. See Table 15 in the appendix for individual σ values.

The bottom graph of Figure 62 illustrates the change of slope for the two sets of data. The lower concentration set (0.0016-0.0126 mM) clearly has a steeper slope, which is proven in the above two graphs. The $r_1$ for the low concentrations is 102 ± 2 $mM^{-1}s^{-1}$, and 66 ± 3 $mM^{-1}s^{-1}$ for the high concentration set (0.0252-0.202 mM). The low concentrations have a $r_1$ relaxivity that is 1.5 times higher than the high concentrations. The $r_2$ values for the low concentrations and high concentrations are 144 ± 9 $mM^{-1}s^{-1}$ and 93 ± 4 $mM^{-1}s^{-1}$, respectively, also a 1.5 times difference. This contrast agent has higher relaxivity at lower concentrations. The explanation for the concentration dependency is not fully understood; however, it may be due to the TNT metallofullerenes forming micelles at higher concentrations.[70, 94, 117] Determination of the critical micelle concentration in future work is necessary to confirm the aggregation phenomenon at a specific concentration. At the lower concentrations, more water exchange can take place with the metallofullerenes because there are no aggregates formed to prevent the water molecules from interacting with the hydroxylated cage. The high relaxivity at low concentrations is especially beneficial when the agent will be used in patients because less would need injected into the body. The relaxivity values for this species are phenomenal, with an $r_1$ value of 144 $mM^{-1}s^{-1}$ compared to an $r_1$ value of 4 $mM^{-1}s^{-1}$ for the currently used MRI contrast agent Omniscan™. This TNT-fMF could be a next generation MRI contrast agent, but other factors could change this prediction (i.e. toxicology, biodistribution, etc.).

Due to the concentration dependency of the $r_1$ and $r_2$ relaxivities noted with $Gd_3N@C_{80}$[DiPEG5000$(OH)_x$], the high and low concentration ranges will be plotted separately, when applicable, for the remaining samples studied.

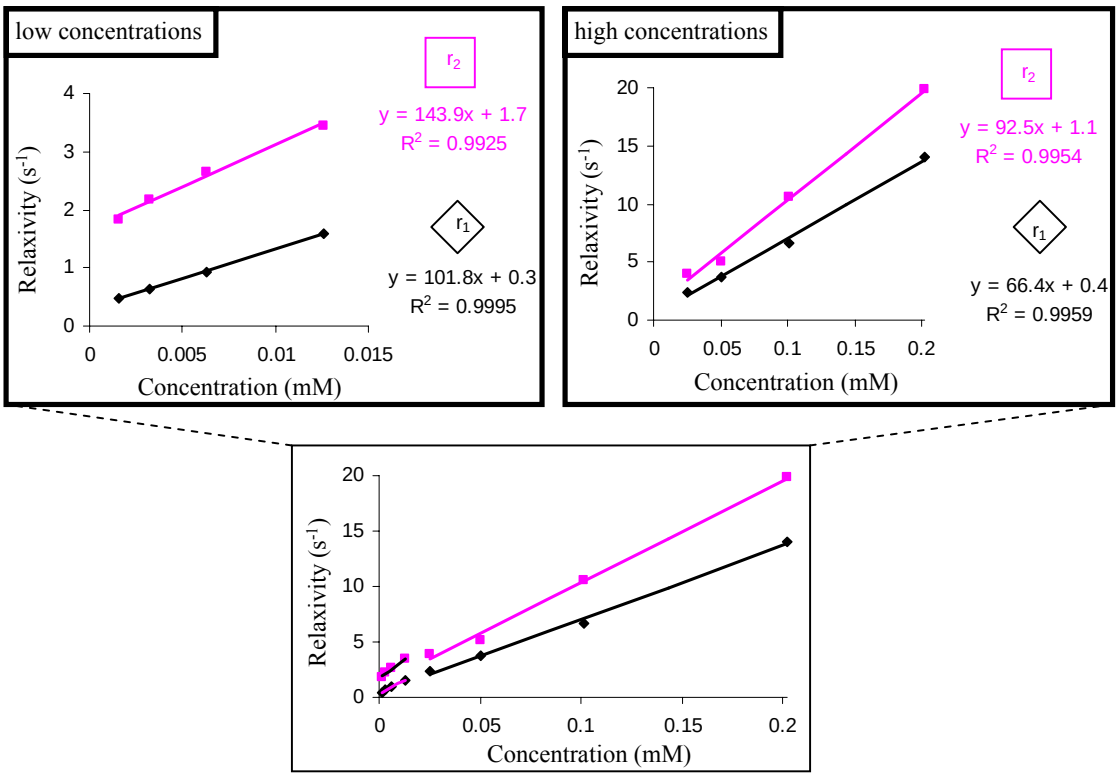


**Figure 62.** $Gd_3N@C_{80}[DiPEG5000(OH)_x]$ 0.35T relaxivity data at high and low concentrations. The standard deviation (σ) for each $r_1$ point is ± 0.0028 to 0.0246, and σ for each $r_2$ point from ± 0.0015 to 0.0866 for the low concentration range. At high concentrations σ for each $r_1$ point ranges from ± 0.0331 to 0.1429, and for each $r_2$ point from ± 0.0330 to 0.8519. See Table 15 in the appendix for individual σ values.

**3.2.5 $Gd_3N@C_{80}[DiPEG2000(OH)_x]$.** $Gd_3N@C_{80}$ was functionalized by Dr. Zhongxin Ge to contain fewer poly(ethylene)glycol units (approximately 46) than the DiPEG5000 (approximately 114) in the previous section. The DiPEG2000 functionalized metallofullerene exhibits relaxivity values very similar to the DiPEG5000 measurements. Figures 116 and 117 in the appendix contain the graphed relaxivity data for the lower and higher concentration ranges. The $r_1$ and $r_2$ values are shown in Table 5 for the low and high concentration sets. The $r_1$ and $r_2$ values for the low concentration set (0.00023-0.00364 mM) are 107 ± 5 and 112 ± 14 $mM^{-1}s^{-1}$, respectively at 0.35 T. The high concentration set (0.00729-0.1166 mM) $r_1$ and $r_2$ values are 64 ± 6 and 97 ± 2 $mM^{-1}s^{-1}$, respectively at 0.35 T. There is no significant change in the relaxivity values when the pegylated chain length is shortened.

**Table 5.** Relaxivity data for $Gd_3N@C_{80}$[DiPEG2000$(OH)_x$] and $Gd_3N@C_{80}$[DiPEG750$(OH)_x$].

| Contrast Agent | $r_1$ ($mM^{-1}s^{-1}$) | | | $r_2$ ($mM^{-1}s^{-1}$) | | |
|---|---|---|---|---|---|---|
| | 0.35T | 2.4T | 9.4T | 0.35T | 2.4T | 9.4T |
| $Gd_3N@C_{80}$[DiPEG2000$(OH)_x$] | | | | | | |
| (0.00023-0.00364 mM) | 107 ± 5 | - | 29 | 112 ± 14 | - | 183 |
| (0.00729-0.1166 mM) | 64 ± 6 | - | 21 | 97 ± 2 | - | 143 |
| $Gd_3N@C_{80}$[DiPEG750$(OH)_x$] | | | | | | |
| (0.00020-0.00317 mM) | 148 ± 12 | - | 39 | 167 ± 7 | - | 199 |
| (0.00634-0.1015 mM) | 73 ± 7 | - | 28 | 108 ± 2 | - | 129 |

**3.2.6 $Gd_3N@C_{80}$[DiPEG750$(OH)_x$].** $Gd_3N@C_{80}$ was functionalized by Dr. Zhongxin Ge with poly(ethylene)glycol units containing fewer units than the DiPEG2000 in the previous section. The DiPEG750 functionalized metallofullerene exhibits relaxivity values that are greater than the DiPEG5000 and DiPEG2000 measurements. Figures 118 and 119 in the appendix contain the graphed relaxivity data for the lower (0.00020-0.00317 mM) and higher (0.00634-0.1015 mM) concentration ranges. The concentration dependent relaxivities are shown in Table 5. The $r_1$ and $r_2$ values for the low concentrations are 148 ± 12 and 167 ± 7 $mM^{-1}s^{-1}$, and 73 ± 7 and 108 ± 2 $mM^{-1}s^{-1}$ for the high concentration set, respectively at 0.35 T. There is a notable increase in relaxivity as the chain length of the dipegylated units decreases.

**3.2.7 Holmium Chloride ($HoCl_3$).** $HoCl_3$ relaxivity data is plotted in Figure 120 (see appendix), and was measured to compare with the $Ho_3N@C_{80}(OH)_m(O)_n$ data. The data are shown in Table 6. The $r_1$ and $r_2$ values are 0.39 ± 0.05 and 1.7 ± 0.1 $mM^{-1}s^{-1}$, respectively, at a concentration range of 0.0476-0.7623 mM at 0.35 T. These relaxivity values are smaller than the Ho TNT-fMF (section 4.2.6) because, there is only one holmium atom per molecule for $HoCl_3$ and three Ho atoms per endohedral metallofullerene. Also, there is less water exchange with the $HoCl_3$, as compared to the hyrodxylated cage of the TNT metallofullerene. $HoCl_3$ exhibits inner sphere water exchange, and $Ho_3N@C_{80}(OH)_m(O)_n$ exhibits outer sphere water exchange. (Figure 63) Due to the hydroxylation of the carbon cage, the water exchange is greater for the TNT metallofullerene because there are more sites for water exchange to occur. Water

exchange with the $HoCl_3$ is less because only a limited number of water molecules can complex, or exchange, with a holmium atom at a time.

**Table 6.** $HoCl_3$ and $GdCl_3$ relaxivity data.

| Contrast Agent | $r_1$ ($mM^{-1}s^{-1}$) | | | $r_2$ ($mM^{-1}s^{-1}$) | | |
|---|---|---|---|---|---|---|
| | 0.35T | 2.4T | 9.4T | 0.35T | 2.4T | 9.4T |
| $HoCl_3$ (0.0476-0.7623 mM) | 0.39 ± 0.05 | - | 1.0 | 1.7 ± 0.1 | - | 0.9 |
| $GdCl_3$ (0.01125-0.36 mM) | 14.0 ± 0.4 | - | 10.4 | 16.6 ± 0.9 | - | 14.4 |

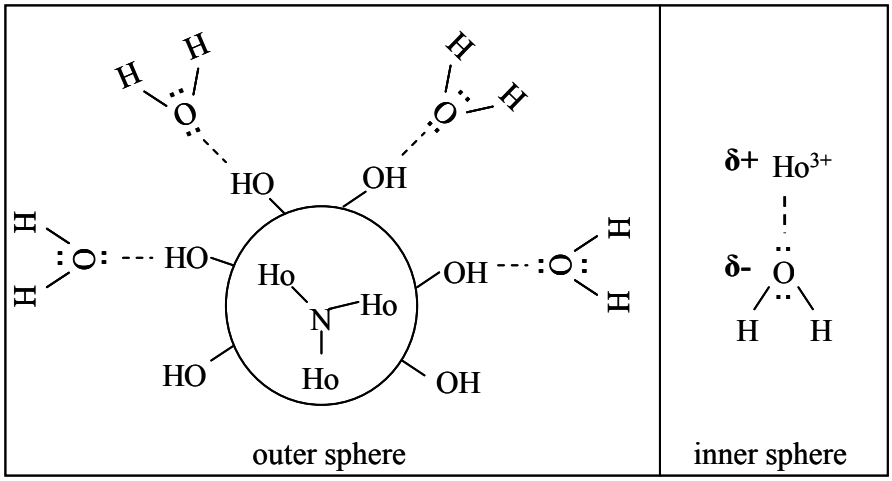


**Figure 63.** Illustration of inner sphere and outer sphere water exchange.

**3.2.8 Gadolinium Chloride ($GdCl_3$).** $GdCl_3$ was measured to compare with the $Gd_3N@C_{80}(OH)_m(O)_n$ data, and is plotted in Figure 123 (see appendix) at a concentration range of 0.01125-0.36 mM. All $GdCl_3$ data is summarized in Table 6. The $r_1$ and $r_2$ relaxivity values are 14.0 ± 0.4 and 16.6 ± 0.9 $mM^{-1}s^{-1}$, respectively. These values are greater than the $HoCl_3$ values, and less than the $Gd_3N@C_{80}(OH)_m(O)_n$ relaxivity values discussed in the next section. This is again due to $GdCl_3$ only having one Gd atom per molecule and $Gd_3N@C_{80}(OH)_m(O)_n$ having three Gd atoms per molecule.

**3.2.9 $Ho_3N@C_{80}(OH)_m(O)_n$.** This TNT-fMF has potential to be used as a diagnostic and radiotherapeutic agent by neutron-activation to yield the radioisotope $^{166}Ho$. The $r_1$ and $r_2$ values are again larger for the low concentration range, 0.000496-0.00794 mM, (Figure 122 in the appendix) than the high concentration range, 0.01588-0.25408 mM, (Figure 121 in the appendix). The $Ho_3N@C_{80}(OH)_m(O)_n$ data is summarized in Table 7. The low concentration $r_1$ and $r_2$ values are 1.1 ± 2.3 and 22 ± 4 $mM^{-1}s^{-1}$, respectively, and the high concentration values are 0.3 ± 0.1 and 12.4 ± 0.1 $mM^{-1}s^{-1}$, respectively at 0.35 T. This is another sample that exhibits higher relaxivity for lower concentrations. Based on the error and $R^2$ values for the relaxivities, it can be noted that the Ho TNT-fMF is a $T_2$ agent instead of a $T_1$ agent. The $r_2/r_1$ ratios in the next chapter will further illustrate this point. The correlations for the high and low $r_1$ values are much smaller than the $r_2$ correlations. For example, the low concentration $r_1$ is 1.1 ± 2.3 $mM^{-1}s^{-1}$ with an $R^2$ of 0.0731. This value is basically one, indicating there is

**Table 7.** Ho, Gd, and Sc hydroxylated TNT-fMF endohedral metallofullerene relaxivity data.

| Contrast Agent | $r_1$ ($mM^{-1}s^{-1}$) | | | $r_2$ ($mM^{-1}s^{-1}$) | | |
|---|---|---|---|---|---|---|
| | 0.35T | 2.4T | 9.4T | 0.35T | 2.4T | 9.4T |
| $Ho_3N@C_{80}(OH)_m(O)_n$ | | | | | | |
| (0.000496-0.00794 mM) | 1.1 ± 2.3 | - | 6.8 | 22 ± 4 | - | 61.9 |
| (0.01588-0.25408 mM) | 0.3 ± 0.1 | - | 1.8 | 12.4 ± 0.1 | - | 51.3 |
| $Gd_3N@C_{80}(OH)_m(O)_n$ | | | | | | |
| (0.0004-0.0072 mM) | 72 ± 1 | - | 29 | 143 ± 15 | - | 110 |
| (0.0075-0.12 mM) | 29 ± 1 | - | 17 | 52 ± 4 | - | 45 |
| $Sc_3N@C_{80}(OH)_m(O)_n$ | | | | | | |
| (0.0098-0.1572 mM) | 1.4 ± 0.2 | - | 1.0 | 5.2 ± 0.2 | - | 5.0 |

little to no change in the $r_1$ relaxivity as a function of concentration for this sample set. However, the $r_2$ value is 22 ± 4 $mM^{-1}s^{-1}$ with an $R^2$ value of 0.9260 (Figure 122 in the appendix). The $r_2$ value of the Ho TNT-fMF is indeed concentration dependent.

**3.2.10 $Gd_3N@C_{80}(OH)_m(O)_n$.** This Gd containing TNT-fMF also demonstrates higher relaxivities at low concentrations (0.0004-0.0072 mM) than at higher

concentrations (0.0075-0.12 mM). The experimental relaxivity values are listed in Table 7. The $r_1$ and $r_2$ values at low concentrations (Figure 124 in the appendix) are 72 ± 1 and 143 ± 15 $mM^{-1}s^{-1}$, respectively, and at high concentrations (Figure 125 in the appendix) are 29 ± 1 and 52 ± 4 $mM^{-1}s^{-1}$, respectively at 0.35 T. These relaxivities are significantly greater than those for Omniscan™ (~4 $mM^{-1}s^{-1}$ for $r_1$ and $r_2$). $Gd_3N@C_{80}(OH)_m(O)_n$ is also a potential MRI contrast agent based on the relaxivity measurements that have been performed. Both water-soluble TNT Gd-based endohedral metallofullerenes ($Gd_3N@C_{80}(OH)_m(O)_n$ and $Gd_3N@C_{80}$[DiPEG5000$(OH)_x$]) have phenomenally high relaxivities compared to Omniscan™.

**3.2.11 $Sc_3N@C_{80}(OH)_m(O)_n$.** The relaxivity values for the Sc-containing species are shown in Table 7. The $r_1$ and $r_2$ relaxivities for $Sc_3N@C_{80}(OH)_m(O)_n$ are 1.4 ± 0.2 and 5.2 ± 0.2 $mM^{-1}s^{-1}$, respectively at the concentration range 0.0098-0.1572 mM at 0.35 T. The scandium species is not expected to have a large relaxivity due to the diamagnetic nature of $Sc^{3+}$. The graphed data is shown in Figure 126 in the appendix.

**3.2.12 Omniscan™.** Omniscan™ is currently used as a contrast agent when MR images are being measured. The $r_1$ and $r_2$ of Omniscan™ at 0.35T are 4.33 ± 0.07 and 5.76 ± 0.09 $mM^{-1}s^{-1}$, respectively from 0.25-5.0 mM. The Omniscan™ data is graphed in Figure 127 located in the appendix. These relaxivity values are significantly lower than the measured values for the gadolinium metallofullerene species. Table 8 presents the relaxivity data for Omniscan™ at all three field strengths studied.

**Table 8.** Omniscan™ relaxivity data.

| Contrast Agent | $r_1$ ($mM^{-1}s^{-1}$) | | | $r_2$ ($mM^{-1}s^{-1}$) | | |
|---|---|---|---|---|---|---|
| | 0.35T | 2.4T | 9.4T | 0.35T | 2.4T | 9.4T |
| Omniscan (0. 25-5.0 mM) | 4.33 ± 0.07 | ~4 | 4.0 | 5.76 ± 0.09 | ~4 | 4.0 |

# 4. Comparing Relaxivities of the New MRI Contrast Agents to Commercial MRI Contrast Agents

## 4.1 Measured Relaxivities of Commercial Agents versus New MRI Contrast Agents

Table 9 summarizes the relaxivity data for all species measured. As expected, the Lu and Sc TNT-fMFs observe very small water $^{1}H$ MRI relaxivity values compared to the Gd TNT-fMFs at all field strengths. Also, Omniscan$^{TM}$ exhibits small relaxivity values compared to the Gd TNT-fMFs. This indicates the relaxivity of Gd TNT-fMFs surpass those of the currently used contrast agent Omniscan$^{TM}$, and at exceedingly lower concentrations. The measured $r_1$ relaxivity of $Gd_3N@C_{80}(OH)_m(O)_n$, 29 $mM^{-1}s^{-1}$ at 9.4 T, is comparable to the relaxivities of other gadolinium based endohedral metallofullerols previously reported.[61, 70, 73] Previous work performed by Shinohara's group is shown in Table 10.[61, 73] Relaxivity measurements were performed on $GdCl_3$ and the TNT-fMF $Gd@C_{82}(OH)_x$ at three field strengths (0.47, 1.0, and 4.7 T).

Comparing the 0.35 T data from Table 9 with the 0.47 T data from Table 10, a very good agreement can be noted for $GdCl_3$. It is surprising that the relaxivity of $GdCl_3$ is about three times higher than that of Omniscan$^{TM}$, but previous measurements by the Shinohara group compare extremely well to the data in Table 9.

The pegylated and hydroxylated functionalized $Gd_3N@C_{80}$ metallofullerenes were studied with three different chain lengths of the dipegylated units. All three pegylated and hydroxylated samples exhibit enhanced relaxivities. Table 9 compares the relaxivities of the samples. The relaxivities of the DiPEG5000 and DiPEG2000 samples are very similar; however, as the chain length decreases, the DiPEG750 exhibits higher $r_1$ and $r_2$ relaxivities than its longer chain counterparts.

**Table 9.** Summary of relaxivity data.

| Contrast Agent | $r_1$ ($mM^{-1}s^{-1}$) | | | $r_2$ ($mM^{-1}s^{-1}$) | | |
|---|---|---|---|---|---|---|
| | 0.35T | 2.4T | 9.4T | 0.35T | 2.4T | 9.4T |
| $Lu_3N@C_{80}[DiPEG5000(OH)_x]$ (0.1-0.8 mM) | 0.60 ± 0.09 | - | 0.4 | 1.5 ± 0.4 | - | 2 |
| $Gd_3N@C_{80}[DiPEG5000(OH)_x]$ (0.0016-0.0126 mM) | 102 ± 2 | 143 | 32 | 144 ± 9 | 222 | 137 |
| (0.0252-0.202 mM) | 66 ± 3 | - | - | 93 ± 4 | - | - |
| $Gd_3N@C_{80}[DiPEG2000(OH)_x]$ (0.00023-0.00364 mM) | 107 ± 5 | - | 29 | 112 ± 14 | - | 183 |
| (0.00729-0.1166 mM) | 64 ± 6 | - | 21 | 97 ± 2 | - | 143 |
| $Gd_3N@C_{80}[DiPEG750(OH)_x]$ (0.00020-0.00317 mM) | 148 ± 12 | - | 39 | 167 ± 7 | - | 199 |
| (0.00634-0.1015 mM) | 73 ± 7 | - | 28 | 108 ± 2 | - | 129 |
| $HoCl_3$ (0.0476-0.7623 mM) | 0.39 ± 0.05 | - | 1.0 | 1.7 ± 0.1 | - | 0.9 |
| $Ho_3N@C_{80}(OH)_m(O)_n$ (0.000496-0.00794 mM) | 1.1 ± 2.3 | - | 6.8 | 22 ± 4 | - | 61.9 |
| (0.01588-0.25408 mM) | 0.3 ± 0.1 | - | 1.8 | 12.4 ± 0.1 | - | 51.3 |
| $GdCl_3$ (0.01125-0.36 mM) | 14.0 ± 0.4 | - | 10.4 | 16.6 ± 0.9 | - | 14.4 |
| $Gd_3N@C_{80}(OH)_m(O)_n$ (0.0004-0.0072 mM) | 72 ± 1 | - | 29 | 143 ± 15 | - | 110 |
| (0.0075-0.12 mM) | 29 ± 1 | - | 17 | 52 ± 4 | - | 45 |
| $Sc_3N@C_{80}(OH)_m(O)_n$ (0.0098-0.1572 mM) | 1.4 ± 0.2 | - | 1.0 | 5.2 ± 0.2 | - | 5.0 |
| Omniscan (0. 25-5.0 mM) | 4.33 ± 0.07 | ~4 | 4.0 | 5.76 ± 0.09 | ~4 | 4.0 |

**Table 10.** Relaxivity data for $Gd@C_{82}(OH)_x$.

| | $r_1$ ($mM^{-1}s^{-1}$) | | | $r_2$ ($mM^{-1}s^{-1}$) | | |
|---|---|---|---|---|---|---|
| | 0.47 T | 1.0 T | 4.7 T | 0.47 T | 1.0 T | 4.7 T |
| $GdCl_3$[73] | 12 | - | - | 14 | - | - |
| $Gd@C_{82}(OH)_x$[73] | 73 | - | - | 80 | - | - |
| $Gd@C_{82}(OH)_{40}$[61] | 67 | 81 | 31 | 79 | 108 | 131 |

**Table 11.** $r_2/r_1$ ratios for Gd, Ho, Lu, and Sc containing species.

| Contrast Agent | $r_2/r_1$ 0.35T | 2.4T | 9.4T |
|---|---|---|---|
| $Lu_3N@C_{80}$[DiPEG5000$(OH)_x$] (0.1-0.8mM) | 2.5 | - | 5 |
| $Gd_3N@C_{80}$[DiPEG5000$(OH)_x$] (0.0016-0.0126 mM) | 1.4 | 1.6 | 4.3 |
| (0.0252-0.202 mM) | 1.4 | - | - |
| $Gd_3N@C_{80}$[DiPEG2000$(OH)_x$] (0.00023-0.00364 mM) | 1.0 | - | 6.3 |
| (0.00729-0.1166 mM) | 1.5 | - | 6.8 |
| $Gd_3N@C_{80}$[DiPEG750$(OH)_x$] (0.00020-0.00317 mM) | 1.1 | - | 5.1 |
| (0.00634-0.1015 mM) | 1.5 | - | 4.6 |
| $HoCl_3$ (0.0476-0.7623mM) | 4.3 | - | 0.9 |
| $Ho_3N@C_{80}(OH)_m(O)_n$ (0.000496-0.00794mM) | 20 | - | 9.1 |
| (0.01588-0.25408mM) | 41.3 | - | 28.5 |
| $GdCl_3$ (0.01125-0.36mM) | 1.2 | - | 1.4 |
| $Gd_3N@C_{80}(OH)_m(O)_n$ (0.0004-0.0072mM) | 2.0 | - | 3.8 |
| (0.0075-0.12mM) | 1.8 | - | 2.6 |
| $Sc_3N@C_{80}(OH)_m(O)_n$ (0.0098-0.1572mM) | 3.7 | - | 5.0 |
| Omniscan (5.0-0.25mM) | 1.3 | 1.0 | 1.0 |

To distinguish a $T_1$ from a $T_2$ agent, the $r_2/r_1$ ratios were determined and tabulated in Table 11. A $T_2$ agent has a high $r_2/r_1$ ratio. According to the data in Table 11, the $r_2/r_1$ ratios of the Ho species are on the order of 9-41 and the $r_2/r_1$ ratios for the other species are from approximately one to seven. This suggests that $Ho_3N@C_{80}(OH)_m(O)_n$ has the potential to be a $T_2$ agent. Further studies (*in vitro* and *in vivo*) are in progress to better understand the medical applications of the Ho-based water-soluble TNT endohedral metallofullerene.

*The 9.4 T relaxivity measurements, performed by Tom Glass and Xuelei Wang and the 2.4 T relaxivity measurements, performed at VCU by Dr. Panos Fatouros and Frank Corwin, were reported for comparison purposes to the 0.35 T relaxivity measurements performed by the author of this work.

## 4.2 Conclusions

Gadolinium based endohedral metallofullerenes are being studied as prime candidates for the next generation MRI contrast agents. The relaxivity studies indicate that water-soluble Gd containing metallofullerenes show greater relaxivities and more efficiency than commercially available MRI contrast agents.[60, 61, 70, 72, 73, 94] The TNT endohedral metallofullerenes have inherent advantages over monometallofullerenes, such as $M@C_{60}$ and $M@C_{82}$, due to the possibility of encapsulating a maximum of three metal (gadolinium) atoms inside the carbon cage, such as $Gd_3N@C_{80}$,[96, 97] or different metals such as lutetium which possesses multimodal imaging potential (X-ray and MRI).[87]

The new TNT endohedral metallofullerene, $Gd_3N@C_{80}[DiPEG5000(OH)_x]$, is an effective proton relaxation agent. This effectiveness was demonstrated in aqueous solutions ($r_1$ relaxivity) and by our VCU collaborators in *in vitro* relaxivity and imaging MR studies, in infusion experiments with agarose gels and *in vivo* rat brain studies simulating clinical conditions of direct intraparenchymal drug delivery for the treatment of brain tumors.[60] $Gd_3N@C_{80}[DiPEG5000(OH)_x]$ provides an improved tumor delineation in comparison with Gd-DTPA.[60] The $r_1$ values of the three dipegylated and hydroxylated TNT metallofullerenes are 40-100% higher than relaxivity values reported

for hydroxylated Gd@$C_{82}$ by Shinohara and coworkers at similar field strengths (Table 12);[61, 73] however, $Gd_3N@C_{80}$[DiPEG5000$(OH)_x$] relaxivity values are based on three Gd atoms per molecular cluster, not one.

**Table 12.** Comparison of dipegylated and hydroxylated TNT metallofullerenes to literature data.[61, 73]

| | $r_1$ ($mM^{-1}s^{-1}$) | | $r_2$ ($mM^{-1}s^{-1}$) | |
|---|---|---|---|---|
| | 0.35 T | 0.47 T | 0.35 T | 0.47 T |
| Gd@$C_{82}(OH)_{40}$[61] | | 67 | | 79 |
| Gd@$C_{82}(OH)_n$[73] | | 73 | | 80 |
| $Gd_3N@C_{80}$[DiPEG5000$(OH)_x$] | 102 ± 2 | | 144 ± 9 | |
| $Gd_3N@C_{80}$[DiPEG2000$(OH)_x$] | 107 ± 5 | | 112 ± 14 | |
| $Gd_3N@C_{80}$[DiPEG750$(OH)_x$] | 148 ± 12 | | 167 ± 7 | |

As expected, the lutetium functionalized $Lu_3N@C_{80}$ agent exhibited very low MRI relaxivity due to the diamagnetic properties. The $Lu_3N@C_{80}$[DiPEG5000$(OH)_x$] sample was used as a diamagnetic control and demonstrated that the enhanced relaxivity of $Gd_3N@C_{80}$[DiPEG5000$(OH)_x$] originates from the $Gd_3N$ cluster inside and not from the significant unpaired electron spin density on the carbon cage. The lutetium agent would exhibit the same biodistribution properties as the $Gd_3N@C_{80}$ species because only the metal cluster inside the cage is changed.[60] The cage undergoes the same functionalization procedure for both samples. This presents a new multi-modal platform, where neutron activation will provide a $^{177}$Lu radiolabelled agent to compliment the MRI agent $Gd_3N@C_{80}$.

The relaxivities studied are concentration dependent and increase with dilution. The relaxivities of low concentration metallofullerenes are significantly higher than those of high concentration metallofullerenes. The explanation for this occurrence remains unclear; however, it is suspected that the metallofullerenes are forming micelles at higher concentrations preventing water molecules from interacting with the metallofullerenes. Relaxivity is remarkedly improved at lower concentrations because aggregation or micelle formation is discouraged and water accessibility to the carbon cage is improved. The TNT gadolinium based metallofullerenes ($Gd_3N@C_{80}$[DiPEG5000$(OH)_x$], $Gd_3N@C_{80}$[DiPEG2000$(OH)_x$], $Gd_3N@C_{80}$[DiPEG750$(OH)_x$], and $Gd_3N@C_{80}(OH)_m(O)_n$) show a higher relaxivity compared to the commercial agent

Omniscan$^{TM}$, suggesting their application as the next generation MRI contrast agent. The increased relaxivity allows the use of significantly lower concentrations of the new Gd-based contrast agents. Future work on this project includes *in vitro* and *in vivo* studies to determine the effects of the dipegylated chain length on the relaxivity of the metallofullerene species, as well as the effects of the hydroxylation of the cage in the Ho and Gd examples from sections 3.2.8 and 3.2.9. The different functionalizations of the cage could result in different biodistribution and relaxivity effects of the TNT-fMF species when injected into the body. Future work also includes *in vitro* and *in vivo* studies of functionalized Ho or Lu endohedral metallofullerene molecules to be used as combinatorial imaging and radiotherapeutic agents that may be neutron-activated to produce radioactive isotopes ($^{166}$Ho and $^{177}$Lu). The Ho and Lu species will be studied both.

# 5. Appendix

## 5.1 Additional Computational Details

The computations were performed on a SGI ALTIX 3700 Supercluster at Virginia Tech, which contains sixteen 1.3 GHz Itanium processors each with 3MB of cache, 24GB of memory, 36GB of internal disk storage and 500GB of RAID disk storage. A typical calculation ran for about 1-4 hours depending on the system size, for example the substituted benzene systems were more expensive than the acetonitrile system. The keywords used on the first three lines of the input file are:

---

```
%mem=6MW
%nproc=1
# ub3lyp geom=connectivity gen
```

---

The basis set used (Chipman DZP+diffuse (with the first d-type polarization function removed for C, N, and O)) is shown below for the H, C, N, and O atoms:[103]

---

```
H   0
S   3  1.00
     127.950000        0.107360000E-01
     19.2406000        0.119544000
     2.89920000        0.926416000
S   1  1.00
    0.653400000         1.00000000
S   1  1.00
    0.177600000         1.00000000
S   1  1.00
    0.483000000E-01      1.00000000
P   1  1.00
     1.00000000         1.00000000
****
C   0
S   5  1.00
     4232.61000        0.202900000E-02
     634.882000        0.155350000E-01
     146.097000        0.754110000E-01
```

```
     42.4974000          0.257121000
     14.1892000          0.596555000
S   1  1.00
     1.96660000          1.00000000
S   1  1.00
     5.14770000          1.00000000
S   1  1.00
    0.496200000          1.00000000
S   1  1.00
    0.153300000          1.00000000
S   1  1.00
    0.479000000E-01      1.00000000
P   4  1.00
     18.1557000          0.185340000E-01
     3.98640000          0.115442000
     1.14290000          0.386206000
    0.359400000          0.640089000
P   1  1.00
    0.114600000          1.00000000
P   1  1.00
    0.358000000E-01      1.00000000
D   1  1.00
     1.12000000          1.00000000
****
N   0
S   5  1.00
     5909.44000          0.200400000E-02
     887.451000          0.153100000E-01
     204.749000          0.742930000E-01
     59.8376000          0.253364000
     19.9981000          0.600576000
S   1  1.00
     2.68600000          1.00000000
S   1  1.00
     7.19270000          1.00000000
S   1  1.00
    0.700000000          1.00000000
S   1  1.00
    0.213300000          1.00000000
S   1  1.00
    0.667000000E-01      1.00000000
P   4  1.00
     26.7860000          0.182570000E-01
     5.95640000          0.116407000
     1.70740000          0.390111000
    0.531400000          0.637221000
P   1  1.00
    0.165400000          1.00000000
P   1  1.00
    0.517000000E-01      1.00000000
D   1  1.00
```

```
     1.48000000          1.00000000
****
O   0
S   5  1.00
     7816.54000          0.203100000E-02
     1175.82000          0.154360000E-01
     273.188000          0.737710000E-01
     81.1696000          0.247606000
     27.1836000          0.611832000
S   1  1.00
     3.41360000          1.00000000
S   1  1.00
     9.53220000          1.00000000
S   1  1.00
    0.939800000          1.00000000
S   1  1.00
    0.284600000          1.00000000
S   1  1.00
    0.862000000E-01      1.00000000
P   4  1.00
     35.1832000          0.195800000E-01
     7.90400000          0.124189000
     2.30510000          0.394727000
    0.717100000          0.627375000
P   1  1.00
    0.213700000          1.00000000
P   1  1.00
    0.648000000E-01      1.00000000
D   1  1.00
     2.20000000          1.00000000
****
```

---

The Cartesian coordinates for the individual molecules are listed in sections 6.1.1-6.1.10. To run a calculation, the optimized individual TEMPO and substrate molecule of interest were joined together using GaussView,[104] which created the input coordinates of the TEMPO-substrate system automatically.

### 5.1.1 TEMPO Cartesian Coordinates.

**5.1.1.1 Optimized Monoclinic Crystal Structure.** This conformation is in best agreement compared to experimental data, and the TEMPO structure used for all calculations. The remaining four conformations (in sections 5.1.1.2-5.1.1.5) did not reproduce the experimental hyperfine coupling constants of the TEMPO molecule.

| | | | |
|---|---|---|---|
| C | -2.12298000 | 0.13246500 | 0.00000000 |
| C | -1.35913500 | 0.58300500 | 1.24493000 |
| C | 0.07306400 | 0.02168600 | 1.33033100 |
| C | 0.07306400 | -1.46007300 | 1.76469400 |
| C | 0.88180400 | 0.84284900 | 2.34634600 |
| H | -2.26223600 | -0.95345700 | 0.00000000 |
| H | -3.12558800 | 0.57079900 | 0.00000000 |
| H | -1.30802700 | 1.67788800 | 1.24471200 |
| H | -1.88931200 | 0.29314300 | 2.15743900 |
| H | -0.26895200 | -1.54187700 | 2.80015600 |
| H | 1.08554000 | -1.86373300 | 1.70211400 |
| H | -0.58351300 | -2.07485900 | 1.14566000 |
| H | 0.96095900 | 1.88533100 | 2.02703800 |
| H | 1.88948900 | 0.44385700 | 2.45730800 |
| H | 0.37916700 | 0.81617300 | 3.31716300 |
| N | 0.76005500 | 0.14566400 | 0.00000000 |
| O | 2.03113200 | -0.06915400 | 0.00000000 |
| C | -1.35913500 | 0.58300500 | -1.24493000 |
| C | 0.07306400 | 0.02168600 | -1.33033100 |
| H | -1.30802700 | 1.67788800 | -1.24471200 |
| H | -1.88931200 | 0.29314300 | -2.15743900 |
| C | 0.07306400 | -1.46007300 | -1.76469400 |
| C | 0.88180400 | 0.84284900 | -2.34634600 |
| H | -0.26895200 | -1.54187700 | -2.80015600 |
| H | 1.08554000 | -1.86373300 | -1.70211400 |
| H | -0.58351300 | -2.07485900 | -1.14566000 |
| H | 0.96095900 | 1.88533100 | -2.02703800 |
| H | 1.88948900 | 0.44385700 | -2.45730800 |
| H | 0.37916700 | 0.81617300 | -3.31716300 |

#### 5.1.1.2 Monoclinic Crystal Structure.

| | | | |
|---|---|---|---|
| C | -2.08655700 | 0.08045500 | 0.00000000 |
| C | -1.34184600 | 0.55986800 | 1.21200000 |
| C | 0.07861400 | 0.01801400 | 1.31680000 |
| C | 0.07861400 | -1.45389800 | 1.74620000 |
| C | 0.87332200 | 0.85982000 | 2.31630000 |
| H | -2.17035200 | -0.88682100 | 0.00000000 |
| H | -2.97242000 | 0.35120700 | 0.00000000 |
| H | -1.24077700 | 1.46622100 | 1.22060000 |
| H | -1.75066400 | 0.28397300 | 1.89550000 |
| H | -0.29882600 | -1.36862900 | 2.57040000 |
| H | 0.78865400 | -1.71348500 | 1.82370000 |
| H | -0.54461700 | -2.06844300 | 1.19190000 |
| H | 0.88409400 | 1.80749400 | 1.96730000 |
| H | 1.73280100 | 0.68412300 | 2.35500000 |
| H | 0.41661200 | 0.86911200 | 3.04430000 |
| N | 0.74667600 | 0.13523400 | 0.00000000 |
| O | 2.02454700 | -0.07751600 | 0.00000000 |
| C | -1.34184600 | 0.55986800 | -1.21200000 |
| C | 0.07861400 | 0.01801400 | -1.31680000 |
| H | -1.24077700 | 1.46622100 | -1.22060000 |
| H | -1.75066400 | 0.28397300 | -1.89550000 |
| C | 0.07861400 | -1.45389800 | -1.74620000 |
| C | 0.87332200 | 0.85982000 | -2.31630000 |
| H | -0.29882600 | -1.36862900 | -2.57040000 |
| H | 0.78865400 | -1.71348500 | -1.82370000 |
| H | -0.54461700 | -2.06844300 | -1.19190000 |
| H | 0.88409400 | 1.80749400 | -1.96730000 |
| H | 1.73280100 | 0.68412300 | -2.35500000 |
| H | 0.41661200 | 0.86911200 | -3.04430000 |

#### 5.1.1.3 Orthorhombic Crystal Structure.

| | | | |
|---|---|---|---|
| N | -0.00594300 | -0.75086900 | -0.17556100 |
| O | 0.00061100 | -2.01851500 | -0.10220400 |
| C | 1.31803900 | -0.05969000 | -0.03236700 |
| C | 1.20518400 | 1.34702000 | -0.58441100 |
| C | 0.00112300 | 2.11301500 | -0.03349300 |
| C | -1.24656400 | 1.34639900 | -0.54349100 |
| C | -1.31426200 | -0.07220700 | -0.01900200 |
| C | 2.34692400 | -0.85723500 | -0.80676600 |
| C | 1.70954400 | -0.07552600 | 1.46637700 |
| C | -2.35672800 | -0.86886600 | -0.82740500 |
| C | -1.65498300 | -0.06510000 | 1.47398400 |
| H | 1.16109500 | 1.33597400 | -1.59993200 |
| H | 2.12156100 | 1.85881800 | -0.24118300 |
| H | -0.01854800 | 2.24016900 | 0.96236600 |
| H | -0.03731700 | 2.99453900 | -0.52868800 |
| H | -2.13549300 | 1.84685000 | -0.20253600 |
| H | -1.23649300 | 1.30850000 | -1.55528100 |
| H | 2.09534900 | -0.95072800 | -1.83003600 |
| H | 2.46204200 | -1.82060700 | -0.40202500 |
| H | 3.24342000 | -0.33096500 | -0.81934600 |
| H | 2.74558000 | 0.20564200 | 1.50338700 |
| H | 1.11494300 | 0.60045500 | 2.01852300 |
| H | 1.69261100 | -1.08889500 | 1.78069200 |
| H | -2.00696500 | -0.94255000 | -1.79517000 |
| H | -2.47748700 | -1.86862200 | -0.37617300 |
| H | -3.25392000 | -0.34655900 | -0.79684200 |
| H | -1.64386200 | -1.12110900 | 1.81770400 |
| H | -1.16750200 | 0.46283900 | 1.97114500 |
| H | -2.67196800 | 0.17360100 | 1.57940000 |

#### 5.1.1.4 Optimized Orthorhombic Crystal Structure.

| | | | |
|---|---|---|---|
| N | -0.00000700 | -0.74848000 | -0.19513200 |
| O | 0.00000300 | -2.03097500 | -0.06417300 |
| C | 1.33017300 | -0.07150200 | -0.02641700 |
| C | 1.24524600 | 1.39508100 | -0.49154900 |
| C | -0.00001100 | 2.12777900 | 0.00760000 |
| C | -1.24524900 | 1.39506700 | -0.49158800 |
| C | -1.33020300 | -0.07149700 | -0.02641200 |
| C | 2.34567600 | -0.82435200 | -0.89969500 |
| C | 1.76565400 | -0.17007700 | 1.45166500 |
| C | -2.34571300 | -0.82437800 | -0.89964500 |
| C | -1.76559700 | -0.17003800 | 1.45168200 |
| H | 1.24593000 | 1.41742700 | -1.58744600 |
| H | 2.15739300 | 1.90475900 | -0.16628200 |
| H | -0.00004400 | 2.19610400 | 1.10031400 |
| H | -0.00002800 | 3.15678900 | -0.36468300 |
| H | -2.15740100 | 1.90477900 | -0.16639600 |
| H | -1.24587600 | 1.41736600 | -1.58748700 |
| H | 2.02686800 | -0.83343100 | -1.94525300 |
| H | 2.45552900 | -1.85656700 | -0.56879700 |
| H | 3.31718700 | -0.32588000 | -0.83900500 |
| H | 2.80018500 | 0.16885100 | 1.55564600 |
| H | 1.14534400 | 0.44132300 | 2.11000300 |
| H | 1.70616800 | -1.20757500 | 1.78594200 |
| H | -2.02721200 | -0.83299700 | -1.94529900 |
| H | -2.45510200 | -1.85673500 | -0.56903300 |
| H | -3.31737700 | -0.32627000 | -0.83847900 |
| H | -1.70657600 | -1.20760100 | 1.78585700 |
| H | -1.14487500 | 0.44094600 | 2.11004300 |
| H | -2.79995100 | 0.16937900 | 1.55582600 |

#### 5.1.1.5 Optimized GaussView Structure.

| | | | |
|---|---|---|---|
| C | 1.33050900 | -0.07141600 | -0.02658900 |
| C | 1.24515400 | 1.39524200 | -0.49117100 |
| C | -0.00000700 | 2.12756800 | 0.00863500 |
| C | -1.24515300 | 1.39523200 | -0.49119300 |
| C | -1.33049500 | -0.07142300 | -0.02660200 |
| N | 0.00001200 | -0.74848900 | -0.19396100 |
| O | 0.00001400 | -2.03085500 | -0.06212000 |
| C | 2.34507200 | -0.82420900 | -0.90096400 |
| C | 1.76740300 | -0.17033800 | 1.45104800 |
| H | 1.24553000 | 1.41807000 | -1.58707000 |
| H | 2.15739600 | 1.90488300 | -0.16608500 |
| H | -0.00000600 | 3.15693900 | -0.36266000 |
| H | -0.00001400 | 2.19493600 | 1.10142300 |
| H | -2.15740700 | 1.90486000 | -0.16611900 |
| H | -1.24551400 | 1.41805700 | -1.58709100 |
| C | -2.34502000 | -0.82424600 | -0.90099800 |
| C | -1.76746800 | -0.17032000 | 1.45101900 |
| H | 2.02592200 | -0.83204600 | -1.94643000 |
| H | 2.45414200 | -1.85681800 | -0.57102300 |
| H | 3.31710100 | -0.32673900 | -0.84020000 |
| H | 1.14626400 | 0.43925400 | 2.11026500 |
| H | 1.71012600 | -1.20819700 | 1.78457100 |
| H | 2.80135000 | 0.17056400 | 1.55452200 |
| H | -2.45417800 | -1.85682000 | -0.57097200 |
| H | -2.02577000 | -0.83220200 | -1.94643300 |
| H | -3.31702700 | -0.32671900 | -0.84037200 |
| H | -1.70968800 | -1.20809100 | 1.78472800 |
| H | -1.14679100 | 0.43975600 | 2.11023400 |
| H | -2.80161600 | 0.17003700 | 1.55429900 |

### 5.1.2 Acetonitrile Cartesian Coordinates.

| | | | |
|---|---|---|---|
| C | -4.00834700 | -0.01231600 | 1.03669100 |
| C | -5.17272300 | 0.02235300 | 0.14805600 |
| N | -6.09490900 | 0.04981000 | -0.55625000 |
| H | -3.08937900 | -0.04094500 | 0.44801000 |
| H | -3.99482900 | 0.87654300 | 1.67042200 |
| H | -4.04902800 | -0.89910000 | 1.67216500 |

### 5.1.3 Acetamide Cartesian Coordinates.

| | | | |
|---|---|---|---|
| C | 3.46506600 | -0.03664400 | -1.44197100 |
| H | 3.88425900 | 0.83672500 | -1.94517900 |
| H | 2.38321600 | -0.05082000 | -1.58870600 |
| H | 3.90172300 | -0.92418900 | -1.90382200 |
| C | 3.88258500 | 0.00187300 | 0.02173000 |
| O | 5.05630900 | 0.02154900 | 0.36420500 |
| N | 2.85673500 | 0.01311400 | 0.93334500 |
| H | 3.08636000 | 0.03844700 | 1.91502200 |
| H | 1.88965300 | -0.00292100 | 0.65884800 |

### 5.1.4 Benzene Cartesian Coordinates.

| | | | |
|---|---|---|---|
| H | -2.94874500 | 2.18030100 | 1.14974000 |
| C | -3.10222800 | 1.22731800 | 0.65383700 |
| C | -3.57231800 | 1.19186100 | -0.66591500 |
| C | -2.83034700 | 0.03209400 | 1.33318000 |
| C | -3.77052700 | -0.03882100 | -1.30632400 |
| H | -3.78285100 | 2.11738700 | -1.19196600 |
| C | -3.02855600 | -1.19858700 | 0.69277100 |
| H | -2.46633100 | 0.05955000 | 2.35513500 |
| C | -3.49864600 | -1.23404500 | -0.62698100 |
| H | -4.13454300 | -0.06627700 | -2.32827900 |
| H | -2.81802300 | -2.12411400 | 1.21882200 |
| H | -3.65212900 | -2.18702800 | -1.12288400 |

### 5.1.5 Toluene Cartesian Coordinates.

| | | | |
|---|---|---|---|
| H | -7.31455800 | 0.88721700 | 0.63281100 |
| C | -6.94403700 | 0.00028200 | 0.11247900 |
| C | -5.43552200 | -0.00005200 | 0.02278100 |
| H | -7.40461400 | -0.02980400 | -0.87830300 |
| H | -7.30102300 | -0.87605200 | 0.66555800 |
| C | -4.71589400 | 1.20529800 | -0.03025400 |
| C | -4.71341200 | -1.20508300 | 0.02045200 |
| C | -3.31663800 | 1.20918000 | -0.07839200 |
| H | -5.25528300 | 2.14823800 | -0.03609700 |
| C | -3.31414900 | -1.20810600 | -0.02754100 |
| H | -5.25086000 | -2.14854300 | 0.05429200 |
| C | -2.60906600 | 0.00075700 | -0.07707300 |
| H | -2.78168300 | 2.15256600 | -0.12108900 |
| H | -2.77725300 | -2.15135000 | -0.03055000 |
| H | -1.52482800 | 0.00103500 | -0.11693200 |

### 5.1.6 Phenylacetylene Cartesian Coordinates.

| | | | |
|---|---|---|---|
| C | 4.52025600 | 1.21840500 | -0.18891700 |
| C | 5.78992900 | 1.24486600 | 0.39266300 |
| C | 3.89649800 | -0.01300100 | -0.47698300 |
| H | 4.00360500 | 2.14171500 | -0.42376900 |
| C | 6.45397600 | 0.04851800 | 0.69449900 |
| H | 6.26054200 | 2.19770900 | 0.61005000 |
| C | 4.57038000 | -1.21319300 | -0.17065100 |
| C | 2.59170900 | -0.04438800 | -1.07465700 |
| C | 5.83988500 | -1.17857500 | 0.41086800 |
| H | 7.43994600 | 0.07223600 | 1.14613300 |
| H | 4.09228900 | -2.16043100 | -0.39145200 |
| C | 1.48780800 | -0.07094200 | -1.58031100 |
| H | 6.34929600 | -2.10784300 | 0.64239200 |
| H | 0.51907000 | -0.09424400 | -2.02405200 |

### 5.1.7 Fluorobenzene Cartesian Coordinates.

| | | | |
|---|---|---|---|
| H | 3.25790100 | 2.31528100 | -0.49075100 |
| C | 3.29469700 | 1.32765500 | -0.04671300 |
| C | 3.84424400 | 0.26619200 | -0.76394900 |
| C | 2.80321700 | 1.07519900 | 1.23991500 |
| C | 3.92129500 | -1.02727300 | -0.25000100 |
| F | 4.32234500 | 0.50094800 | -2.00974300 |
| C | 2.86612900 | -0.21407800 | 1.78473000 |
| H | 2.37188000 | 1.88848500 | 1.81352800 |
| C | 3.42457600 | -1.26003900 | 1.03832700 |
| H | 4.35784600 | -1.81861300 | -0.84760700 |
| H | 2.48356100 | -0.40192400 | 2.78159000 |
| H | 3.47571000 | -2.26001000 | 1.45541100 |

### 5.1.8 Nitrobenzene Cartesian Coordinates.

| | | | |
|---|---|---|---|
| H | -1.42095200 | 0.00008500 | -0.11281900 |
| C | -2.50487800 | 0.00006300 | -0.08004500 |
| C | -3.20258400 | -1.21551700 | -0.05730700 |
| C | -3.20274000 | 1.21560400 | -0.06058700 |
| C | -4.59868500 | -1.22493200 | -0.01507900 |
| H | -2.66191400 | -2.15489200 | -0.07238800 |
| C | -4.59884900 | 1.22494500 | -0.01838500 |
| H | -2.66220400 | 2.15501200 | -0.07820100 |
| C | -5.27123800 | -0.00001100 | 0.00360500 |
| H | -5.16386700 | -2.14713300 | 0.00325600 |
| H | -5.16414400 | 2.14711900 | -0.00253900 |
| N | -6.74989800 | -0.00004800 | 0.04831700 |
| O | -7.32670800 | -1.09098100 | 0.06710300 |
| O | -7.32686800 | 1.09085100 | 0.06411500 |

### 5.1.9 Nitromethane Cartesian Coordinates.

| | | | |
|---|---|---|---|
| H | 3.78292300 | -0.85466800 | -1.71906300 |
| C | 3.65024000 | 0.03334100 | -1.10312700 |
| H | 2.66570800 | 0.01428400 | -0.63898200 |
| H | 3.82087200 | 0.94679600 | -1.66398000 |
| N | 4.66441000 | -0.03697800 | 0.00169500 |
| O | 5.49087000 | 0.87126200 | 0.08138200 |
| O | 4.59746300 | -1.00790200 | 0.75522800 |

### 5.1.10 Ethane Cartesian Coordinates.

| | | | |
|---|---|---|---|
| H | -4.59331400 | 0.85346400 | 1.34706600 |
| C | -4.88752900 | -0.01288600 | 0.74698200 |
| H | -4.59797000 | -0.91188700 | 1.29941200 |
| H | -5.97909400 | -0.00797100 | 0.67156800 |
| C | -4.23378000 | 0.02282300 | -0.63971800 |
| H | -4.52799500 | -0.84352600 | -1.23980200 |
| H | -4.52333900 | 0.92182500 | -1.19214800 |
| H | -3.14221500 | 0.01790900 | -0.56430400 |

## 5.2 Additional Computational Coupling Constant Data

### 5.2.1 Acetonitrile/TEMPO.

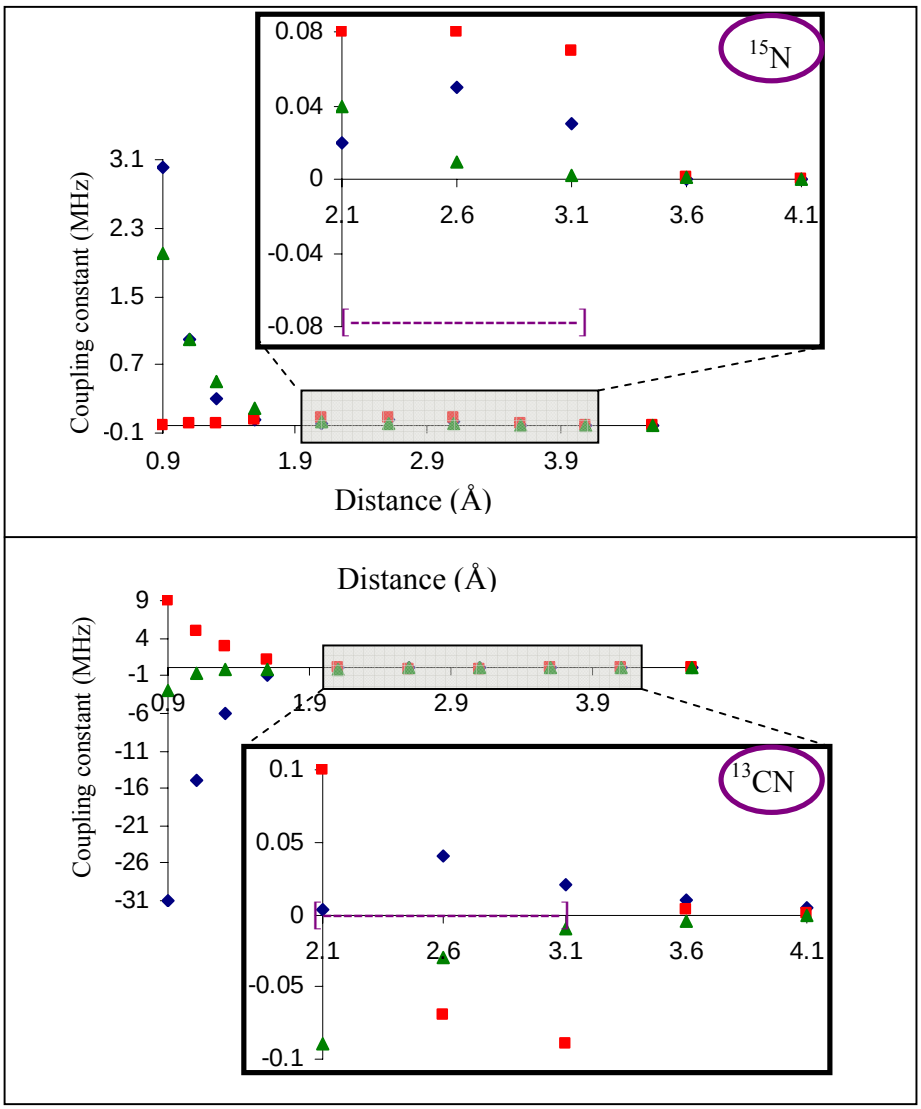


**Figure 64.** Acetonitrile/TEMPO ($^{15}$N and $^{13}$CN) coupling constant data for interactions (a), (b), and (c).

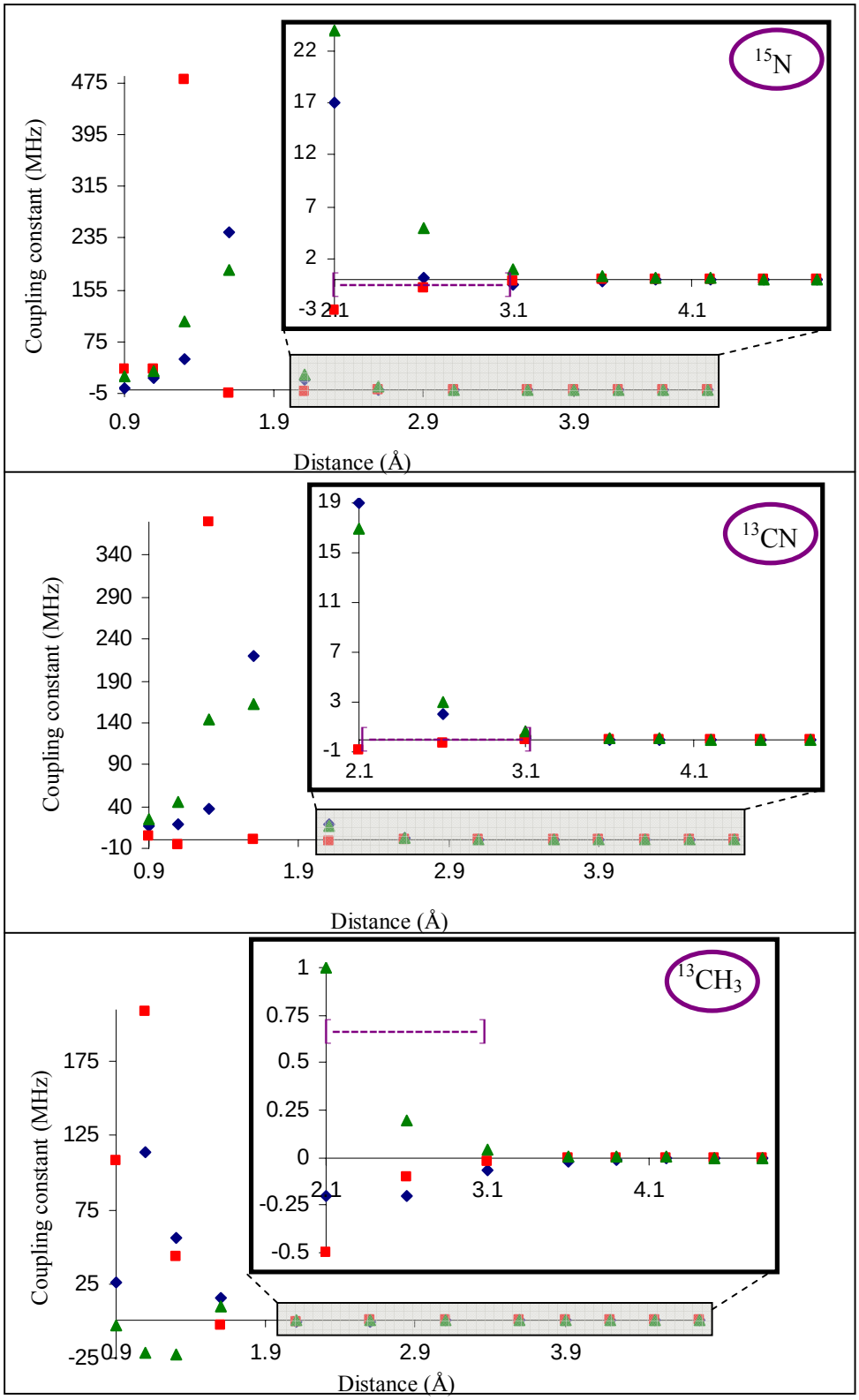


**Figure 65.** Acetonitrile/TEMPO coupling constant data for interactions (e), (f), and (g).

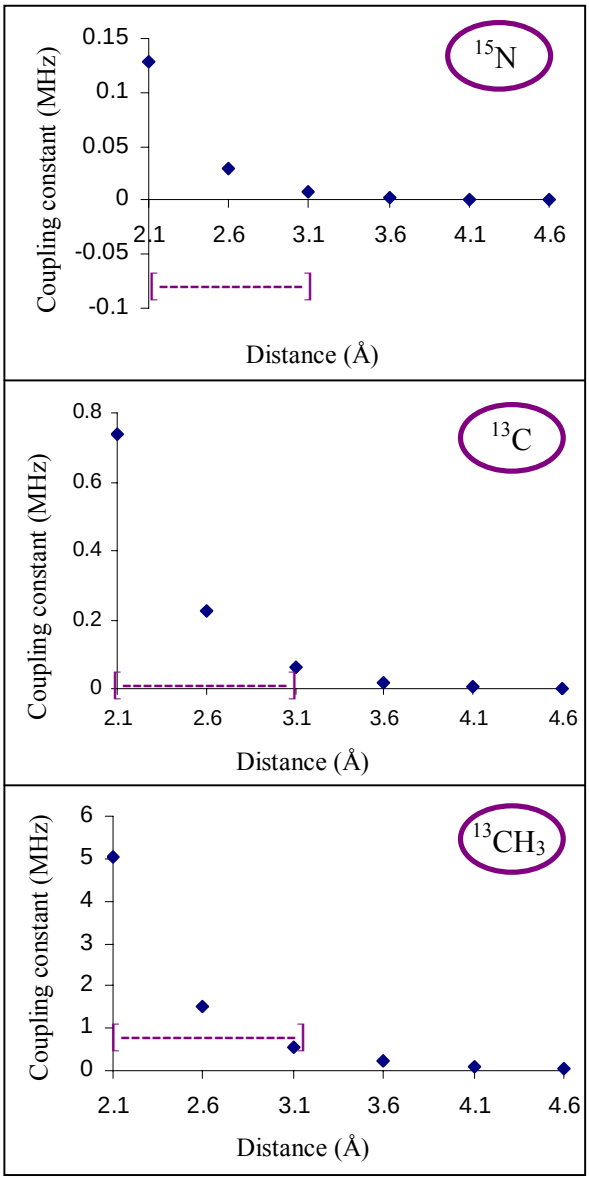


**Figure 66.** Acetonitrile/TEMPO coupling constant data for interaction (d).

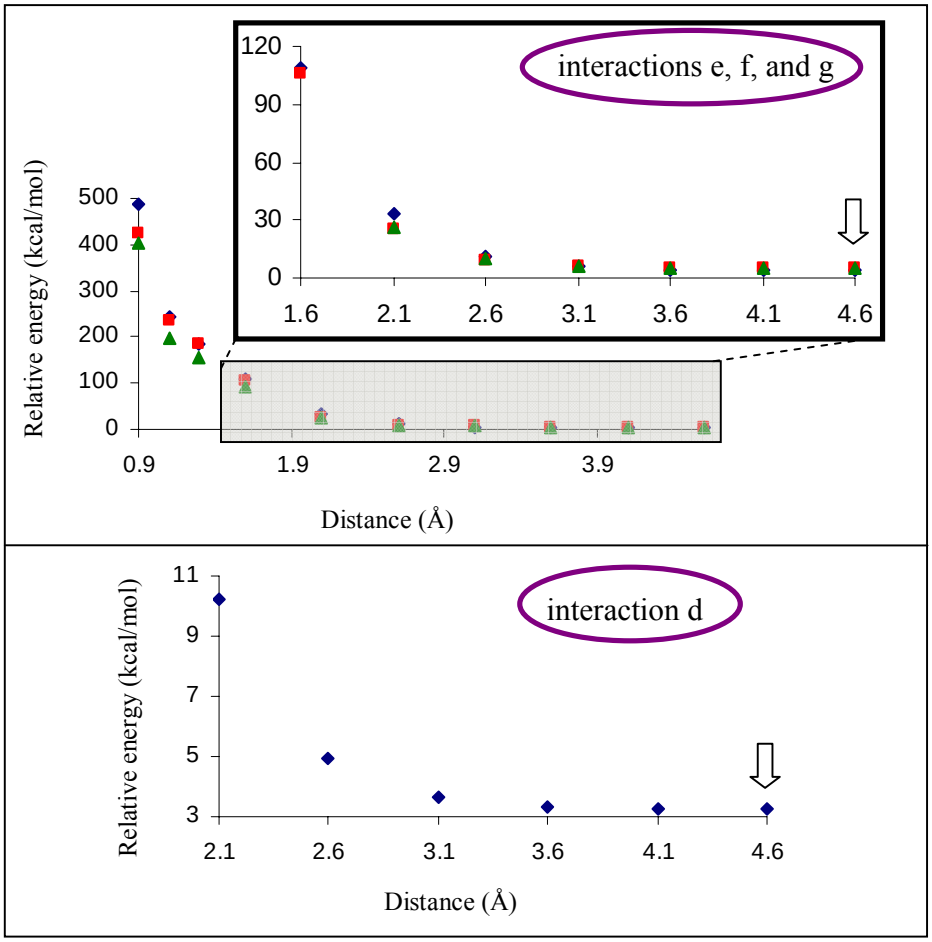


**Figure 67.** Acetonitrile/TEMPO relative energy curves for interactions (d)-(g).

### 5.2.2 Acetamide/TEMPO.

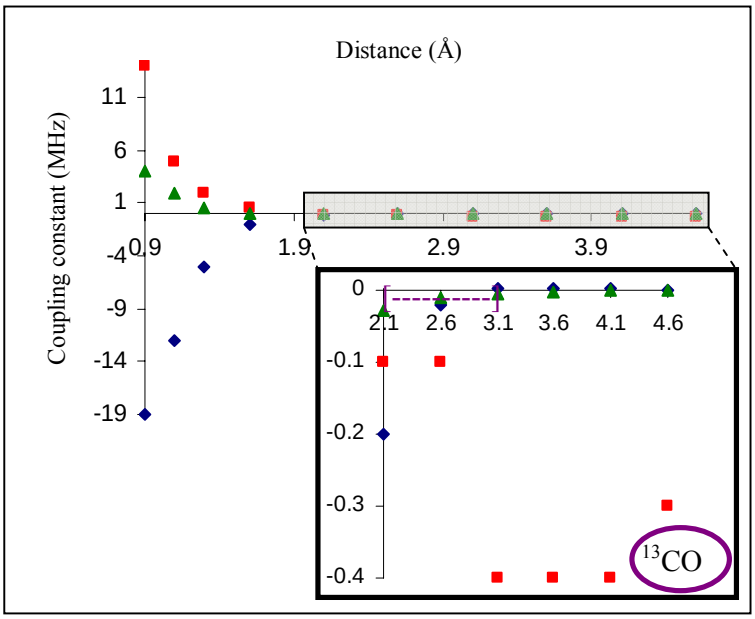


**Figure 68.** Acetamide/TEMPO $^{13}CO$ coupling constant data for interactions (a), (b), and (c) (to $^{1}H_3C$).

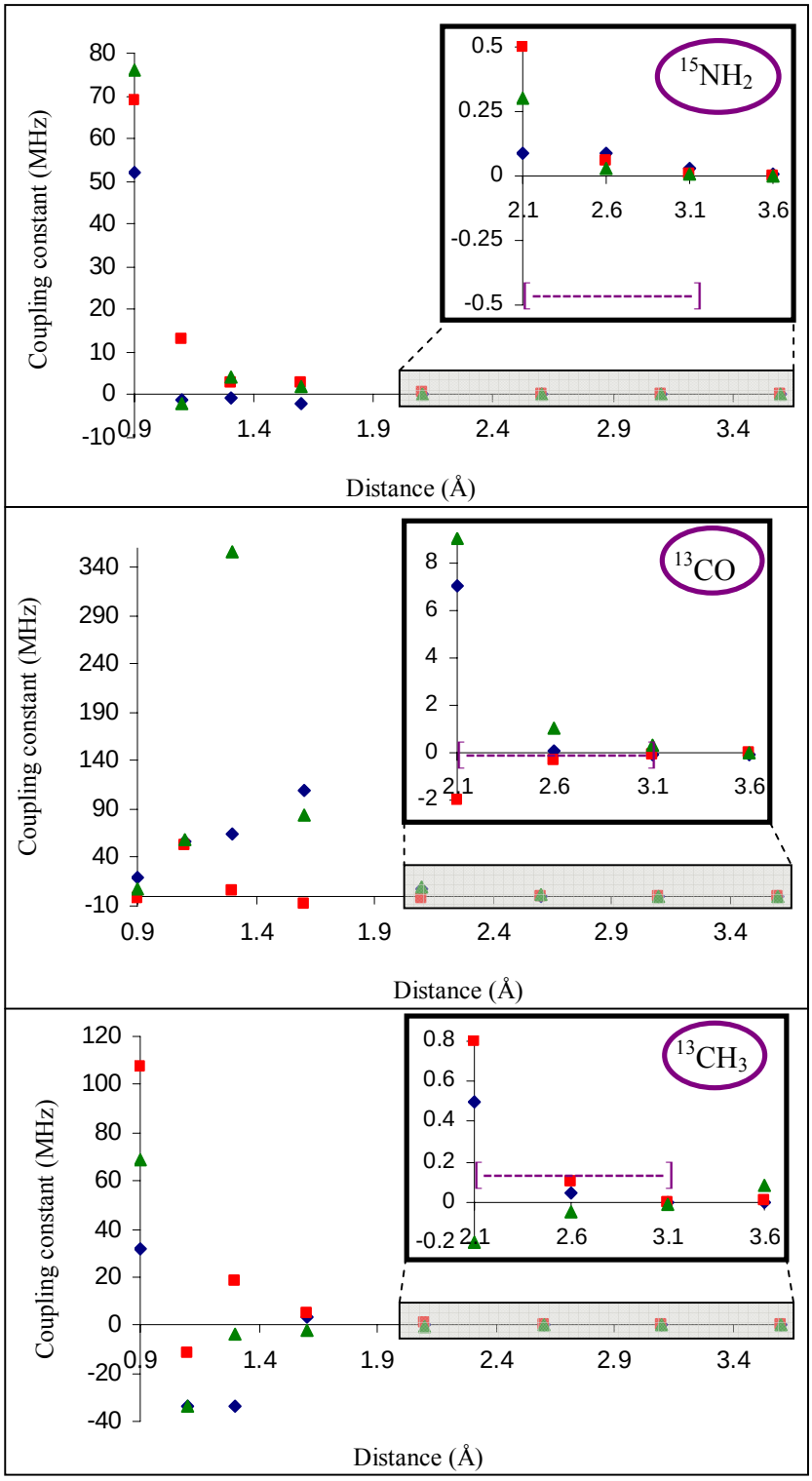


**Figure 69.** Acetamide/TEMPO coupling constant data for interactions (d), (e), and (f) (to $^{16}O$).

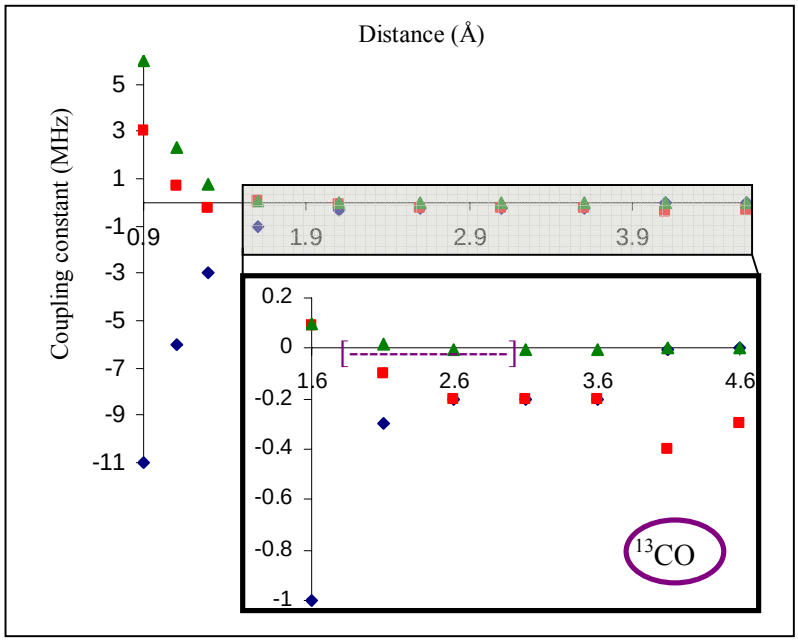


**Figure 70.** Acetamide/TEMPO ($^{13}CO$) coupling constant data for interactions (g), (h), and (i) (to $^{1}H_2N$).

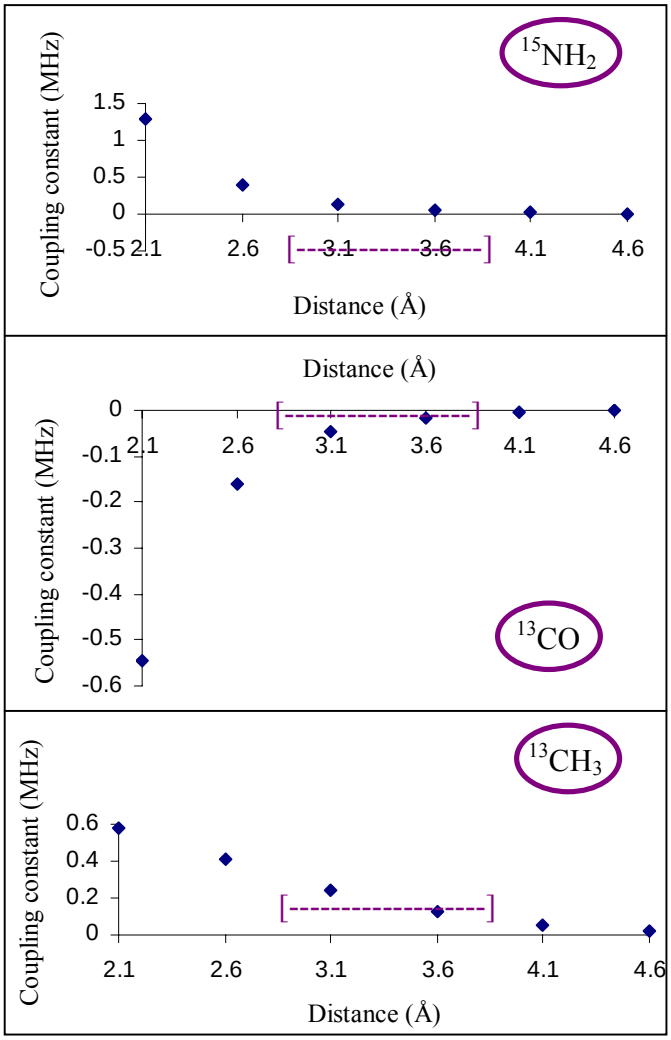


**Figure 71.** Acetamide/TEMPO coupling constant data for interaction (j) (to N on TEMPO).

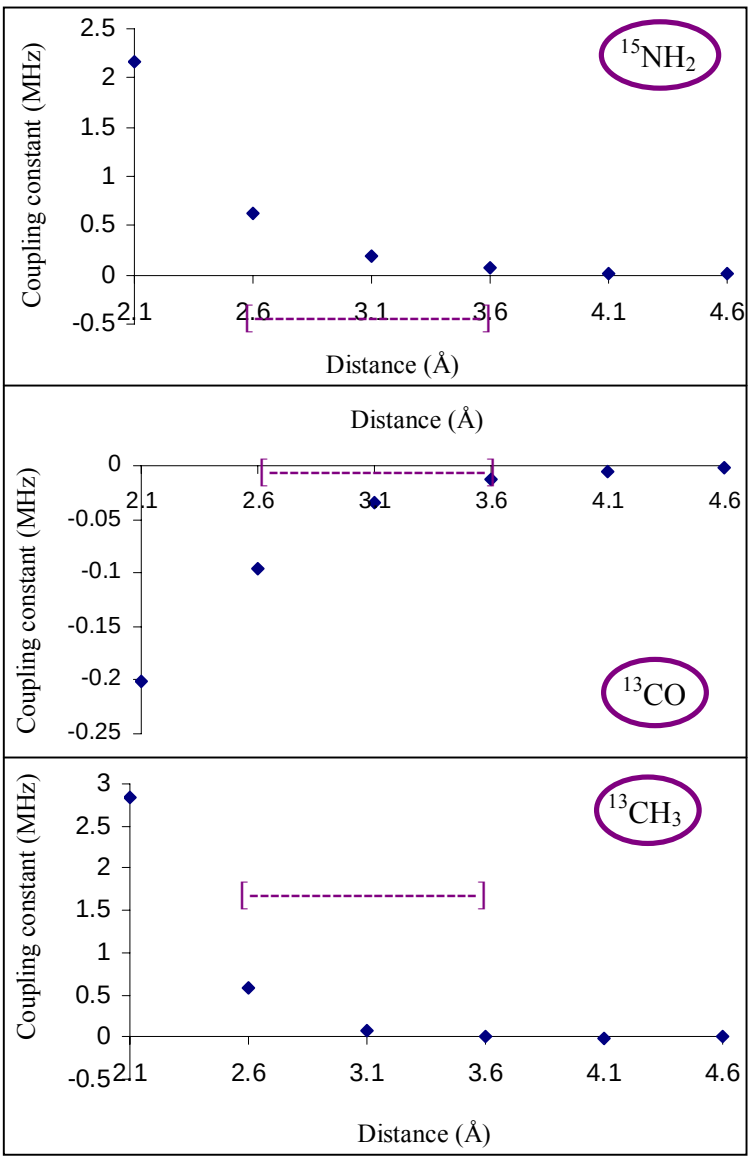


**Figure 72.** Acetamide/TEMPO coupling constant data for interaction (k) (to N on TEMPO).

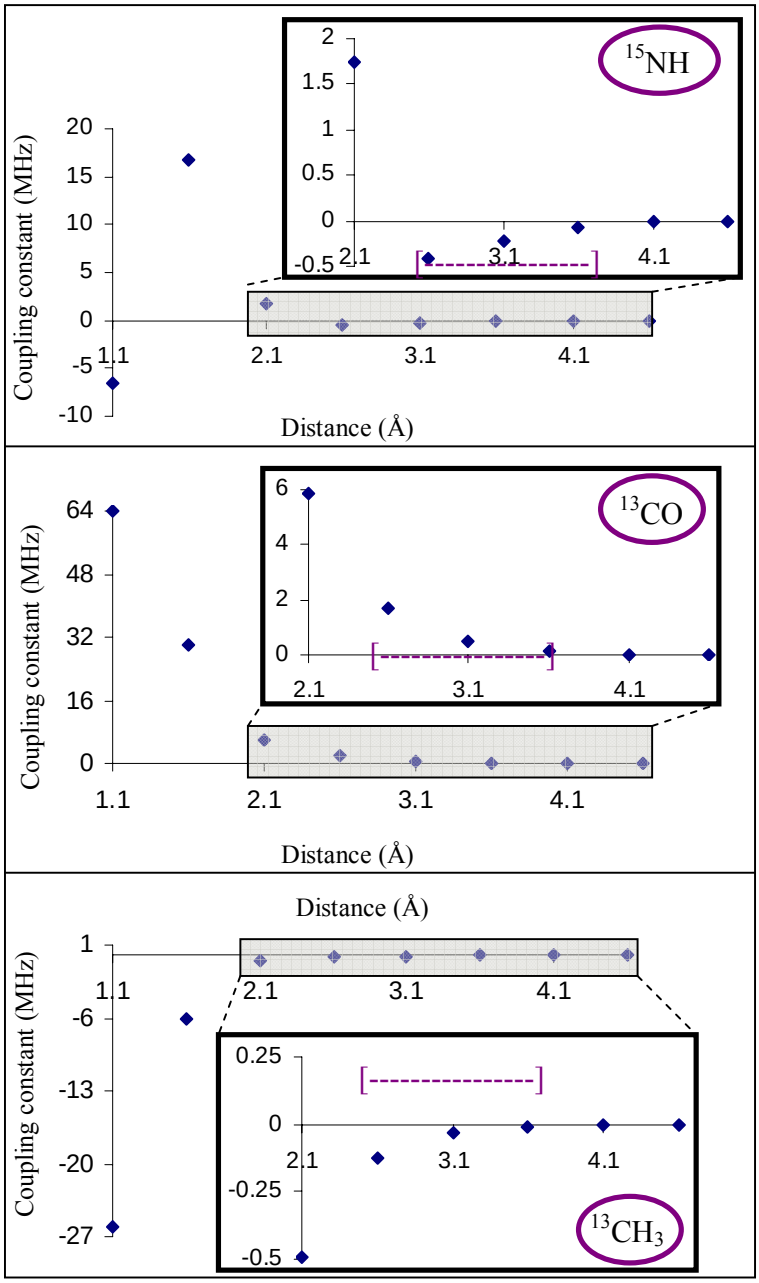


**Figure 73.** Acetamide/TEMPO coupling constant data for interaction (l) (to N on acetamide).

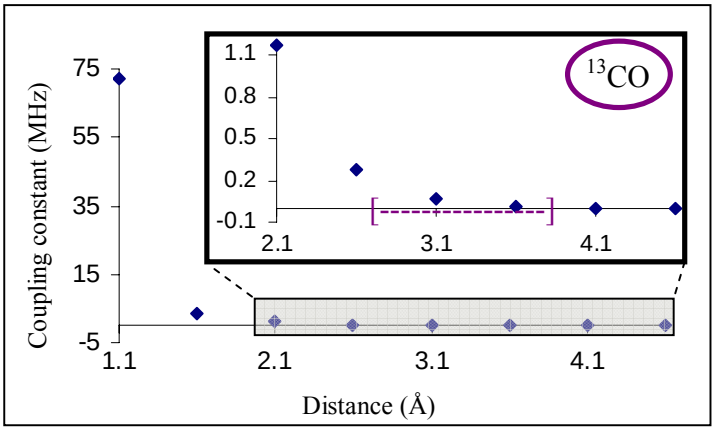


**Figure 74.** Acetamide/TEMPO ($^{13}$CO) coupling constant data for interaction (m) (to N on acetamide).

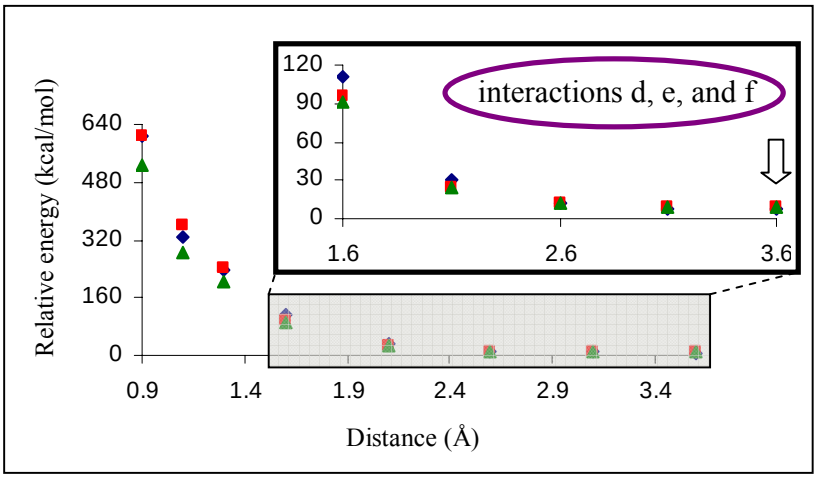


**Figure 75.** Acetamide/TEMPO relative energy curves for interactions (d)-(f).

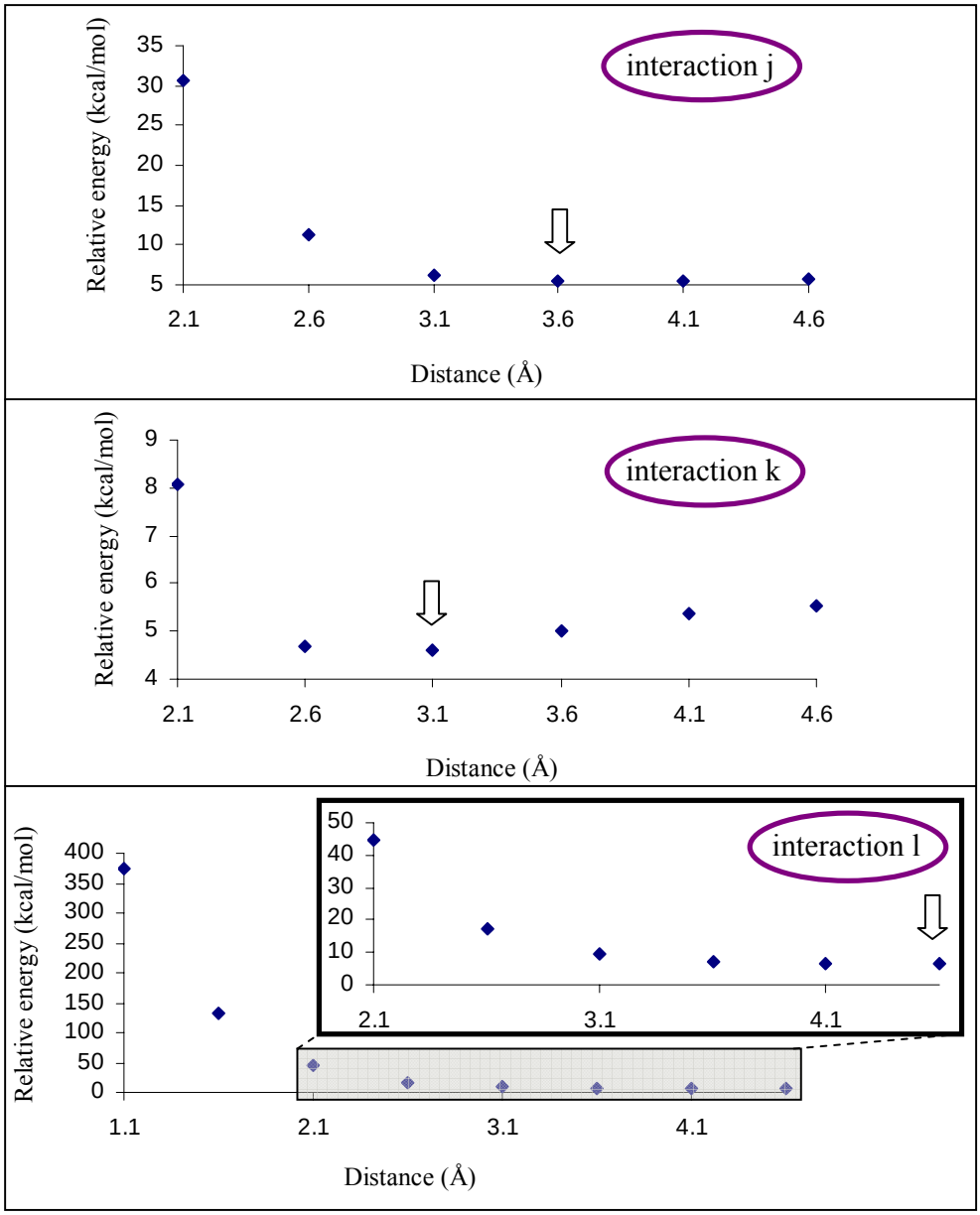


**Figure 76.** Acetamide/TEMPO relative energy curves for interactions (j)-(l).

### 5.2.3 Benzene/TEMPO.

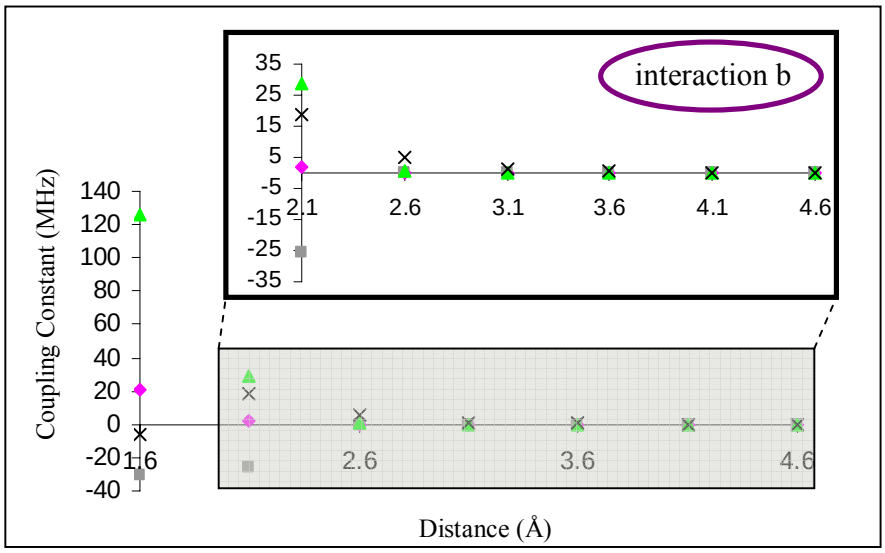


**Figure 77.** Benzene/TEMPO coupling constant data for interaction (b).

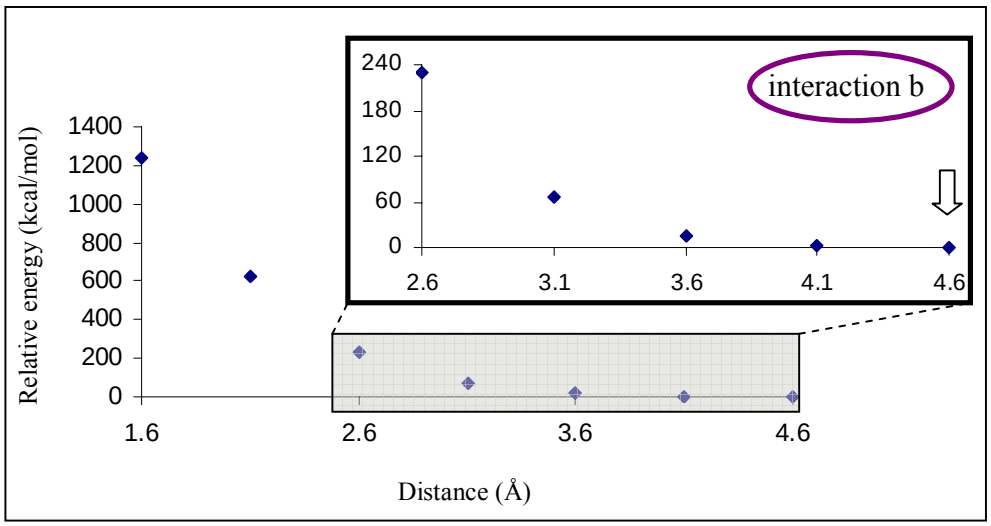


**Figure 78.** Benzene/TEMPO relative energy curve for interaction (b).

### 5.2.4 Toluene/TEMPO.

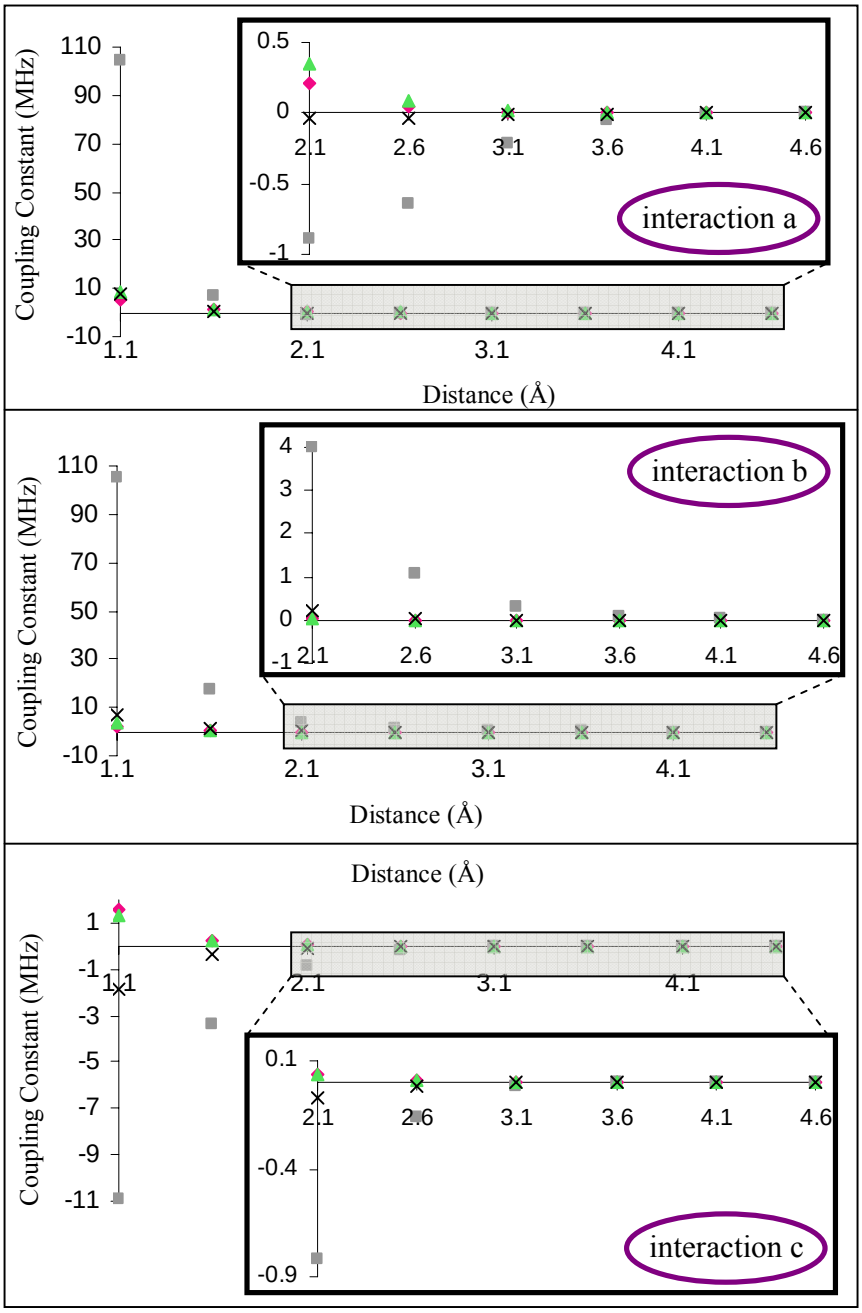


**Figure 79.** Toluene/TEMPO coupling constant data for interactions (a)-(c).

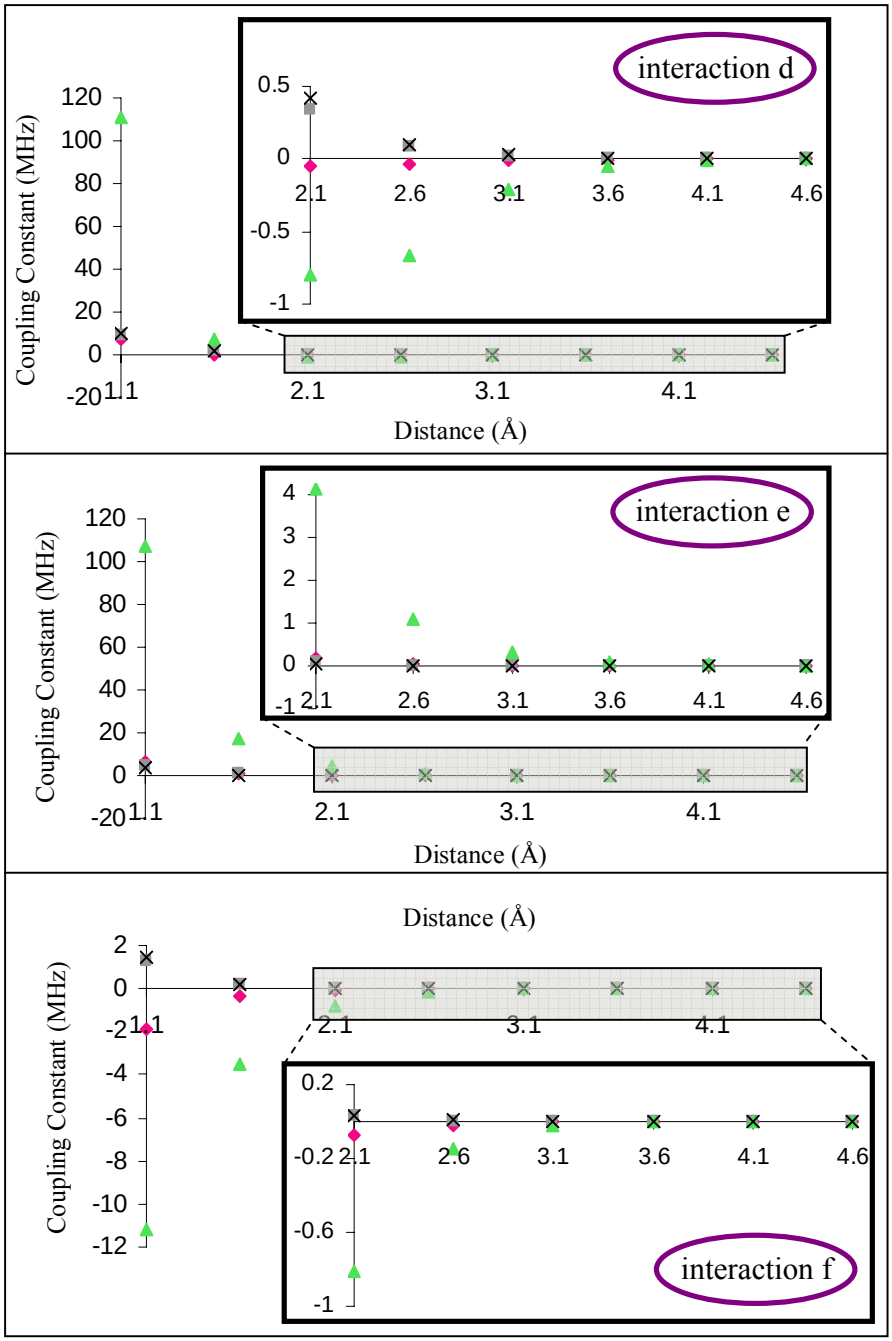


**Figure 80.** Toluene/TEMPO coupling constant data for interactions (d)-(f).

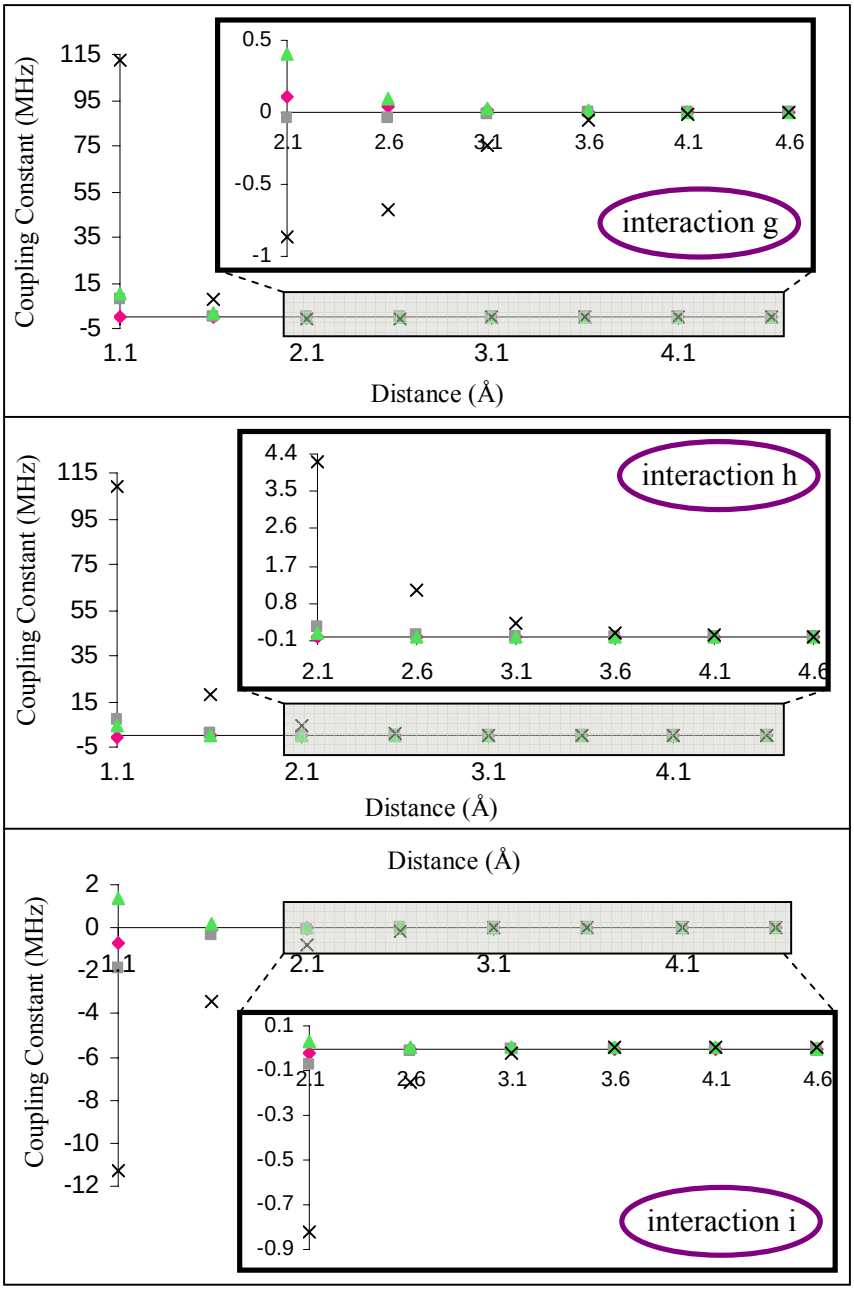


**Figure 81.** Toluene/TEMPO coupling constant data for interactions (g)-(i).

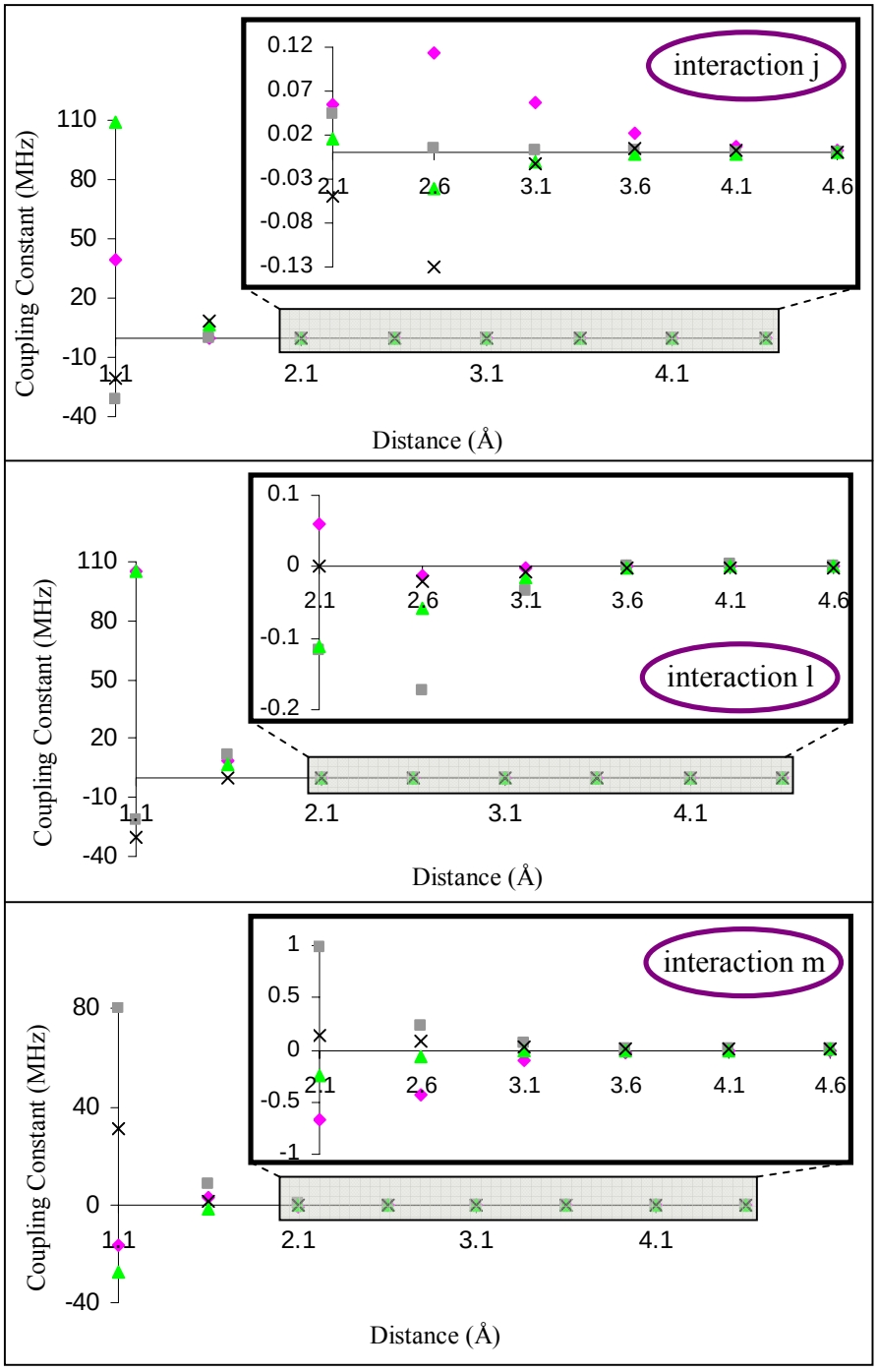


**Figure 82.** Toluene/TEMPO coupling constant data for interactions (j), (l), and (m).

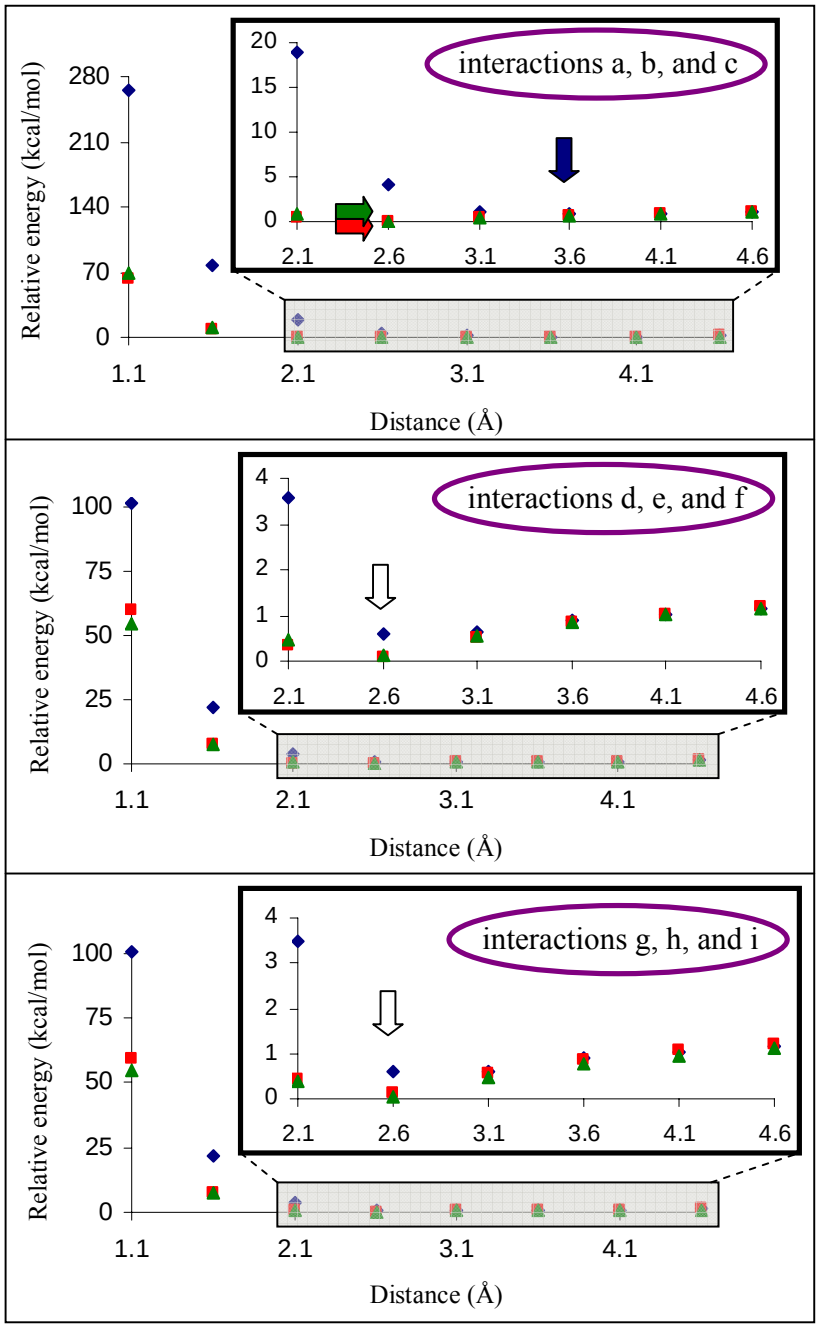


**Figure 83.** Toluene/TEMPO relative energy curves for interactions (a)-(i).

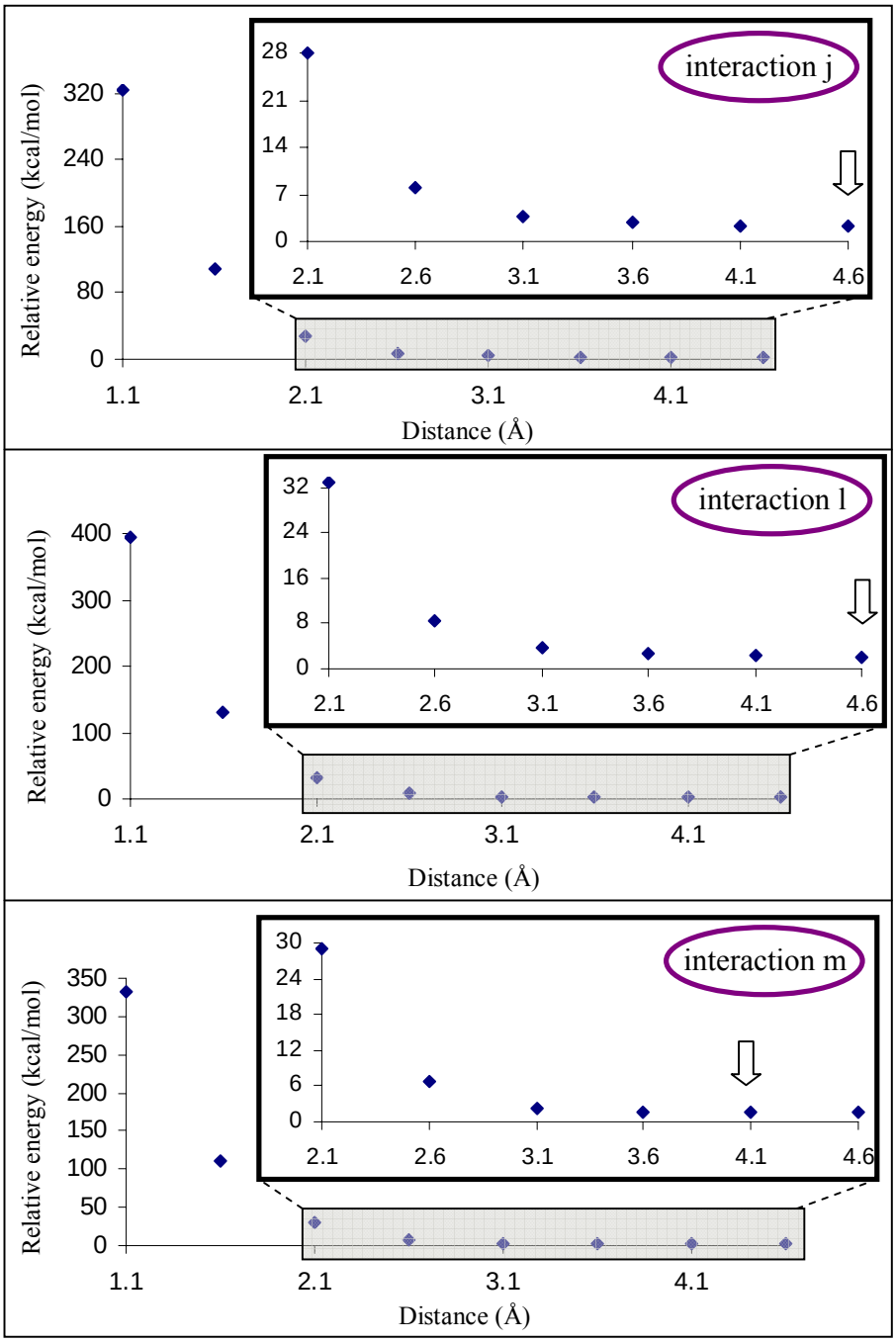


**Figure 84.** Toluene/TEMPO relative energy curves for interactions (j), (l), and (m).

### 5.2.5 Phenylacetylene/TEMPO.

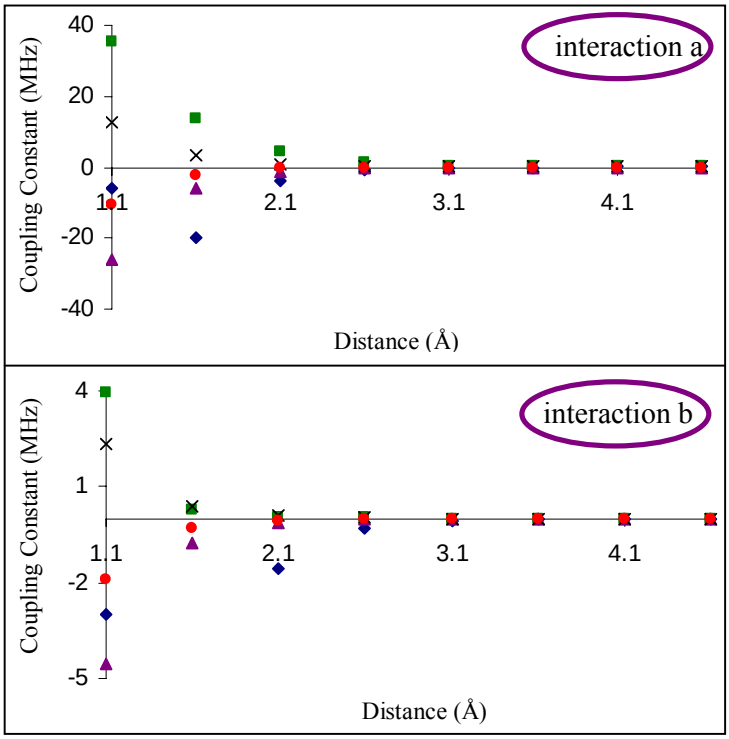


**Figure 85.** Phenylacetylene/TEMPO coupling constant data for interactions (a) and (b).

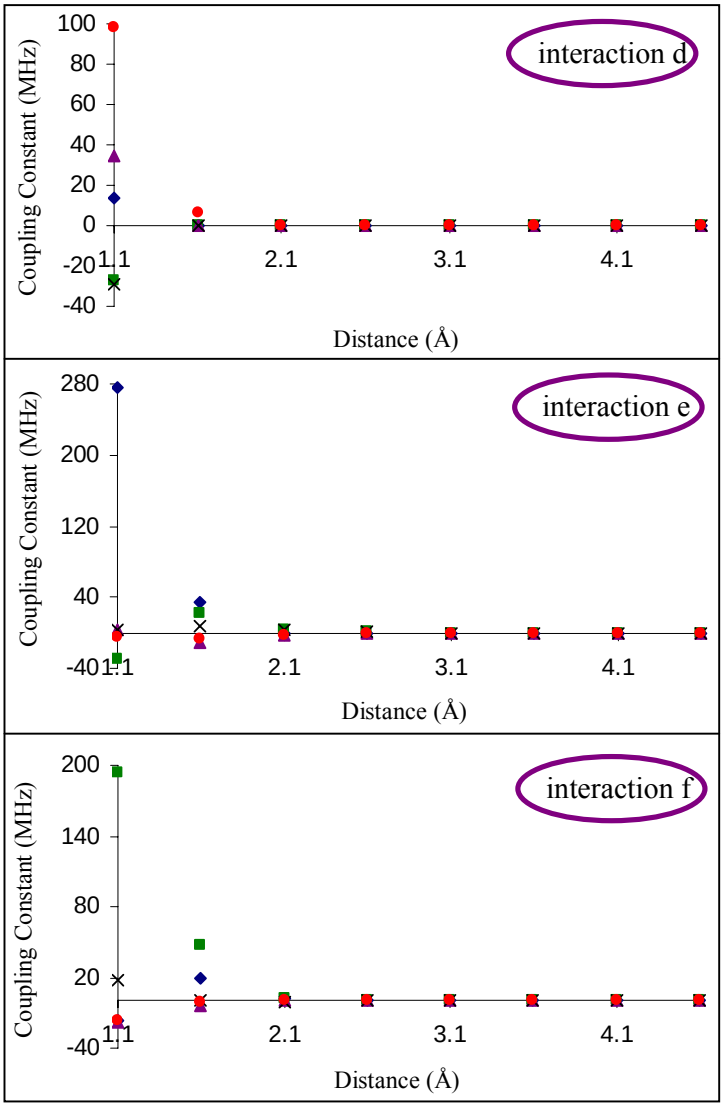


**Figure 86.** Phenylacetylene/TEMPO coupling constant data for interactions (d)-(f).

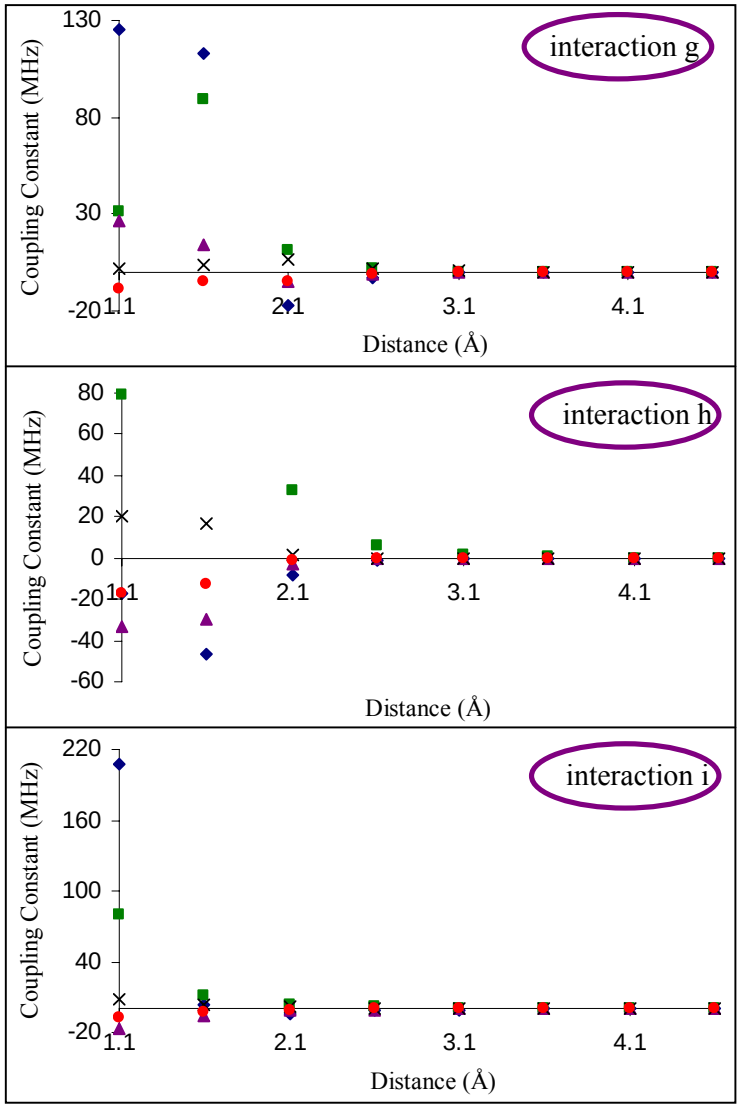


**Figure 87.** Phenylacetylene/TEMPO coupling constant data for interactions (g)-(i).

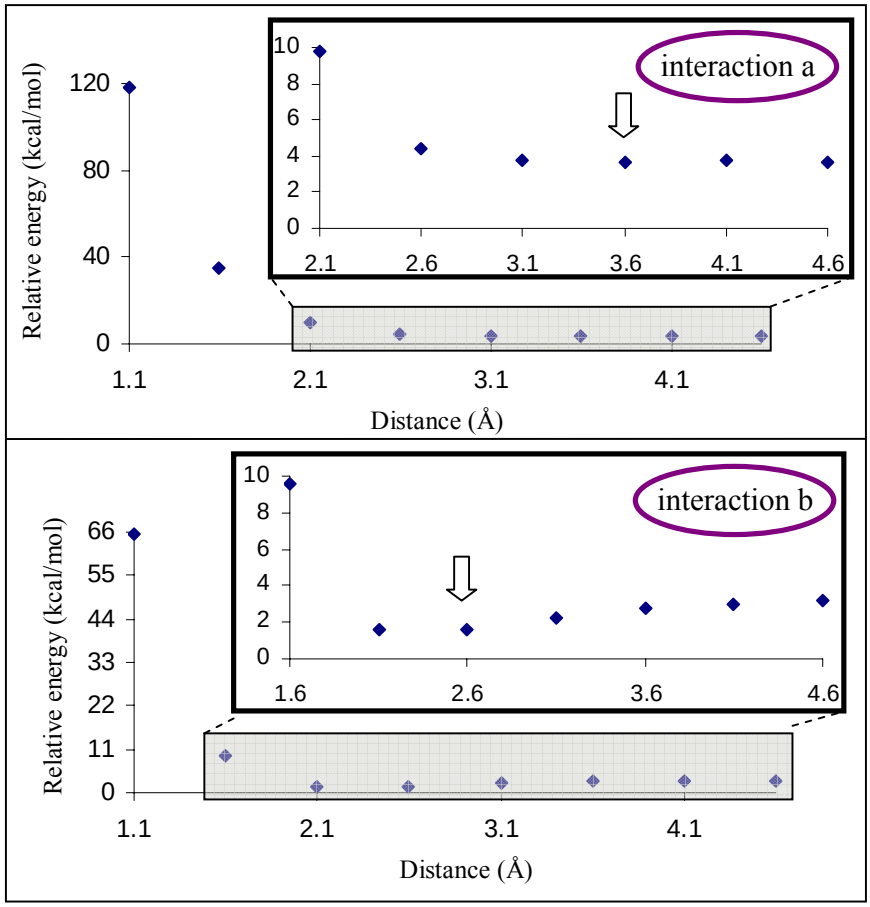


**Figure 88.** Phenylacetylene/TEMPO relative energy curves for interactions (a) and (b).

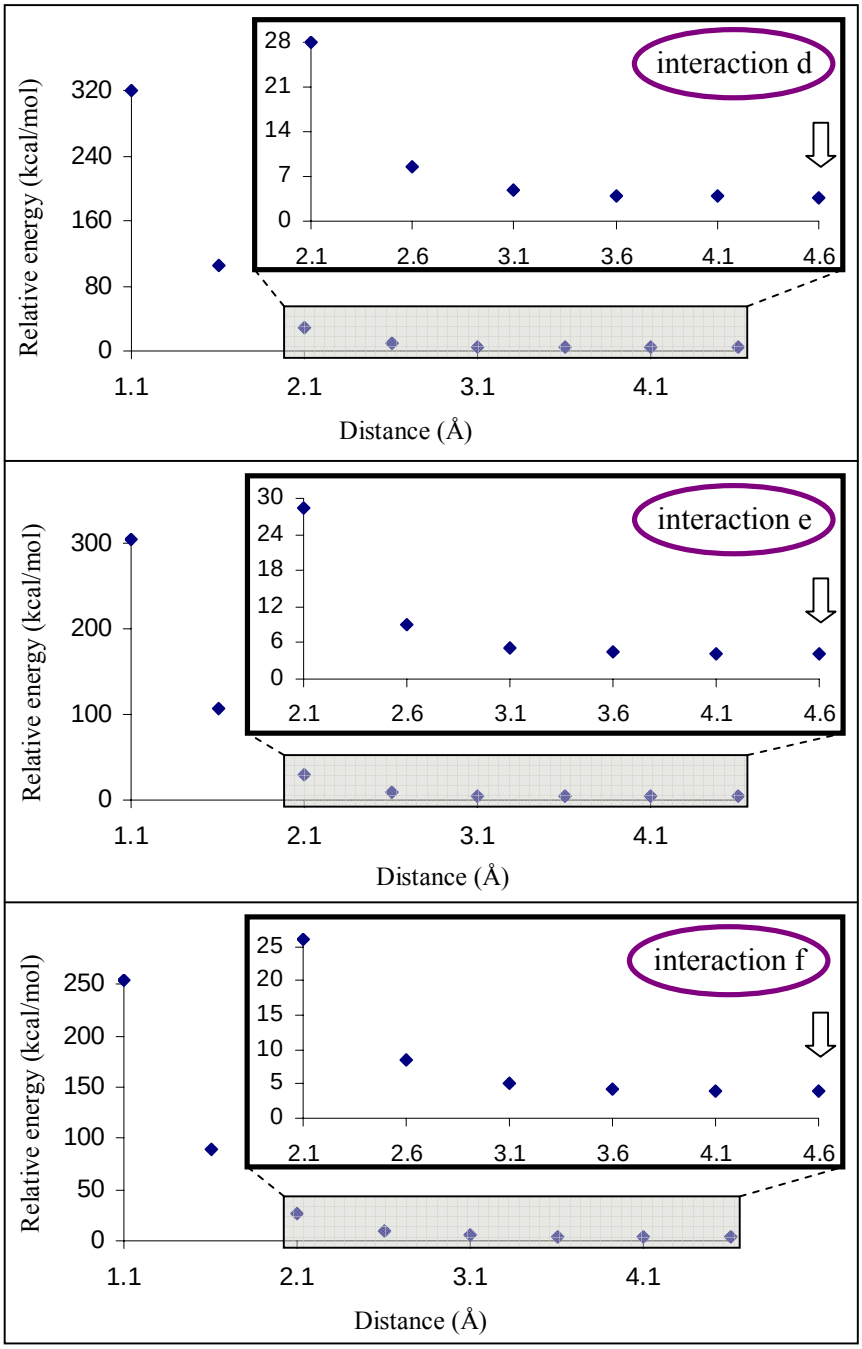


**Figure 89.** Phenylacetylene/TEMPO relative energy curves for interactions (d)-(f).

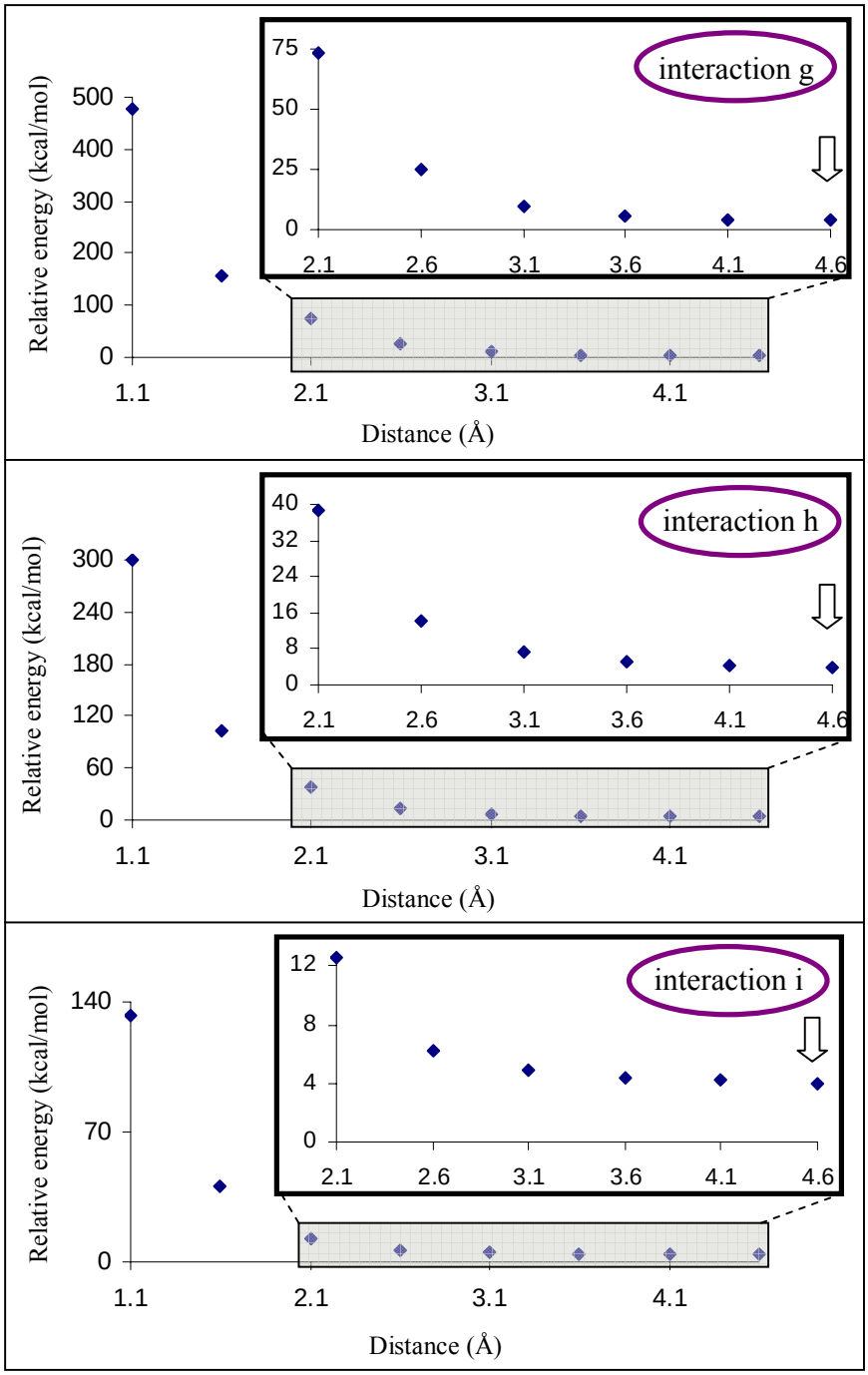


**Figure 90.** Phenylacetylene/TEMPO relative energy curves for interactions (g)-(i).

### 5.2.6 Fluorobenzene/TEMPO.

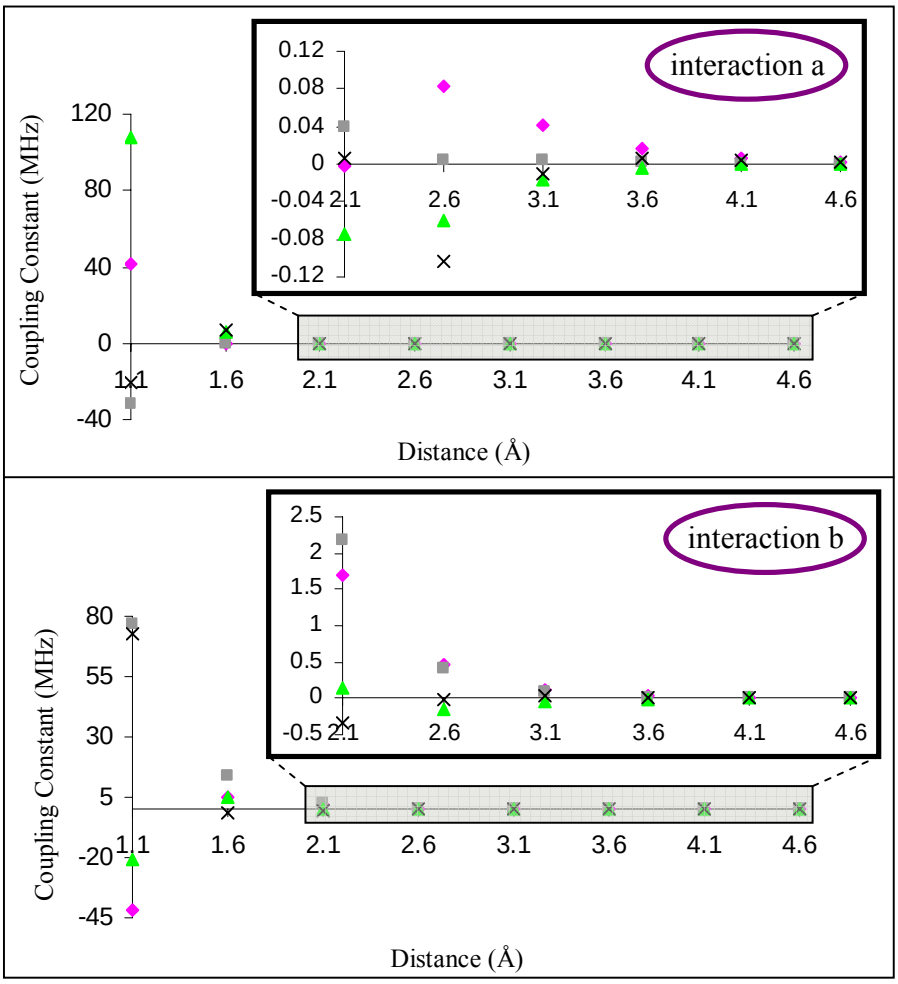


**Figure 91.** Fluorobenzene/TEMPO coupling constant data for interactions (a) and (b).

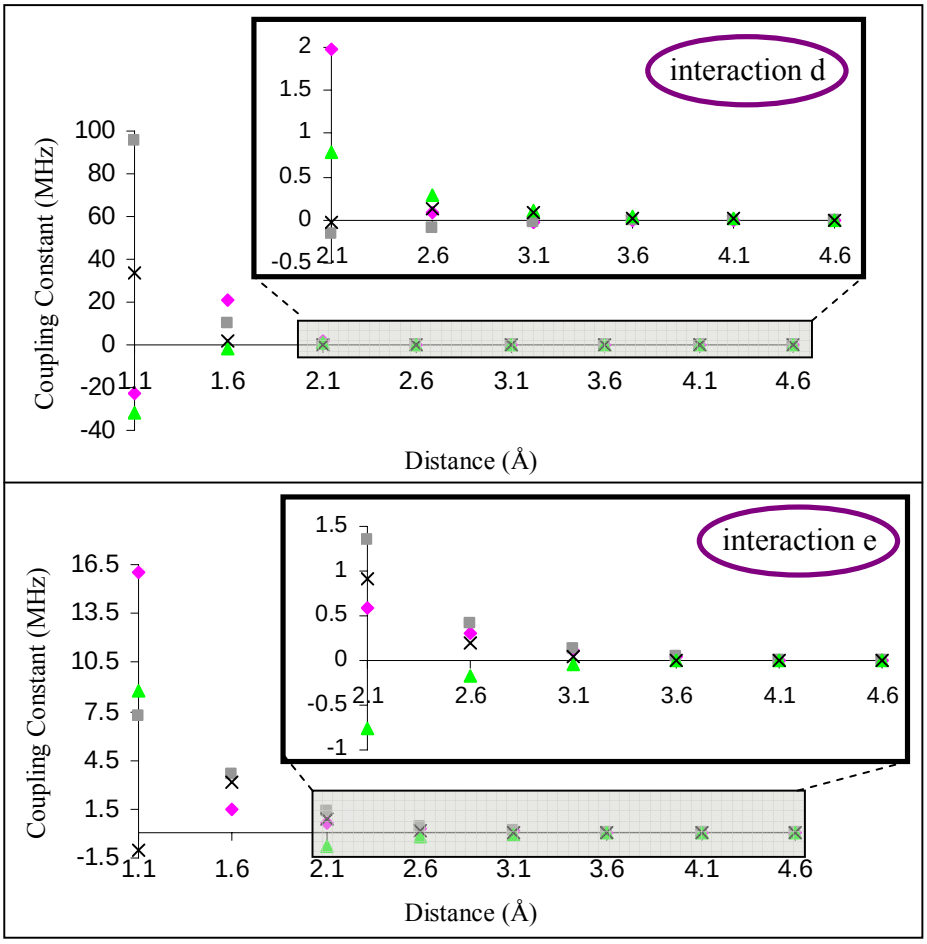


**Figure 92.** Fluorobenzene/TEMPO coupling constant data for interactions (d) and (e).

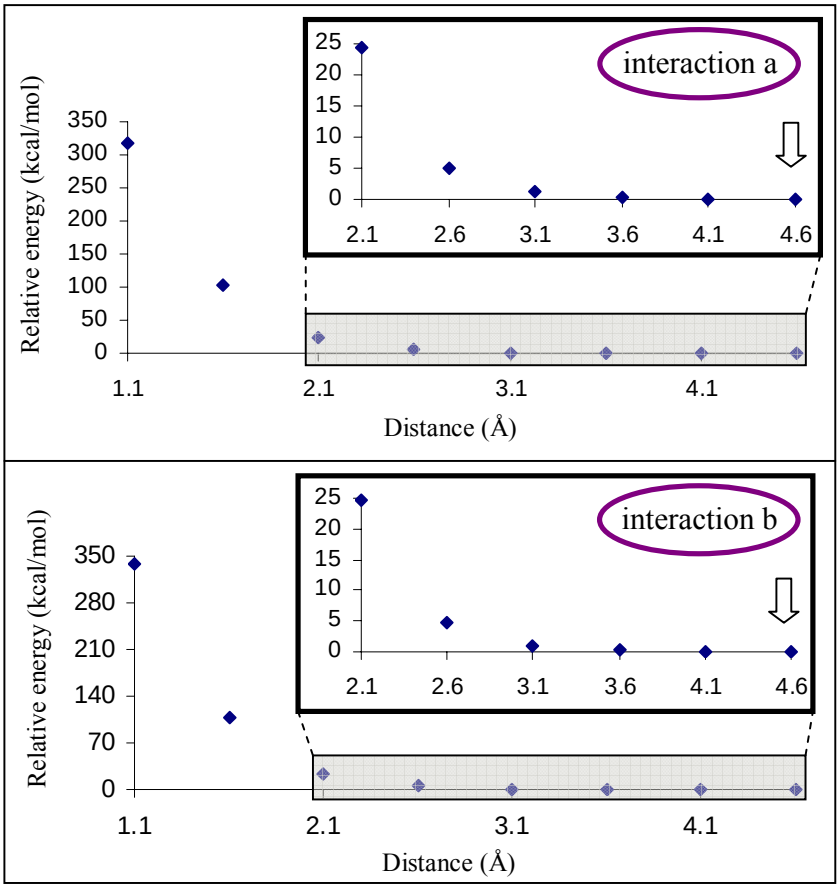


**Figure 93.** Fluorobenzene/TEMPO energy curves for interactions (a) and (b).

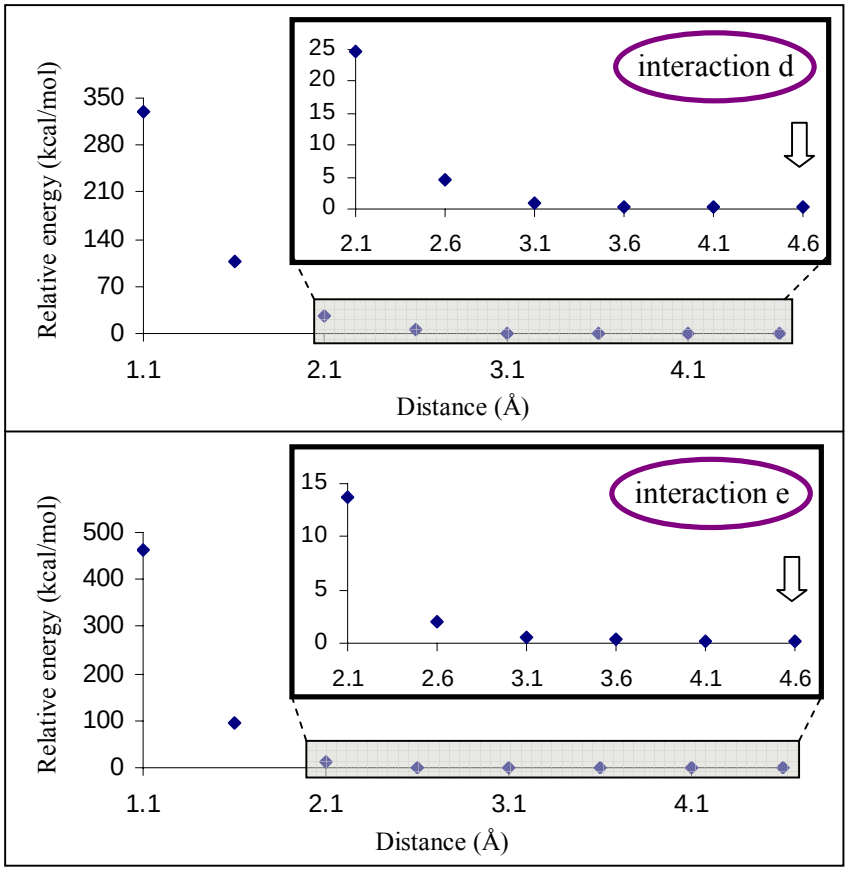


**Figure 94.** Fluorobenzene/TEMPO energy curves for interactions (d) and (e).

### 5.2.7 Nitrobenzene/TEMPO.

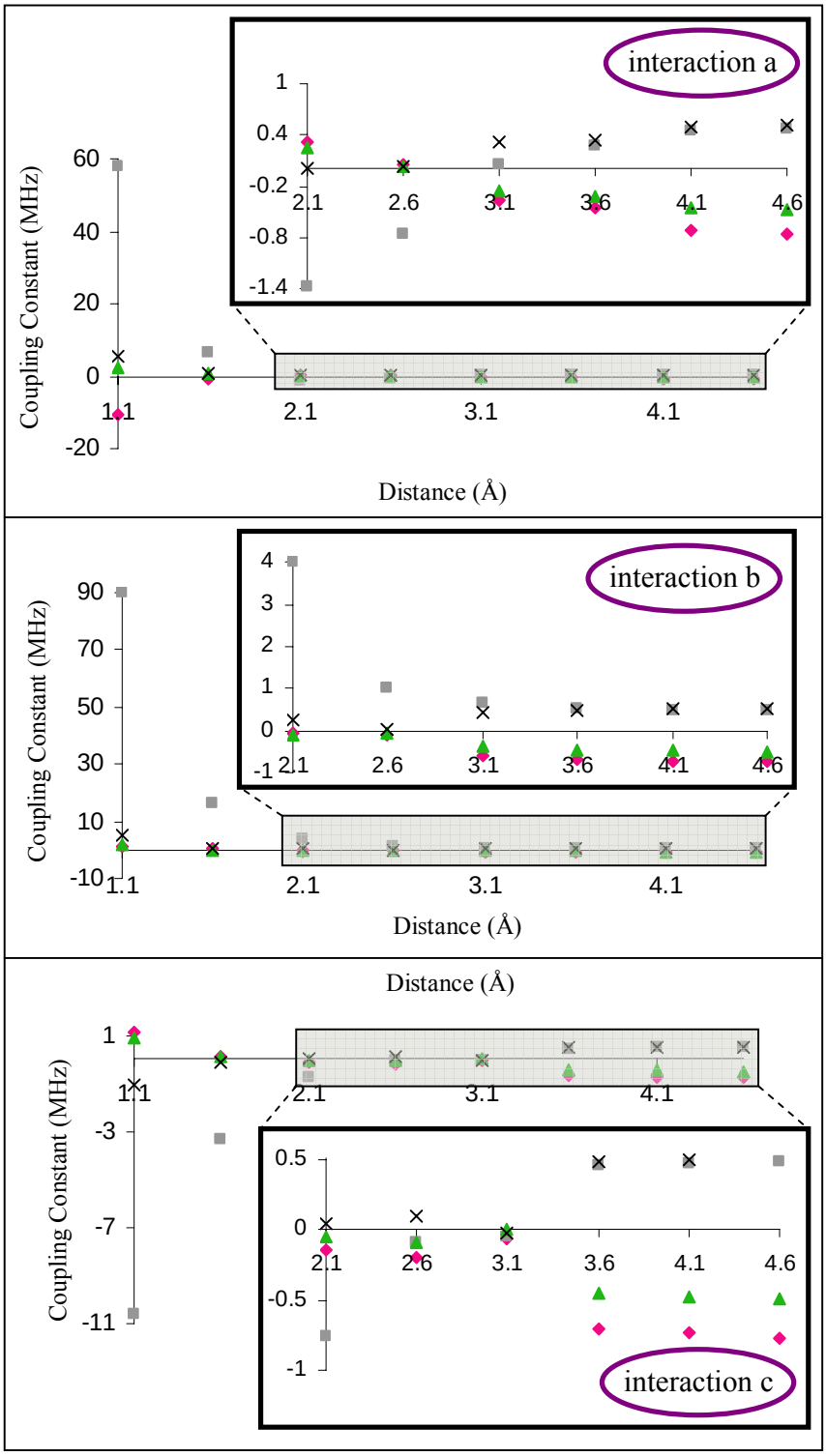


**Figure 95.** Nitrobenzene/TEMPO coupling constant data for interactions (a)-(c).

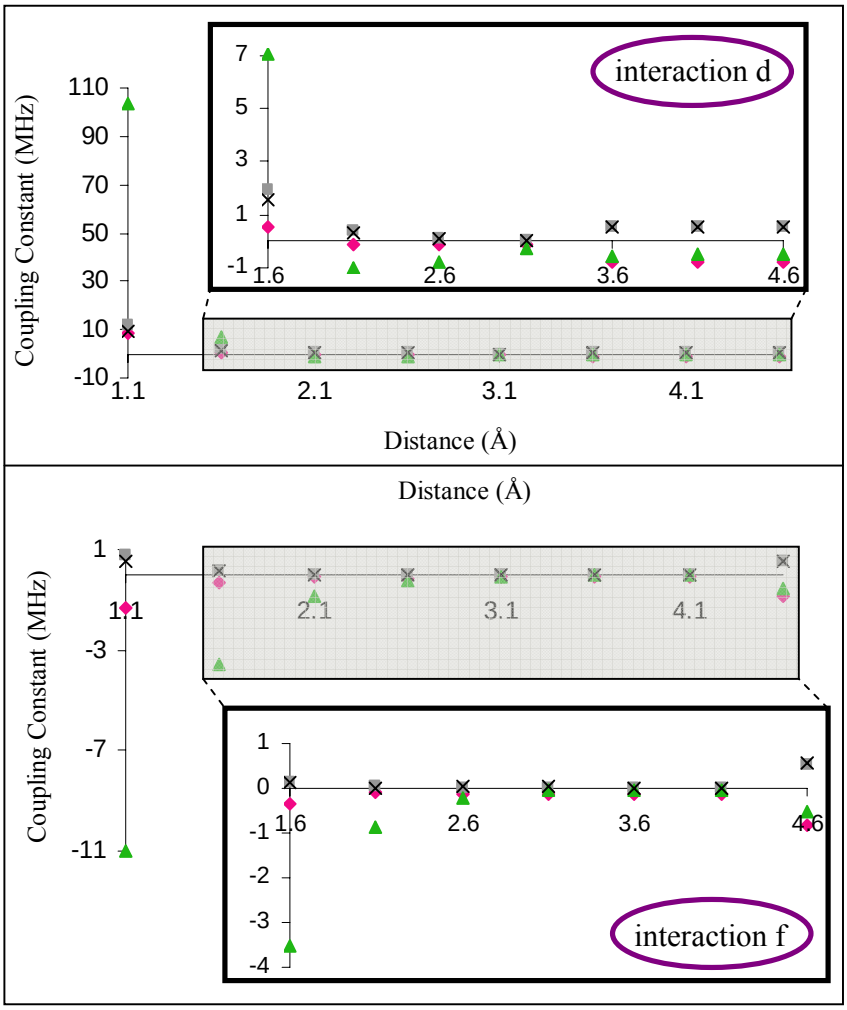


**Figure 96.** Nitrobenzene/TEMPO coupling constant data for interactions (d) and (f).

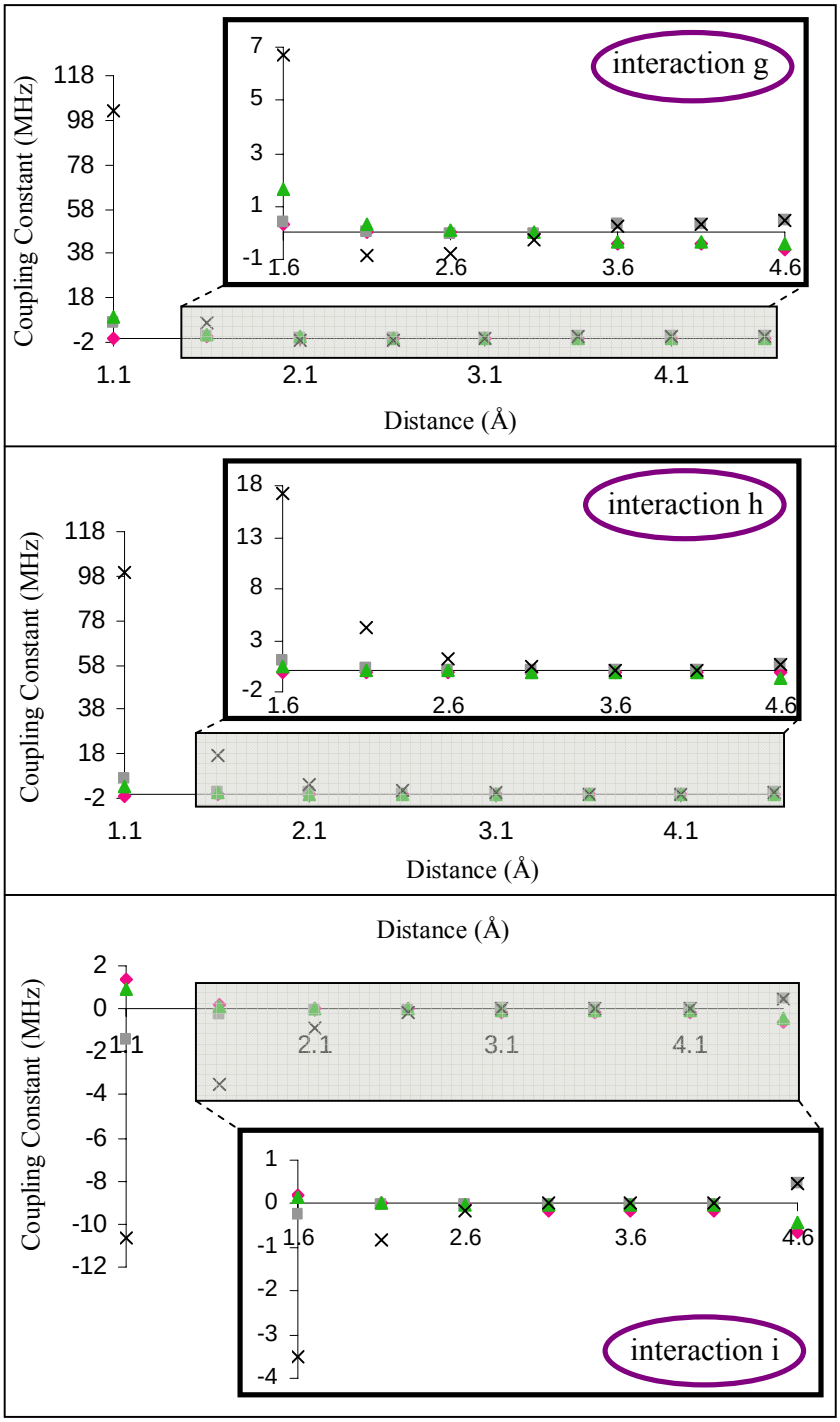


**Figure 97.** Nitrobenzene/TEMPO coupling constant data for interactions (g)-(i).

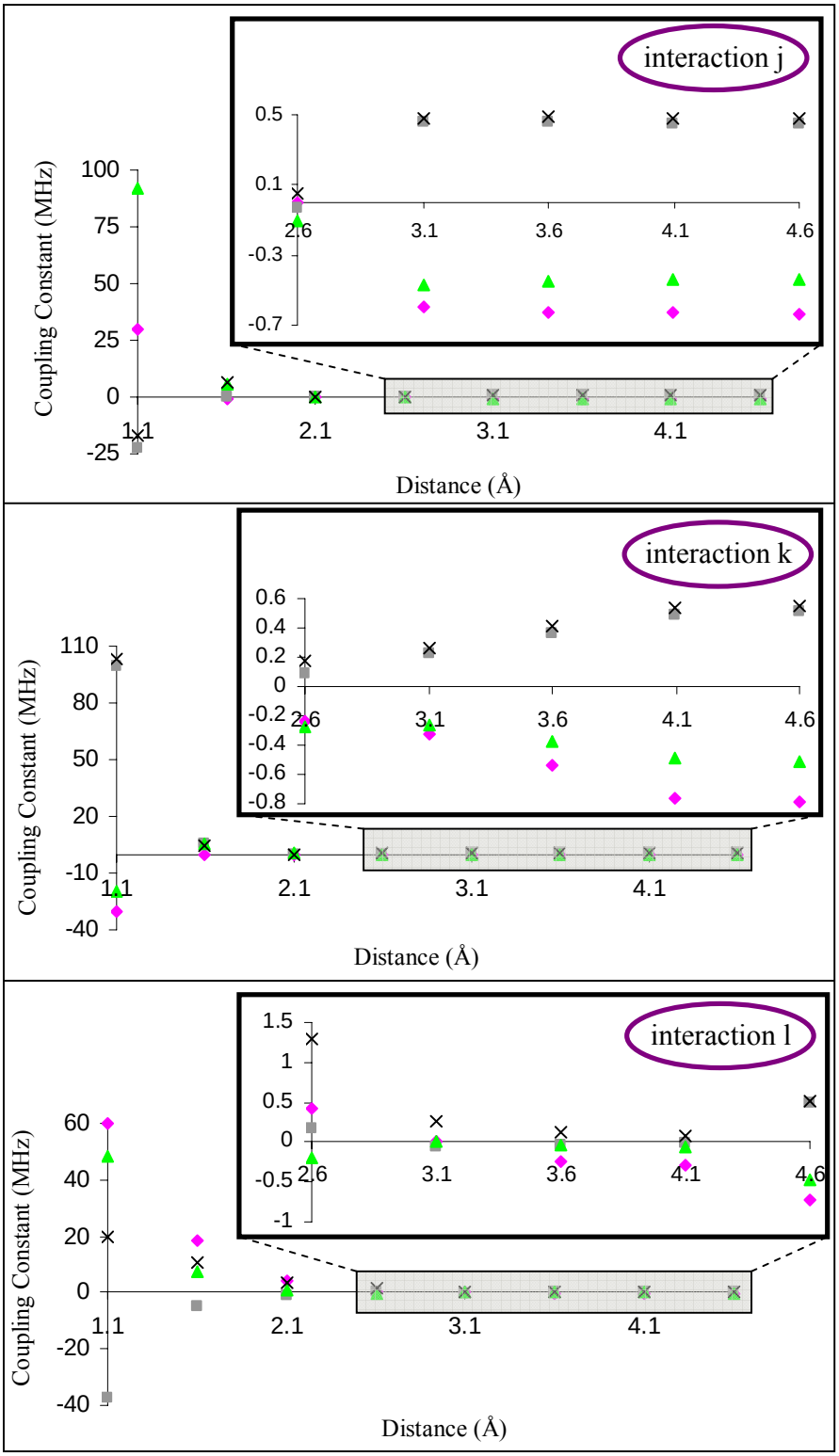


**Figure 98.** Nitrobenzene/TEMPO coupling constant data for interactions (j)-(l).

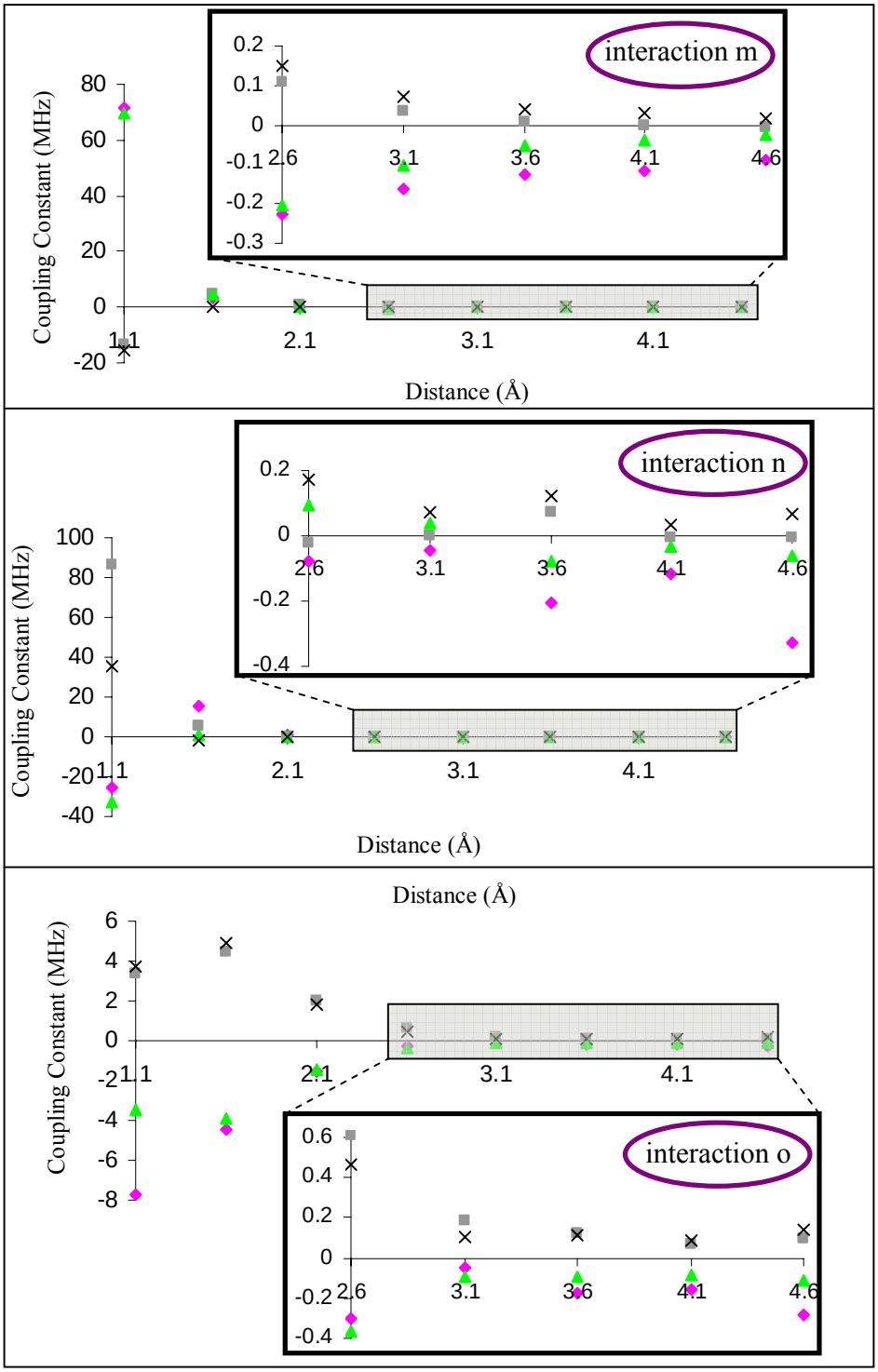


**Figure 99.** Nitrobenzene/TEMPO coupling constant data for interactions (m)-(o).

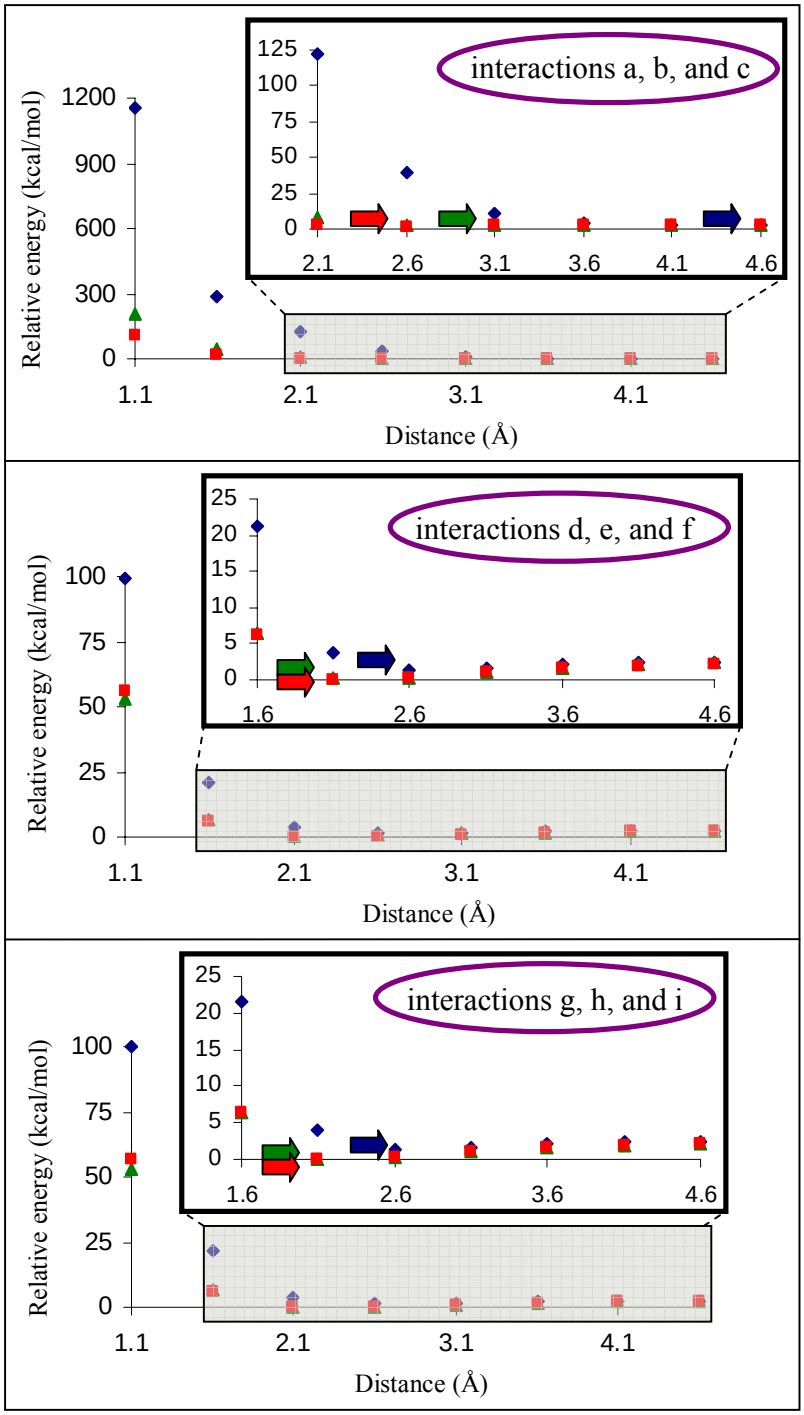


**Figure 100.** Nitrobenzene/TEMPO energy curves for interactions (a)-(i).

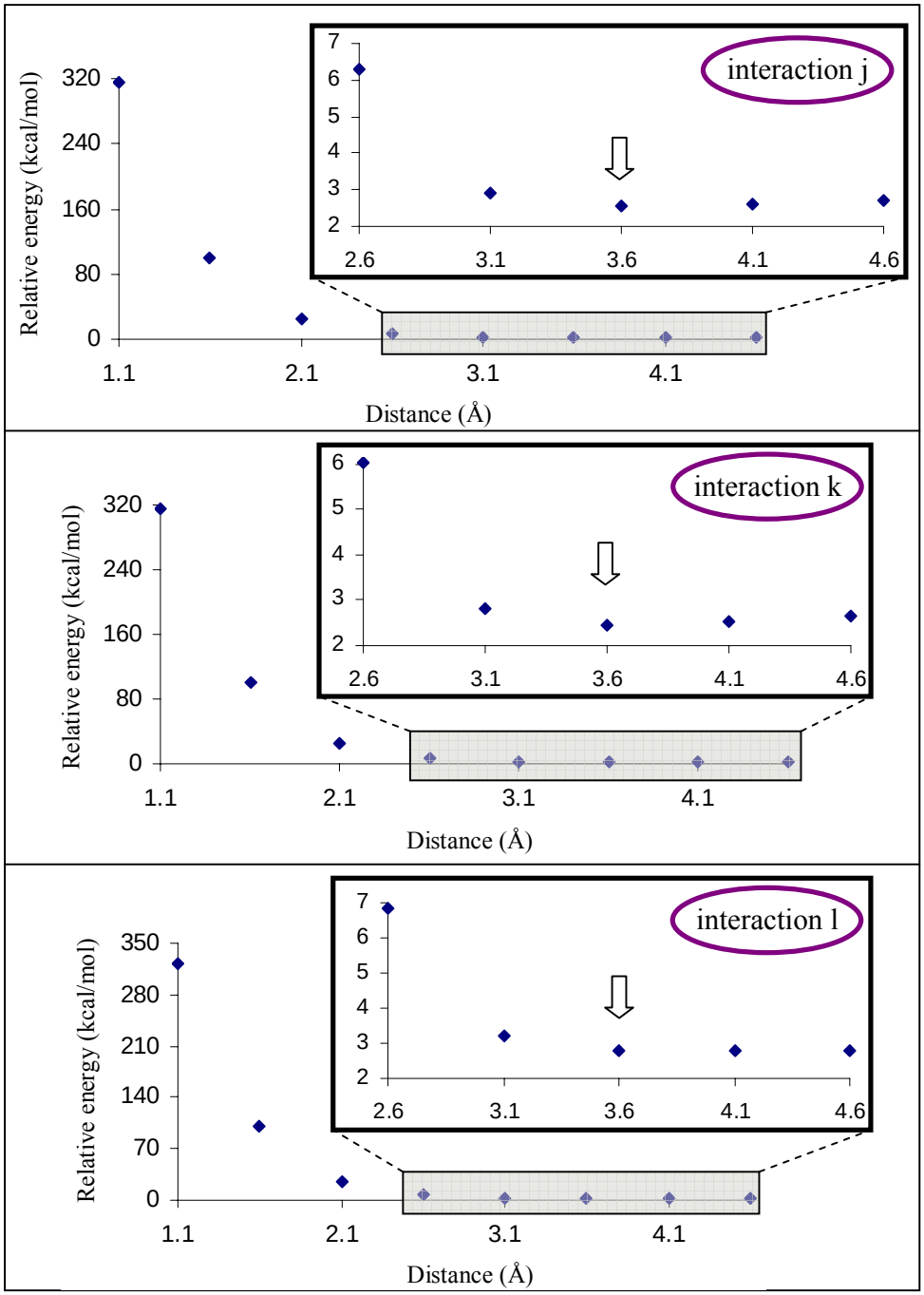


**Figure 101.** Nitrobenzene/TEMPO energy curves for interactions (j)-(l).

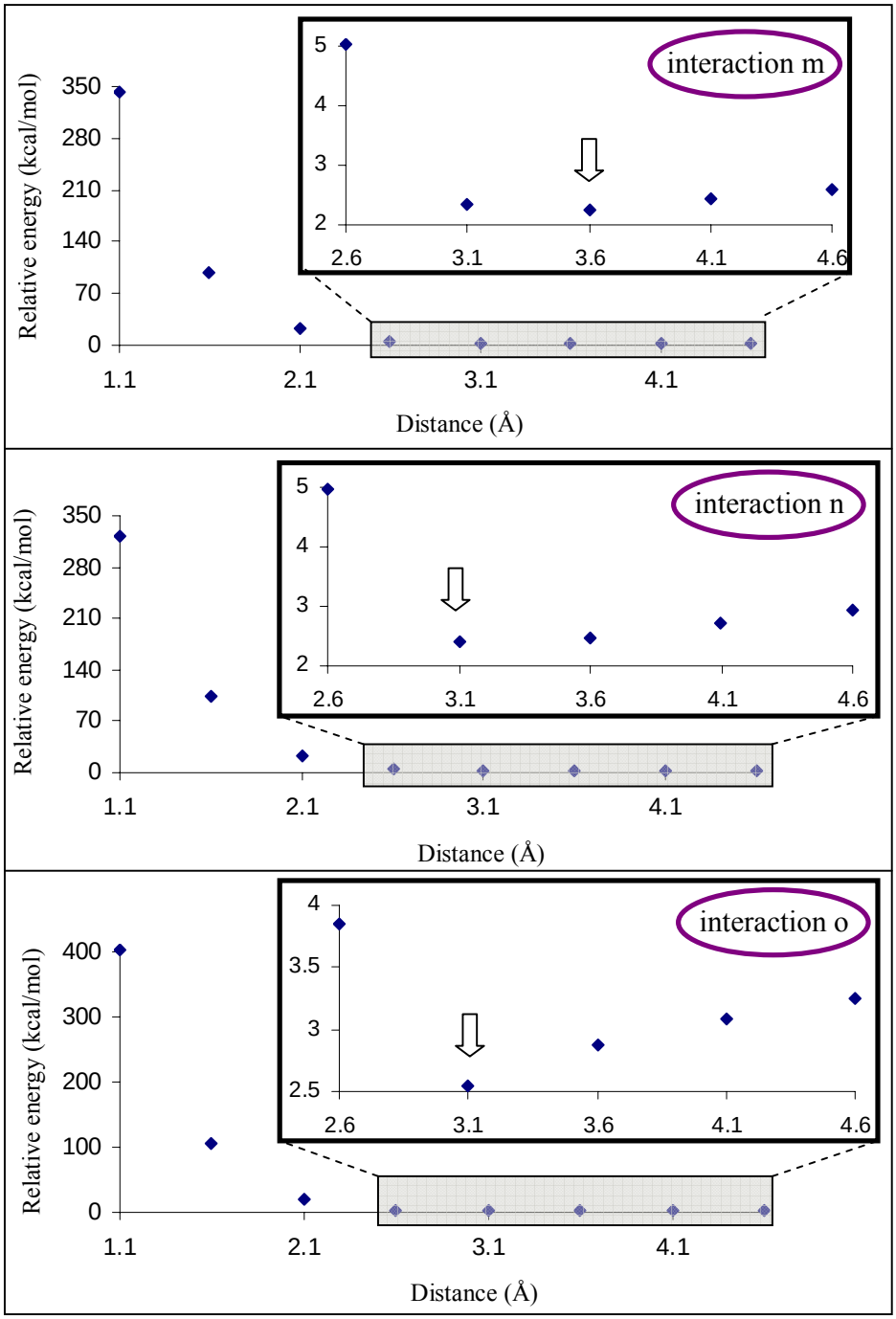


**Figure 102.** Nitrobenzene/TEMPO energy curves for interactions (m)-(o).

### 5.2.8 Nitromethane/TEMPO.

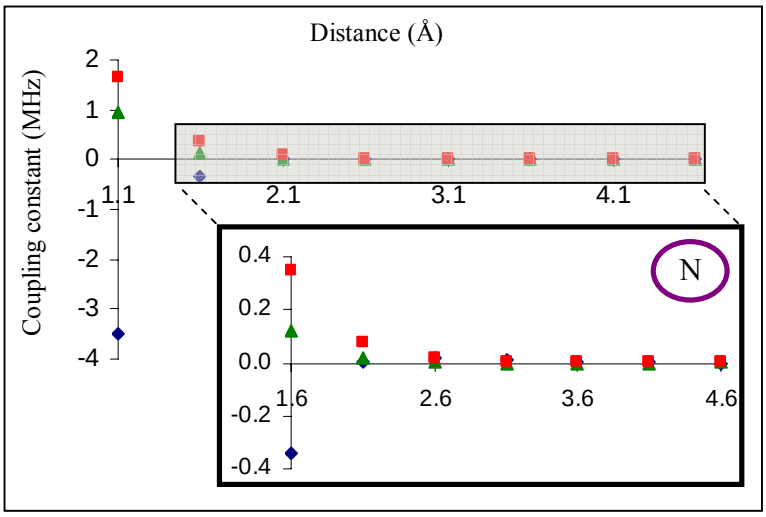


**Figure 103.** Nitromethane/TEMPO ($^{15}$N) coupling constant data for interactions (a)-(c).

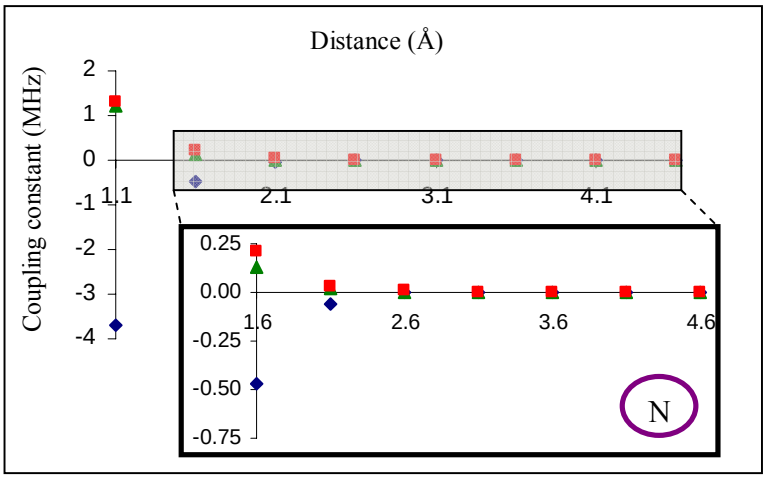


**Figure 104.** Nitromethane/TEMPO ($^{15}$N) coupling constant data for interactions (d)-(f).

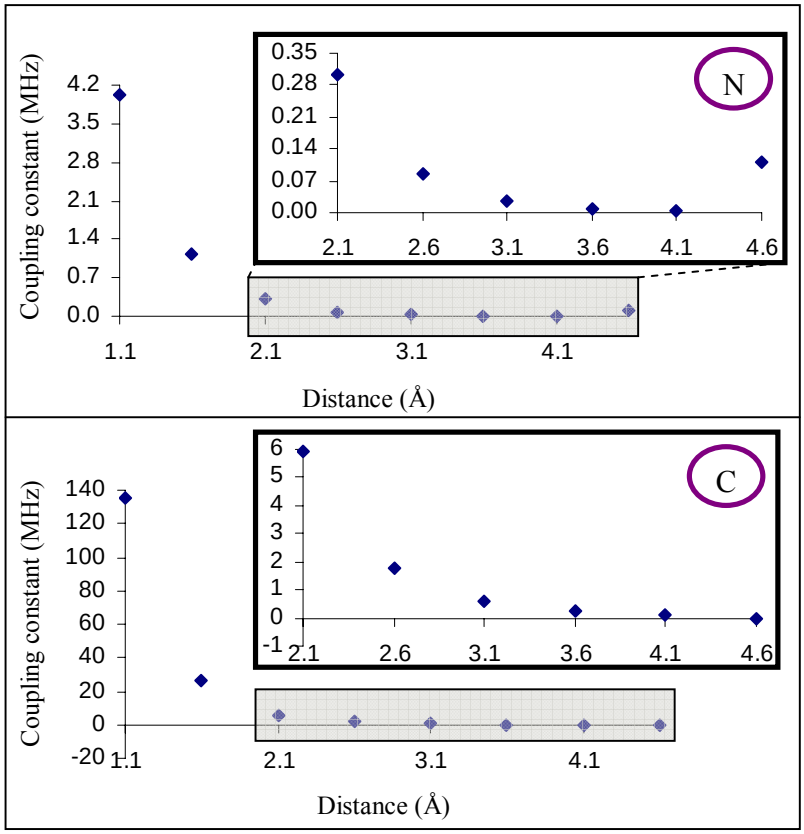


**Figure 105.** Nitromethane/TEMPO coupling constant data for interaction (g).

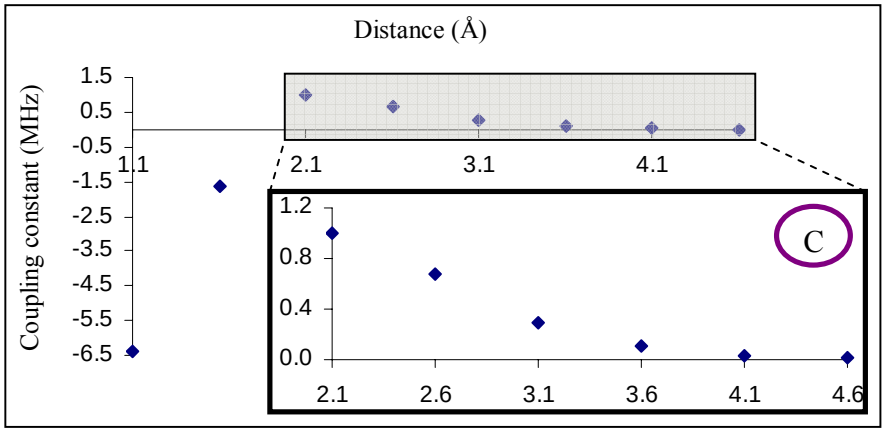


**Figure 106.** Nitromethane/TEMPO ($^{13}C$) coupling constant data for interaction (h).

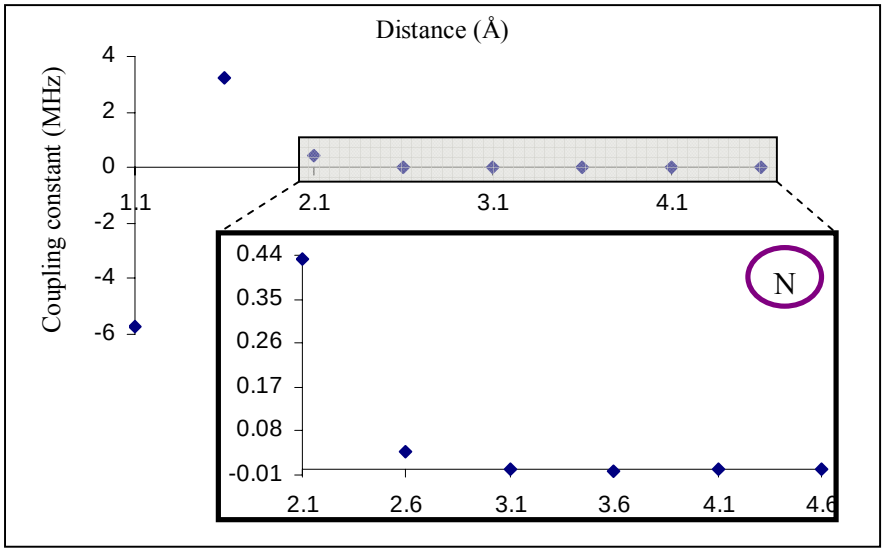


**Figure 107.** Nitromethane/TEMPO ($^{15}$N) coupling constant data for interaction (h).

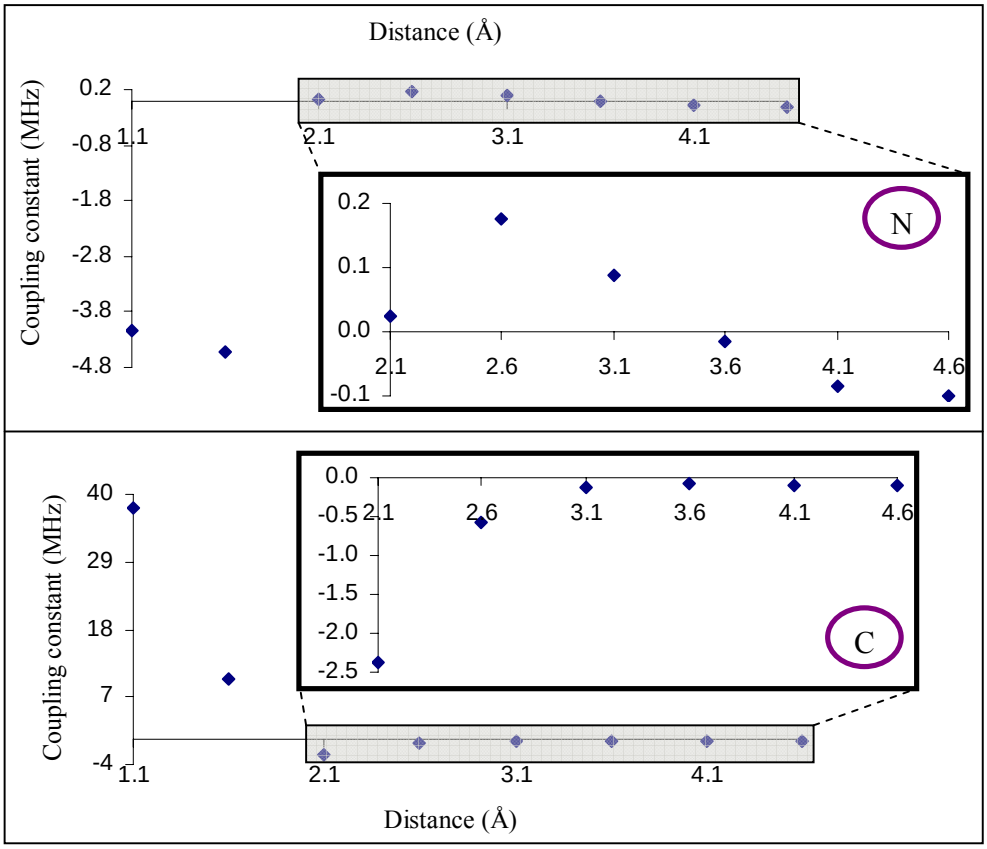


**Figure 108.** Nitromethane/TEMPO coupling constant data for interaction (i).

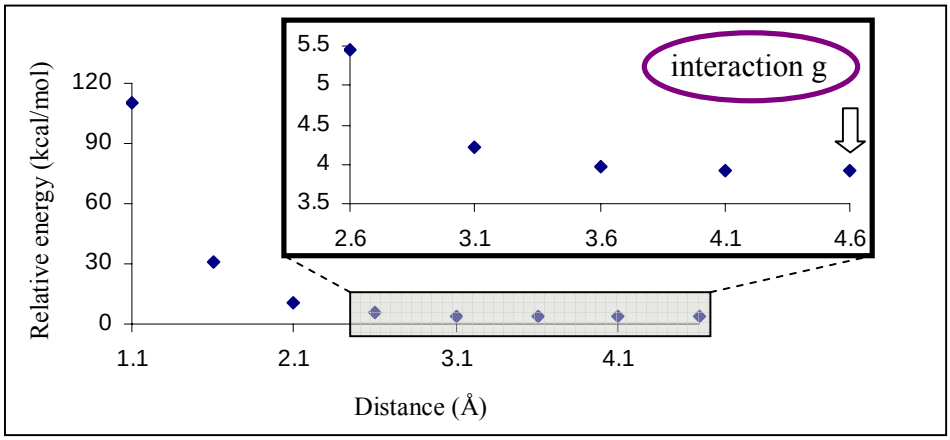


**Figure 109.** Nitromethane/TEMPO relative energy curve for interaction (g).

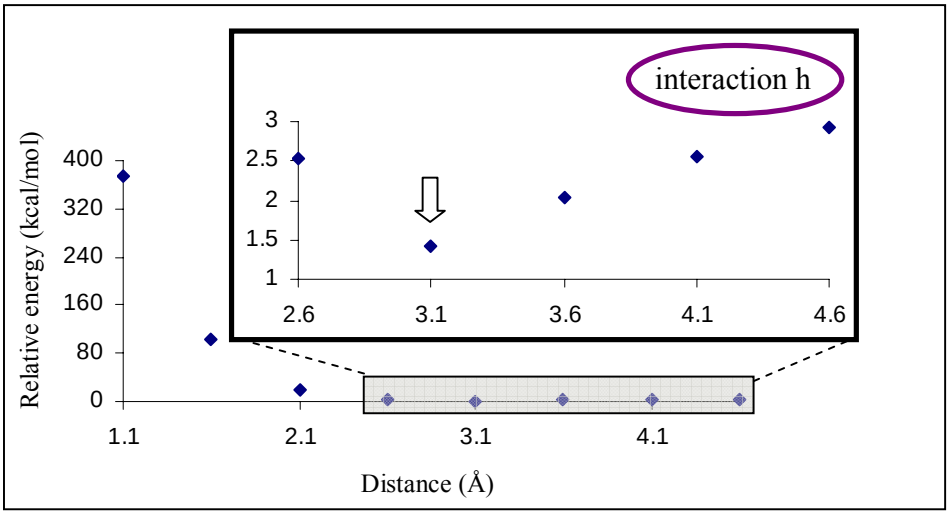


**Figure 110.** Nitromethane/TEMPO relative energy curve for interaction (h).

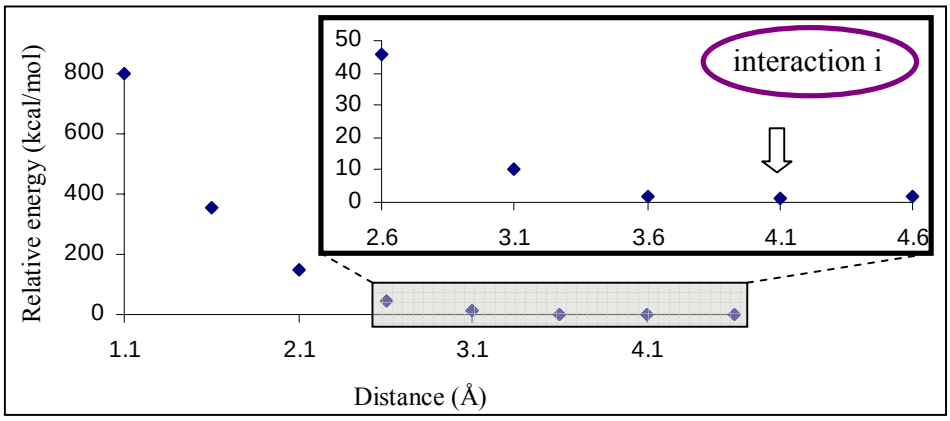


**Figure 111.** Nitromethane/TEMPO relative energy curve for interaction (i).

### 5.2.9 Ethane/TEMPO.

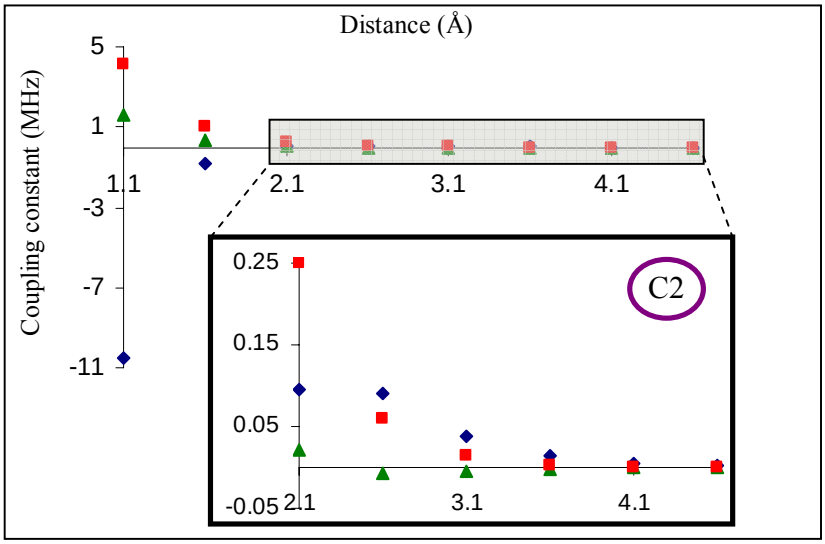


**Figure 112.** Ethane/TEMPO (C2) coupling constant data for interactions (a)-(c).

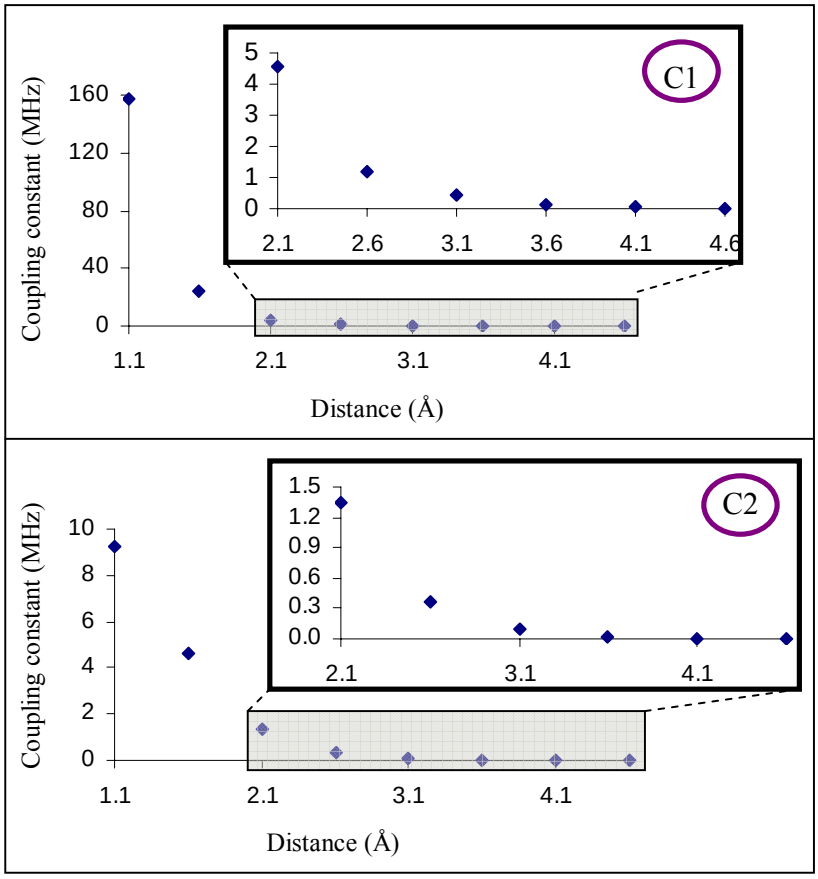


**Figure 113.** Ethane/TEMPO coupling constant data for interaction (d).

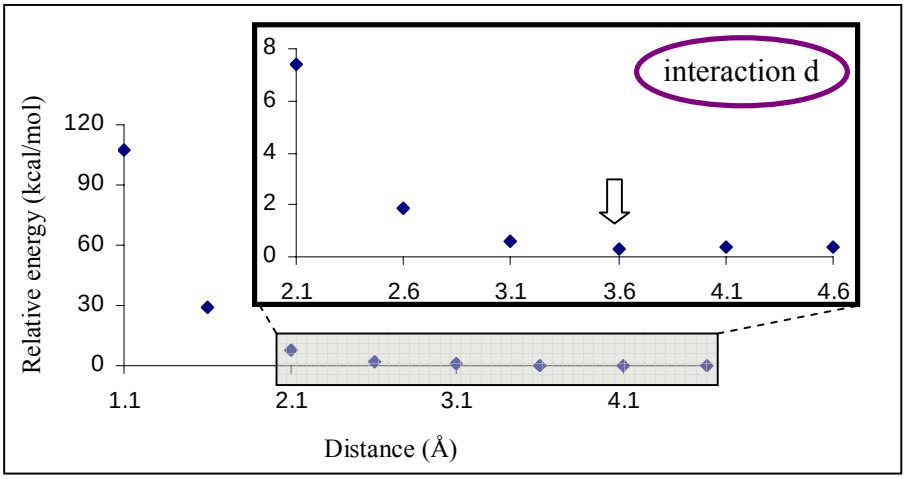


**Figure 114.** Ethane/TEMPO relative energy curve for interaction (d).

## 5.3 Metallofullerene Sample Preparation

The TNT metallofullerenes were prepared in a Krätschmer-Huffman generator (Figure 115).[118] Solid graphite rods were drilled longitudinally through the center, and packed with a metal oxide, iron nitride and graphite powder mixture. The metal oxide is $Gd_2O_3$, $Lu_2O_3$, $Sc_2O_3$, or $Ho_2O_3$ depending on the metallofullerene of interest. In a typical preparation of $Gd_3N@C_{80}$, the rods were packed with a mixture of 1.909 g $Gd_2O_3$, 0.400 g $Fe_xN$, and 1.000 g graphite powder.

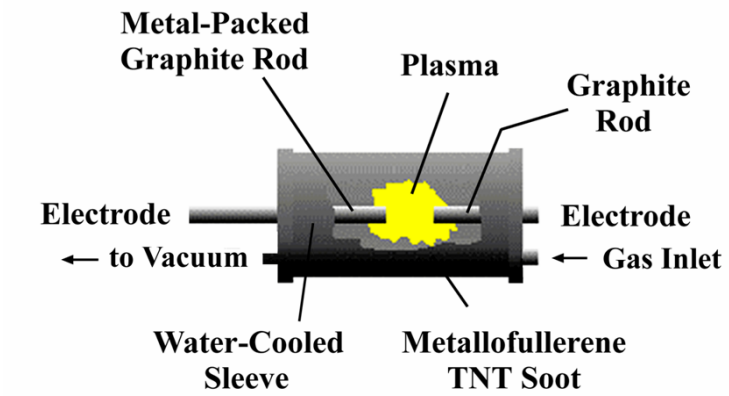


**Figure 115.** Krätschmer-Huffman apparatus.

The packed rods were then loaded into the Krätschmer-Huffman generator; the chamber was evacuated, filled, and maintained at a total pressure of 300 torr with a mixture of $N_2$ and He. After each rod had been consumed by the arcing process, the resulting soot was collected and Soxhlet extracted overnight with toluene. The solution was purified by multiple-stage high-pressure liquid chromatography (HPLC).

The functionalized $Gd_3N@C_{80}(OH)_m(O)_n$, $Ho_3N@C_{80}(OH)_m(O)_n$, and $Sc_3N@C_{80}(OH)_m(O)_n$ metallofullerols were prepared by Xuelei Wang.[119]

The functionalized $Lu_3N@C_{80}$[DiPEG5000$(OH)_x$] and $Gd_3N@C_{80}$[DiPEG5000$(OH)_x$] metallofullerenes were prepared by Dr. Zhongxin Ge via organic synthesis methods.[60] Poly(ethylene glycol) malonate (DiPEG5000) was prepared first. Malonyl chloride was distilled under reduced pressure and dichloromethane was distilled and dried under an inert atmosphere. The following reaction mixture was stirred

for 4 h at room temperature: 200 mL $CH_2Cl_2$, 0.282 g malonyl chloride, 20 g poly(ethylene glycol) methyl ether, and 0.316 g pyridine. The reaction mixture was concentrated, then fractioned using a silica gel column. A white solid, poly(ethylene glycol) malonate was obtained. Next the pegylated metallofullerenes was prepared, either $Gd_3N@C_{80}$ or $Lu_3N@C_{80}$ was used in the procedure. For example: 8 mg of $Gd_3N@C_{80}$ and 2.7 mg of $CBr_4$ were dissolved in 50 mL of toluene using sonication; 94.6 mg of poly(ethylene glycol) malonate and 2.6 mg of DBU were then added. The reaction mixture was stirred for 20 h under nitrogen at room temperature and the product was isolated using a silica gel column. The pegylated metallofullerenes was hydoxylated next. For example: 8 mg of $Gd_3N@C_{80}$[DiPEG5000] was dissolved in 40mL of toluene. Next, 5 drops of 50% sodium hydroxide and 3 drops of tetrabutylammonium hydroxide were added. The solvent was removed after 4 h, and 20 mL of distilled water and 5 drops of 50% sodium peroxide were added. The mixture was vigorously stirred overnight and separated using a G-25 Sephadex column. The lutetium pegylated and hydroxylated metallofullerenes was prepared in the same way.

*The metallofullerene sample preparations described in this section were performed by Xuelei Wang and Dr. Zhongxin Ge.

## 5.4 Inductively Coupled Plasma Optical Emission Spectroscopy (ICP-OES)

The concentrations of the metallofullerenes samples were measured using ICP-OES (Perkin-Elmer Optima 4300 DV). ICP is an analytical technique used to detect trace metals in various samples. An inductively coupled plasma is a very high temperature (7000-10,000K) excitation source that efficiently vaporizes, excites, and ionizes atoms.[120] Then as the ions return to their ground state, the number of photons emitted at a particular wavelength can be measured.

ICP instrumentation is designed to generate plasma, an electrical conducting gas containing atoms present in an ionized state.[120, 121] The torch of an ICP contains three concentric tubes, usually made of silica. The torch is positioned inside a water-cooled

coil of a radio frequency (RF) generator. The plasma is formed when the gas introduced into the torch is made electrically conductive in the coil region. The plasma formation is dependent on an adequate magnetic field strength and is maintained by inductive heating of the flowing gases. An outer gas, intermediate gas, and carrier gas flow through the system. The outer gas, usually argon or nitrogen, maintains and stabilizes the plasma, as well as thermally isolates the plasma from the outer tube. The intermediate and carrier gases are typically argon. The carrier gas simply transports the sample to the plasma.

The light emitted by atoms in a sample must be converted to an electrical signal to be measured quantitatively. The light emitted by the ions in the ICP is converted to electrical signals by the photomultiplier in the spectrometer. The intensity of the signal is compared to previously measured intensities of known concentration of the element. Most elements have several prominent lines to be used for identification and determination purposes. An appropriate line(s) or specific wavelengths can generally be obtained. Selection depends on the consideration of other elements that could be present in the sample with overlapping lines. The detection limit and number of useful lines for the Gd, Lu, Sc, and Ho atoms are indicated in Table 13.

**Table 13.** The ICP detection limit and number of lines for select metals.[120]

| Element | Detection Limit (ng/mL) | Number of Lines |
|---|---|---|
| Gd | 10-30 | 11-16 |
| Lu | <10 | 11-16 |
| Sc | <10 | 17-24 |
| Ho | 10-30 | 10-30 |

The ICP measurements for $Gd_3N@C_{80}$[DiPEG5000$(OH)_x$] and $Lu_3N@C_{80}$[DiPEG5000$(OH)_x$] performed by Xuelei Wang with the help of Dr. Gary Long, Wes Gordon, and David Roach is summarized below.[60] A standard solution is prepared in addition to the sample of interest. A baseline was created based on the number of photon emissions from that standard solution, and then concentration was calculated. For example: the gadolinium concentration for the water-soluble pegylated hydroxylated metallofullerenes, $Gd_3N@C_{80}$[DiPEG5000$(OH)_x$] was determined at wavelengths of 336.223, 342.247, and 335.047 nm. The ICP instrument was calibrated using a 10,000 ppm Gd stock solution from Aldrich, after which three sample dilutions

(20x, 200x, and 400x with distilled water) were analyzed to determined the gadolinium concentration. The concentrations are determined assuming each $Gd_3N@C_{80}$[DiPEG5000$(OH)_x$] molecule contains three gadolinium atoms.

The ICP procedure for the remaining samples ($Gd_3N@C_{80}$[DiPEG2000$(OH)_x$], $Gd_3N@C_{80}$[DiPEG750$(OH)_x$], $HoCl_3$, $Ho_3N@C_{80}(OH)_m(O)_n$, $GdCl_3$, $Gd_3N@C_{80}(OH)_m(O)_n$, and $Sc_3N@C_{80}(OH)_m(O)_n$) performed by Dr. Zhongxin Ge with the help of Dr. Gary Long is slightly different. The ICP instrument was calibrated using a series of metal (Gd, Ho, and Sc) standard solutions (10 ppm, 5 ppm, 1 ppm, 0.5 ppm, 0.2 ppm, and 0.1 ppm) prepared from a stock standard of 10 ppm purchased from Inorganic Ventures Corp. The gadolinium concentration was determined at wavelengths of 342.247, 336.223, 335.047, and 308.199 nm. The holmium concentration was determined at wavelengths of 345.600, 339.898, and 347.426 nm. The scandium concentration was determined at wavelengths of 361.383, 357.253, 424.683, 357.634 nm. The sample of interest was analyzed to determine the metal concentration assuming each TNT metallofullerene has three metal atoms inside.

* The ICP measurements were performed by Dr. Zhongxin Ge and Xuelei Wang with the help of Dr. Gary Long, Wes Gordon, and David Roach.

## 5.5 Relaxivity Data and Errors (0.35T)

Each point on each relaxivity graph represents one sample at a specific concentration. Multiple measurements were performed for each sample, and the points on the relaxivity graphs are an average of the multiple runs for that sample. All data tabulated in section 6.2 is the average value for each sample at a specific concentration with the correlating standard deviations of all runs. The standard deviation ($\sigma$) was determined by the equation

$$\sigma = \sqrt{\frac{\sum_i (x_i - \bar{x})^2}{N}} \qquad [27]$$

where $x_i$ is a data value, $\bar{x}$ is the average value of all data points, and $N$ is the total number of measurements performed on a sample. Essentially, the data tabulated are the raw data that was plotted to determine the concentration dependent relaxivity values reported.

### 5.5.1 $Lu_3N@C_{80}$[DiPEG5000$(OH)_x$].

**Table 14.** $Lu_3N@C_{80}$[DiPEG5000$(OH)_x$] relaxivity data and standard deviations.

| Concentration (mM) | $r_1$ ($s^{-1}$) | $\sigma$ ($r_1$) | $r_2$ ($s^{-1}$) | $\sigma$ ($r_2$) |
|---|---|---|---|---|
| 0.8 | 0.8980 | 0.0013 | 2.7827 | 0.0283 |
| 0.4 | 0.7384 | 0.0106 | 2.5924 | 0.0169 |
| 0.2 | 0.5513 | 0.0003 | 1.8981 | 0.0047 |
| 0.1 | 0.4774 | 0.0034 | 1.8037 | 0.0118 |

### 5.5.2 $Gd_3N@C_{80}$[DiPEG5000$(OH)_x$].

**Table 15.** $Gd_3N@C_{80}$[DiPEG5000$(OH)_x$] relaxivity data and standard deviations.

| Concentration (mM) | $r_1$ ($s^{-1}$) | $\sigma$ ($r_1$) | $r_2$ ($s^{-1}$) | $\sigma$ ($r_2$) |
|---|---|---|---|---|
| 0.202 | 14.0387 | 0.0478 | 19.8083 | 0.8519 |
| 0.101 | 6.6769 | 0.0724 | 10.5342 | 0.3285 |
| 0.0505 | 3.7349 | 0.1429 | 5.0809 | 0.0389 |
| 0.0252 | 2.3904 | 0.0331 | 3.9147 | 0.0330 |
| 0.0126 | 1.5960 | 0.0246 | 3.4494 | 0.0015 |
| 0.0063 | 0.9315 | 0.0142 | 2.6472 | 0.0866 |
| 0.0032 | 0.6398 | 0.0028 | 2.1594 | 0.0530 |
| 0.0016 | 0.4736 | 0.0159 | 1.8355 | 0.0280 |

### 5.5.3 $Gd_3N@C_{80}[DiPEG2000(OH)_x]$.

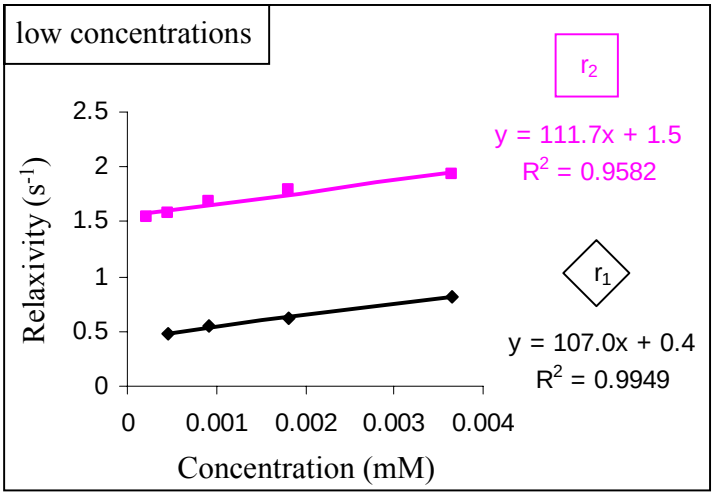


(The data is not corrected for diamagnetic water and the sample could contain impurities, such as iron and oxygen.)

**Figure 116.** $Gd_3N@C_{80}[DiPEG2000(OH)_x]$ 0.35T relaxivity data at low concentrations.

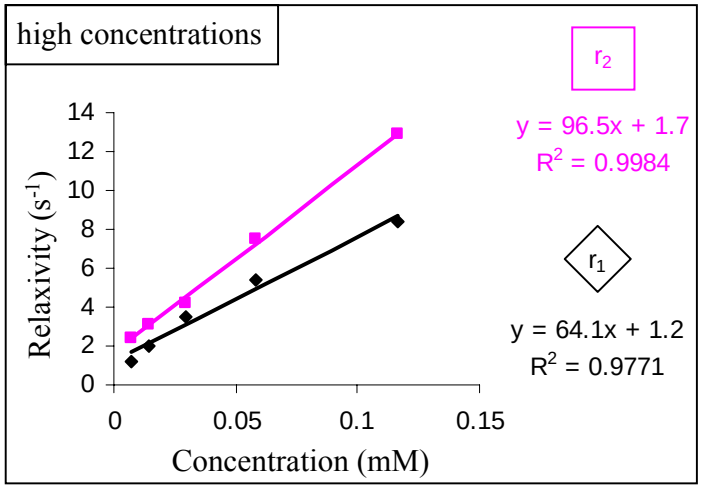


(The data is not corrected for diamagnetic water and the sample could contain impurities, such as iron and oxygen.)

**Figure 117.** $Gd_3N@C_{80}[DiPEG2000(OH)_x]$ 0.35T relaxivity data at high concentrations.

**Table 16.** $Gd_3N@C_{80}$[DiPEG2000$(OH)_x$] relaxivity data and standard deviations.

| Concentration (mM) | $r_1$ ($s^{-1}$) | σ ($r_1$) | $r_2$ ($s^{-1}$) | σ ($r_2$) |
|---|---|---|---|---|
| 0.1166 | 8.3779 | 0.0809 | 12.8554 | 0.0536 |
| 0.0583 | 5.3916 | 0.0055 | 7.4991 | 0.0999 |
| 0.0292 | 3.5213 | 0.0478 | 4.2123 | 0.0729 |
| 0.0146 | 2.0186 | 0.0366 | 3.0870 | 0.0221 |
| 0.00729 | 1.1695 | 0.0086 | 2.4235 | 0.0301 |
| 0.00364 | 0.8226 | 0.0068 | 1.9310 | 0.0412 |
| 0.00182 | 0.6226 | 0.0185 | 1.7887 | 0.0479 |
| 0.00091 | 0.5450 | 0.0150 | 1.6805 | 0.0651 |
| 0.00046 | 0.4713 | 0.0040 | 1.5820 | 0.0652 |
| 0.00023 | 0.4012 | 0.0041 | 1.5418 | 0.0146 |

### 5.5.4 $Gd_3N@C_{80}$[DiPEG750$(OH)_x$].

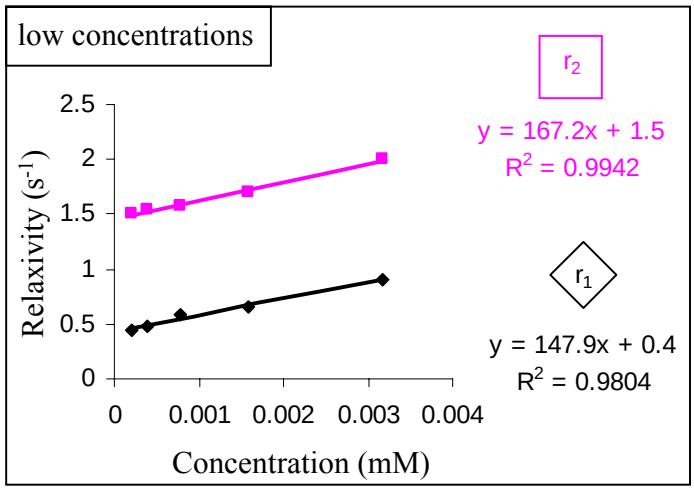


(The data is not corrected for diamagnetic water and the sample could contain impurities, such as iron and oxygen.)

**Figure 118.** $Gd_3N@C_{80}$[DiPEG750$(OH)_x$] 0.35T relaxivity data at low concentrations.

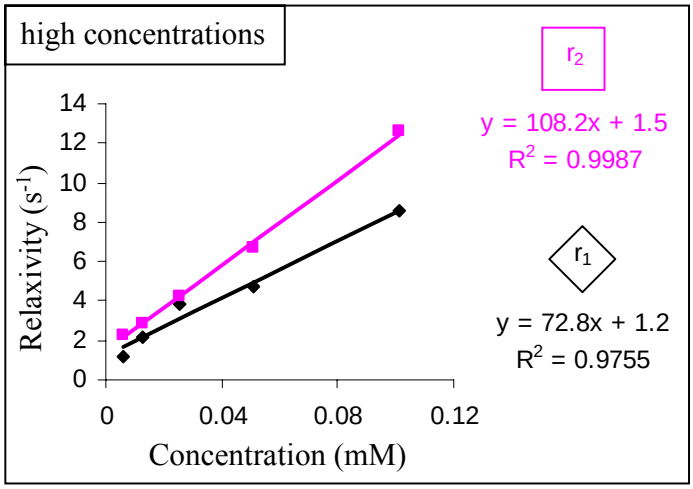


(The data is not corrected for diamagnetic water and the sample could contain impurities, such as iron and oxygen.)

**Figure 119.** $Gd_3N@C_{80}[DiPEG750(OH)_x]$ 0.35T relaxivity data at high concentrations.

**Table 17.** $Gd_3N@C_{80}[DiPEG750(OH)_x]$ relaxivity data and standard deviations.

| Concentration (mM) | $r_1$ ($s^{-1}$) | $\sigma$ ($r_1$) | $r_2$ ($s^{-1}$) | $\sigma$ ($r_2$) |
|---|---|---|---|---|
| 0.1015 | 8.5476 | 0.0840 | 12.5754 | 0.1971 |
| 0.0508 | 4.7715 | 0.0306 | 6.7065 | 0.1073 |
| 0.0254 | 3.8049 | 0.0577 | 4.2658 | 0.0778 |
| 0.0127 | 2.1405 | 0.0332 | 2.8535 | 0.0550 |
| 0.00634 | 1.2017 | 0.0108 | 2.2649 | 0.0404 |
| 0.00317 | 0.8971 | 0.0256 | 2.0021 | 0.0478 |
| 0.00159 | 0.6643 | 0.0121 | 1.7104 | 0.0163 |
| 0.00079 | 0.5939 | 0.0050 | 1.5768 | 0.0123 |
| 0.00040 | 0.4855 | 0.0006 | 1.5419 | 0.0305 |
| 0.00020 | 0.4380 | 0.0047 | 1.5043 | 0.0289 |

### 5.5.5 Holmium Chloride.

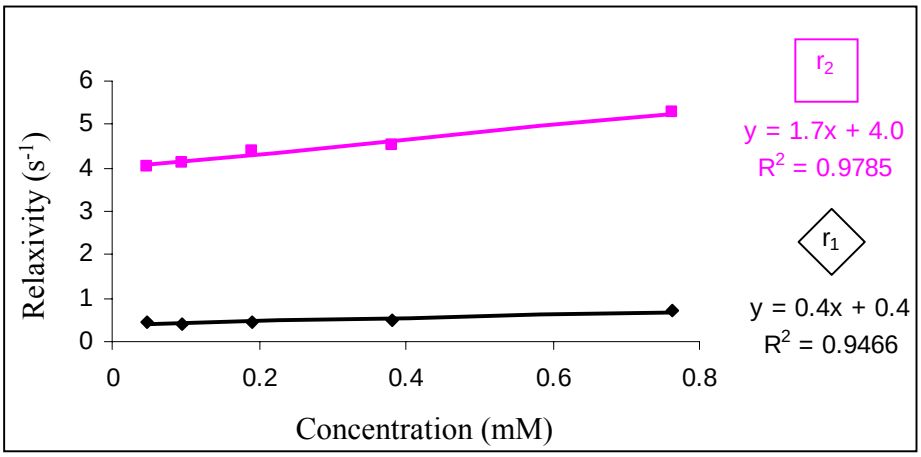


(The data is not corrected for diamagnetic water and the sample could contain impurities, such as iron and oxygen.)

**Figure 120.** $HoCl_3$ 0.35T relaxivity data.

**Table 18.** Holmium chloride relaxivity data and standard deviations.

| Concentration (mM) | $r_1$ ($s^{-1}$) | $\sigma$ ($r_1$) | $r_2$ ($s^{-1}$) | $\sigma$ ($r_2$) |
|---|---|---|---|---|
| 0.7623 | 0.7024 | 0.0171 | 5.2695 | 0.2148 |
| 0.3811 | 0.4952 | 0.0032 | 4.5326 | 0.1896 |
| 0.1906 | 0.4557 | 0.0108 | 4.4076 | 0.1313 |
| 0.0953 | 0.4134 | 0.0148 | 4.1102 | 0.2116 |
| 0.0476 | 0.4345 | 0.0034 | 4.0309 | 0.0771 |

### 5.5.6 $Ho_3N@C_{80}(OH)_m(O)_n$.

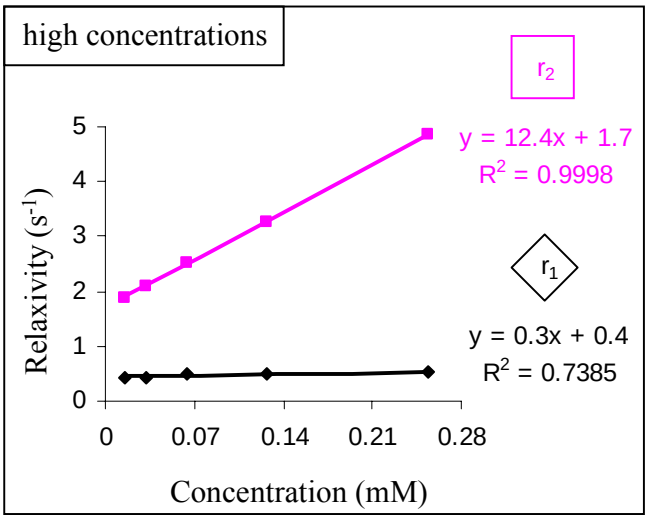


(The data is not corrected for diamagnetic water and the sample could contain impurities, such as iron and oxygen.)

**Figure 121.** $Ho_3N@C_{80}(OH)_m(O)_n$ 0.35T relaxivity data at high concentrations.

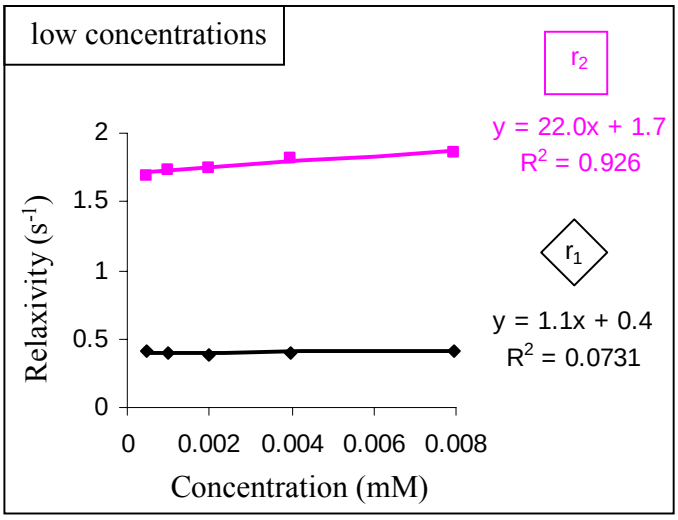


(The data is not corrected for diamagnetic water and the sample could contain impurities, such as iron and oxygen.)

**Figure 122.** $Ho_3N@C_{80}(OH)_m(O)_n$ 0.35T relaxivity data at low concentrations.

**Table 19.** $Ho_3N@C_{80}(OH)_m(O)_n$ relaxivity data and standard deviations.

| Concentration (mM) | $r_1$ ($s^{-1}$) | σ ($r_1$) | $r_2$ ($s^{-1}$) | σ ($r_2$) |
|---|---|---|---|---|
| 0.2541 | 0.5162 | 0.0172 | 4.8436 | 0.2071 |
| 0.1270 | 0.4952 | 0.0142 | 3.2767 | 0.1045 |
| 0.0635 | 0.4921 | 0.0051 | 2.5200 | 0.0101 |
| 0.0318 | 0.4388 | 0.0012 | 2.0797 | 0.2378 |
| 0.0159 | 0.4368 | 0.0127 | 1.8952 | 0.1110 |
| 0.00794 | 0.4168 | 0.0014 | 1.8646 | 0.0552 |
| 0.00397 | 0.3950 | 0.0072 | 1.8106 | 0.0569 |
| 0.00199 | 0.3891 | 0.0051 | 1.7502 | 0.0417 |
| 0.00099 | 0.4036 | 0.0055 | 1.7346 | 0.0129 |
| 0.00050 | 0.4160 | 0.0059 | 1.6868 | 0.0750 |

### 5.5.7 Gadolinium Chloride.

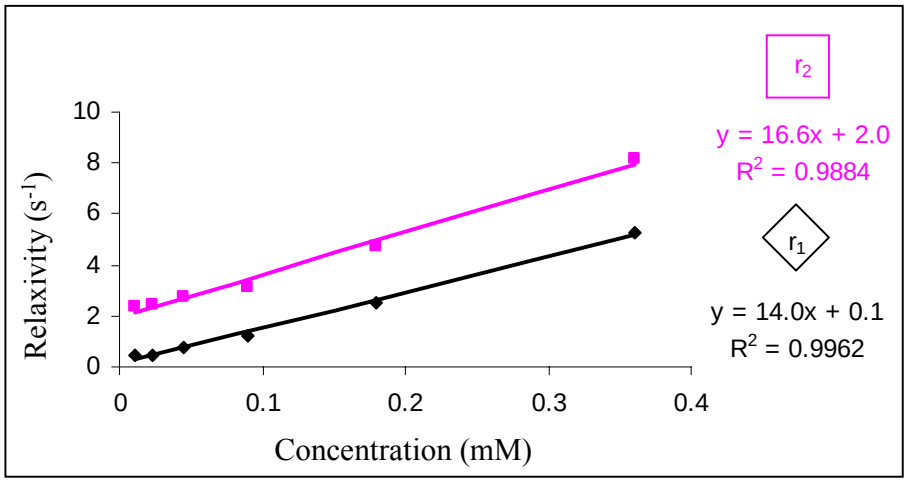


(The data is not corrected for diamagnetic water and the sample could contain impurities, such as iron and oxygen.)

**Figure 123.** $GdCl_3$ 0.35T relaxivity data.

**Table 20.** Gadolinium chloride relaxivity data and standard deviations.

| Concentration (mM) | $r_1$ ($s^{-1}$) | σ ($r_1$) | $r_2$ ($s^{-1}$) | σ ($r_2$) |
|---|---|---|---|---|
| 0.36 | 5.2605 | 0.0800 | 8.1332 | 0.2144 |
| 0.18 | 2.5441 | 0.0459 | 4.7200 | 0.0821 |
| 0.090 | 1.2325 | 0.0524 | 3.1138 | 0.0114 |
| 0.045 | 0.7870 | 0.0258 | 2.7227 | 0.0731 |
| 0.023 | 0.4687 | 0.0110 | 2.4753 | 0.0222 |
| 0.011 | 0.4332 | 0.0206 | 2.3938 | 0.0262 |

### 5.5.8 $Gd_3N@C_{80}(OH)_m(O)_n$.

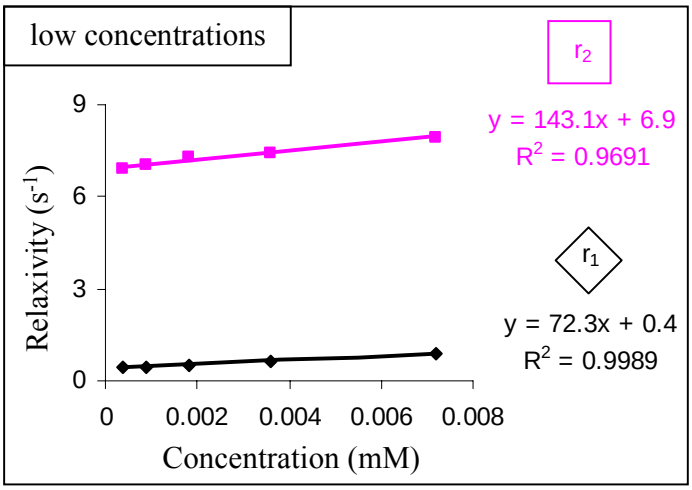


(The data is not corrected for diamagnetic water and the sample could contain impurities, such as iron and oxygen.)

**Figure 124.** $Gd_3N@C_{80}(OH)_m(O)_n$ 0.35T relaxivity data at low concentrations.

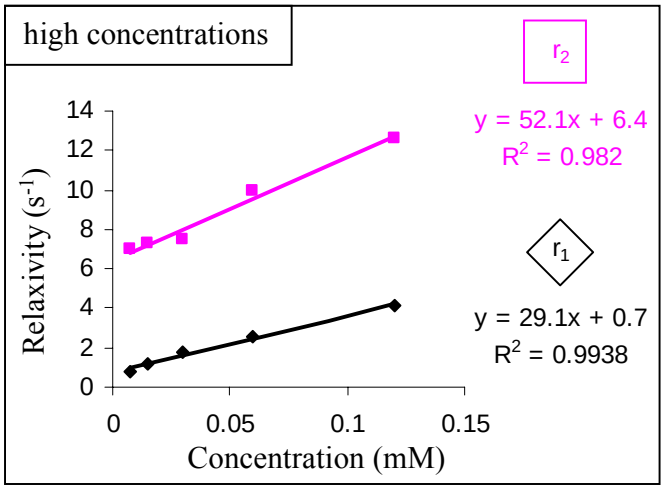


(The data is not corrected for diamagnetic water and the sample could contain impurities, such as iron and oxygen.)

**Figure 125.** $Gd_3N@C_{80}(OH)_m(O)_n$ 0.35T relaxivity data at high concentrations.

**Table 21.** $Gd_3N@C_{80}(OH)_m(O)_n$ relaxivity data and standard deviations.

| Concentration (mM) | $r_1$ ($s^{-1}$) | σ ($r_1$) | $r_2$ ($s^{-1}$) | σ ($r_2$) |
|---|---|---|---|---|
| 0.12 | 4.1569 | 0.0605 | 12.6212 | 0.1442 |
| 0.060 | 2.5275 | 0.0609 | 9.9241 | 0.1952 |
| 0.030 | 1.7275 | 0.0190 | 7.4951 | 0.0923 |
| 0.015 | 1.1559 | 0.0242 | 7.3220 | 0.0647 |
| 0.0075 | 0.7993 | 0.0047 | 6.9511 | 0.0300 |
| 0.0072 | 0.9166 | 0.0101 | 7.9475 | 0.0549 |
| 0.0036 | 0.6422 | 0.0233 | 7.4241 | 0.1689 |
| 0.0018 | 0.5172 | 0.0149 | 7.3060 | 0.1199 |
| 0.0009 | 0.4565 | 0.0137 | 7.0482 | 0.0959 |
| 0.0004 | 0.4274 | 0.0036 | 6.9157 | 0.1360 |

### 5.5.9 $Sc_3N@C_{80}(OH)_m(O)_n$.

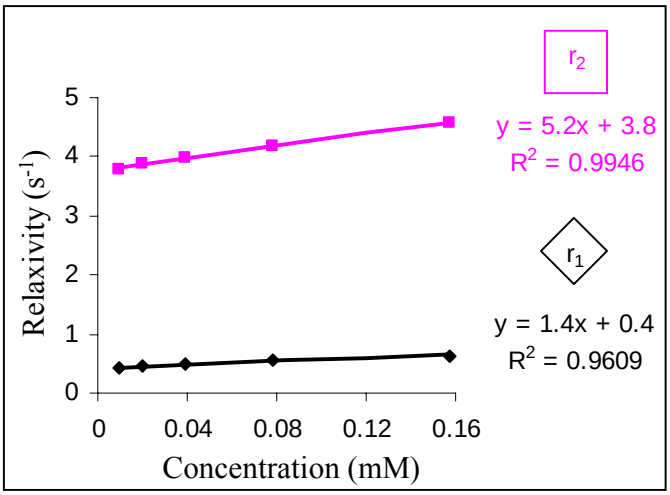


(The data is not corrected for diamagnetic water and the sample could contain impurities, such as iron and oxygen.)

**Figure 126.** $Sc_3N@C_{80}(OH)_m(O)_n$ 0.35T relaxivity data.

**Table 22.** $Sc_3N@C_{80}(OH)_m(O)_n$ relaxivity data and standard deviations.

| Concentration (mM) | $r_1$ ($s^{-1}$) | σ ($r_1$) | $r_2$ ($s^{-1}$) | σ ($r_2$) |
|---|---|---|---|---|
| 0.1572 | 0.6401 | 0.0045 | 4.5824 | 0.0361 |
| 0.0786 | 0.5538 | 0.0189 | 4.1655 | 0.2294 |
| 0.0393 | 0.4988 | 0.0062 | 3.9903 | 0.3848 |
| 0.0197 | 0.4575 | 0.0046 | 3.8860 | 0.1751 |
| 0.0098 | 0.4165 | 0.0054 | 3.7799 | 0.0929 |

### 5.5.10 Omniscan™ and Water.

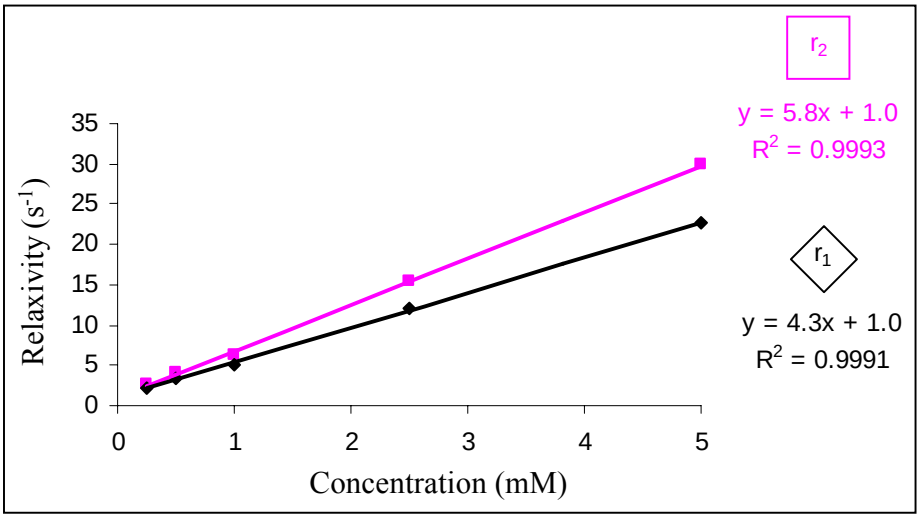


(The data is not corrected for diamagnetic water and the sample could contain impurities, such as iron and oxygen.)

**Figure 127.** Omniscan™ 0.35T relaxivity data.

**Table 23.** Omniscan™ relaxivity data and standard deviations.

| Concentration (mM) | $r_1$ ($s^{-1}$) | $\sigma$ ($r_1$) | $r_2$ ($s^{-1}$) | $\sigma$ ($r_2$) |
|---|---|---|---|---|
| 5.0 | 22.6090 | 0.5930 | 29.8524 | 1.4079 |
| 2.5 | 12.1525 | 0.1861 | 15.3491 | 0.4006 |
| 1.0 | 5.0355 | 0.1454 | 6.2500 | 0.0866 |
| 0.50 | 3.4311 | 0.0097 | 4.1580 | 0.0503 |
| 0.25 | 2.0603 | 0.0276 | 2.6007 | 0.1009 |

**Table 24.** Water relaxivity data and standard deviations.

| $r_1$ ($s^{-1}$) | $\sigma$ ($r_1$) | $r_2$ ($s^{-1}$) | $\sigma$ ($r_2$) |
|---|---|---|---|
| 0.4218 | 0.0265 | 0.9935 | 0.0156 |

# 6. References


1. Morishima, I.; Kawakami, K.; Yonezawa, T.; Goto, K.; Imanari, M., Interactions Between Closed- and Open-Shell Molecules. 13C Contact Shift Studies on the Interaction Between Aromatic Hydrocarbons and Nitroxide Radical. *Journal of the American Chemical Society* **1972,** 94, 6555-6557.
2. Morishima, I.; Toyoda, K.; Yoshikawa, K.; Yonezawa, T., Interaction Between Closed-Shell and Open-Shell Molecules. *Journal of the American Chemical Society* **1973,** 95, (26), 8627-8630.
3. Morishima, I.; Ishihara, K.; Tomishima, T.; Inubushi, T.; Yonezawa, T., Nitroxide Radical Induced Nuclear Magnetic Resonance Contact Shift Studies. Potential Utility of Specific Downfield 1H Contact Shifts Induced by Hydrogen Bonding with Di-tert-butyl Nitroxide Radical. *Journal of the American Chemical Society* **1975,** 97, (10), 2749-2756.
4. Gu, J. Nuclear Magnetic Resonance and Dynamic Nuclear Polarization Studies of Liquid/Liquid and Liquid/Solid Interfaces. Virginia Polytechnic Institute and State University, Blacksburg, VA, 1992.
5. Tsai, K. High Resolution 1H, 2D, 13C, 29Si, and 15N Dynamic Nuclear Polarization: Development and Applications. Dissertation, Virginia Polytechnic Institute & State University, Blacksburg, VA, 1990.
6. Tsai, K.; Dorn, H., A Model for Establishing the Ultimate Enhancements (A(infinity)) in the Low to High Magnetic Field Transfer Dynamic Nuclear Polarization Experiment. *Applied Magnetic Resonance* **1990,** 1, (2), 231-254.
7. LaMar, G., *NMR of Paramagnetic Molecules; Principles and Applications*. Academic Press: New York, 1973.
8. McConnell, H. M.; Chestnut, D., Theory of Isotropic Hyperfine Interactions in pi-Electron Radicals. *Journal of Chemical Physics* **1958,** 28, 107-117.
9. Abragam, A., *The Principles of Nuclear Magnetism*. Clarendon: Oxford, England, 1961.
10. Bloemberger, N.; Purcell, E.; Pound, R., Relaxation Effects in Nuclear Magnetic Resonance Absorption. *Physical Review* **1948,** 73, (7), 679-712.
11. Hubbard, P., Theory of Electron-Nucleus Overhauser Effects in Liquids Containing Free Radicals. *Proceedings of the Royal Society of London. Series A: Mathematical and Physical Sciences* **1966,** 291, (1427), 537-555.
12. Poindexter, E.; Caplan, P.; Wagner, B.; Bates Jr, R., Relaxation of Fluorine Nuclei by Collisions with Free Radicals. *Journal of Chemical Physics* **1974,** 61, (9), 3821-3827.
13. Solomon, I., Relaxation Processes in a System of Two Spins. *Physical Review* **1955,** 99, (2), 559-565.
14. Solomon, I., Nuclear Magnetic Interactions in the HF Molecule. *Journal of Chemical Physics* **1956,** 25, (2), 261-266.
15. Borah, B.; Bates Jr, R., Dynamics of Interspecies Hydrogen Bonding of Partially Fluorinated Compounds and a Stable Nitroxide Radical Studied by Proton and Fluorine-19 Relaxation and Low-Field DNP Measurements. *Journal of Chemical Physics* **1981,** 75, (9), 4289-4293.

16. Wertz, J.; Bolton, J., *Electron Spin Resonance*. McGraw-Hill Book Company: New York, 1972.
17. Fermi, E., Magnetic Moments of Atomic Nuclei. *Zeitschrift fuer Physik* **1930,** 60, 320-333.
18. Otsuka, T.; Motozaki, W.; Nishikawa, K.; Endo, K., Intermolecular H-Bond of Solvent Molecule with Nitroxide Radical Using ab initio MO Calculations. *Journal of Molecular Structure* **2002,** 615, 147-151.
19. Forrester, A.; Hay, J.; Thomson, R., *Organic Chemistry of Stable Free Radicals*. Academic Press: New York, 1968.
20. Rozantsev, E. G., *Free Nitroxyl Radicals*. Plenum Press: New York, 1970.
21. Rozantsev, E. G.; Sholle, V. D., Synthesis and Reactions of Stable Nitroxyl Radicals. II. Reactions. *Synthesis* **1971,** 8, 401-414.
22. Rozantsev, E. G.; Sholle, V. D., Synthesis and Reactions of Stable Nitroxyl Radicals. I. Synthesis. *Synthesis* **1971,** 4, 190-202.
23. Keana, J., Newer Aspects of the Synthesis and Chemistry of Nitroxide Spin Labels. *Chemical Reviews* **1978,** 78, (1), 37-64.
24. Dagonneau, M.; Kagan, E. S.; Mikhailov, V. I.; Rozantsev, E. G.; Sholle, V. D., Chemistry of Hindered Amines from the Piperidine Series. *Synthesis* **1984,** 11, 895-916.
25. Vordarsky, L., *Imidazoline Nitroxides*. CRC Press: Boca Raton, FL, 1988; Vol. 1 & 2.
26. Aulich, H., *Nitrones, Nitronates, and Nitroxides*. John Wiley and Sons: New York, 1989.
27. Brik, M.-E., Chemistry of Persistent Free Bi- and Polyradicals. *Heterocycles* **1995,** 41, (12), 2827-2873.
28. Janzen, E., Spin Trapping. *Accounts of Chemical Research* **1971,** 4, 31-40.
29. Pou, S.; Halpern, H.; tsai, P.; Rosen, G., Issues Pertinent to the in Vivo in Situ Spin Trapping of Free Radicals. *Accounts of Chemical Research* **1999,** 32, 155-161.
30. Hamilton, C.; McConnell, H. M., *Structural Chemistry and Molecular Biology*. W. H. Freeman and Co.: San Francisco, CA, 1968.
31. Griffith, O. H.; Waggoner, A. S., Nitroxide Free Radicals: Spin Labels for Probing Biomolecular Structure. *Accounts of Chemical Research* **1969,** 2, (1), 17-24.
32. McConnell, H. M.; McFarland, B. G., Physics and Chemistry of Spin Labels. *Quarterly Reviews of Biophysics* **1970,** 3, (1), 91-136.
33. Likhtenstein, G., *Spin Labeling Methods in Molecular Biology*. Wiley-Interscience: New York, 1976.
34. Berliner, L., *Spin Labeling: Theory and Applications*. Academic Press: New York, 1976; Vol. 1.
35. Berliner, L., *Spin Labeling: Theory and Applications*. Academic Press: New York, 1979; Vol. 2.
36. Hideg, K.; Hankovszky, H., *Biological Magnetic Resonance*. Plenum Press: New York, 1989; Vol. 8.
37. Rasset, A., Magnetic Properties of Nitroxide Multiradicals. *Pure and Applied Chemistry* **1990,** 62, (2), 223-227.
38. Iwamura, H.; Koga, N., Studies of Organic Di-, Oligo-, and Polyradicals by Means of Their Bulk Magnetic Properties. *Accounts of Chemical Research* **1993,** 26, (6), 346-351.

39. Rajca, A., Organic Diradicals and Polyradicals: From Spin Coupling to Magnetism? *Chemical Reviews* **1994,** 94, (4), 871-893.
40. Bobbitt, J. M.; Flores, M., Organic Nitrosonium Salts as Oxidants in Organic Chemistry. *Heterocycles* **1988,** 27, (2), 509-533.
41. Yamaguchi, M.; Miyazawa, T.; Takata, T.; Endo, T., Application of Redox System System Based on Nitroxides to Organic Synthesis. *Pure and Applied Chemistry* **1990,** 62, (2), 217-222.
42. Inokuchi, T.; Matsumoto, S.; Torii, S., Recent Advances in the Catalytic Oxidation of Alcohols with 2,2,6,6-tetramethylpiperidine-1-oxyl (TEMPO) and its Application to Organic Synthesis. *Yuki Gosei Kagaku Kyokaishi* **1993,** 51, (10), 910-920.
43. De Nooy, A.; Besemer, A.; Van Bekkum, H., On the use of Stable Organic Nitroxyl Radicals for the Oxidation of Primary and Secondary Alcohols. *Synthesis* **1996,** 10, 1153-1174.
44. Hawker, C.; Bosman, A.; Harth, E., New Polymer Synthesis by Nitroxide Mediated Living Radical Polymerizations. *Chemical Reviews* **2001,** 101, 3661-3688.
45. Grucker, D.; Guiberteau, T.; Eclancher, B.; Chambron, J.; Chaiarelli, R.; Rassat, A.; Subra, G.; Gallez, B., Dynamic nuclear polarization with nitroxides dissolved in biological fluids. *Journal of Magnetic Resonance* **1995,** 106, 101-109.
46. Iannone, A.; Tomasi, A., Nitroxide radicals, their use as metabolic probes in biological model systems: an overview. *Acta Pharmaceutica Jugoslavica* **1991,** 41, (4), 277-297.
47. Bales, B.; Peric, M., EPR line shifts and line shape changes duw to spin exchange of nitroxide free radicals in liquids. *Journal of Physical Chemistry B* **1997,** 101, 8707-8716.
48. Lepley, A., The nuclear magnetic resonance spectrum of a phenoxy radical. Di-t-butyl nitroxide as a spin relaxer. *Journal of the American Chemical Society* **1968,** 90, (10), 2711-2713.
49. Knauer, B.; Napier, J., The nitrogen hyperfine splitting constant of the nitroxide functional group as a solvent polarity parameter. The relative importance for a solvent polarity parameter of its being a cybotactic probe vs. its being a model process. *Journal of the American Chemical Society* **1976,** 98, 4395-4400.
50. Beckwith, A.; Bowry, V.; Ingold, K., Kinetics of nitroxide radical trapping. 1. Solvent effects. *Journal of the American Chemical Society* **1992,** 114, 4983-4992.
51. Carr, H.; Purcell, E., Effects of diffusion on free precession in nuclear magnetic resonance experiments. *Physical Review* **1954,** 94, (3), 630-638.
52. Hahn, E., Spin Echoes. *Physical Review* **1950,** 80, (4), 580-594.
53. Bloembergen, N.; Purcell, E.; Pound, R., Relaxation effects in nuclear magnetic resonance absorption. *Physical Review* **1948,** 73, (7), 679-712.
54. Waugh, J.; Wang, C.; Huber, L.; Vold, R., Multiple-pulse nuclear magnetic resonance experiments. *Journal of Chemical Physics* **1968,** 48, (2), 662-670.
55. Vold, R.; Waugh, J.; Klein, M.; Phelps, D., Measurement of spin relaxation in complex systems. *Journal of Chemical Physics* **1968,** 48, (8), 3831-3832.
56. Farrer, T.; Becker, E., *Pulse and Fourier Transform NMR*. Academic: New York, 1971.
57. Lauterbur, P.; Jacobson, M.; Rudin, A.; al., e. In *Augmentation of the Water Spin-lattice Relaxation in Tissues by In Vivo Injection of Manganese Ion*, 19th Experimental

Nuclear Magnetic Resonance Conference, Blacksburg, VA, April 1978; Blacksburg, VA, April 1978; p B19.
58. Young, I.; Clarke, G.; Bailes, D.; Pennock, J.; Doyle, F.; Bydder, G., Enhancement of Relaxation Rate with Paramagnetic Contrast Agents in NMR Imaging. *Journal of Computed Tomography* **1981,** 5, (6), 543-547.
59. Carr, D.; Brown, J.; Bydder, G.; Weinmann, H.; Speck, U.; Thomas, D.; Young, I., Intravenous Chelated Gadolinium as a Contrast Agent in NMR Imaging of Cerebral Tumours. *Lancet* **1984,** 1, (8375), 484-486.
60. Fatouros, P.; Corwin, F.; Chen, Z.; Broaddus, W.; Tatum, J.; Ge, Z.; Gibson, H.; Russ, J.; Leonard, A.; Duchamp, J.; Dorn, H., In Vitro and In Vivo Imaging Studies of a New Gadolinium Endohedral Metallofullerene MRI Contrast Agent. *Radiology* **2006,** in press.
61. Mikawa, M.; Kato, H.; Okumura, M.; Narazaki, M.; Kanazawa, Y.; Miwa, N.; Shinohara, H., Paramagnetic Water-Soluble Metallofullerenes Having the Highest Relaxivity for MRI Contrast Agents. *Bioconjugate Chemistry* **2001,** 12, (4), 510-514.
62. Kroto, H.; Heath, J.; O'Brien, S.; Curl, R.; Smalley, R., C60: Buckminsterfullerene. *Nature* **1985,** 318, (6042), 162-163.
63. Chai, Y.; Guo, T.; Jin, C.; Haufler, R.; Chibante, L.; Fure, J.; Wang, L.; Alford, J.; Smalley, R., Fullerenes with Metals Inside. *Journal of Physical Chemistry* **1991,** 95, (20), 7564-7568.
64. Bethune, D.; Johnson, R.; Salem, J.; de Vries, M.; Yannoni, C., Atoms in Carbon Cages: The Structure and Properties of Endohedral Fullerenes. *Nature* **1993,** 366, (6451), 123-128.
65. Nagase, S.; Kobayashi, K.; Akasaka, T., Endohedral Metallofullerenes: New Spherical Cage Molecules with Interesting Properties. *Bulletin of the Chemical Society of Japan* **1996,** 69, (8), 2131-2142.
66. Liu, S.; Sun, S., Recent Progress in the Studies of Endohedral Metallofullerenes. *Journal of Organometallic Chemistry* **2000,** 599, (1), 74-86.
67. Nagase, S.; Kobayashi, K.; Akasaka, T.; Wakahara, T., *Fullerenes Chemistry, Physics, and Technology*. John Wiley & Sons: New York, 2000.
68. Shinohara, H., Endohedral Metallofullerenes. *Reports on Progress in Physics* **2000,** 63, (6), 843-892.
69. Akasaka, T.; Nagase, S., *Endofullerenes: A new family of carbon clusters*. Kluwer: Dordrecht, The Netherlands, 2002.
70. Bolskar, R.; Benedetto, A.; Husebo, L.; Price, R.; Jackson, E.; Wallace, S.; Wilson, L.; Alford, J., First Soluble M@C60 Derivatives Provide Enhanced Access to Metallofullerenes and Permit in Vivo Evaluation of Gd@C60[C(COOH)2]10 as a MRI Contrast Agent. *Journal of the American Chemical Society* **2003,** 125, (18), 5471-5478.
71. Tagmatarchis, N.; Shinohara, H., Fullerenes in Medicinal Chemistry and Their Biological Applications. *Mini-Reviews in Medicinal Chemistry* **2001,** 1, (4), 339-348.
72. Toth, E.; Bolskar, R.; Borel, A.; Gonzalez, G.; Helm, L.; Merbach, A.; Sitharaman, B.; Wilson, L., Water-Soluble Gadofullerenes: Toward High-Relaxivity, pH-Responsive MRI Contrast Agents. *Journal of the American Chemical Society* **2005,** 127, (2), 799-805.

73. Kato, H.; Kanazawa, Y.; Okumura, M.; Taninaka, A.; Yokawa, T.; Shinohara, H., Lanthanoid Endohedral Metallofullerenols for MRI Contrast Agents. *Journal of the American Chemical Society* **2003,** 125, (14), 4391-4397.
74. Cagle, D.; Kennel, S.; Mirzadeh, S.; Alford, J.; Wilson, L., In Vivo Studies of Fullerene-based Materials Using Endohedral Metallofullerene Radiotracers. *Proceedings of the National Academy of Sciences of the United States of America* **1999,** 96, (9), 5182-5187.
75. Kodama, T.; Ozawa, N.; Miyake, Y.; Sakaguchi, K.; Nishikawa, H.; Ikemoto, I.; Kikuchi, K.; Achiba, Y., Structural Study of Three Isomers of Tm@C82 by 13C NMR Spectroscopy. *Journal of the American Chemical Society* **2002,** 124, (7), 1452-1455.
76. Krause, M.; Liu, X.; Wong, J.; Pichler, T.; Knupfer, M.; Dunsch, L., The electronic and vibrational structure of endohedral Tm3N@ C80 (I) Fullerene - proof of an encaged Tm3+. *Journal of Physical Chemistry A* **2005,** 109, (32), 7088-7093.
77. Ding, J.; Weng, L.-T.; Yang, S., Electronic structure of Ce@C82: An experimental study. *Journal of Physical Chemistry* **1996,** 100, (26), 11120-11121.
78. Ding, J.; Yang, S., Isolation and characterization of Pr@C82 and Pr2@C80. *Journal of the American Chemical Society* **1996,** 118, (45), 11254-11257.
79. Funasaka, H.; Sakurai, K.; Oda, Y.; Yamamoto, K.; Takahashi, T., Magnetic properties of Gd@C82 metallofullerene. *Chemical Physics Letters* **1995,** 232, (3), 273-277.
80. Stevenson, S.; Phillips, J.; Reid, J.; Olmstead, M.; Rath, S.; Balch, A., Pyramidalization of Gd3N inside a C80 cage. The synthesis and structure of Gd3N@ C80. *Chemical Communications* **2004,** 24, 2814-2815.
81. Stevenson, S.; Dorn, H.; Burbank, P.; Harich, K.; Haynes, J., J.; Kiang, C.; Salem, J.; DeVries, M.; van Loosdrecht, P.; al., e., Automated HPLC separation of endohedral metallofullerene Sc@C2n and Y@C2n fractions. *Analytical Chemistry* **1994,** 66, (17), 2675-2679.
82. Sun, B.-Y.; Sugai, T.; Nishibori, E.; Iwata, K.; Sakata, M.; Takata, M.; Shinohara, H., An anomalous endohedral structure of Eu@C82 metallofullerenes. *Angewandte Chemie, International Edition* **2005,** 44, (29), 4568-4571.
83. Wang, X.; Russ, J.; Ge, Z.; Glass, T.; Harich, K.; Cromer, F.; Gibson, H.; Dorn, H., *in progress*.
84. Stevenson, S.; Rice, G.; Glass, T.; Harlch, K.; Cromer, F.; Jordan, M.; Craft, J.; Hadju, E.; Bible, R.; Olmstead, M.; Maltra, K.; Fisher, A.; Balch, A.; Dorn, H., Small-bandgap endohedral metallofullerenes in high yield and purity. *Nature* **1999,** 401, (6748), 55-57.
85. Iezzi, E.; Cromer, F.; Stevenson, P.; Dorn, H., Synthesis of the first water-soluble trimetallic nitride endohedral metallofullerols. *Synthetic Metals* **2002,** 128, (3), 289-291.
86. Stevenson, S.; Lee, H.; Olmstead, M.; Kozikowski, C.; Stevenson, P.; Balch, A., Preparation and crystallographic characterization of a new endohedral, Lu3N @ C80. 5 (o-xylene), and comparison with Sc3N@ C80. 5 (o-xylene). *Chemistry (Weinheim an der Bergstrasse, Germany)* **2002,** 8, (19), 4528-4535.
87. Iezzi, E.; Duchamp, J.; Fletcher, K.; Glass, T.; Dorn, H., Lutetium-based trimetallic nitride endohedral metallofullerenes: new contrast agents. *Nano Letters* **2002,** 2, (11), 1187-1190.

88. Dunsch, L.; Georgi, P.; Krause, M.; Wang, C.-R., New clusters in endohedral fullerenes: The metalnitrides. *Synthetic Metals* **2003,** 135-136, 761-762.
89. Friedman, S.; DeCamp, D.; Sijbesma, R.; Srdanov, G.; Wudl, F.; Kenyon, G., Inhibition of the HIV-1 Protease by Fullerene Derivatives: Model Building Studies and Experimental Verification. *Journal of the American Chemical Society* **1993,** 115, (15), 6506-6509.
90. Fulton, D.; O'Halloran, M.; Parker, D.; Senanayake, K.; Botta, M.; Aime, S., Efficient Relaxivity Enhancement in Dendritic Gadolinium Complexes: Effective Motional Coupling in Medium Molecular Weight Conjugates. *Chemical Communications* **2005,** 4, 474-476.
91. Aime, S.; Botta, M.; Fasano, M.; Terreno, E., Prototropic and Water-Exchange Processes in Aqueous Solutions of Gd(III) Chelates. *Accounts of Chemical Research* **1999,** 32, (11), 941-949.
92. Thrash, T.; Cagle, D.; Alford, J.; Wright, K.; Ehrhardt, G.; Mirzadeh, S.; Wilson, L., Toward Fullerene-Based Radiopharmaceuticals: High-Yield Neutron Activation of Endohedral 165Ho Metallofullerenes. *Chemical Physics Letters* **1999,** 308, (3,4), 329-336.
93. Campanera, J.; Bo, C.; Poblet, J., General rule for the stabilization of fullerene cages encapsulationg trimetallic nitride templates. *Angewandte Chemie, International Edition* **2005,** 44, 7230-7233.
94. Sitharaman, B.; Bolskar, R.; Rusakova, I.; Wilson, L., Gd@C60[C(COOH)2]10 and Gd@C60(OH)x: Nanoscale Aggregation Studies of Two Metallofullerene MRI Contrast Agents in Aqueous Solution. *Nano Letters* **2004,** 4, (12), 2373-2378.
95. Wharton, T.; Wilson, L., Highly-Iodinated Fullerene as a Contrast Agent For X-ray Imaging. *Bioorganic & Medicinal Chemistry* **2002,** 10, (11), 3545-3554.
96. Stevenson, S.; Phillips, J.; Reid, J.; Olmstead, M.; Rath, S.; Balch, A., Pyramidalization of Gd3N Inside a C80 Cage. The Synthesis and Structure of Gd3N@C80. *Chemical communications* **2004,** 24, 2814-2815.
97. Krause, M.; Dunsch, L., Gadolinium Nitride Gd3N in Carbon Cages: The Influence of Cluster Size and Bond Strength. *Angewandte Chemie, International Edition* **2005,** 44, (10), 1557-1560.
98. Stevenson, S.; Lee, H.; Olmstead, M.; Kozikowski, C.; Stevenson, P.; Balch, A., Preparation and Crystallographic Characterization of a New Endohedral, Lu3N@C80⩤5(o-xylene), and Comparison with Sc3N@C80⩤5(o-xylene). *Chemistry--A European Journal* **2002,** 8, (19), 4528-4535.
99. M. J. Frisch, G. W. T., H. B. Schlegel, G. E. Scuseria, M. A. Robb, J. R. Cheeseman, V. G. Zakrzewski, J. A. Montgomery, Jr., R. E. Stratmann, J. C. Burant, S. Dapprich, J. M. Millam, A. D. Daniels, K. N. Kudin, M. C. Strain, O. Farkas, J. Tomasi, V. Barone, M. Cossi, R. Cammi, B. Mennucci, C. Pomelli, C. Adamo, S. Clifford, J. Ochterski, G. A. Petersson, P. Y. Ayala, Q. Cui, K. Morokuma, P. Salvador, J. J. Dannenberg, D. K. Malick, A. D. Rabuck, K. Raghavachari, J. B. Foresman, J. Cioslowski, J. V. Ortiz, A. G. Baboul, B. B. Stefanov, G. Liu, A. Liashenko, P. Piskorz, I. Komaromi, R. Gomperts, R. L. Martin, D. J. Fox, T. Keith, M. A. Al-Laham, C. Y. Peng, A. Nanayakkara, M. Challacombe, P. M. W. Gill, B. Johnson, W. Chen, M. W. Wong, J. L. Andres, C. Gonzalez, M. Head-Gordon, E. S. Replogle, and J. A. Pople *Gaussian 98*, Gaussian, Inc.: Pittsburgh, PA, 2001.

100. Frisch, M. J. T., G. W.; Schlegel, H. B.; Scuseria, G. E.; Robb, M. A.; Cheeseman, J. R.; Montgomery, Jr., J. A.; Vreven, T.; Kudin, K. N.; Burant, J. C.; Millam, J. M.; Iyengar, S. S.; Tomasi, J.; Barone, V.; Mennucci, B.; Cossi, M.; Scalmani, G.; Rega, N.; Petersson, G. A.; Nakatsuji, H.; Hada, M.; Ehara, M.; Toyota, K.; Fukuda, R.; Hasegawa, J.; Ishida, M.; Nakajima, T.; Honda, Y.; Kitao, O.; Nakai, H.; Klene, M.; Li, X.; Knox, J. E.; Hratchian, H. P.; Cross, J. B.; Bakken, V.; Adamo, C.; Jaramillo, J.; Gomperts, R.; Stratmann, R. E.; Yazyev, O.; Austin, A. J.; Cammi, R.; Pomelli, C.; Ochterski, J. W.; Ayala, P. Y.; Morokuma, K.; Voth, G. A.; Salvador, P.; Dannenberg, J. J.; Zakrzewski, V. G.; Dapprich, S.; Daniels, A. D.; Strain, M. C.; Farkas, O.; Malick, D. K.; Rabuck, A. D.; Raghavachari, K.; Foresman, J. B.; Ortiz, J. V.; Cui, Q.; Baboul, A. G.; Clifford, S.; Cioslowski, J.; Stefanov, B. B.; Liu, G.; Liashenko, A.; Piskorz, P.; Komaromi, I.; Martin, R. L.; Fox, D. J.; Keith, T.; Al-Laham, M. A.; Peng, C. Y.; Nanayakkara, A.; Challacombe, M.; Gill, P. M. W.; Johnson, B.; Chen, W.; Wong, M. W.; Gonzalez, C.; and Pople, J. A. *Gaussion 03, Revision C.02*, Gaussian, Inc.: Wallingford, CT, 2004.
101. Becke, A., Density-Functional Thermochemistry. III. The Role of Exact Exchange. *Journal of Chemical Physics* **1993,** 98, (7), 5648-5652.
102. Lee, C.; Yang, W.; Parr, R., Development of the Colle-Salvetti Correlation-Energy Formula into a Functional of the Electron Density. *Physical Review B* **1988,** 37, (2), 785-789.
103. Basis sets were obtained from the Extensible Computational Chemistry Environment Basis Set Database, V., as developed and distributed by the Molecular Science Computing Facility, Environmental and Molecular Sciences Laboratory which is part of the Pacific Northwest Laboratory, P.O. Box 999, Richland, Washington 99352, USA, and funded by the U.S. Department of Energy. The Pacific Northwest Laboratory is a multi-program laboratory operated by Battelle Memorial Institute for the U.S. Department of Energy under contract DE-AC06-76RLO 1830. Contact Karen Schuchardt for further information. In., In.
104. Dennington II, R.; Keith, T.; Millam, J.; Eppinnett, K.; Hovell, W.; Gilliland, R. *GaussView Version 3.09*, Semichem, Inc.: Shawnee Mission, KS, 2003.
105. Hatch, G.; Kreilick, R., NMR of Some Nitroxide Radicals: 13C Coupling Constants. *Journal of Chemical Physics* **1972,** 57, (9), 3696-3699.
106. Briere, R.; Lemaire, H.; Rassat, A., Nitroxides. XV. Synthesis and investigation of free, stable piperidinyl and pyrrolidinyl radicals. *Bulletin de la Societe Chimique de France* **1965,** 11, 3273-3283.
107. Briere, R.; Chapelet-Letourneux, G.; Lemaire, H.; Rassat, A., Nitroxides. XXXV. Electron-carbon-13 hyperfine interaction; nitroxide radicals selectively labeled to the nitrogen. *Molecular Physics* **1971,** 20, (2), 211-224.
108. Rissi, E.; Fileti, E.; Canuto, S., Rayleigh and raman light scattering in hydrogen-bonded acetonitrile-water. *Theoretical Chemistry Accounts* **2003,** 110, 360-366.
109. Coussan, S.; Bouteiller, Y.; Perchard, J.; Brenner, V.; Millie, P.; Zheng, W.; Talbot, F., Methanol-acetonitrile complexes trapped in argon and nitrogen matrices: Infrared induced isomerization and theoretical calculations. *Journal of Chemical Physics* **1999,** 110, (20), 10046-10057.
110. George, W.; Jones, B.; Lewis, R.; Price, J., Computations of medium strength hydrogen bonds-complexes of mono- and bi-functional carbonyl and nitrile compounds with hydrogen chloride. *Physical Chemistry Chemical Physics* **2000,** 2, 4910-4917.

111. Buck, M.; Karplus, M., Hydrogen bond energetics: A simulation and statistical analysis of N-methyl acetamide (NMA), water, and human lysozyme. *Journal of Physical Chemistry B* **2001,** 105, 11000-11015.
112. Lancelot, G.; Helene, C., Model studies of interactions between nucleic acids and proteins: hydrogen bonding of amides with nucleic acid bases. *Nucleic Acids Research* **1979,** 6, (3), 1063-1072.
113. Senti, F.; Harker, D., The crystal structure of rhombohedral acetamide. *Journal of the American Chemical Society* **1940,** 62, 2008-2019.
114. Song, L. Liquid Phase 13C Dynamic Nuclear Polarization Study of Monosubstituted Aromatic Compounds. Virginia Polytechnic Institute and State University, Blacksburg, VA, 1997.
115. Sun, Z. Studies of liquid phase intermolecular interactions utilizing 1H and 13C dynamic nuclear polarization and nuclear magnetic resonance techniques. Virginia Tech, Blacksburg, VA, 1996.
116. TEACHSPIN, *Pulsed NMR spectrometer (PS1-B) manual*. Buffalo, NY.
117. Nath, S.; Pal, H.; Sapre, A.; Bubnov, V.; Estrin, Y.; Parnyuk, T.; Koltover, V., Aggregation of endometallofullerene Y@C82 in polar solvents. *Fullerenes, Nanotubes, and Carbon Nanostructures* **2004,** 12, (1&2), 53-57.
118. Kraetschmer, W.; Lamb, L.; Fostiropoulos, K.; Huffman, D., Solid C60: a new form of carbon. *Nature* **1990,** 347, (6291), 354-358.
119. Wang, X. Master's Thesis. Virginia Tech, Blacksburg, VA, 2006.
120. Boumans, P., *Inductively coupled plasma emission spectroscopy. Part I. Methodology, instrumentation, and performance*. John Wiley & Sons: Eindhoven, The Netherlands, 1987.
121. Skoog, D.; Holler, F.; Nieman, T., *Principles of instrumental analysis*. Fifth ed.; Harcourt Brace College Publishers and Saunders College Publishing: 1998.

# Vita

Jennifer Lynn Russ was born on April 21, 1979 in Cumberland, MD. Her parents are Roger and Tammy Kile, and she has one sister, Jessica Mick. She married Nicholas J. Russ on September 24, 2005. She graduated with a Bachelor of Science degree in Chemistry and Mathematics from Frostburg State University, Frostburg, MD in May 2001. In the fall of 2001, she began graduate school at Virginia Polytechnic Institute and State University. She studied under the guidance of Dr. Richard Gandour studying the prediction of the critical micelle concentration of surfactants using solvation energy calculations, and graduated with a Master of Science in Physical Chemistry in the fall of 2004. Immediately following completion of her Master's degree, she began her PhD studies at Virginia Tech under the direction of Dr. Harry Dorn. She is studying nuclear and electron interactions between paramagnetic molecules and substrates using NMR and density functional theory calculations, which lead to the completion of her PhD work in May 2006.